Simulation and Characterization of Energetic Disorder and Recombination in Organic Solar Cells

Von der Fakultät für Ingenieurwissenschaften,
Abteilung Elektrotechnik und Informationstechnik
der Universität Duisburg-Essen

zur Erlangung des akademischen Grades

Doktor der Naturwissenschaften

genehmigte Dissertation

von

Paula Hartnagel
aus
Hamburg

Gutachter: Prof. Dr. Thomas Kirchartz
Gutachter: Prof. Dr. René A.J. Janssen
Tag der mündlichen Prüfung: 09. April 2024

DOI: 10.17185/duepublico/81933
URN: urn:nbn:de:hbz:465-20240611-113310-3

Abstract

Organic solar cells are constantly improving towards the milestone of 20% power-conversion efficiency. In the search for more and more efficient and stable material systems, some characterization techniques for reporting the newly processed solar cells have been established. Asides from classic current-voltage and external quantum efficiency measurements, light-intensity dependent measurements of the short-circuit current density and quantification of the energetic disorder are frequently used to characterize recombination in organic solar cells. In this thesis, I deliver deeper theoretical understanding on these measurement techniques with the help of device simulations and measurements on the eco-friendly material system PBDB-TF-T1:BTP-4F-12.

Firstly, I discuss how taking into account the spatial dependences inside the solar cell is essential in analyzing the light-intensity dependence of the short-circuit current density. Numerical drift-diffusion simulations reveal that both trap-assisted recombination and direct recombination feature a linear dependence between the short-circuit current density and the irradiance over a wide range of light intensities. Non-intuitively, the filling of shallow defect states and space-charge effects caused by charged defect states can result in sublinearity. Therefore, the traditional evaluation of this measurement technique has to be adapted accordingly.

Secondly, I focus on the characterization of these shallow defect states that often originate in energetic disorder, which is especially important for such structurally disordered systems as organic solar cells. Both a meta-analysis of literature data as well as and the experiments show that different techniques of characterizing this energetic disorder yield different results. With the help of simulations, I show that measurements based on electrical scanning of the density of states potentially probe different energy regimes compared to optical techniques. Further discrepancies are caused by the higher sensitivity of electrical measurements to transport issues.

After discussing these specific characterization techniques that focus on classifying the dominant recombination mechanisms or identifying one single material parameter, I propose an alternative method for estimating multiple material parameters at once by fitting experimental data. To speed up computation, I utilize a neural network as a surrogate model for the numerical simulation software. The application of the fitting routine highlights the importance of a sensible choice of fitting parameters. This work thereby sets an example, how machine learning can facilitate highly dimensional fitting processes and the exploration of the entire parameter space.

Zusammenfassung

Organische Solarzellen verbessern sich stetig hin zum Meilenstein von 20% Effizienz. Auf der Suche nach immer effizienteren und stabileren Materialsystemen haben sich einige Charakterisierungsmethoden etabliert, mit denen neuprozessierte Solarzellen vorgestellt werden. Neben klassischen Strom-Spannungs- und externen Quanteneffizienzmessungen werden beleuchtungsabhängige Messungen der Kurzschlussstromdichte und Quantifizierung der energetischen Unordnung häufig verwendet, um Rekombination in organischen Solarzellen zu charakterisieren. In dieser Arbeit liefere ich tieferes, theoretisches Verständnis dieser Messtechniken mit der Hilfe von Simulationen und Messungen an dem umweltfreundlichen Materialsystem PBDB-TF-T1:BTP-4F-12.

Als Erstes diskutiere ich, wie das Berücksichtigen von Ortsabhängigkeiten essenziell ist zur Analyse der Beleuchtungsabhängigkeit der Kurzschlussstromdichte. Numerische Drift-Diffusions-Simulationen zeigen, dass sowohl Rekombination über einen Defekt als auch direkte Rekombination eine lineare Abhängigkeit zwischen der Kurzschlussstromdichte und der Beleuchtungsstärke über eine weite Spanne an Lichtintensitäten aufweisen. Stattdessen können das Füllen von flachen Defektzuständen und Raumladungseffekte durch geladene Defekte Sublinearität hervorrufen. Daher muss die traditionelle Interpretation dieser Messtechnik dementsprechend angepasst werden.

Als Zweites untersuche ich die Charakterisierung dieser flachen Defektzuständen, die häufig ihren Ursprung in energetischer Unordnung haben, welche besonders relevant ist für organische Solarzellen aufgrund ihrer strukturellen Unordnung. Sowohl die Metaanalyse der Literatur als auch meine Experimente zeigen, dass unterschiedliche Techniken der Charakterisierung dieser Unordnung unterschiedliche Ergebnisse liefern. Durch Simulationen zeige ich, dass elektrische Verfahren potenziell in einem anderen Energieregime messen als optischen Messtechniken. Die höhere Anfälligkeit von elektrischen Messungen gegenüber Transportproblemen verursacht weitere Diskrepanzen.

Nach dieser Diskussion der Klassifizierung des dominanten Rekombinationsmechanismus und der Identifizierung eines einzelnen Materialparameters stelle ich eine alternative Methode vor, um mehrere Materialparameter durch Fitten von experimentellen Daten auf einmal abzuschätzen. Um die Berechnung zu beschleunigen, nutze ich ein neuronales Netzwerk als Behelfsmodell anstelle der numerischen Simulationssoftware. Die Anwendung der Fitroutine zeigt, wie wichtig eine sinnvolle Auswahl der Fitparameter ist. Dadurch setzt diese Arbeit ein Beispiel, wie maschinelles Lernen hochdimensionales Fitten und die Erkundung des gesamten Parameterraums ermöglichen kann.

Contents

1 Introduction

The international energy agency predicts a need for 633 GW of solar power installed annually between 2030 and 2050 to achieve the goal of carbon neutrality by 2050, meaning a 20-fold of the capacity installed in 2020 is required.[1] While silicon solar cells are already a mature technology that is used for reaching this goal, thin-film technologies could decrease the material and energy costs in manufacturing.[2,3] Such light-weight and potentially flexible thin-film solar cells are also highly relevant in the market of small autonomous devices such as WiFi receivers, sensors or GPS trackers. Around a trillion autonomous devices are projected to require a power source by 2035, which could not be supplied with batteries due to limiting lithium production.[4] In contrast, especially thin-film solar cells consisting of organic semiconductors bring the advantage that they only require elements which are abundant such as carbon, nitrogen or oxygen. The high absorption coefficients of these organic semiconductors enable particularly thin layers of the photoactive material down to 100 nm.[5] Thereby, overall less material is used compared to crystalline silicon solar cells. Even though these organic molecules are sometimes very expensive on the lab scale,[6,7] the solution processability of organic solar cells promises easy scalability to industrial fabrication using roll-to-roll printing.[8–10]

To achieve this goal of commercialization, improvements in the cheap synthesis of the organic semiconductors and efficiency and stability of the solar cells have to be made.[7] Organic solar cell efficiencies have improved drastically within the last two decades from 3%[11] to 19% in a single-junction[12] and 20% as a tandem solar cell,[13] but still lag behind other thin-film technologies such as perovskite solar cells.[14] For further improvements, the knowledge of recombination and transport properties inside

the solar cell is crucial. Only by identifying the limiting factors, strategic changes can be made. However, a major obstacle in the development of more efficient and stable organic solar cells is the fact that their device physics is not fully understood yet. The disordered nature of the organic semiconductor materials makes it difficult to apply models to organic photovoltaics that were established for crystalline solar cells. Therefore, to characterize the properties of an organic solar cell, some measurement techniques have been adapted from traditional photovoltaics.[15–18] However, the limited understanding of the organic solar cells' device physics always bears the risk of misinterpreting measurement results. Also, the most commonly applied characterization techniques often owe their popularity to the simplicity of the models used for interpretation. While a detailed theoretical framework has already been proposed for some of the measurement techniques,[15, 19] others still lack validation or a fair comparison between different approaches.

One of the most frequently used tools to identify dominant recombination mechanisms is in organic photovoltaics is light-intensity dependent measurements of the short-circuit current density.[20–45] However, the rationale underlying its interpretation neglects any dimensionality of the solar cell. The same issue underlies some techniques to quantify energetic disorder caused by the organic semiconductor's structural disorder. As energetic disorder is often considered significant for the solar cell's performance,[46–48] new material systems are regularly characterized in terms of their energetic disorder. To do so, a variety of techniques is used, but an overall comparison is currently missing. Therefore, this thesis delivers such a comparison, a more in-depth understanding of the physics behind these measurements as well as behind the light-intensity dependence of the short-circuit current density with the help of numerical device simulations.

For this purpose, Chapter 2 first introduces the basics of solar cell physics that are also relevant to organic photovoltaics. These include the fundamental differential equations that are numerically solved for the simulations in this work. Afterwards, I specify the properties characteristic to organic solar cells in Chapter 3 and present the materials, experiments and simulation tools used in this work. To highlight the need for more advanced interpretation of popular measurements, in Chapter 4, I first analyze a set of data on one material system according to the models prevalent in literature. Then, Chapter 5 goes more into detail on the device physics behind the light-intensity dependence of the short-circuit current density. Next, Chapter 6 high-

lights discrepancies in literature and measurements between different approaches to characterizing energetic disorder and finds explanations for them. Thereby, I provide a more theoretically sound framework to interpret some of the most frequently used characterization techniques in organic photovoltaics with the help of numerical simulations. In Chapter 7, I then suggest a workflow, in which these device simulations can be used in a combination with machine learning for the estimation of material properties. Lastly, I summarize the findings of this thesis in Chapter 8 and give an outlook how the routine of material-parameter estimation using machine learning can aid future characterization of organic solar cells.

2
Fundamentals of Solar Cell Physics

This chapter serves as an introduction to the physics of photovoltaics. It provides the basic equations and terminology used in this work to describe the working principles and interpret measurements. For this purpose, Chapter 2.1 first introduces the photovoltaic principle on the example of an ideal solar cell in the Shockley-Queisser limit. Chapter 2.2 focuses on the energetics of a solar cell and explains how to interpret band diagrams. Finally, in Chapter 2.3, I present the continuity equations and explain how charge generation, recombination and transport make up the current density inside a solar cell.

2.1. The Shockley-Queisser Model

To understand the basic working principles of a solar cell, it is helpful to first look at the ideal solar cell. The theoretical efficiency limit of such a device was introduced by Shockley and Queisser in 1961.[49] Their assumptions for an ideal solar cell include perfect absorption properties. More specifically, the absorptance

$$a(E) = \Theta(E - E_\mathrm{g}), \tag{2.1}$$

where E_g is the band-gap energy. So, all photons with an energy below the energy gap are transmitted whereas all photons with energies above E_g are absorbed.[50] Even without the solar irradiation, photons reach the solar cell from the surrounding's black body radiation $\Phi_\mathrm{bb}(E, T_\mathrm{sur})$ which depends on the ambient temperature T_sur as illustrated by the schematic in Figure 2.1a. Therefore, the photon flux $\Phi_\mathrm{sur}(E, T_\mathrm{sur})$ absorbed by the

solar cell from the surrounding is[51]

$$\Phi_{\mathrm{sur}} = a(E)\Phi_{\mathrm{bb}}(E, T_{\mathrm{sur}}). \tag{2.2}$$

The absorbed photons each create exactly one electron-hole pair. When an incoming photon has an energy higher than the band gap energy E_{g}, the excited electron will instantaneously thermalize to the conduction band edge. The current density resulting from this absorption of the black-body spectrum of the surrounding is the saturation-current density[52]

$$J_{0,\mathrm{SQ}} = q \int_0^\infty a(E)\Phi_{\mathrm{bb}}(E, T_{\mathrm{sur}})\mathrm{d}E \tag{2.3}$$

$$= q \int_{E_{\mathrm{g}}}^\infty \Phi_{\mathrm{bb}}(E, T_{\mathrm{sur}})\mathrm{d}E \tag{2.4}$$

with the elementary charge q. When looking at the black-body photon spectrum illustrated in Figure 2.1a, this saturation-current density represents the area below the curve and above the band gap marked in blue. In the Shockley-Queisser model, the only loss mechanism of electron-hole pairs is radiative recombination. In this process, according to the principle of detailed balance,[53] the emissivity of the solar cell is equal to its absorptance, yielding an emitted photon flux

$$\Phi_{\mathrm{em}} = a(E)\Phi_{\mathrm{bb}}(E, T_{\mathrm{SC}}), \tag{2.5}$$

where T_{SC} is the temperature of the solar cell. When integrating the emitted photon flux over the entire energy range, the recombination-current density[51,52]

$$J_{\mathrm{rec,SQ}} = q \int_0^\infty a(E)\Phi_{\mathrm{bb}}(E, T_{\mathrm{SC}}) \exp\left(\frac{qV}{k_{\mathrm{B}}T_{\mathrm{SC}}}\right) \mathrm{d}E. \tag{2.6}$$

The exponential term containing the applied voltage V and the thermal energy $k_{\mathrm{B}}T_{\mathrm{SC}}$ accounts for changes in the chemical potential when the solar cell is brought out of equilibrium by an external voltage. Using the step function absorptance from Equation (2.1), the recombination-current density can be further simplified as

$$J_{\mathrm{rec,SQ}} = q \int_{E_{\mathrm{g}}}^\infty \Phi_{\mathrm{bb}}(E, T_{\mathrm{SC}}) \exp\left(\frac{qV}{k_{\mathrm{B}}T_{\mathrm{SC}}}\right) \mathrm{d}E. \tag{2.7}$$

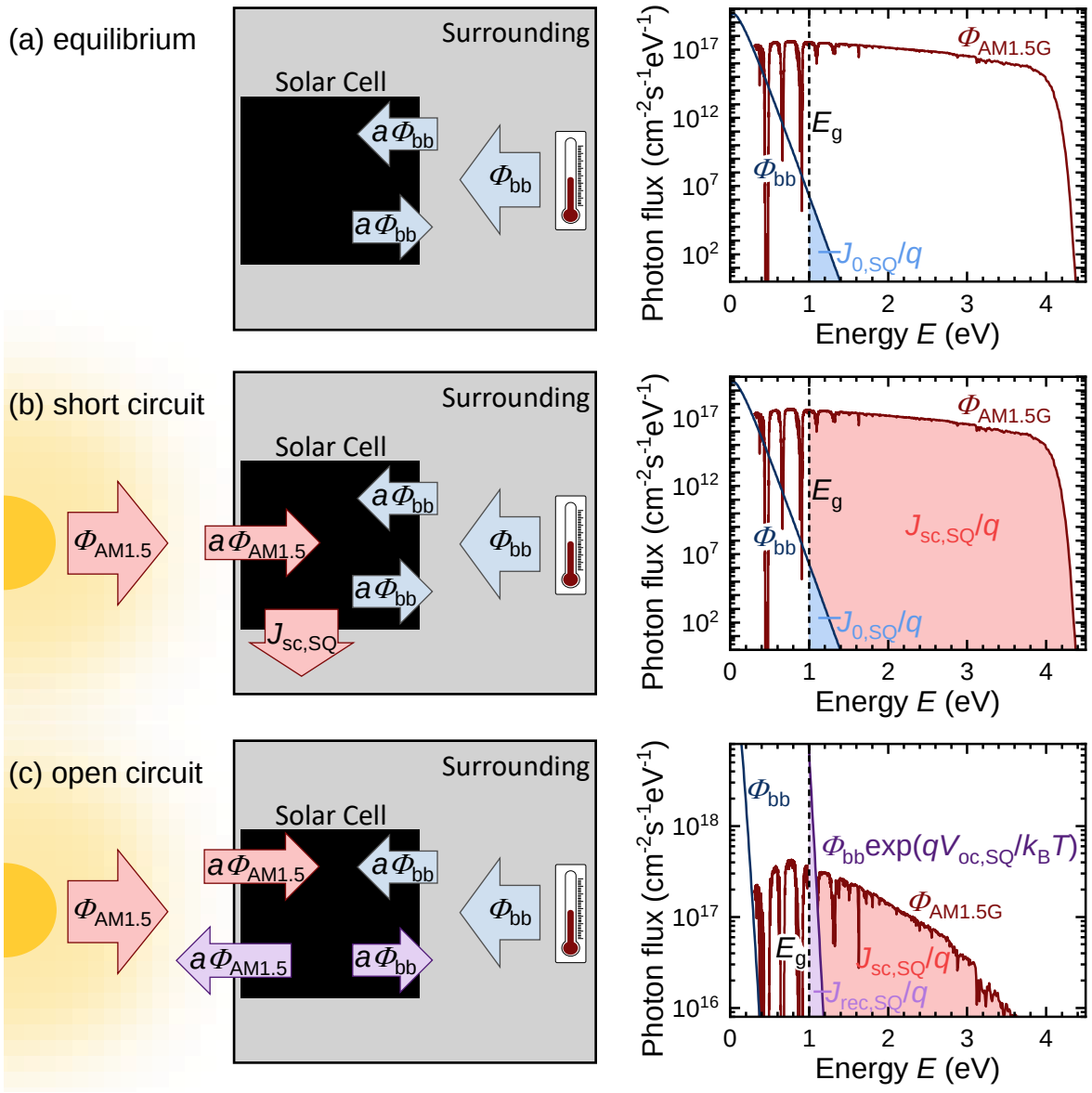

Figure 2.1: Schematics and photon spectra to illustrate the principles of the Shockley-Queisser model. (a) In equilibrium, the blue area under the black-body spectrum Φ_{bb} is absorbed and emitted by the solar cell. (b) Under solar illumination at short circuit, the area underneath the solar spectrum $\Phi_{\mathrm{AM1.5}}$ marked in red is extracted as the short-circuit current density $J_{\mathrm{sc,SQ}}$. (c) At open circuit, no current is extracted and all light that is absorbed from the sun and the surrounding is emitted back by the solar cell and marked in purple. The emitted black-body spectrum is shifted according to the open-circuit voltage $V_{\mathrm{oc,SQ}}$.

Under the assumption that the solar cell is in thermal equilibrium with its surrounding, where the temperature of the charge carriers $T = T_{\mathrm{SC}} = T_{\mathrm{sur}}$,[50] one can simplify the

recombination current density to

$$J_{\mathrm{rec,SQ}} = J_{0,\mathrm{SQ}} \exp\left(\frac{qV}{k_{\mathrm{B}}T}\right). \tag{2.8}$$

In addition to an applied voltage, the solar cell can also be brought out of equilibrium by an incoming photon flux $\Phi_{\mathrm{AM1.5}}$ from the sun as shown in Figure 2.1b under short-circuit conditions. This solar spectrum represents the part of the sun's black body radiation that reaches the surface of the earth at an air mass of 1.5 (AM1.5) and is plotted in Figure 2.1 in red. When integrating the part of the solar spectrum that is absorbed by the solar cell, one gets the short-circuit current density[52]

$$J_{\mathrm{sc,SQ}} = q \int_0^\infty a(E)\Phi_{\mathrm{AM1.5}}(E)\mathrm{d}E \tag{2.9}$$

$$= q \int_{E_{\mathrm{g}}}^\infty \Phi_{\mathrm{AM1.5}}(E)\mathrm{d}E, \tag{2.10}$$

which is marked as the red area underneath the solar spectrum in Figure 2.1b. When adding up all incoming and outgoing current densities to the total current density J_{SQ} in the Shockley-Queisser model, we get[52]

$$J_{\mathrm{SQ}} = J_{\mathrm{rec,SQ}} - J_{0,\mathrm{SQ}} - J_{\mathrm{sc,SQ}} \tag{2.11}$$

$$= J_{0,\mathrm{SQ}}(\exp\left(\frac{qV}{k_{\mathrm{B}}T}\right) - 1) - J_{\mathrm{sc,SQ}} \tag{2.12}$$

$$= J_{\mathrm{d,SQ}} - J_{\mathrm{sc,SQ}}, \tag{2.13}$$

where $J_{\mathrm{d,SQ}}$ is the current density of the diode in the dark, which is shifted in the fourth quadrant by the short-circuit current density $J_{\mathrm{sc,SQ}}$. Another characteristic parameter for solar cell characterization is the intercept with the x-axis, the open-circuit voltage $V_{\mathrm{oc,SQ}}$. At this point, all radiation that is absorbed from the sun and the surrounding is reemitted, which is shown in the schematic of Figure 2.1c in purple. Therefore, no net current density is flowing $J_{\mathrm{SQ}}(V_{\mathrm{oc,SQ}}) = 0$. Thus, Equation (2.12) can be rewritten as

$$J_{\mathrm{rec,SQ}}(V_{\mathrm{oc,SQ}}) = J_{0,\mathrm{SQ}} + J_{\mathrm{sc,SQ}}, \tag{2.14}$$

which means the purple area in Figure 2.1c would be equivalent to the sum of the red and blue area on a linear scale. Now, solving Equation (2.14) for the voltage yields the

open-circuit voltage in the Shockley-Queisser limit[52]

$$V_{\mathrm{oc,SQ}} = \frac{k_{\mathrm{B}}T}{q} \ln\left(\frac{J_{\mathrm{sc,SQ}}}{J_{0,\mathrm{SQ}}} + 1\right) \tag{2.15}$$

$$= \frac{k_{\mathrm{B}}T}{q} \ln\left(\frac{\int_{E_{\mathrm{g}}}^{\infty} \Phi_{\mathrm{AM1.5}}(E,T)\mathrm{d}E}{\int_{E_{\mathrm{g}}}^{\infty} \Phi_{\mathrm{bb}}(E,T)\mathrm{d}E} + 1\right). \tag{2.16}$$

This voltage is the maximum open-circuit voltage that is theoretically achievable when operating under the assumptions of the Shockley-Queisser model. It generally increases with the band gap energy E_{g}, which can be seen in Figure 2.2a, which shows the total current density J_{SQ} as a function of voltage V for different band gaps E_{g}. It also illustrates how the short-circuit current density $J_{\mathrm{sc,SQ}}$ decreases with an increasing band gap as less light can be absorbed. However, both at short and open circuit, no power density P can be extracted from a solar cell with current density J, since[54]

$$P = J\ V. \tag{2.17}$$

Instead, the power density, which is plotted in Figure 2.2a in green, is highest at some point under forward bias. The voltage at this point is consequently called the maximum-power point voltage V_{mpp}, and the corresponding current density $J_{\mathrm{mpp}} = -J(V_{\mathrm{mpp}})$.[54] The achievable power can therefore be maximized, when the maximum-power point voltage and current density move towards the open-circuit voltage and the short-circuit current density. For that reason, another figure-of-merit for solar cell performance is the fill factor[54]

$$FF = \frac{V_{\mathrm{mpp}}J_{\mathrm{mpp}}}{V_{\mathrm{oc}}J_{\mathrm{sc}}}, \tag{2.18}$$

which describes the ratio of the maximum power and the product of open-circuit voltage V_{oc} and short-circuit current density J_{sc} of any solar cell. The most frequently used figure-of-merit is the power-conversion efficiency η, though. It shows, how much of the power density of the incoming light, the irradiance E_{e}, is converted into electrical power and is therefore given by [52]

$$\eta = \frac{V_{\mathrm{mpp}}J_{\mathrm{mpp}}}{E_{\mathrm{e}}}. \tag{2.19}$$

Figure 2.2b shows this power-conversion efficiency η_{SQ} in the Shockley-Queisser limit

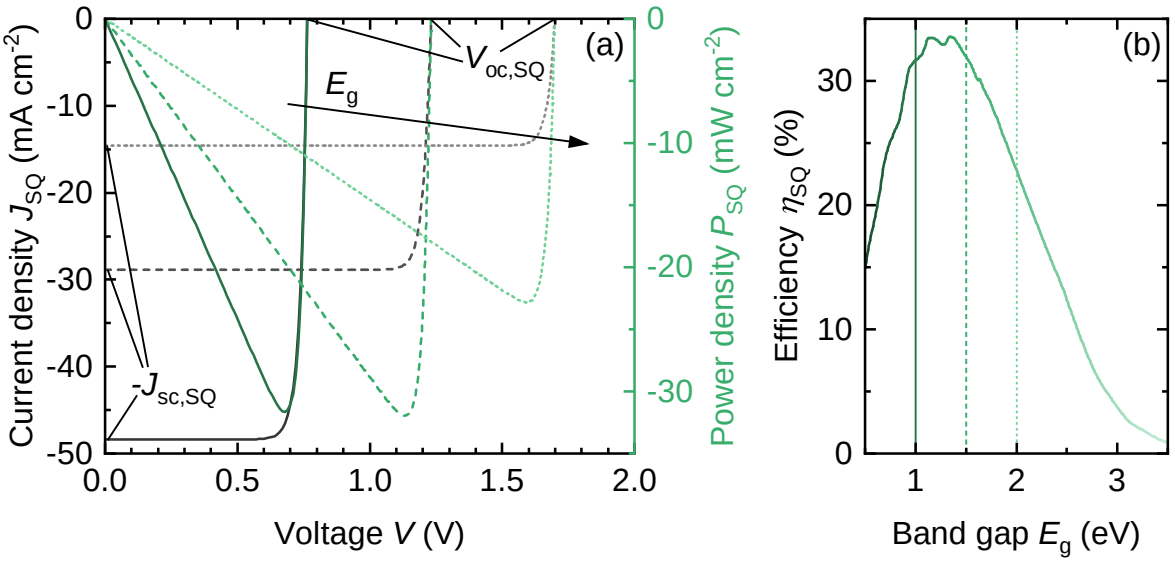

Figure 2.2: (a) Current density J_{SQ} as a function of voltage V according to the Shockley-Queisser model at three different band gaps E_g. At $V = 0$, the short-circuit current density $J_{sc,SQ}$ is flowing, while there is no net-current flow at $V = V_{oc,SQ}$. The green lines are the corresponding power densities P_{SQ} in the Shockley-Queisser model for each JV characteristic. (b) Resulting efficiency η_{SQ} as a function of band gap E_g. A maximum efficiency for the solar spectrum is reached between 1 and 1.5 eV.

as a function of band-gap energy E_g, illustrating how there is an optimum band gap that balances the trade-off between absorption losses and the operating voltage. The dents in the curve stem from the absorption bands in the solar spectrum. Therefore, the Shockley-Queisser model facilitates on the one hand the finding of an optimum band gap for the solar spectrum and on the other hand yields theoretical limitations for the performance parameters of a solar cell such as the efficiency η.

2.2. Understanding Band Diagrams

As introduced in the Shockley-Queisser limit, even in equilibrium, there are always charge carriers present inside the solar cell that make up the saturation-current density J_0. In consequence of the band gap dependence of J_0, this intrinsic carrier concentration n_i^2 also depends on the band gap E_g according to [55]

$$n_i^2 = N_C N_V \exp\left(\frac{-E_g}{k_B T}\right), \tag{2.20}$$

where N_C and N_V are the densities of states in the conduction and valence band. These densities of states are filled according to the position of the Fermi level E_F relative to the band edge. Therefore, in a band diagram in equilibrium as shown in Figure 2.3a, the small difference between conduction band edge E_C and Fermi energy E_F near the cathode indicates a higher concentration of electrons and similarly the small difference to the valence band edge E_V at the anode causes a higher hole concentration. This energy difference remains relevant also when the solar cell is brought out of equilibrium by illumination like in the band diagram in Figure 2.3b. Here, the illumination causes a splitting of the Fermi level into a quasi-Fermi level E_qFn for electrons and E_qFp for holes. Now, the electron concentration n in the conduction band is given by[56]

$$n = N_\mathrm{C} \exp\left(\frac{E_\mathrm{qFn} - E_\mathrm{C}}{k_\mathrm{B}T}\right) \tag{2.21}$$

and the hole concentration p follows as

$$p = N_\mathrm{V} \exp\left(\frac{E_\mathrm{V} - E_\mathrm{qFp}}{k_\mathrm{B}T}\right). \tag{2.22}$$

In Figure 2.3b, the quasi-Fermi levels change with the position x in the active layer. This gradient in the quasi-Fermi levels is related to a current flow inside the device. More specifically, the electron-current density[57]

$$J_\mathrm{n} = n\mu_\mathrm{n}\frac{\mathrm{d}E_\mathrm{qFn}}{\mathrm{d}x} \tag{2.23}$$

with the electron mobility μ_n and the hole-current density[57]

$$J_\mathrm{p} = p\mu_\mathrm{p}\frac{\mathrm{d}E_\mathrm{qFp}}{\mathrm{d}x}, \tag{2.24}$$

where μ_p is the hole mobility. Therefore, a low charge-carrier density can be compensated by a high mobility or Fermi-level gradient and vice-versa. When the applied voltage V is increased as shown in Figure 2.3c, the potential difference of the contacts reflects this voltage. When operating the solar cell at open circuit, the quasi-Fermi levels are flat as displayed in Figure 2.3d and there is no current flow inside the solar cell according to (2.23) and (2.24). Therefore, in the entire solar cell, the quasi-Fermi level splitting is approximately equal to the potential difference of the contacts, which is qV_oc.

So, the quasi-Fermi levels are related to the carrier concentrations and the current

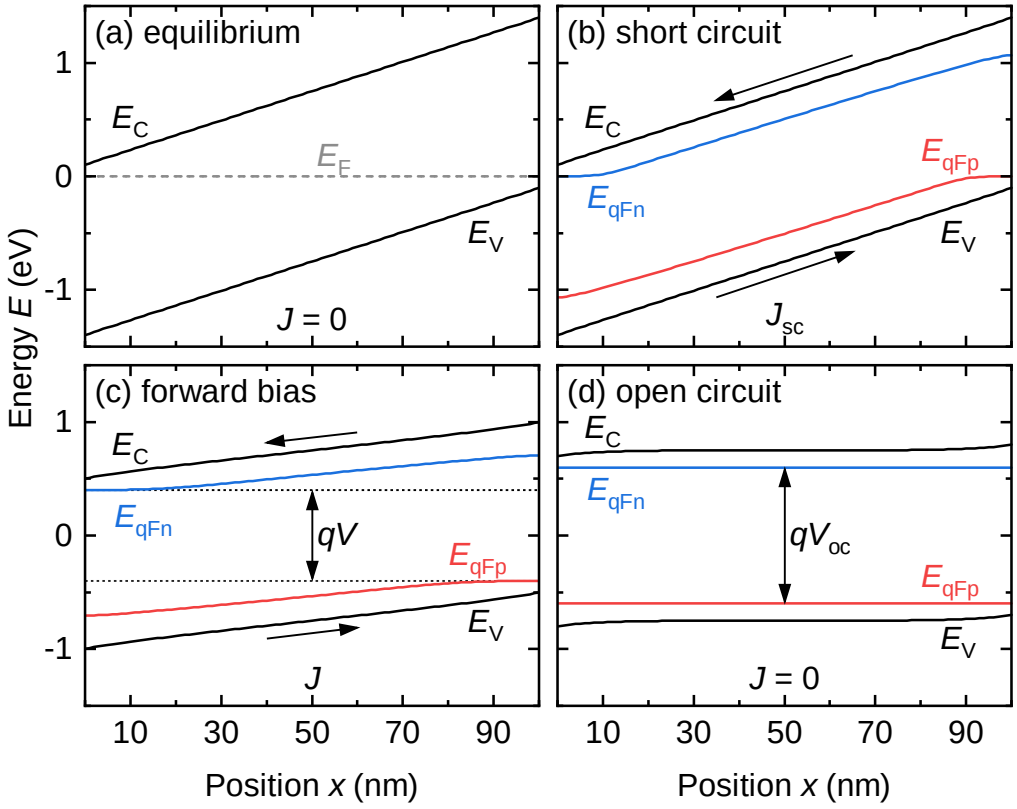

Figure 2.3: Band diagrams at different characteristic working points of the solar cell: (a) at equilibrium and under illumination (b) at short circuit, (c) under forward bias and (d) at open circuit. The potential difference of the injecting contacts reflects the applied voltage V. At open circuit, the splitting of the quasi-Fermi levels gives the open-circuit voltage V_{oc}.

flow inside the solar cell. However, also the conduction and valence band themselves are related to the carrier density via the electrostatic potential φ, which is linked to the electric field F and the charge density ρ via Poisson's equation

$$\frac{\mathrm{d}^2\varphi(x)}{\mathrm{d}x^2} = -\frac{\mathrm{d}F(x)}{\mathrm{d}x} = -\frac{\rho(x)}{\varepsilon_0\varepsilon_{\mathrm{r}}}. \tag{2.25}$$

Here, ε_0 is the vacuum permittivity and ε_{r} the relative permittivity of the material.[58] The effect of Poisson's equation is illustrated in Figure 2.4a, where a positive space charge near the anode on the right causes an upward bending of the bands. In this so-called space-charge region, there is a high electric field since the slope of the bands is high, which in turn results in a low-field region where the space charge is low. Such space-charge effects are especially relevant for materials with a low relative dielectric permittivity ε_{r}. When ε_{r} becomes infinitely high, the right side of Poisson's equation

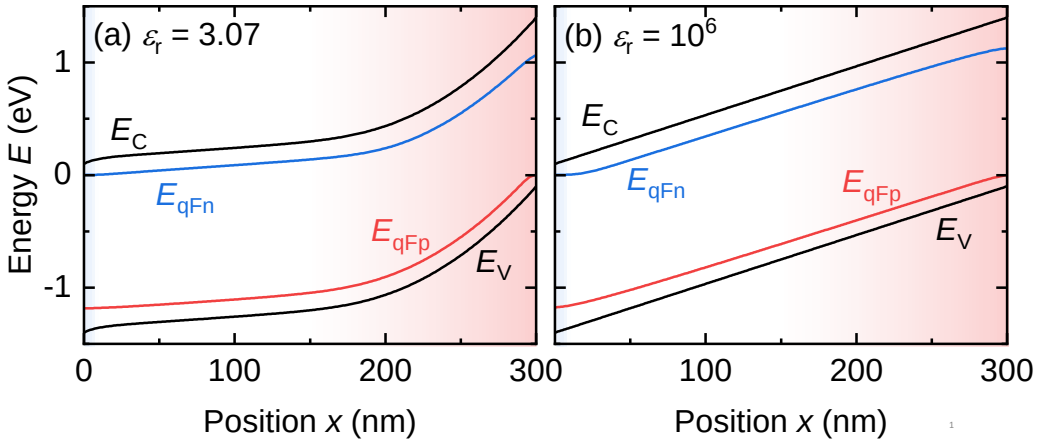

Figure 2.4: Band diagrams of a solar cell with asymmetric charge-carrier mobilities and resulting positive space charge near the anode for (a) a low dielectric and (b) a high permittivity. The high permittivity prevents band bending caused by space charge according to Poisson's equation.

approaches zero, meaning there is no curvature in the electrostatic potential φ. Consequently, the bands in Figure 2.4b remain straight despite the positive space-charge near the anode. So, a band diagram is not only a relatively intuitive way of plotting the energy levels of a solar cell but can also teach about charge-carrier densities, current flows and electrostatics inside a solar cell.

2.3. The Continuity Equations

To further understand the performance of a solar cell away from the ideal behavior of in the Shockley-Queisser model, one needs to examine the charge carriers inside the device. However, there are many factors controlling the charge-carrier densities of electrons and holes. The charge carriers are generated within the photoactive layer by incoming radiation. Also, they can recombine again upon encounter of an electron-hole pair. Additionally, to extract a current from the device, they need to be able to move towards an electrode. These processes are considered in the continuity equations that describe how the electron density n and the hole density p change with time t at a certain position x in the active layer. In one dimension, the continuity equation for electrons is

$$\frac{\mathrm{d}n(x)}{\mathrm{d}t} = G(x) - U(x) + \frac{1}{q}\frac{\mathrm{d}J_\mathrm{n}(x)}{\mathrm{d}x} \tag{2.26}$$

and the continuity equation for holes is

$$\frac{\mathrm{d}p(x)}{\mathrm{d}t} = G(x) - U(x) - \frac{1}{q}\frac{\mathrm{d}J_{\mathrm{p}}(x)}{\mathrm{d}x}. \tag{2.27}$$

Here, G is the generation rate, U the total recombination rate, q the elementary charge and $J_{\mathrm{n/p}}$ the electron or hole-current density.[59,60] Under steady-state condition, where $\mathrm{d}p(x)/\mathrm{d}t = 0$ and $\mathrm{d}n(x)/\mathrm{d}t = 0$, Equation (2.26) and (2.27) yield

$$J = J_{\mathrm{n}}(x_{\mathrm{cat}}) = J_{\mathrm{p}}(x_{\mathrm{an}}) = q\int_0^d [U(x) - G(x)]\mathrm{d}x = J_{\mathrm{rec}} - J_{\mathrm{gen}} \tag{2.28}$$

for the current densities flowing at the position x_{an} and x_{cat} of the anode and cathode. Here, d is the active layer thickness, J_{rec} the total recombination-current density and J_{gen} the generation-current density. Therefore, understanding the continuity equations is important to be able to correctly analyze the current density measured on a solar cell. For this purpose, I will explain each element of the continuity equation in more detail, starting with the generation of free charge carriers.

2.3.1. Generating Free Charge Carriers

As introduced in Chapter 2.1 in the scope of the Shockley-Queisser limit, electron-hole pairs are created in a solar cell by the absorption of incoming photons above the band gap. The absorptance is, however, in reality not a step function but rather depends on the material properties. The absorption coefficient α herein defines the material's ability to absorb light of a certain energy E while it travels through the material. As the light penetrates further into the absorber layer of the solar cell, more photons are absorbed. In a simple case, the remaining photon flux $\Phi(x)$ at a depth x follows an exponential[61]

$$\Phi(x, E) = \Phi(0, E)\exp(-\alpha(E)x), \tag{2.29}$$

which is known as the Lambert-Beer law. The position-dependent generation rate $g(x, E) = \mathrm{d}\Phi(x, E)/\mathrm{d}x$[62] of free charge carriers from an incident photon flux $\Phi(0, E)$ then follows as

$$g(x, E) = \Phi(0, E)\alpha(x, E)\exp(-\alpha x). \tag{2.30}$$

However, in modern thin film solar cells with active layer thicknesses in the order of the absorbed wavelengths, the absorbed light intensity does not follow a strict exponential.[5] Especially in the presence of a reflective back contact such as silver or aluminum, interference effects occur and the absorbed intensity can exhibit one or more maxima away from the illuminated contact.[63] Further details on how to handle such optical phenomena will be provided in Chapter 3.4.1 on optical simulations. No matter how the light is absorbed throughout the active layer, charge carriers generated by all photon energies contribute to the total generation rate[61]

$$G(x) = \int g(x, E)\mathrm{d}E. \tag{2.31}$$

All these charge carriers throughout the active layer then make up the generation-current density

$$J_{\mathrm{gen}} = q \int_0^d G(x)\mathrm{d}x. \tag{2.32}$$

In the ideal picture of the Shockley-Queisser model, this generation-current density is equivalent to the short-circuit current density $J_{\mathrm{sc,SQ}}$. In that way, charge-carrier generation is an integral part in the functioning of a solar cell.

2.3.2. Recombination Mechanisms

The term reducing the charge-carrier densities in the continuity equation is the recombination rate of electrons and holes. This process can either be geminate between carriers that originate from the same generation event or nongeminate between independent carriers.[64,65] As there is always free charge carriers involved in a recombination event, the average recombination rate

$$U_{\mathrm{av}} \propto n_{\mathrm{av}}^{\delta} \tag{2.33}$$

throughout the active layer of a solar cell, where n_{av} is the spatially averaged electron density. The degree of correlation is described by the recombination order δ.[66,67] Alternatively, the spatial dependence of the recombination rate can be eliminated by

integrating over the thickness d to get the recombination current density[68]

$$J_{\mathrm{rec}} = q \int_0^d U(x)\mathrm{d}x \approx qdU_{\mathrm{av}} \approx qdkn_{\mathrm{av}}^{\delta}, \tag{2.34}$$

where k is a recombination coefficient. There are different ways that recombination in a semiconductor can occur. In the following, I will introduce the most relevant recombination mechanisms for the scope of this work, which are illustrated in Figure 2.5. These include (a) recombination via a trap state, (b) band-to-band recombination and (c) recombination of minority-charge carriers at the contact.

In the Shockley-Queisser model described in Chapter 2.1, an electron-hole pair recombines directly by releasing the energy of the band gap. This process involves two free charge carriers from different molecules coining the term bimolecular recombination.[69] While the energy of such a transition for most crystalline materials is emitted radiatively, organic semiconductors also exhibit significant nonradiative, direct recombination due to their high-energy vibrational modes.[70,71] The recombination rate U_{dir} of radiative and nonradiative recombination alike depends on both free carrier densities according to

$$U_{\mathrm{dir}}(x) = k_{\mathrm{dir}}(n(x)p(x) - n_{\mathrm{i}}^2). \tag{2.35}$$

Here, k_{dir} is the direct recombination coefficient.[72] In case $n(x)p(x) >> n_{\mathrm{i}}^2$ and for the zero-dimensional approximation $n(x) \approx p(x) \approx n_{\mathrm{av}}$, the average recombination rate

$$U_{\mathrm{av,dir}} \approx k_{\mathrm{dir}} n_{\mathrm{av}}^2. \tag{2.36}$$

Hence, the recombination order $\delta = 2$ in this approximation.[65] Accordingly, the recombination-current density

$$J_{\mathrm{rec,dir}} = q \int_0^d U_{\mathrm{dir}}(x)\mathrm{d}x \approx qdk_{\mathrm{dir}}\, n_{\mathrm{av}}^2 \tag{2.37}$$

for direct recombination throughout the device.[73] To understand the influence of one recombination mechanism on the performance, it can further help to calculate the open-circuit voltage that results from the given recombination-current density as $J_{\mathrm{gen}} = J_{\mathrm{rec}}$ at open circuit. For direct recombination, Equation (2.37) thus results in an open-

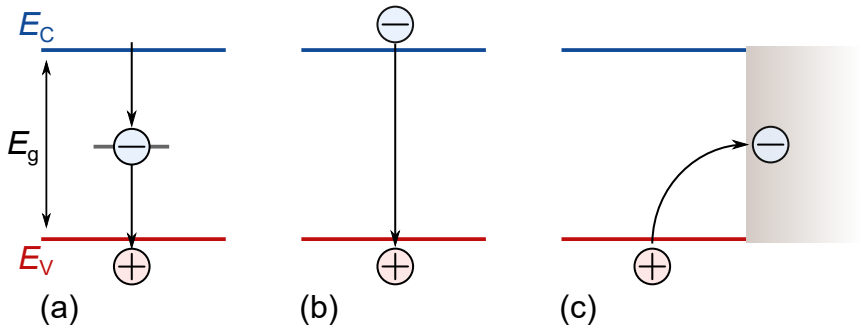

Figure 2.5: Recombination pathways of an electron from the conduction band E_C to the valence band E_V: (a) Trap-assisted recombination, (b) band-to-band recombination and (c) surface recombination of a minority-charge carrier at the contact.

circuit voltage[74]

$$V_{oc,dir} = \frac{k_B T}{q} \ln\left(\frac{G_{av}}{k_{dir} n_i^2}\right), \tag{2.38}$$

with the spatial average G_{av} of the generation rate. Such direct, bimolecular recombination is often assumed to be the dominant recombination mechanism in organic solar cells.[65,75,76]

Impurities, air-exposure and other morphological disorder can lead to the formation of defect states in the energy gap which act as recombination centers for monomolecular, non-geminate recombination.[77–81] This mechanism describes the recombination of one free charge carrier with another charge carrier that is trapped in such a defect state. The process can be described by Shockley–Read–Hall (SRH) recombination statistics.[82,83] It distinguishes between four events that can happen at a defect site and are depicted in Figure 2.6a. First, an unoccupied trap can capture a free electron from the conduction band. Then, the electron can be emitted to the conduction band. Equivalently, a hole can be captured from the valence band with a certain probability or emitted into the valence band. Therefore, a recombination event occurs when an electron and a hole are subsequently captured in the trap state. The corresponding rates for the transitions are[84]

$$u_1 = \beta_n n p_T = \beta_n n N_t (1-\theta), \tag{2.39}$$

$$u_2 = e_n n_T = e_n N_t \theta, \tag{2.40}$$

$$u_3 = \beta_p p n_T = \beta_p p N_t \theta, \tag{2.41}$$

$$u_4 = e_p p_T = e_p N_t (1-\theta). \tag{2.42}$$

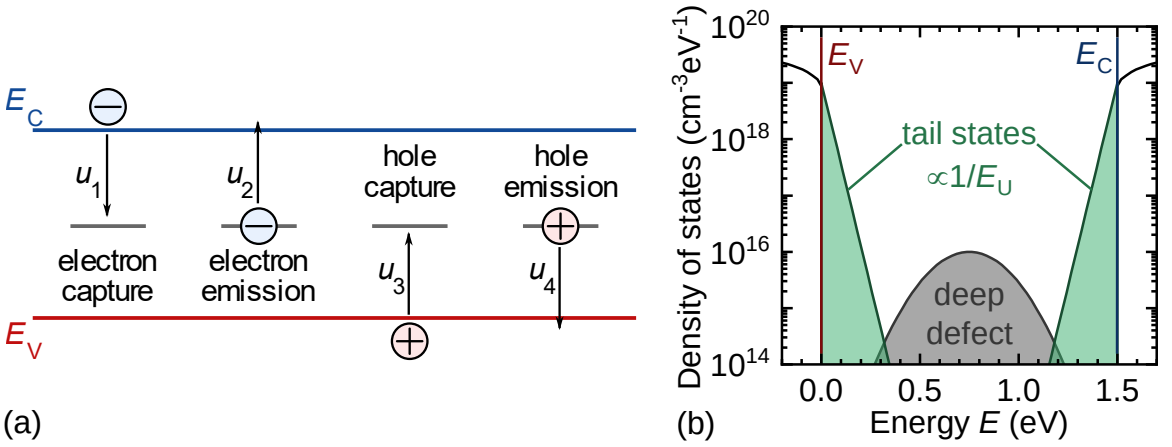

Figure 2.6: (a) Possible transitions at a defect state. An electron can be either captured (1) or emitted (2). Vice versa, a hole can also be captured by a trap occupied with an electron (3) or emitted by an electron-free trap state. (b) Typical distributions of defect states. Shallow defect states can occur in the shape of exponential band tails with an inverse slope of the Urbach energy E_U, while deeper defects follow a Gaussian distribution.

Here, u_1 is the electron capture rate, where β_n is the recombination coefficient for electrons and p_T is the density of trapped holes. The trapped hole density can be further described by the density of trap states N_t and its occupation probability $(1-\theta)$ by holes. Equation (2.40) shows the rate u_2 of electron emission with the emission coefficient e_n for electrons and the occupation probability θ of the trap states by electrons. Equivalently, u_3 is the hole capture rate with the recombination coefficient β_p for holes and the density n_T of trapped electrons and Equation (2.42) describes the hole emission rate u_4 with the emission coefficient e_p.

In thermal equilibrium the capture and emission of one type of charge carrier should be equal, i.e. $u_1 = u_2$. Furthermore, under steady-state conditions, all charge carriers that are captured and not reemitted recombine, resulting in the recombination rate $U_\mathrm{SRH} = u_1 - u_2 = u_3 - u_4$. Assuming that the occupation probability θ resembles the Fermi-Dirac distribution, it follows that the recombination rate[84]

$$U_\mathrm{SRH}(x) = \int_{E_\mathrm{V}}^{E_\mathrm{C}} \frac{\mathrm{d}N_\mathrm{t}(E,x)}{\mathrm{d}E} \beta_\mathrm{n}\beta_\mathrm{p} \frac{n(x)p(x) - n_\mathrm{i}^2}{n(x)\beta_\mathrm{n} + p(x)\beta_\mathrm{n} + e_\mathrm{n} + e_\mathrm{p}} \mathrm{d}E. \tag{2.43}$$

Here, $dN_\mathrm{t}(E,x)/dE$ is the trap density per volume and energy interval and the integral from the valence band energy E_V to the conduction band energy E_C accounts for a distribution of defects. Figure 2.6b shows examples for such a distribution of trap

states. Shallow defects can occur in the form of exponential band tails, while deeper traps are often assumed to a follow a Gaussian distribution.[85]

In the simplest case of a single defect in the energy gap, the density of trap states becomes a delta function so that the integral disappears. Assuming that $n(x)p(x) >> n_{\mathrm{i}}^2$ and that the emission is negligible for deep defects, Equation (2.43) can be further simplified to

$$U_{\mathrm{SRH}}(x) = \frac{n(x)\, p(x)}{\tau_{\mathrm{p}}\, n(x) + \tau_{\mathrm{n}}\, p(x)} \tag{2.44}$$

Here, $\tau_{\mathrm{n/p}} = 1/(N_{\mathrm{T}}\beta_{\mathrm{n/p}})$ and is the charge-carrier lifetime.[82,86] By assuming $\tau_{\mathrm{n}} \approx \tau_{\mathrm{p}}$ and by using the 0D approximation that neglects all spatial dependences, the recombination-current density $J_{\mathrm{rec,SRH}}$ can be written as

$$J_{\mathrm{rec,SRH}} = q \int_0^d U_{\mathrm{SRH}}(x)\mathrm{d}x \approx qdU_{\mathrm{av,SRH}} \approx qd\frac{n_{\mathrm{av}}}{2\tau_{\mathrm{n}}} \tag{2.45}$$

with the average recombination rate $U_{\mathrm{av,SRH}}$ via deep traps and the average charge-carrier density n_{av}.[73] Since the recombination rate scales linearly with the charge-carrier density in this approximation, the recombination process is often denoted as first-order recombination with $\delta = 1$.[21,65,69,87] In analogy to the case of direct recombination, this recombination-current density also allows calculating the open-circuit voltage[74]

$$V_{\mathrm{oc,SRH}} = \frac{2k_{\mathrm{B}}T}{q} \ln\left(\frac{2G_{\mathrm{av}}\tau_{\mathrm{n}}}{n_{\mathrm{i}}}\right). \tag{2.46}$$

Therefore, the open-circuit voltage increases twice as fast with the logarithmic generation rate when recombination via deep defects is dominant compared to direct recombination in Equation (2.38). This relation is also illustrated in Figure 2.7, which shows the open-circuit voltage V_{oc} as a function of generation rate G_{av} of a system including both direct and trap assisted recombination with varying lifetimes. For very high light intensities or good charge-carrier lifetimes, direct recombination dominates in the solar cell, leading to a slow increase of V_{oc} with generation rate G_{av}. At low light intensities, Shockley-Read-Hall recombination is dominant and the V_{oc} decreases with decreasing carrier lifetime. Thus, trap-assisted recombination can lead to a higher sensitivity to variations in the generation rate and can deteriorate the open-circuit voltage.

However, the density of defect states is often not localized to only one trap energy

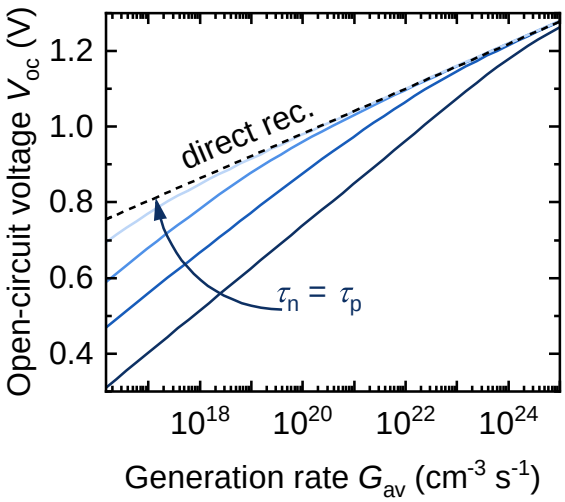

Figure 2.7: Open-circuit voltage V_{oc} as a function of generation rate G_{av} for a variation in charge-carrier lifetimes τ_n and τ_p. With increasing lifetime, the generation rate, where direct recombination starts dominating, shifts towards lower values.

as discussed previously but instead a distribution of defects as illustrated in Figure 2.6b. A phenomenon often observed in amorphous semiconductors is the formation of an exponential distribution of shallow defect states, so called band tails.[47,88–91] Their density of states

$$N_{VBT}(E) = \frac{N_{eff,VBT}}{E_U} \exp\left(-\frac{E - E_V}{E_U}\right) \tag{2.47}$$

for the valence-band tails and

$$N_{CBT}(E) = \frac{N_{eff,CBT}}{E_U} \exp\left(-\frac{E_C - E}{E_U}\right) \tag{2.48}$$

for the conduction-band tails. It is characterized by the effective density of states $N_{eff,CBT}$ and the Urbach energy E_U.[67,92] A high Urbach energy corresponds to defect states that reach further into the energy gap whereas a low Urbach energy describes a steep distribution of shallow defect states. The recombination U_{tail} via tail states is given by

$$U_{tail}(x) = \beta_p n_T(x) p(x) + \beta_p n(x) p_T(x). \tag{2.49}$$

So, a recombination event occurs either between a trapped electron in the conduction-band tail and a free hole or a free electron and a hole in the valence-band tail. Neglecting once again spatial dependences and assuming $n(x) \approx p(x) \approx n_{av}$ and $n_T(x) \approx p_T(x) \approx$

$n_{\mathrm{av}}^{k_{\mathrm{B}}T/E_{\mathrm{U}}}$, the recombination rate can be rewritten as

$$U_{\mathrm{av,tail}} \propto n_{\mathrm{av}}^{k_{\mathrm{B}}T/E_{\mathrm{U}}+1} = n_{\mathrm{av}}^{\delta}. \tag{2.50}$$

This relation implies that the recombination rate depends superlinearly on the charge-carrier density and therefore has a recombination order $\delta = 1 + k_{\mathrm{B}}T/E_{\mathrm{U}} > 1$.[67]

Especially in more advanced solar cell materials, the trap centers are mainly located at the surface of grain boundaries and at the interface to the contact layers. In this case, the dominant recombination mechanism is surface recombination of the minority-charge carriers. Since this process is spatially localized, the recombination rate $U_{\mathrm{sur}}(x)\delta x$ can be viewed as recombination event per area at the position of the surface and is given by[93]

$$U_{\mathrm{sur}}\delta x = S_{\mathrm{n}}(n(x_{\mathrm{an}}) - n_i) \tag{2.51}$$

in case the electrons are the minority at the position x_{an} of the anode or

$$U_{\mathrm{sur}}\delta x = S_{\mathrm{p}}(p(x_{\mathrm{cat}}) - p_i) \tag{2.52}$$

for a minority of holes at the position of the cathode x_{cat}, where p_{i} is the intrinsic hole density. Here, $S_{\mathrm{n/p}}$ is the surface recombination velocity of the charge carriers. Consequently, the recombination-current density is given by

$$J_{\mathrm{rec,sur}} = q[S_{\mathrm{n}}(n(x_{\mathrm{an}}) - n_0) + S_{\mathrm{p}}(p(x_{\mathrm{cat}}) - p_0)]. \tag{2.53}$$

Such surface recombination is mitigated by the introduction of selective contacts at the electrodes to prevent the recombination of minority-charge carriers. Also, a high electric field inside the active layer reduces the number of charge carriers at the wrong contact.[67,94]

2.3.3. Current-Driving Forces

Apart from generation and recombination, the density of carriers can also change due to current flow. As there ideally is no lateral current flowing inside a solar cell, I only discuss the current driving forces in one dimension. During charge-carrier transport, one can distinguish between two competing processes. First, the charge carriers

experience a driving force originating in the internal electric field F. So, under short-circuit conditions, for instance, the electrons will be pushed towards the cathode and the holes towards the anode by an electric field due to the built-in potential. The resulting current density $J_{\mathrm{n,drift}}$ caused by electron drift can be written as[95]

$$J_{\mathrm{n,drift}}(x) = q\mu_{\mathrm{n}} n(x) F(x) \tag{2.54}$$

Similarly, the hole-drift current density

$$J_{\mathrm{p,drift}}(x) = q\mu_{\mathrm{p}} p(x) F(x). \tag{2.55}$$

Apart from electrostatic driving forces, a carrier flow can also be caused by equilibration of carrier-density gradients $\mathrm{d}n/\mathrm{d}x$. When the charge-carrier density is high in a certain region of the active layer, the charge carriers will diffuse to a position with lower concentration. This diffusion-current density

$$J_{\mathrm{n,diff}} = qD_{\mathrm{n}} \frac{\mathrm{d}n(x)}{\mathrm{d}x} \tag{2.56}$$

for electrons and

$$J_{\mathrm{p,diff}} = -qD_{\mathrm{p}} \frac{\mathrm{d}p(x)}{\mathrm{d}x} \tag{2.57}$$

for holes with the diffusion constant $D_{\mathrm{n/p}}$ that incorporates the carrier mobility.[95] Together, the drift and diffusion current make up the total electron- and hole-current density in the solar cell with

$$J_{\mathrm{n}}(x) = J_{\mathrm{n,drift}} + J_{\mathrm{n,diff}} \tag{2.58}$$

$$J_{\mathrm{p}}(x) = J_{\mathrm{p,drift}} + J_{\mathrm{p,diff}}. \tag{2.59}$$

So overall, the electron and hole current density can be written as[95]

$$J_{\mathrm{n}}(x) = q\mu_{\mathrm{n}} n(x) F(x) + qD_{\mathrm{n}} \frac{\mathrm{d}n(x)}{\mathrm{d}x} \tag{2.60}$$

$$J_{\mathrm{p}}(x) = q\mu_{\mathrm{p}} p(x) F(x) - qD_{\mathrm{p}} \frac{\mathrm{d}p(x)}{\mathrm{d}x}. \tag{2.61}$$

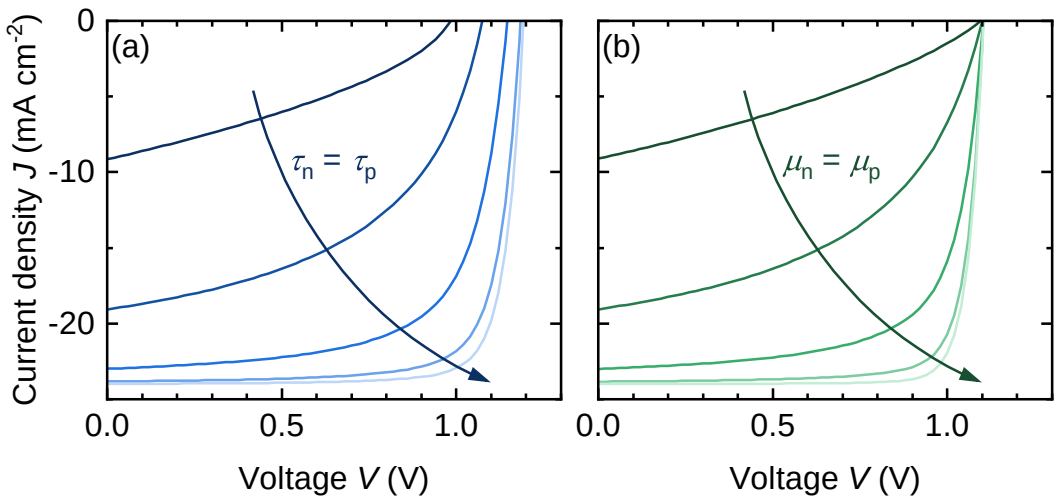

Figure 2.8: Current-density voltage characteristics for a solar cell with varying (a) lifetimes τ_n and τ_p and (b) mobilities μ_n and μ_p. While both material properties have a similar impact at low voltages, the open-circuit voltage V_{oc} is not affected by the charge-carrier mobility as there is no current flow inside the solar cell.

Whereas for example silicon solar cells have a relevant diffusion current, in organic solar cells, the drift current typically dominates Equation (2.58) and Equation (2.59). Their very thin active layer evokes a very high electric field compared to other photovoltaic technologies.

In this chapter, I have described how the current density that can be measured on a solar cell can be expressed by a sum of the generation-current density J_{gen} in Equation (2.32) and the recombination-current densities J_{rec} in Equation (2.37), (2.45) and (2.53), but also in terms of drift and diffusion in Equation (2.60) and (2.61). In an ideal case, they can be solved by the current density from Equation (2.12) derived in the Shockley-Queisser model. But in a more realistic scenario with finite charge-carrier mobilities and recombination beyond the radiative limit, they allow a better understanding of the influence of material properties on the JV characteristic. For example, the impact of a variation in charge-carrier lifetimes τ_n and τ_p is shown in Figure 2.8a for a solar cell that is dominated by trap-assisted recombination. For good lifetimes, mainly the fill factor is affected. The open-circuit voltage decreases according to Equation (2.46). At low lifetimes, even the short-circuit current density J_{sc} is heavily affected since the recombination-current density is large even at low voltages. To illustrate the drift-diffusion equations (2.60) and (2.61), Figure 2.8b shows the JV curves for different charge-carrier mobilities. With increasing mobilities μ_n and μ_p, both J_{sc} and fill factor improve, similar to the case in Figure 2.8a. Only

V_{oc} remains constant as there is no current flow and therefore transport properties are irrelevant at open circuit. Thereby, I have illustrated, how the Equations and physical principles presented in this chapter are relevant to understand the influence of absorption, recombination and transport parameters on the measurements introduced and evaluated in the following chapters.

3
Materials and Methods

In the previous chapter, I introduced models applicable to any solar cell, including organic solar cells. In this chapter, I go more into detail about the material systems used in this work and specify the measurements that were conducted. In Chapter 3.1, I first introduce the working principles that set apart organic solar cells from other material systems and then present the specific organic semiconductors used in this work and explain how the solar cells have been fabricated. These solar cells were characterized with electrical measurements that are explained in Chapter 3.2. These measurements include the current-voltage measurements and also admittance spectroscopy. The optical measurements are briefly introduced in Chapter 3.3. As device simulations are a substantial part of this work, the underlying assumptions and the software used are presented in Chapter 3.4.

3.1. Organic Photovoltaics

Organic solar cells play a relevant role in the search for efficient, thin-film photovoltaic technologies. The high tunability of the absorption coefficient also allows tailoring organic solar cells towards different application. For example, transparency in the visible wavelength region is suitable for window-integrated photovoltaics.[96] For indoor use, the absorption coefficient can be designed to match the spectrum of the light sources such as light-emitting diodes or fluorescent lamps.[97] Additionally, as organic semiconductors are soluble in common organic solvents, they can be processed from solution, which promises good scalability for industrial processes.[98] However, to reach commercialization, further progress has to be made in terms efficiency and sta-

bility of the organic solar cells.[7,99] For that purpose, it is relevant to understand the working mechanisms that are specific to organic solar cells.

3.1.1. The Bulk Heterojunction

The key principle underlying every solar cell is the conversion of incoming light into free charge carriers. However, to facilitate this process in organic materials, researchers in photovoltaics have to overcome obstacles unique to this material class.

Contrary to inorganic semiconductors, organic semiconductors are inherently disordered. This structural disorder prevents the formation of continuous bands known from crystalline materials such as silicon or germanium. Instead, there is a high number of discrete molecular orbitals. The highest molecular orbital occupied by an electron is called the HOMO level, whereas the lowest unoccupied molecular orbital is the LUMO. In an organic semiconductor, these orbitals are separated by an energy gap of around 1-3 eV.[100] However, in the process of absorbing a photon, the ground state and the excited state might be displaced in terms of their nuclear coordinate,[101] as illustrated in Figure 3.1a. As a result, an electron cannot directly be excited from its ground state to the lowest excited stated but requires an extra energy, the reorganization energy E_{re} for excitation. In the excited state, it will then thermalize to the lowest excited state.[101] Similarly, during recombination, the electron will emit an energy that is given by the difference between energy gap and reorganization energy,[101] see Figure 3.1a. The process of absorption creates a negative charge in the excited state, the LUMO, and leaves a positively charged hole in the HOMO. In an inorganic semiconductor, this generated electron-hole pair can separate and move freely in the energy bands. However, disordered organic materials exhibit a low relative permittivity ($\varepsilon_{\mathrm{r}} = 2 - 4$) causing the electron and hole to be tightly bound by Coulomb forces.[102–105] The two charge carriers form an exciton, a quasi-particle with its own spin, which is schematically illustrated in step 1 of Figure 3.1b. The exciton can move from one molecule to another via hopping for a few tens of nanometers before the electron and hole recombine.[100,106,107]

Yet, the exciton needs to be separated into free charge carriers to extract a photocurrent from the materials. For this purpose, Ching W. Tang introduced a second organic semiconductor that has slightly different energy levels into the system.[108] At the interface of the two materials, a resulting energy offset drives the electron into the material with the energetically lower LUMO and the hole into the higher HOMO.[109]

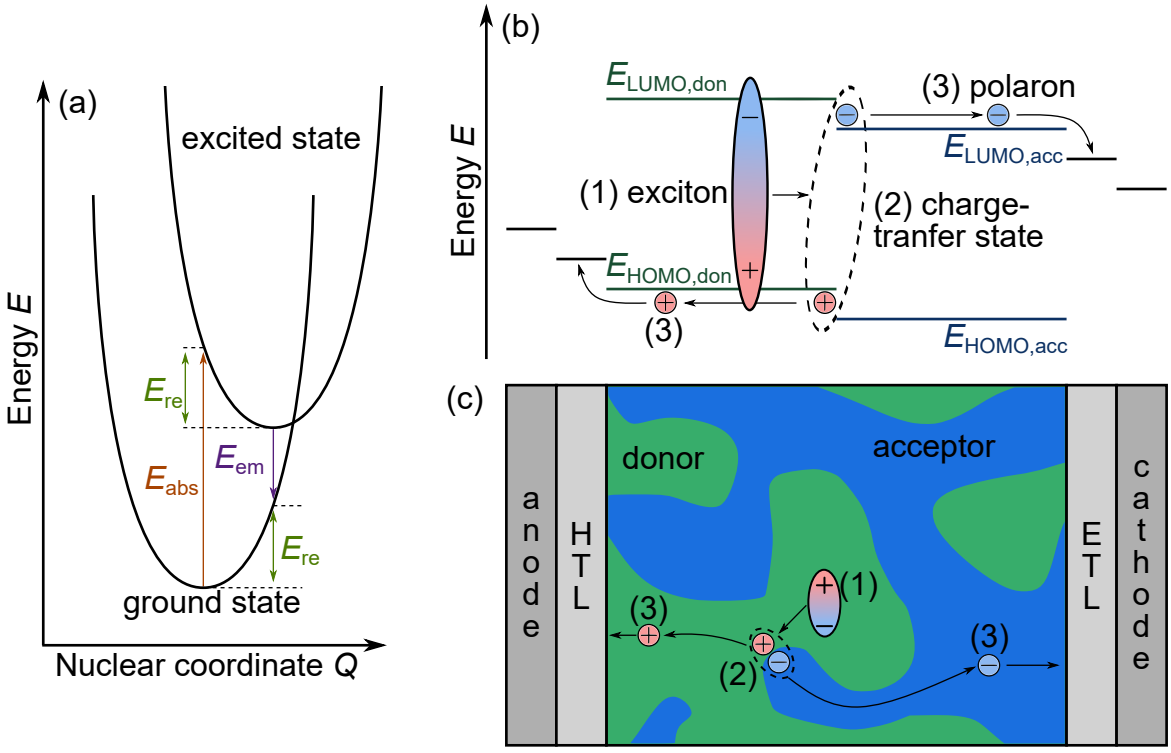

Figure 3.1: (a) Energy levels of the excited and ground state as a function of the nuclear coordinate Q. Due to the displacement of the states, the reorganization energy E_{re} is reflected in the energy E_{abs} needed to excite an electron and in the energy E_{em} emitted during the recombination of an excited electron. (b) Schematic of the energy levels during the process of photocurrent generation. (1) An exciton is generated and diffuses to the donor-acceptor interface, where (2) it forms a charge-transfer state, where the charge carriers are on different molecules but still coulombically attracted to each other. (3) The charge-transfer state is separated into two polarons that drift to their respective extraction layers. For simplicity, the binding energy of the exciton and the energy levels of the polarons are not differentiated here. (c) Illustration of the same working principle in the schematic of a bulk heterojunction.

The material now carrying the electron is called the acceptor and the material with the hole is the donor in the system.[100] The energy levels of these materials are also illustrated in Figure 3.1b. At the interface of the donor and acceptor material, the electron and hole then first occupy the so-called charge-transfer state (step 2), where they sit on different molecules but are still coulombically attracted to each other. Afterwards, they travel as free charge carriers in the form of polarons to their respective contacts (step 3). However, for the exciton to dissociate it needs to reach the donor-acceptor interface, which can be critical in a bilayer system, where the layer thickness is much higher than the exciton diffusion length.[104,110] To overcome this limitation,

a common approach is to mix the two semiconducting materials into a so-called bulk heterojunction.[110,111] Here, a network of donor and acceptor domains forms, maximizing the donor-acceptor interface as shown in Figure 3.1c. The size of the domains is limited by the diffusion length of the exciton to ensure it reaches the interface.[100] Still, the two phases need to be sufficiently separated to allow good transport of the separated charges.[100] Therefore, to facilitate the generation of free electrons and holes in organic semiconductors, the usage of two materials in a bulk heterojunction is key with special focus on optimum energy level and morphology adjustment.

3.1.2. Selection of Organic Semiconductors

Such bulk-heterojunction solar cells are subject to characterization in this work. These solar cells comprise of one of the polymer donors poly[(2,6-(4,8-bis(5-(2-ethylhexyl-3-fluoro)thiophen-2-yl)-benzo[1,2-b:4,5-b']dithiophene))-alt-(5,5-(1',3'-di-2-thienyl-5',7'-bis(2-ethylhexyl)benzo[1',2'-c:4',5'-c']dithiophene-4,8-dione)]-ran-poly[(2,6-(4,8-bis(5-(2-ethylhexyl)thiophen-2-yl)-benzo[1,2-b:4,5-b']dithiophene))-alt-(2,2-ethyl-3(or4)-carboxylate-thiophene)] (PBDB-TF-T1, Figure 3.2a) and poly[(5,6-difluoro-2,1,3-benzothiadiazol-4,7-diyl)-alt-(3,3"'-di(2-octyldodecyl)-2,2';5',2";5",2"'-quaterthiophen-5,5"'-diyl)] (PffBT4T-2OD, Figure 3.2b) and one nonfullerene acceptor, which is either (2,2´-((2Z,2´Z)-((12,13-bis(2-butyloctyl)-3,9-diundecyl-12,13-dihydro-[1,2,5]thiadiazolo[3,4-e]thieno[2,"3´´:4',5´]thieno[2´,3´:4,5]pyrrolo[3,2-g]thieno[2´,3´:4,5]thieno[3,2-b]indole-2,10-diyl)bis(methanylylidene))bis(5,6-difluoro-3-oxo-2,3-dihydro-1H-indene-2,1-diylidene))dimalononitrile) (BTP-4F-12, Figure 3.2c) or (Z)-5-[5-(15-5-[(Z)-(3-ethyl-4-oxo-2-thioxo-1,3-thiazolidin-5-ylidene)methyl]-8thia-7.9-diazabicyclo[4.3.0]nona-1(9),2,4,6-tetraen-2-yl-9,9,18,18-tetrakis(2-ethylhexyl)-5.14-dithiapentacyclo[10.6.0.03,10.04,8.013,17]octadeca-1(12),2,4(8),6,10,13(17),15-heptaen-6-yl)-8-thia-7.9diazabicyclo[4.3.0]nona-1(9),2,4,6-tetraen-2-yl]methylidene-3-ethyl-2-thioxo-1,3-thiazolidin-4one (EH-IDTBR, Figure 3.2d). Together, they are used in the combinations PBDB-TF-T1:BTP-4F-12 and PffBT4T-2OD:EH-IDTBR, while the main focus of this work lies on the characterization of PBDB-TF-T1:BTP-4F-12-based solar cells. The material system has been first presented by Hong et al. who modified the workhorses of current organic photovoltaic research poly[(2,6-(4,8-bis(5-(2-ethylhexyl-3-fluoro)thiophen-2-yl)-benzo[1,2-b:4,5-b']dithiophene))-alt-(5,5-(1',3'-di-2-thienyl-5',7'-bis(2-ethylhexyl)benzo[1',2'-c:4',5'-c']dithiophene-4,8-dione)] (PM6) and

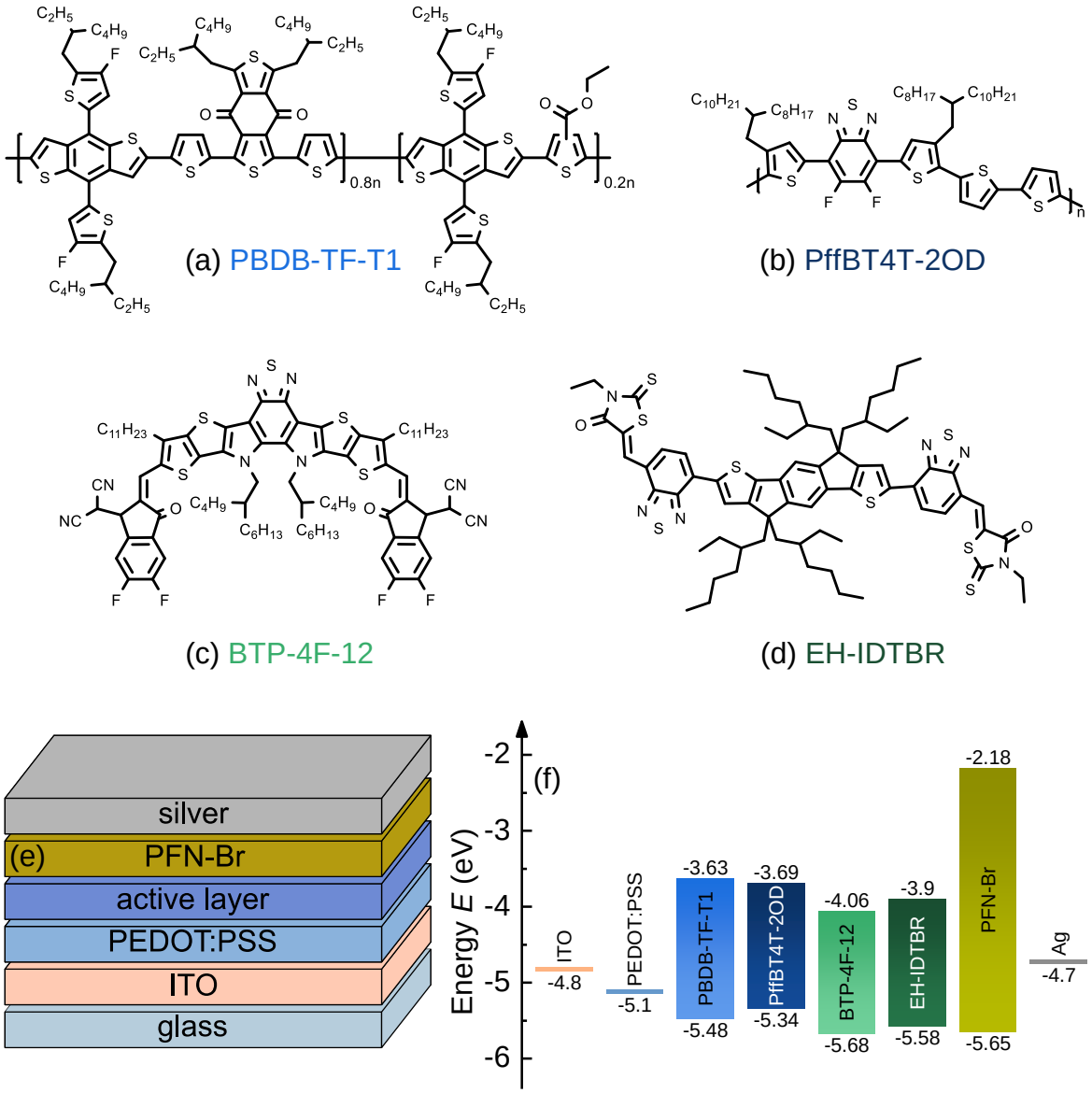

Figure 3.2: Chemical structures of the molecules used in this work, the donors (a) PBDB-TF-T1 and (b) PffBT4T-2OD and the acceptors (c) BTP-4F-12 and (d) EH-IDTBR, which I use in the blend combination PBDB-TF-T1:BTP-4F-12 and PffBT4T-2OD:EH-IDTBR. (e) Stack configuration in which the solar cells are processed and (f) energy levels[97,112–114] for the materials used in this work. For ITO, PEDOT:PSS and silver, the values represent the work functions, while the lower values correspond to the HOMO and the upper value for the LUMO level in the case of PBDB-TF-T1, PffBT4T-2OD, BTP-4F-12, EH-IDTBR and PFN-Br.

2,2'-((2Z,2'Z)-((12,13-bis(2-ethylhexyl)-3,9-diundecyl-12,13-dihydro-[1,2,5]thiadiazolo[3,4-e]thieno[2",3":4',5']thieno[2',3':4,5]pyrrolo[3,2-g]thieno[2',3':4,5]thieno[3,2-b]indole-2,10-diyl)bis(methanylylidene))bis(5,6-difluoro-3-oxo-2,3-dihydro-1H-indene-

2,1-diylidene))dimalononitrile (Y6) to be more soluble in non-halogenated solvents.[113] This step is essential for the commercialization of organic solar cells as mass fabrication requires the use of these less environmentally harmful solvents.[115] The solar cells based on PBDB-TF-T1:BTP-4F-12 reach power-conversion efficiencies of above 16% in a non-halogenated solvent,[113] which was among the highest efficiencies for green-solvent processed solar cells and close to the overall best organic solar cells at the time of publication.[42,113,116] Since then, power-conversion efficiencies have reached 18% for organic solar cells processed with non-halogenated solvents.[117] Due to its relevance as an eco-friendly system, PBDB-TF-T1:BTP-4F-12 is specifically characterized in this thesis. For the characterization of the energetic disorder in this material system, I chose PffBT4T-2OD:EH-IDTBR based solar cells as a comparison, since they have been reported to have a high degree of disorder.[118] Both material systems were used in the same cell architecture, which is schematically displayed in Figure 3.2e. Both types of solar cell were fabricated on a glass substrate with an indium tin oxide (ITO) anode, and poly(3,4-ethylenedioxythiophene) polystyrene sulfonate (PEDOT:PSS) as the hole-transport layer. On top of the active layer, a thin layer of poly(9,9-bis(3'-(N,N-dimethyl)-N-ethylammoinium-propyl-2,7-fluorene)-alt-2,7-(9,9-dioctylfluorene)) dibromide (PFN-Br) creates the electron-transport layer and a silver cathode is used. Figure 3.2f lists the energy levels of these materials. While the electrodes themselves do not provide a built-in voltage as there is almost no work function difference, the transport layers are responsible for creating the potential difference in the solar cell. Especially the thin PFN-Br layer potentially creates a tunneling contact for the electrons to the silver which lowers the work function of the silver electrode.[119–121]

3.1.3. Fabrication of Organic Solar Cells

The organic solar cells prepared for this work use glass substrates covered by ITO that are purchased from the brand PsiOTec Ltd. For this work, two different sizes of substrates where used, $12 \times 12\,\mathrm{mm}^2$ and $2 \times 2\,\mathrm{cm}^2$. For protection, they are covered by a layer of photoresist, which is removed by washing the substrates with acetone. Afterwards, the substrates are cleaned in a bath of distilled water using ultrasonication for ten minutes. This step is repeated with acetone and isopropyl alcohol. After the last ultrasonication, residue isopropyl alcohol is removed using a nitrogen gun and heating on a hot plate for ten minutes at 100°C. For the last step of substrate

Table 3.1: Fabrication parameters of the solar cells characterized in this work. Thick devices were fabricated with the parameters in the brackets.

Parameter	PffBT4T-2OD:EH-IDTBR	PBDB-TF-T1: BTP-4F-12
D:A ratio	1:1	1:1.2
Solvent	chlorobenzene	ortho-xylene
Concentration (mg/ml)	13	18(32)
Solution temperature (°C)	100	room temperature
DIO content (%)	0	0.5
Pre-treatment	heating substrate, spin-coater chuck, pipette tips to 100°C	-
Spin speed (rpm)	2200	Chapter 6: 2200 Chapter 4, 5, 7: 1000-3500 (800-3500)
Spin coating duration (s)	40	30
Annealing temperature (°C)	80	100
Annealing time (min)	5	10

preparation, they are treated with oxygen plasma for ten minutes. The hole-transport layer PEDOT:PSS is deposited in the next step. The material PEDOT:PSS Al4083 is purchased from Ossila and stored under constant cooling. Around 1 ml of PEDOT:PSS solution is treated for 15 min with ultrasound while keeping the solution at a low temperature. Prior to spin coating, the solution is filtered with a 0.45 µm-PVDF filter. Then, around 60 µl of solution are dropped on the small substrate (90 µl on the large substrate), so it is fully covered in PEDOT:PSS. The spin coating proceeds with an acceleration of 10000 rpm/s and a spin speed of 4000 rpm for 30 s. When the spin coating is finished, a cotton swab and water remove a stripe of around 1 mm width to enable contacting with the underlying ITO later. For drying, the substrates covered with PEDOT:PSS are placed on a hotplate at 150°C for 15 min. Then, the substrates are transferred into a nitrogen filled glovebox for active layer deposition. The active layer solution is prepared a day prior to deposition. First, the amount of donor polymer is weighed before adding the acceptor material. For the ratios of the materials used, I refer to Table 3.1. The solvents chlorobenzene or the non-halogenated ortho-xylene are finally added and the sealed solutions are left to stir over night. Table 3.1 also

includes the temperature, at which the solution is stirred. Around one hour before spin coating, a certain volume percentage of 1,8-diiodooctane (DIO) in added to the solution. For some blend materials, special pre-treatment of the substrate and spin coating equipment is needed as listed in Table 3.1. For the coating process, 40 µl (70 µl for the large substrates) of the blend solution are deposited onto the spinning substrate. The spinning parameters vary between samples as shown in Table 3.1. For post-treatment, the samples are placed on a hot plate to dry. Next, a thin layer of PFN-Br is solution deposited onto the active layer. PFN-Br is dissolved in methanol at a concentration of 0.5 mg/ml and stirred at room temperature for one day to two weeks before solar cell fabrication. When spinning at 2500rpm, 40 µl (70 µl for the large substrates) of the solution are dropped on the substrate. The resulting PFN-Br layer requires no further heating step. Next, the area without the PEDOT:PSS is also scratched to uncover the ITO contact. In a last step, evaporation creates the silver contacts. The samples are placed on shadow masks in a sample holder and transferred into an evaporation chamber. Under a pressure of less than 5×10^{-7} mbar, around 100 nm of silver are deposited at a maximum rate of 1 Å/s. The overlap between the silver area from the shadow masks and the ITO defines the active cell area to 0.06 cm^2 on the small substrates and 0.16 cm^2 on the large substrates. Thereby, the evaporation of the silver cathode marks the end of the solar cell fabrication process.

3.2. Electrical Characterization

There are numerous techniques to characterize a solar cell that was fabricated in the lab. The most frequently used characterization techniques are current-density J measurements as a function of voltage V. The basics on JV characteristics were already introduced in the previous chapter. Here, I focus on characterization and interpretation of measurements in terms or resistive effects and recombination mechanisms and introduce the measurement setup that was used for this work. Another technique based on electrical measurements that is a focus in this work is admittance spectroscopy, which I introduce after the JV measurements.

3.2.1. Understanding Real JV characteristics

In Chapter 2.1 on the Shockley-Queisser model, we have learned how the current-voltage characteristic can follow from an idealistic thermodynamic logic. Chapter 2.3 further revealed the influence of charge-carrier mobilities and lifetimes. This chapter now focuses on the quantities that can be directly extracted from JV curves and how to interpret them. This information includes external resistances and an indicator on the dominant recombination mechanism, the ideality factor. In the most simple picture, these resistive effects in a solar cell can be divided into the contribution of a parallel resistance R_p and a series resistance R_s to the diode. This equivalent circuit of the solar cell is also shown in Figure 3.3a. The series resistance R_s typically stems from the limited conductivity of the contact layers or the absorber itself.[122,123] On the other hand, the parallel resistance R_p is a measure for leakage currents in the solar cell.[122] So, for example, pinholes in the absorber layer may often occur in new material systems due to a lack of optimization and offer an alternative current pathway.[124] Thereby, the presence of pinholes lowers the parallel resistance R_p. The effect of a reduction in R_p on the dark JV curves is visualized in Figure 3.3a. A low parallel resistance R_p causes the leakage currents to dominate the total current density more and more at low voltages where the exponential of the diode current is still low. In contrast, the series resistance R_s gains in significance at higher diode currents where an increasingly high voltage drops over the resistance. Therefore, the internal voltage V_int that actually controls the diode current, is given by $V_\mathrm{int} = V_\mathrm{ext} - J(V_\mathrm{ext})AR_\mathrm{s}$, where V_ext is the external voltage and A the solar cell area. This voltage drop $J(V_\mathrm{ext})AR_\mathrm{s}$ causes the dark JV curve to flatten at high voltages in Figure 3.3a. So, only in the intermediate voltage regime, the shape reflects the diode. When illuminating such a solar cell with external resistances, the series and parallel resistance affect the current-density voltage curve in different regimes. As the photocurrent J_ph under solar illumination dominates over leakage currents that inflict a low parallel resistance R_p, there is no visible influence of the parallel resistance in the illuminated JV curves in Figure 3.3b. However, the series resistance R_s causes the fill factor of the solar cell to deteriorate. With these resistances, the JV characteristic of the equivalent circuit in Figure 3.3b can be written as[125]

$$J(V_\mathrm{ext}) = J_0 \left(\exp\left[\frac{q(V_\mathrm{ext} - J(V_\mathrm{ext})AR_\mathrm{s})}{n_\mathrm{id} k_\mathrm{B} T} \right] - 1 \right) + \frac{V_\mathrm{ext} - J(V_\mathrm{ext})AR_\mathrm{s}}{AR_\mathrm{p}} - J_\mathrm{ph}. \quad (3.1)$$

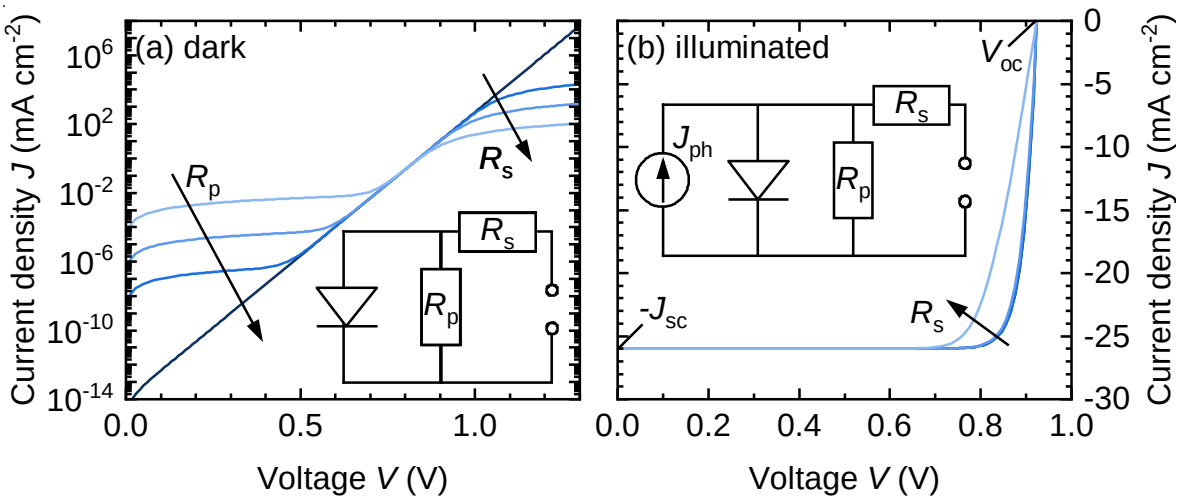

Figure 3.3: (a) Dark current-density voltage characteristics under the influence of resistances as sketched in the equivalent circuit. The darkest line represents a solar cell with no external resistances, while the influence of the resistances increases for the lighter colors. At low voltages, the leakage currents dominate and at high voltages, current flow is limited by the series resistance R_s. (b) Corresponding JV curves under illumination. While the photocurrent density J_ph dominates over any leakage current, the series resistance R_s causes a drop in fill factor.

In case the photocurrent J_ph is voltage-independent, J_ph simplifies to J_sc. In Equation (3.1), n_id is the so-called ideality factor which accounts for recombination that differs from the direct recombination in the Shockley-Queisser model. In the model, the ideality factor $n_\mathrm{id} = 1$, since the recombination-current density, which is the first term in Equation (3.1), scales quadratically with charge-carrier densities according to Equation (2.37). As long as $n \propto p \propto \exp[qV/(2k_\mathrm{B}T)]$, the recombination-current density $J_\mathrm{rec} \propto \exp[qV/(k_\mathrm{B}T)]$ as known from Equation (2.8). However, as discussed in Chapter 2.3.2, in the case of recombination via midgap traps, only one carrier density scales with voltage. Hence, the recombination current density $J_\mathrm{rec} \propto \exp[qV/(2k_\mathrm{B}T)]$. The factor 2 in the denominator is accordingly also found in the current-voltage characteristic as the ideality factor.[126] As charge-carrier densities from more shallow trap states can be slightly voltage dependent, the ideality factor can also lie between 1 and 2.[127] Due to its relation to the dominating recombination mechanism, it is of interest to extract the ideality factor from experimental data. One approach is to take the derivative of the logarithmic dark JV curve, which can be disturbed by resistive effects, though.[19] Alternatively, measuring the open-circuit voltage V_oc as a function of short-circuit current density J_sc can yield the ideality factor since the logarithmic slope is related

to the ideality factor[19]

$$n_{\mathrm{id}} = \frac{q}{k_{\mathrm{B}}T}\frac{\mathrm{d}V_{\mathrm{oc}}}{\mathrm{d}\ln(J_{\mathrm{sc}})}. \tag{3.2}$$

The estimation of the ideality factor with Equation (3.2) brings the advantage that the series resistance R_{s} has no influence on the measurement since there is no current flowing through the resistance at open circuit.[19]

3.2.2. Basics of Organic Indoor Photovoltaics

The field of indoor photovoltaics is a rapidly growing market as more and more small electronic devices need to be powered by batteries or solar cells.[128,129] The so-called Internet of Things constitutes of such electronics for smart systems such as temperature or humidity sensors, GPS trackers or WiFi signal receivers.[130] A large part of these applications are not operated under outdoor conditions but rather in factories, warehouses, office or residential buildings.[130] Hence, the solar cells that act as power supplies face illumination conditions different from the standardized solar spectrum. Instead, the light sources relevant for indoor photovoltaics are light-emitting diodes, fluorescent lamps and incandescent light bulbs. These light sources feature sometimes drastically different emission spectra than the sun.[128] For this type of illumination, organic solar cells bring the advantage that their absorption spectrum can be tailored to the emission spectrum of a specific indoor light source.[97,131] Thereby, the power conversion efficiency is maximized. Also, organic photovoltaics is promising in terms of system integration in the Internet of Things due to its light weight and optional features such as flexibility and semi-transparency.[132]

Outdoor standards for solar cell characterization are defined in terms of radiometric quantities such as the irradiance[133]

$$E_{\mathrm{e}} = \int_0^\infty E_{\mathrm{e},\lambda}(\lambda)\mathrm{d}\lambda \tag{3.3}$$

with the spectral irradiance $E_{\mathrm{e},\lambda}$ in [W/(m²nm)]. For example, the solar spectrum AM1.5G has an irradiance $E_{\mathrm{e}} = 1000\,\mathrm{W/m^2}$.[134] However, light sources indoors focus on human perception rather than absolute power densities and therefore use photometric quantities. Consequently, for comparison of indoor photovoltaics, current-density

voltage curves are measured at the same illuminance[133]

$$E_{\mathrm{m}} = K_{\mathrm{m}} \int_0^\infty M(\lambda) E_{\mathrm{e},\lambda}(\lambda) \mathrm{d}\lambda, \tag{3.4}$$

which is the integral over the spectral irradiance of the light source weighted by the luminous efficacy $M(\lambda)$. It is the normalized sensitivity of the human eye to certain wavelengths. The prefactor K_{m} scales the luminous efficacy to its maximum for daytime vision at 555 nm and is given by $K_{\mathrm{m}} = 683$ lumen/W.[133] The unit of the illuminance is lux. Typical illuminances for indoor photovoltaics are between 200 and 1000 lux.[131]

3.2.3. Admittance Spectroscopy

So far, I have only discussed the response of a solar cell to a DC voltage. But in addition to steady state measurements, the perturbation by an alternating voltage can contain information on charge-carrier transport and recombination. While a solar cell typically does not show inductive features, the charge separation inside the active layer and on the contacts leads to capacitive effects,[135] which manifest in an out-of-phase response of the current density to an alternating voltage. Consequently, the current response is not described by a conductance anymore but by the complex admittance $Y = \mathrm{Re}[Y] + i\mathrm{Im}[Y]$.[136] For the calculation of the admittance, it is important that the DC response of the system is linear. Since the JV characteristic of a solar cell is exponential, the amplitude of the alternating voltage has to be only a few mV to allow a small signal approximation.[137]

For the analysis of the admittance, the real and imaginary part are typically viewed separately as the resistance and capacitance of a parallel RC-element as displayed in Figure 3.4a.[138] However, for such a complex system as a solar cell, it is not trivial what contributes to the real and imaginary part of the admittance. Part of the out-of-phase response of the solar-cell current is caused by the charges sitting on the electrodes. The electrodes therefore can be modeled by a plate capacitor with the electrode capacitance C_σ.[73] When the solar cell is operated at reverse bias, as schematically illustrated in Figure 3.4b, the active layer is assumed to be depleted and all lines of the electric field reach from the cathode to the anode. The capacitance of such a depleted system is termed the geometric capacitance C_{geo} as it only depends on the area and thickness of the active layer. At forward bias, though, charge carriers are injected into the active

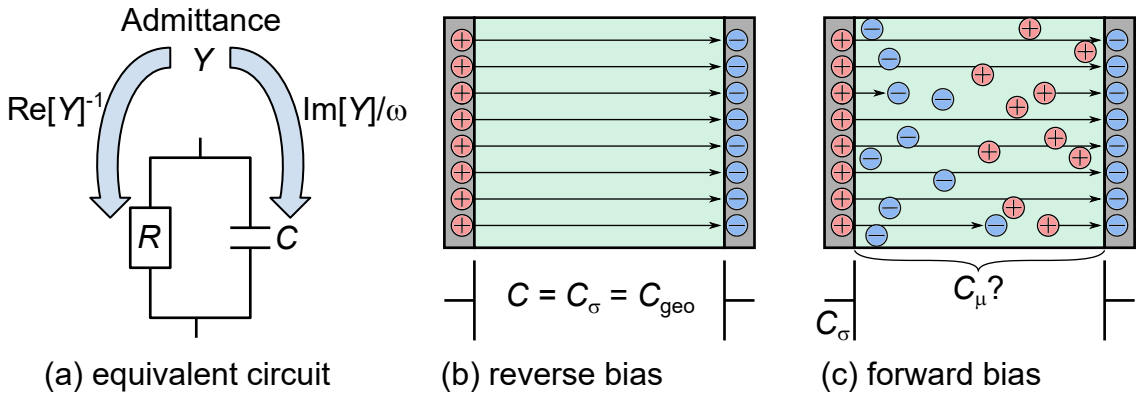

Figure 3.4: (a) Equivalent circuit[138] with a resistance R and a capacitance C that is used for the analysis of the admittance Y of a solar cell. (b) Illustration how the electrodes can be approximated as a plate capacitor under reverse bias with the electrode capacitance C_σ given by the geometric capacitance C_{geo}. (c) Illustration of the situation under forward bias, where charge carriers inside the active layer also contribute to the out-of-phase response, which is termed the chemical capacitance C_μ.[135]

layer, partly screening the contacts' electric field as shown in Figure 3.4c and causing an out-of-phase current themselves. In the same ways that the steady-state current density inside the active layer follows from solving the continuity equations (2.26) and (2.27), this out-of-phase current response to an alternating perturbation can also be derived from them. For this purpose, the electron current $J_{\text{n}}(x,t)$ at any position x in the active layer can be split into a steady-state contribution $\bar{J}_{\text{n}}(x)$ and an alternating electron-current density $\hat{J}_{\text{n}}(x,t)$. Equivalently, the charge-carrier density in such a system is given by $n\,(x,t) = \bar{n}\,(x) + \hat{n}(x,t)$ and the recombination rate $U\,(x,t) = \bar{U}\,(x) + \hat{U}\,(x,t)$. Only the generation of charge carriers ideally remains unaffected by time-dependent changes in the electric field, so $G(x,t) = \bar{G}(x)$. In consequence, the continuity equation (2.26) becomes

$$\frac{\mathrm{d}\left[\bar{n}\,(x) + \hat{n}(x,t)\right]}{\mathrm{d}t} = \frac{1}{q}\frac{\mathrm{d}\left[\bar{J}_{\text{n}}\,(x) + \hat{J}_{\text{n}}(x,t)\right]}{\mathrm{d}x} - \left[\bar{U}\,(x) + \hat{U}\,(x,t)\right] + \bar{G}(x). \tag{3.5}$$

Since the continuity equation holds in steady state, the sum of all steady state quantities has to be zero. In consequence, all the time-dependent contributions also need to sum up to zero and hence can be treated separately.

$$\frac{\mathrm{d}\hat{n}(x,t)}{\mathrm{d}t} = \frac{1}{q}\frac{\mathrm{d}\hat{J}_{\text{n}}(x,t)}{\mathrm{d}x} - \hat{U}\,(x,t)\,. \tag{3.6}$$

For a periodic perturbation, it can be useful to look at the problem in the frequency domain. For this purpose, Laplace transformation can be used that transforms a function $\hat{y}$ from time (hat) into frequency domain (tilde) with the angular frequency ω according to $\widetilde{y}(\omega) = \int_0^\infty \hat{y}(t) \exp(-i\omega t)\,\mathrm{d}t$. Using Laplace transformation on the continuity equation in Equation (3.6), we get

$$i\omega\widetilde{n}(x,\omega) = \frac{1}{q}\frac{\mathrm{d}\widetilde{J}_\mathrm{n}(x,\omega)}{\mathrm{d}x} - \widetilde{U}(x,\omega)\,. \tag{3.7}$$

Rearranging the terms and integrating over the entire thickness d of the active layer gives

$$\widetilde{J}_\mathrm{n}(d,\omega) - \widetilde{J}_\mathrm{n}(0,\omega) = q\int_0^d \left[i\omega\widetilde{n}(x,\omega) + \widetilde{U}(x,\omega)\right]\mathrm{d}x \tag{3.8}$$

Now, the admittance Y is the function connecting the current response to the alternating external voltage $\widetilde{V}_\mathrm{ext}(\omega)$. Assuming a blocking contact for electrons at the anode ($\widetilde{J}_\mathrm{n}(0,\omega) = 0$), we get the admittance as

$$Y = \frac{\widetilde{J}_\mathrm{n}(d,\omega)}{\widetilde{V}_\mathrm{ext}(\omega)} = \frac{q}{\widetilde{V}_\mathrm{ext}(\omega)}\int_0^d \left[i\omega\widetilde{n}(x,\omega) + \widetilde{U}(x,\omega)\right]\mathrm{d}x. \tag{3.9}$$

To solve this equation, numerical methods are needed. However, we can estimate the admittance by using a first-order approximation for the carrier density

$$\widetilde{n}(x,\omega) = \left(\frac{\partial\bar{n}(x)}{\partial\bar{V}_\mathrm{int}(x)}\right)\widetilde{V}_\mathrm{int}(x,\omega) \tag{3.10}$$

and the recombination rate

$$\widetilde{U}(x,\omega) = \left(\frac{\partial\bar{U}(x)}{\partial\bar{V}_\mathrm{int}(x)}\right)\widetilde{V}_\mathrm{int}\ (x,\omega)\,, \tag{3.11}$$

where $\bar{V}_\mathrm{int}(x)$ reflects the quasi Fermi level splitting in the bulk. Thereby, the admittance can be expressed as

$$Y(\omega) = q\int_0^d \frac{\widetilde{V}_\mathrm{int}(x,\omega)}{\widetilde{V}_\mathrm{ext}(\omega)}\left[i\omega\left(\frac{\partial\bar{n}(x)}{\partial\bar{V}_\mathrm{int}(x)}\right) + \left(\frac{\partial\bar{U}(x)}{\partial\bar{V}_\mathrm{int}(x)}\right)\right]\mathrm{d}x. \tag{3.12}$$

Assuming $\widetilde{V}_{\mathrm{int}}(x,\omega) = \widetilde{V}_{\mathrm{ext}}(\omega)$, one can write the imaginary part of the admittance as

$$\mathrm{Im}\left[Y(\omega)\right] = q\int_0^d \omega\left(\frac{\partial\bar{n}(x)}{\partial\bar{V}_{\mathrm{int}}(x)}\right)\mathrm{d}x. \tag{3.13}$$

Therefore, the out-of-phase response of the current inside an active layer is given by the change of the charge-carrier density with voltage. In literature, this response is typically called the chemical capacitance C_μ and treated with position-independent quantities as[135,139]

$$C_\mu = qdA\frac{\mathrm{d}n}{\mathrm{d}V}. \tag{3.14}$$

However, this equation is often introduced without a derivation simply based on the definition of the capacitance as $C = \mathrm{d}Q/\mathrm{d}V$. Equation (3.14) is frequently used to extract the charge-carrier density n. However, since this is a position independent quantity, it remains unclear what charge-carrier density is reflected in this equation. The derivation based on the continuity equation on the one hand brings the advantage of knowing the assumptions going into Equation (3.14), but on the other hand also gives an expression of the real part of the admittance

$$\mathrm{Re}[Y] = q\int_0^d \frac{\partial\bar{U}(x)}{\partial\bar{V}_{\mathrm{int}}(x)}\mathrm{d}x, \tag{3.15}$$

which is given by the voltage-dependence of the recombination rate. This result coincides well with the expression typically used in literature to describe the resistance in parallel to the chemical capacitance in the RC circuit of Figure 3.4a. This recombination resistance R_{rec} is given by[140]

$$R_{\mathrm{rec}} = \mathrm{d}V/\mathrm{d}J_{\mathrm{rec}}, \tag{3.16}$$

where J_{rec} is the recombination-current density. Similar to the expression used for the chemical capacitance, Equation (3.16) ignores the position dependence that follows from the continuity equation and therefore has to be handled with care.

As visible in Equation (3.13), the out-of-phase response of the solar cell depends on both the steady-state voltage and the angular frequency. Therefore, admittance spectroscopy can be applied in two different modes of operation that are shown in Figure 3.5. Either the applied DC voltage is varied at a constant frequency or the frequency

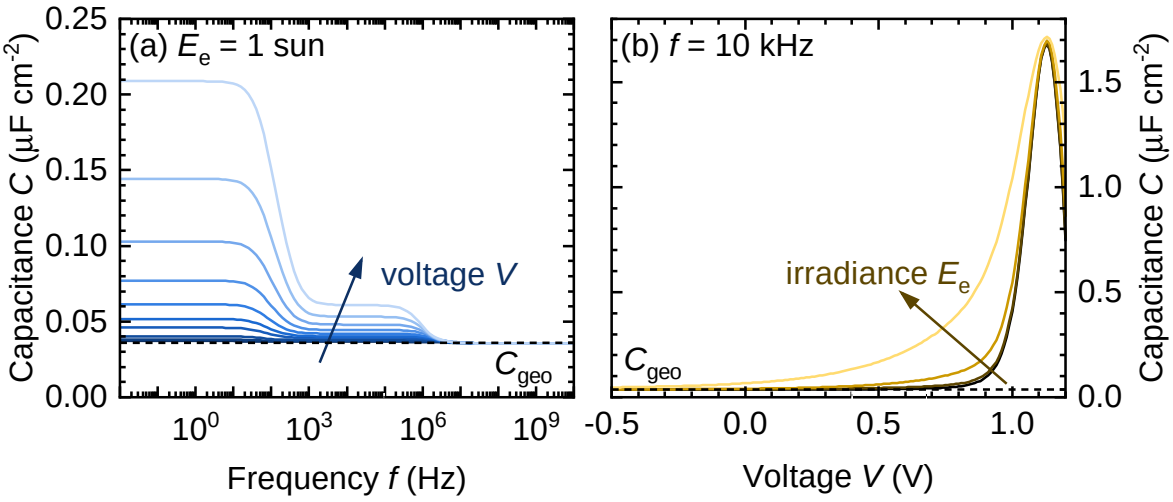

Figure 3.5: (a) Capacitance C as a function frequency f at different DC voltages V under 1 sun illumination. The plateau at low frequencies contains the AC response of free and trapped charge carriers. At medium frequencies, only the free charge-carriers can follow the AC signal and at high frequencies, none can and the capacitance saturates to the geometric capacitance C_{geo}. (b) Voltage-dependent capacitance of the free charge carriers at $f = 10\,\text{kHz}$ under varying irradiance E_e. At forward bias, more charge carriers inside the device cause a higher capacitance C, whereas a depleted active layer at reverse bias leads to $C = C_{geo}$.

is swept at one external DC voltage point. In an experimental context, typically the frequency $f = \omega/2\pi$ is used instead of the angular frequency. For frequency-dependent measurements, the capacitance in the simple RC circuit features several plateaus in Figure 3.5a. At very high frequencies, the charge carriers inside the device cannot follow the change in the electric field anymore and the capacitance only reflects the geometric capacitance C_{geo}.[141] At a certain frequency, the free charge carriers start moving with the alternating field and the capacitance increases to a second plateau.[73] A third plateau at even lower frequencies can be observed in the presence of trap states. The frequency, at which this plateau appears, depends on the trapping and detrapping rates, meaning that trapped charge carriers also contribute to the capacitance.[142] When the DC voltage or the irradiance increases, there are more charge carriers inside the device and the lower frequency plateaus increase.[73] Similarly, when you measure the capacitance at a fixed low frequency as a function of voltage, it will be constant under reverse bias as long as the active layer is depleted as shown in Figure 3.5b.[16] With increasing voltage, the charge-carrier density increases exponentially and thus the capacitance.[16] Following the same logic, with increasing irradiance, the charge-carrier density in the positive voltage region increases and therefore the capacitance in Figure

3.5b. Thereby, admittance spectroscopy can be a tool to characterize charge-carrier densities under different biases and illumination conditions.

3.2.4. Measurement Setup

To measure impedance spectroscopy and current-voltage characteristics, the sample is placed in a sample box to protect it from ambient air. The setup to perform these measurements is sketched in Figure 3.6. A switch box allows the selection of the solar cell that is contacted and characterized. The voltage is either supplied by a source meter (Keithley 2450) for the *JV* measurements or a potentiostat (Gamry Instruments Interface 1000) for impedance spectroscopy, which are controlled via a computer. For measurements under illumination, a solar simulator by the company LOT Quantum Design and a white LED by the company CreeLED can supply a photon spectrum. A variation in light intensity is achieved by either using neutral density filters by Edmund Optics in the light beam of the light source, by varying the driving current of the LED or with a combination of both. The optical density of the filters used in this work range from 0.1 to 2.5.

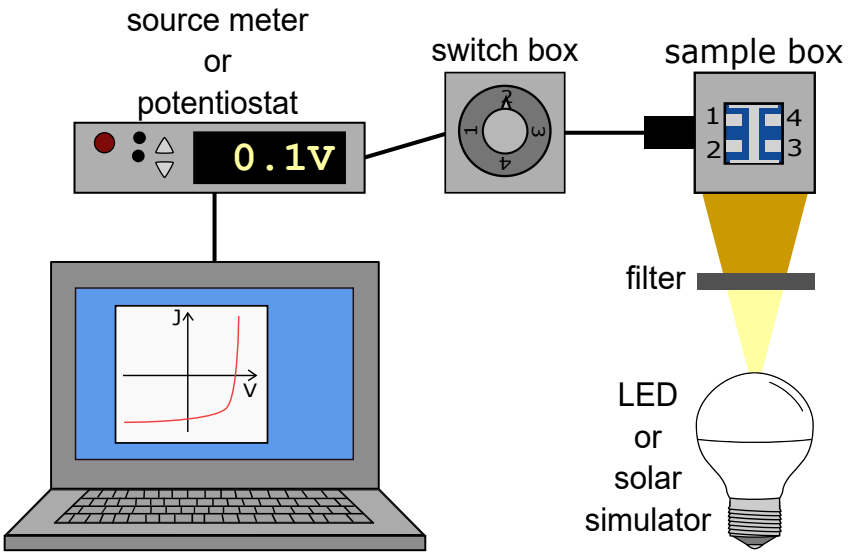

Figure 3.6: Measurement setup for *JV* measurements and impedance spectroscopy. A source meter or potentiostat is controlled by a computer program and applies a voltage to the solar cell which is sealed in a sample box. A switch box allows choosing which solar cell on a substrate to measure. The sample box can be illuminated by a solar simulator or an LED. Neutral density filters in the light beam can change the intensity of the incoming light. Adapted from Reference [143] with permission.

3.3. Optical Characterization

In the ideal case of a solar cell in the Shockley-Queisser limit, the absorptance is simply 1 for energies E above the bandgap E_g and 0 for $E < E_\mathrm{g}$. But in reality, not all photons incident on the surface of the solar cell with $E > E_\mathrm{g}$ are converted into free charge carriers. Instead, they can be lost due to reflection, transmission or parasitic absorption. Therefore, it is essential to probe the absorption properties of a solar cell.

3.3.1. External Quantum Efficiency

The efficiency, at which incoming photons are converted into charge carriers and extracted at the contacts at short circuit is called external quantum efficiency[144]

$$Q_\mathrm{e} = \frac{1}{q}\frac{\mathrm{d}J_\mathrm{sc}}{\mathrm{d}\Phi}. \tag{3.17}$$

Therefore, when varying the energy of the incoming photon flux Φ, the short-circuit current density J_sc changes according to absorption and collection properties of the solar cell at each point of the spectrum. Hence, the quantum efficiency can be used to calculate the short-circuit current density for any given spectrum $E_{\mathrm{e},\lambda}$ by integrating Equation (3.17) according to[131]

$$J_\mathrm{sc} = \frac{q}{hc}\int Q_\mathrm{e}(\lambda)E_{\mathrm{e},\lambda}(\lambda)\lambda \,\mathrm{d}\lambda, \tag{3.18}$$

where h is Planck's constant and c is the speed of light. Thereby, quantum efficiency measurements can be used to verify the current density measured during current-voltage characterization. For the quantum efficiency measurements, the variation in wavelength is often realized by a grating monochromator. To ensure that the incoming photon flux is known, the spot size of the incoming light beam needs to be smaller than the active area. For the quantum efficiency measurements shown in this work, a monochromator TM300 by the company Bentham is used in combination with a halogen and xenon lamp supplied by Bentham 605 lamp power supply. The current densities measured are typically relatively low causing a bad signal-to-noise ratio at low photon energies. Hence, external quantum efficiency measurements work best for the energy range above the bandgap to facilitate the calculation of the short-circuit current density J_sc with any given spectrum (e.g. AM1.5G solar spectrum). However,

for measurements below the bandgap, which can be desired when investigating defect states, simple external quantum efficiency measurements are no longer sufficient.[144]

3.3.2. Photothermal Deflection Spectroscopy

One technique that is frequently used to characterize subgap absorption is photothermal deflection spectroscopy (PDS). It is performed on a layer of the material on glass and utilizes the fact that a semiconductor heats up under illumination due to absorption and thermalization. When the sample is placed in a cuvette filled with a transparent liquid, the heating of the sample and the subsequent heating of the surrounding liquid causes a change in the liquid's refractive index. This change can then be probed by a laser beam in parallel to the sample's surface, which is deflected according to the refractive index as illustrated in Figure 3.7. This effect is called the "mirage" effect and can be observed, for example, in a desert. A quadrant detector measures the angle of deflection which can be related to the absorption coefficient of the material at the incident wavelength. To increase the dynamic range, the signal can be further corrected by the glass substrate's parasitic absorption.[145]

For PDS measurements, the samples in this work are places in a cuvette filled with

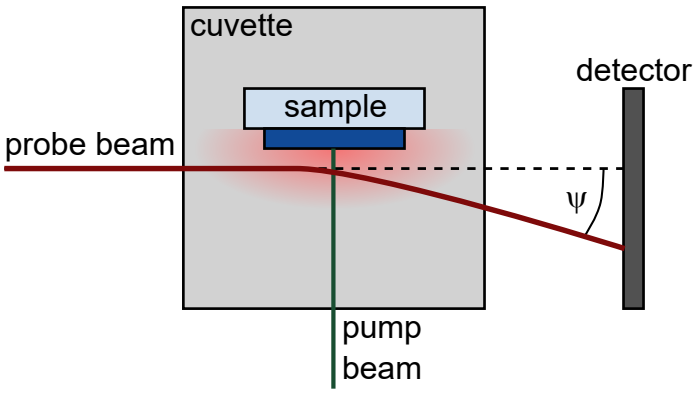

Figure 3.7: Illustration of the measurement principle behind photocurrent deflection spectroscopy (PDS) redrawn after Reference [145]. A sample with the material on glass is placed in a cuvette filled with a liquid. A pump beam of variable wavelength heats the sample according to its absorption coefficient at that wavelength. A laser beam in parallel to the sample probes the liquid that is heated by the sample and deflects the laser beam according to the refractive index change. A detector tracks the angle ψ in which the probe laser is deflected.

2,2,3,3,4,4,5-heptafluoro-5-(1,1,2,2,3,3,4,4,4-nonafluorobutyl)tetrahydrofuran (FC-75) supplied by Alfa Aesar. The sample is illuminated by a halogen lamp (Osram HLX100W) in combination with a monochromator (Newport Cornerstone CS260) with filters (OG590, RG715). The probe beam with a wavelength of 632 nm is supplied by a Uniphase diode laser system and detected by a quadrant diode (Hamamatsu Photonics Quadrant Detector S1557). The detector's signal is amplified by a lock-in amplifier SR850 by Stanford research systems. For the evaluation of the raw data in terms of the absolute absorption coefficient, a refractive index of 2.5 is assumed. This measurement setup is also described in Reference [146].

3.3.3. Fourier-Transform Photocurrent Spectroscopy

An alternative approach to measuring the absorption properties below the band gap with even higher dynamic range is Fourier-transform photocurrent spectroscopy (FTPS). Similar to external quantum efficiency measurements, FTPS probes the photocurrent of a functioning solar cell. To increase the signal-to-noise ratio, all wavelengths are probed at the same time with just one light source. Before reaching the solar cell, the light is directed through a Michelson interferometer, which is illustrated in Figure 3.8a. At a certain mirror position, some wavelengths will interfere constructively, others deconstructively. Now changing the mirror position, the interference will change accordingly as shown in Figure 3.8b. The total signal in Figure 3.8c then is a superposition of all wavelengths. Fourier transformation then yields the spectrum as a function of wavenumber as in Figure 3.8d. As the photocurrent response changes according to the mirror position, the quantum efficiency can be extracted from the signal. For very low energies, additional cutoff filters are used.[147]

The setup for Fourier-transform photocurrent spectroscopy used for this work was previously described in References [146] and [148]. It involves a Fourier-transform infrared spectrometer Vertex 80v by the company Bruker. A mirror speed of 25 kHz was used with a resolution of 12 cm^{-1}. An external halogen lamp HLX100W by Osram serves as an additional light source. The solar cell is connected to a low noise current amplifier Femto DLPCA-200, which amplifies the solar cell's photocurrent and creates an output voltage that is used to create the spectrum with a software. Additional filters suppressing wavelengths above 830 nm and 1000 nm are used for better dynamic

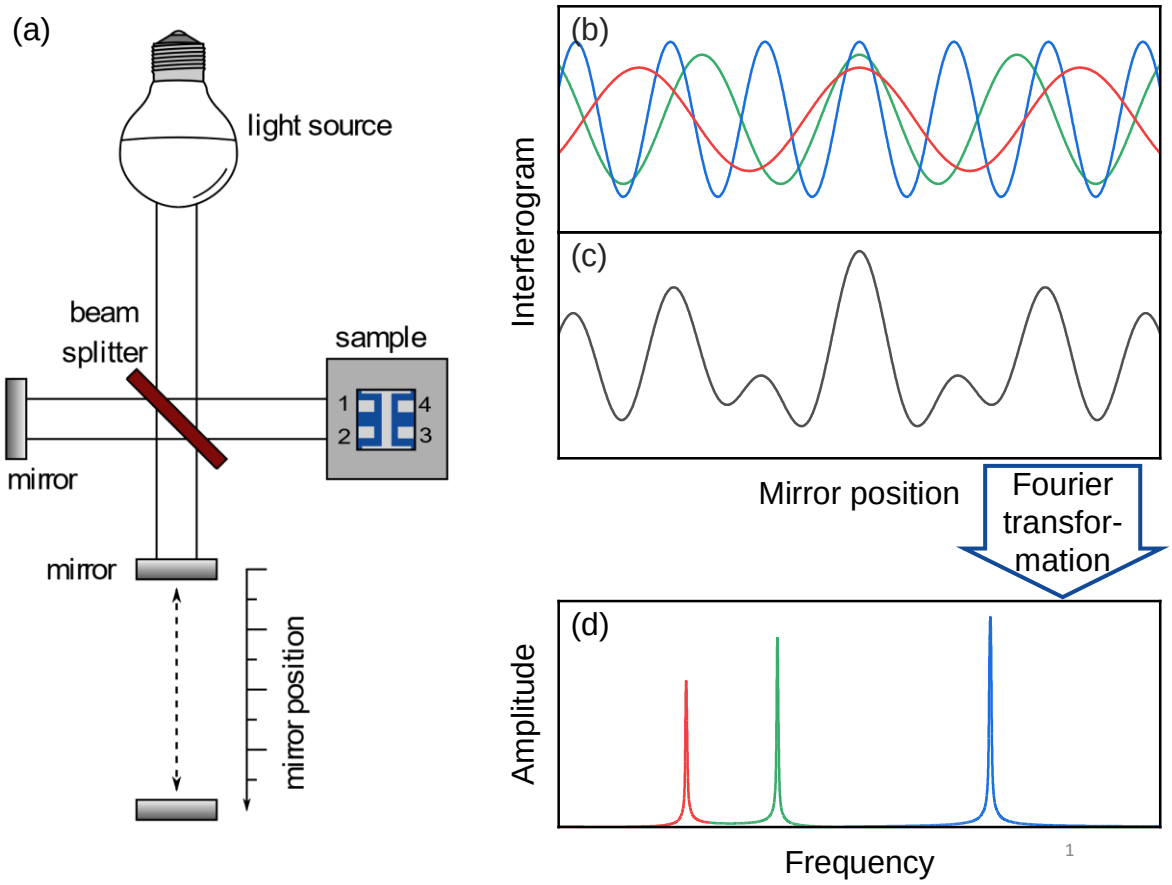

Figure 3.8: (a) Schematic illustration of a Fourier-transform photocurrent spectroscopy (FTPS) setup. A light beam containing multiple wavelengths is emitted by a light source, split by a beam splitter and reflected by two mirrors. The beams from the mirrors interfere with each other before hitting the sample. (b) Changing the mirror position changes the interference for different wavelengths. The sample's photocurrent will change according to (c) the total interferogram. (d) Fourier transformation then yields frequency-dependent data. Panel (b-d) redrawn after Reference [147].

range, where the photocurrents are low. In each filter setting, 500 scans were performed for an improved signal-to-noise ratio.

3.3.4. Spectroscopic Ellipsometry

While photothermal deflection spectroscopy can yield the absorption coefficient α of a material, spectroscopic ellipsometry is needed to measure the full optical properties. More specifically, it yields the complex refractive index consisting of the real part ν of the refractive index and its imaginary part, the extinction coefficient κ. During spectroscopic ellipsometry, a light beam from a monochromator is elliptically polarized

before it hits the sample. The polarization of the light beam that is reflected from the sample is changed according to its optical properties. Thus, from the difference in the elliptical polarization, the refractive index ν and the extinction coefficient κ can be extracted. A change in the wavelength of the incoming light beam can give the full spectral range of the optical constants.[149]

The spectroscopic ellipsometry results used in this work were measured on a ellipsometer by the company HORIBA. Its intrinsic monochromator was replaced with a spectrometer USB2000+ by Ocean Optics and the motor by the stepper driver SMCI33 by the company Nanotec.[150]

3.4. Modeling Organic Solar Cells

Organic solar cells are a complicated, multilayered device, which can make it difficult to extract specific material properties from a functioning device or isolate one specific effect to better investigate it. So, to better understand the device physics and implementations of different measurements, numerical simulations can be used. These device simulations typically consist of an optical model and a solver of Poisson's equation and the continuity equations.

3.4.1. Optical Simulations

In the most simplistic optical model, one can assume a constant generation rate throughout the device. This assumption can be useful when trying to understand an effect in a more ideal device by assuming full symmetry. One step towards more realistic optical modeling is implementing Lambert-Beer's law from Equation (2.29) and assuming an exponential decay for the position-dependent generation rate.[61] However, this model only includes the absorption coefficient and neglects any reflection on the interfaces of the active layer and its contact layers. These are very important, though, as they cause interference effects that are especially relevant as the active layer thickness is comparable to the wavelength of the absorbed light.[5] Therefore, the generation of charge carriers is amplified at certain positions in the active layer while it is reduced due to deconstructive interference at others. An optical model that includes these interference effects is transfer matrix theory.[63] Here, the superposition of the electromagnetic waves that propagate forwards and backwards through the different layers is

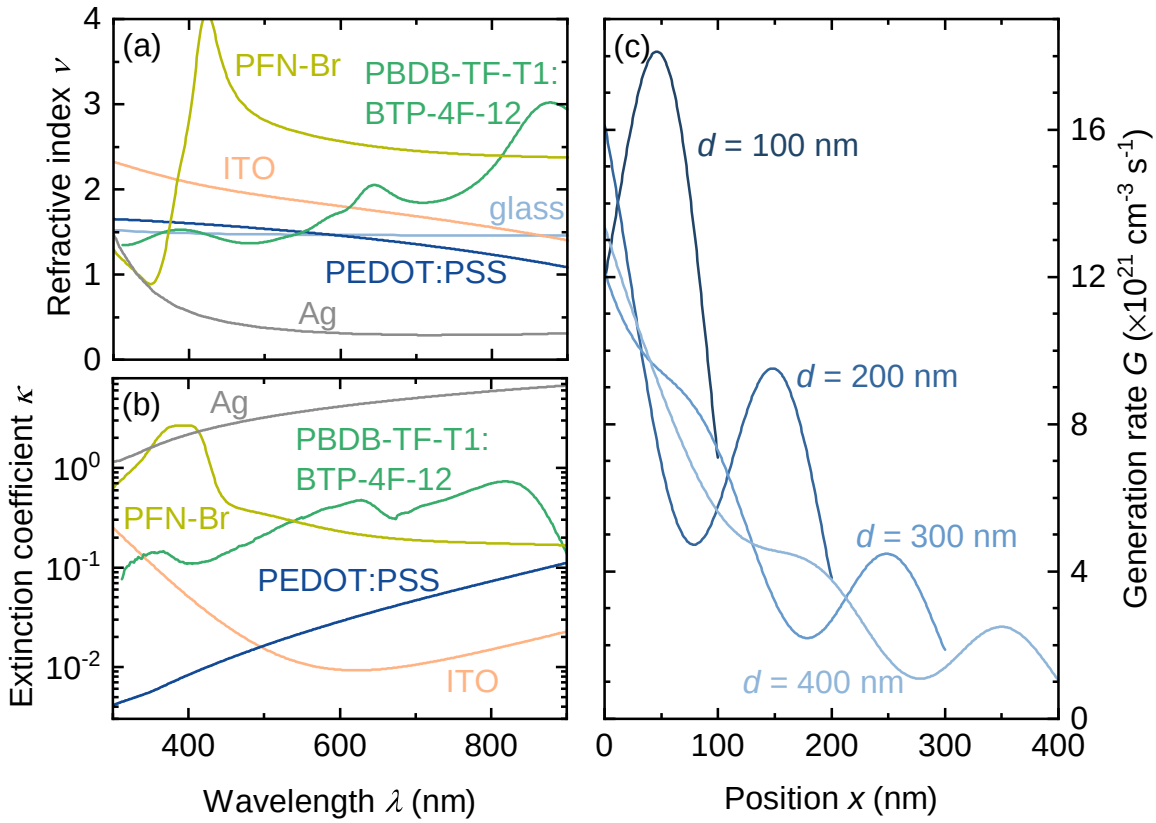

Figure 3.9: (a) Refractive index ν of the layers that constitute the solar cells simulated in this work. (b) Extinction coefficient κ of all layers except glass, which is zero in the wavelength region displayed here. The optical constants were measured in our institute except for silver that is taken from Reference [151]. (c) Generation rate profile simulated with transfer matrix theory and the optical constants of (a) and (b) for varying active layer thickness d.

calculated. For this purpose, matrices describe each interface and layer in a stack. The squared norm of the electric field then correlates to the amount of charge carriers that are generated at each wavelength and point in the solar cell. For more detail on the method itself, I refer to Reference [63]. In the scope of this work, optical simulations are performed using the built-in tools from the Advanced Semiconductor Analysis (ASA) software.[152] It was developed by the group of Prof. Miro Zeman at Technical University of Delft and is commercially available under `https://asa.ewi.tudelft.nl/` (accessed 22/05/2023).[5] For the implementation of transfer-matrix theory, the knowledge of the refractive index, the extinction coefficient and thickness of all layers is essential. Figure 3.9a shows the refractive index of the layers used in this work. The data has been recorded at our institute except for the silver which is taken from Reference [151]. With the drastic refractive index change between PFN-Br and silver, the

silver acts as a back reflector in the device to cause interference effects. The respective extinction coefficient for the layers is plotted in Figure 3.9b. In the optical simulations such as in Figure 3.9c, the glass is assumed to have a thickness of 1 mm. Due to its high thickness, light is set to be incoherent in this layer. The ITO is set at a thickness of 131 nm, 22 nm for the PEDOT:PSS layer, PFN-Br is assumed to be 13 nm thick and the silver to have a thickness of 109 nm. The generation rate G of free charge carriers as a function of position in the active layer x that is displayed in Figure 3.9c is simulated using ASA. The variation of the active layer thicknesses d reveals different interference maxima. While the maximum generation rate can be found in the center of a thin 100 nm device, thicker active layers exhibit a maximum at the illuminated contact. This variation illustrates how important optical modeling can be to properly simulate an organic solar cell. Aside from this typical use, in this work, optical simulations are also applied to estimate the active layer thickness of the solar cells. Chapter A.4 gives further details on this procedure.

3.4.2. Drift-Diffusion Simulations

Once an optical model is chosen, one can use the position-dependent generation rate in the continuity equations and numerically solve them together with Poisson's equation. These so-called drift-diffusion simulations have been a tool used for decades to deepen the understanding of solar cell technologies based on silicon,[152–154] GaAs,[155,156] CuInGaSe[157,158] or perovskites[159–162]. However, they assume a classical semiconductor with a valence and conduction band, which is not directly applicable to the concept of a bulk heterojunction in organic photovoltaics. Still, drift-diffusion simulations have been frequently used on organic solar cells[47,163–171] using the effective medium approximation[5,172] illustrated in Figure 3.10. In the bulk heterojunction, the donor and acceptor material are intermixed but still form their own phases with their respective HOMO and LUMO level (see Figure 3.10a). However, after the generation of free charge carriers, only the LUMO of the acceptor serves for electron transport and the HOMO level of the donor for hole transport. Therefore, in drift-diffusion simulations, the LUMO of the acceptor is treated as the conduction band and the HOMO of the donor as valence band[5,172] as shown in Figure 3.10b. Equilibrating the Fermi level E_F yields a built-in voltage V_bi according to the work function difference of the contact layers if the organic semiconductor itself is intrinsic.[5] The potential difference between

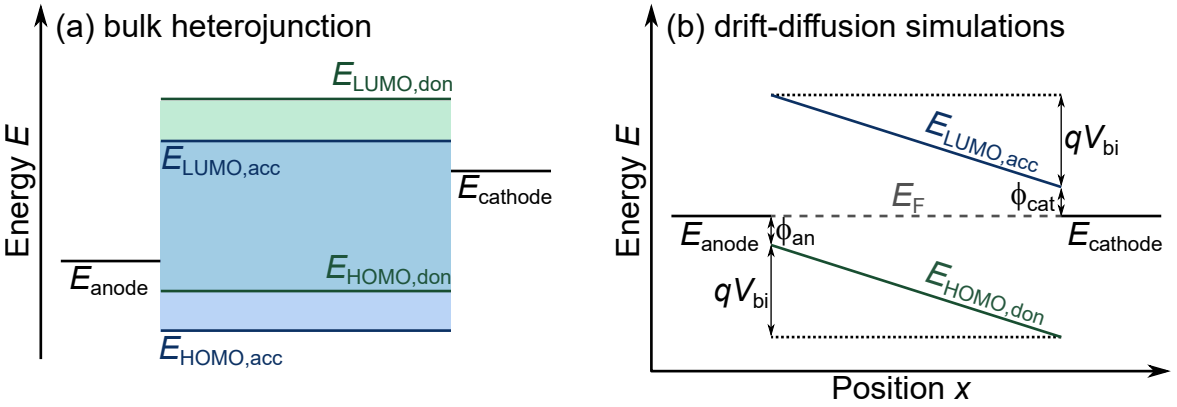

Figure 3.10: (a) Schematic of the energy levels in an uncontacted bulk heterojunction. The active layer consists of a mixture of donor and acceptor material. (b) Simplified energy diagram of the bulk-heterojunction only considering the energy levels that contribute to charge transport. The difference in the contact layers' work functions constitutes the built-in voltage V_{bi}, while their difference to the active layer's energy levels is set as the injection barriers $\phi_{\mathrm{an/cat}}$ in the drift-diffusion simulations.

the work function of the anode and the HOMO of the donor gives the injection barrier ϕ_{an} for holes and the difference between the LUMO of the acceptor and the cathode work function is injection barrier ϕ_{cat} for electrons.[5] Thereby, a band structure as a function of position x is created that allows solving the drift-diffusion equations for organic solar cells.

In this work, the energetic disorder of the organic semiconductor is implemented with the use of exponential band tails. In the simulations, the exponential density of tail states is discretized to a certain number of energy levels. The conduction-band tail states are treated as acceptor-like defects which are negatively charged when occupied by an electron. Vice versa, the donor-like valence band tail states are positively charged when occupied by a hole. This charge trapped in the defect states also contributes to the total charge inside the solar cell in the drift-diffusion simulations. All simulation parameters are summarized in Table 3.2.

For the simulations performed for this work, I use Matlab or Python to control solar cell simulation software that uses finite differences method to solve the coupled differential equations that describe a solar cell. I use two software tools for different purposes. Firstly, the Advanced Semiconductor Analysis (ASA) software introduced for optical simulations also offers a robust numerical solver. Apart from the advantage of combining optical and electrical simulations in one tool, it also brings high computational speed and offers easy control via the command line and external code.

Table 3.2: Values of the material parameters that were used as input in the numerical simulation software ASA or SCAPS for the modeling of organic solar cells in this work if not stated otherwise.

Parameter	Unit	Value
Active layer thickness d	nm	100
Temperature T	K	300
Effective density of states conduction band/valence band $N_{\mathrm{CB/VB}}$	cm^{-3}	10^{19}
Energy gap E_{g}	eV	1.4
Injection barrier anode/cathode $\phi_{\mathrm{an/cat}}$	eV	0.1
Electron/hole mobility $\mu_{\mathrm{n/p}}$	$\mathrm{cm}^2\,\mathrm{V}^{-1}\,\mathrm{s}^{-1}$	8×10^{-4}
Relative permittivity ε_{r}		3.07
Direct recombination coefficient k_{dir}	$\mathrm{cm}^3\,\mathrm{s}^{-1}$	2×10^{-11}
Density of conduction/valence band tail states $N_{\mathrm{CBT/VBT}}$	$\mathrm{cm}^{-3}\mathrm{eV}^{-1}$	10^{19}
Urbach energy E_{U}	meV	30
VBT hole/CBT electron capture coefficient β_1	$\mathrm{cm}^3\,\mathrm{s}^{-1}$	10^{-8}
VBT electron/CBT hole capture coefficient β_2	$\mathrm{cm}^3\,\mathrm{s}^{-1}$	5×10^{-11}
Energy level deep traps E_{dt}	eV	$E_{\mathrm{g}}/2$
Density N_{dt} of deep trap states	cm^{-3}	10^{16}
Deep trap Gaussian width ΔE_{dt}	eV	0.1
Capture coefficient deep traps β_{dt}	$\mathrm{cm}^3\,\mathrm{s}^{-1}$	10^{-9}
Surface recombination velocity S	$\mathrm{cm\ s}^{-1}$	10^{-5}
Series resistance R_{s}	$\Omega\ \mathrm{cm}^2$	0
Parallel resistance R_{p}	$\Omega\ \mathrm{cm}^2$	10^{22}

Even though ASA has been developed for silicon solar cells,[152] it has already been successfully applied to organic photovoltaics as well.[47,68,173] However, ASA is limited to steady-state simulations, which is why I use an additional software, the Solar Cell Capacitance Simulator (SCAPS) developed by Prof. Marc Burgelman and his coworkers at the University of Gent.[5,174] It is publicly available under the following link: `https://scaps.elis.ugent.be/` The software was originally designed for other thin-film technologies[157] but has been applied to organic solar cells as well.[73,169] SCAPS does not offer optical modeling with transfer-matrix theory and is optimized for usage via a graphic user interface rather than code but offers the simulation of measurements

in the frequency domain, which are relevant for this work. Therefore, for all simulations of admittance spectroscopy that were performed in this work, ASA is used for the optical simulations and SCAPS for the electrical simulations. Otherwise, ASA is the simulation software of choice here.

4

Traditional Evaluation of a Material System

In the field of organic photovoltaics, the development of solar cells takes place at a rapid pace with new solar cell systems being reported daily. Especially the variety of already existing and newly synthesized organic semiconductors offers endless opportunities to fabricate solar cells with novel material systems in the active layer. To report these new devices, researchers typically conduct basic measurements to characterize them and often compare them to preexisting solar cell systems. These measurements almost always include current-voltage curves under a solar simulator and external quantum efficiency measurements,[24–45, 107, 116, 175–184] often accompanied by light-intensity dependent measurements of the short-circuit current density or the open-circuit voltage[20–45] as the measurement setup is often easily available. In addition, numerous publication add further optical measurements, such as photothermal deflection spectroscopy, to characterize the subgap absorption of the material system that is presented.[20, 182, 183, 185–193] However, the analysis of these measurements often follows simple models which bear the risk of losing information on the device physics or even misinterpreting the data. Therefore, I aim at providing an example on how to correctly characterize recombination with these basic measurements. For this purpose, I use the measurements conducted by Barbara Urbano in the scope of her master thesis[194] on the material system PBDB-TF-T1:BTP-4F-12 with additional impedance spectroscopy and optical measurements. While Barbara Urbano has already used some characterization techniques to analyze JV curve and external quantum efficiency measurements, I will focus in the following on the methods most frequently used in literature and analyze it according to the prevalent models in the current chapter. So, I first present JV curves and quantum efficiency measurements in Chapter 4.1 and then use light-intensity de-

pendent measurements and photothermal deflection spectroscopy in Chapter 4.2 for basic characterization of recombination according to traditional models. Only with this knowledge of what is currently applied in literature, it is sensible to move on to further modeling and understanding the PBDB-TF-T1:BTP-4F-12 material system and these characterization techniques in the later chapters of my thesis.

4.1. Analysis of Current-Voltage Characteristics

In a first step, to understand a material system, one needs to look at the current-density voltage characteristics of the solar cells. There are multiple JV curves available for solar cells with active layer thicknesses from 32 to 352 nm under light intensities ranging from around 30 lux LED illumination to about solar illumination. Figure 4.1 features exemplary current-density voltage curves measured (a) under a solar simulator at approximately 1 sun light intensity and (b) under an LED with an illuminance of around 200 lux for the solar cell that performs best under the illumination condition in (a) and the best one for the low light condition in (b). They differ in active layer thickness by around 100 nm. Under the solar simulator in Figure 4.1a, the solar cells feature a similar open-circuit voltage V_{oc} but the fill factor FF of the thin device is significantly better and its short-circuit current density is 2 mA/cm^2 higher, which hints towards collection problems in the thicker solar cell.[195] While the thick device maintains good performance even under very low illumination levels in Figure 4.1b, the thin one that was previously the best features almost linear behavior between J_{sc} and V_{oc} which is indicative of a high ohmic leakage current.[196] Therefore, first conclusions on the limiting factors of a solar cell can already be drawn from comparing the JV curves. External quantum efficiency Q_{e} measurements are often reported alongside JV curves to verify the photocurrent measured during the current-voltage characterization and to give first insights into the absorption properties of the material system. Figure 4.1c shows the external quantum efficiencies Q_{e} for the two solar cells discussed previously. At intermediate wavelengths, both devices exhibit a similar external quantum efficiency. Only at high and low wavelengths, they differ with the thin device having a maximum at a wavelength of around 820 nm and the thick device at 360 nm. These differences possibly stem from a change in interference due to their different active layer thickness.[197] The external quantum efficiency Q_{e} can be used to find the calculated short-circuit current density $J_{\mathrm{sc,Q}}$ for a given incoming photon spectrum by integrating

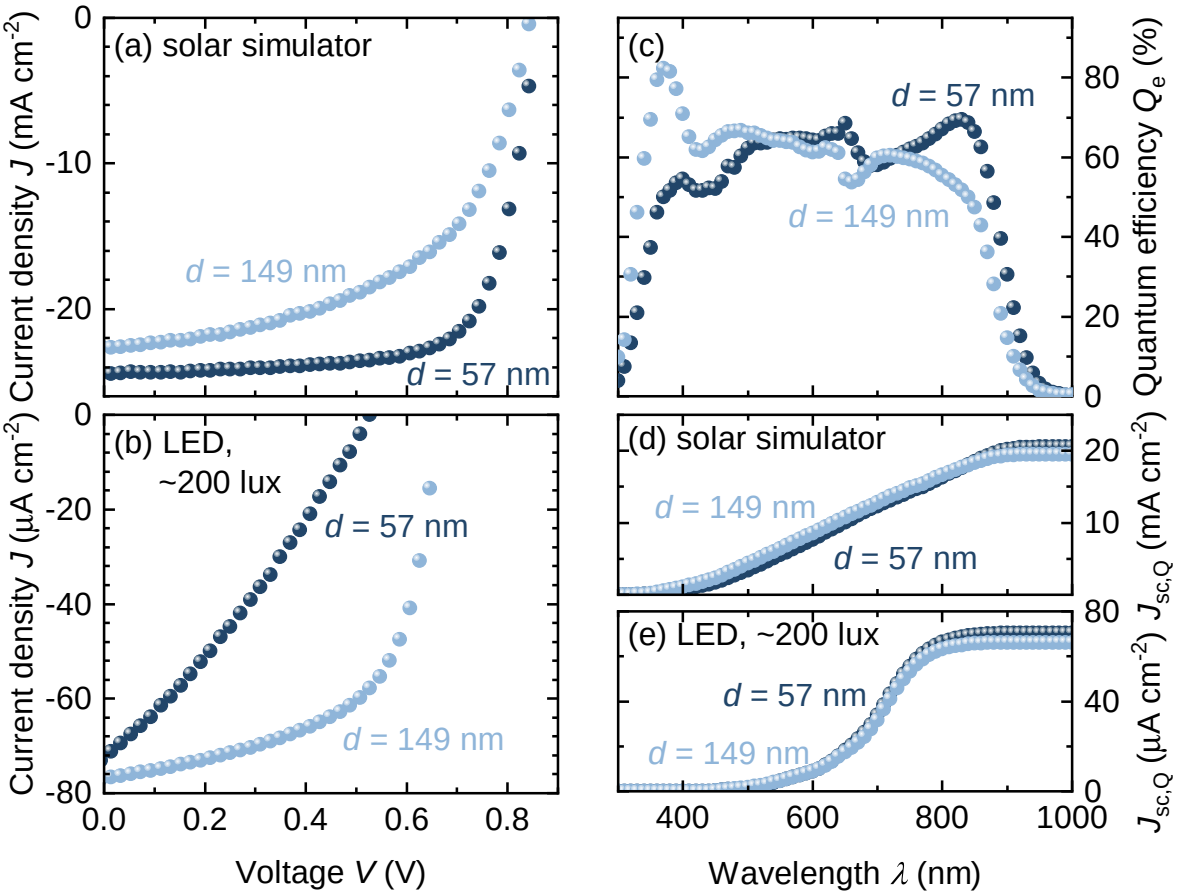

Figure 4.1: Current density J as a function of voltage V for organic solar cells with different active layer thicknesses d measured (a) under a solar simulator at a light intensity of roughly 1 sun and (b) under LED illumination of around 200 lux. The thin solar cell in dark blue is the device that performs best under the solar simulator and the device in light blue is the best solar cell at 200 lux. (c) External quantum efficiency Q_e measurements of both solar cells. (d) Integrated short-circuit current density $J_{sc,Q}$ using the respective external quantum efficiencies and the AM1.5G spectrum or (e) the LED spectrum at 200 lux.

the product of Q_e and the photon spectrum over all wavelengths as given by Equation (3.18) and illustrated in Figure 4.1d and 4.1e for both illumination conditions. Integrating up the short-circuit current density $J_{sc,Q}$ in Figure 4.1d with the solar spectrum AM1.5G also results in the thinner cell having a higher J_{sc} than the thicker device. However, the integrated $J_{sc,Q}$ values lie below the ones extracted during JV measurements. On the one hand, this discrepancy might be caused by the spectrum of the solar simulator not matching the AM1.5G spectrum well, on the other hand, the solar cells might have degraded between the initial measurement of the JV curves and the

quantum efficiency measurements. When doing the same calculation for the spectra associated to the LED measurements in Figure 4.1e, the thin cell still yields the higher $J_{sc,Q}$ contrary to the JV measurements and the values are overall lower. Here, a source of error is the LED spectrum itself as it depends on a variety of factors. Chapter A.5 in the Appendix further discusses how LED spectra are calculated in this work. As this work does not report record efficiencies or other notable performance parameters that require comparison with literature, but rather aims at a qualitative understanding of the underlying solar cell physics, accurate calibration of the solar simulator is not essential. Instead, a lot can be learned from the trends that the solar cells feature with variation of parameters such as thickness and illumination intensity on the working mechanisms of PBDB-TF-T1:BTP-4F-12-based solar cells.

For example, the thickness dependence of the characteristic parameters of a solar cell is further summarized in Figure 4.2 beyond the two devices that were selected in Figure 4.1. It shows (a) the short-circuit current density J_{sc} normalized by the highest value measured, (b) the open-circuit voltage V_{oc} normalized by its maximum value, (c) the fill factor FF and (d) the power-conversion efficiency η which were calculated from JV curves of solar cells illuminated by a solar simulator or by an LED with an illuminance of around 200 lux. The short-circuit current density in Figure 4.2a features one maximum at slightly below 100 nm and one between 200 and 300 nm active layer thickness for both illumination intensities. These coinciding maxima show that despite the different incoming photon spectra, the interference maxima of the light inside the active layer appear at the same thicknesses. However, under the solar spectrum, the second maximum is more pronounced than under low light illumination. The open-circuit voltage in Figure 4.2b is overall higher under solar illumination than under the low light illumination since it increases logarithmically with light intensity according to Equation (2.16). For both illumination conditions, the open-circuit voltage V_{oc} decreases with active layer thickness. To allow better comparison of the thickness-dependent behavior, I normalized V_{oc} to its respective maximum value. This normalization reveals much more significant scattering of the values for low light illumination. Also, in Figure 4.2c, the fill factor for thin devices under low illumination scatters more significantly than for thick devices. This behavior might be caused by leakage currents through pinholes in the active layer. These ohmic currents decrease the open-circuit voltage and fill factor and are especially relevant when the photocurrent, which flows in parallel, is low such as for the 200 lux measurements.[198, 199] As

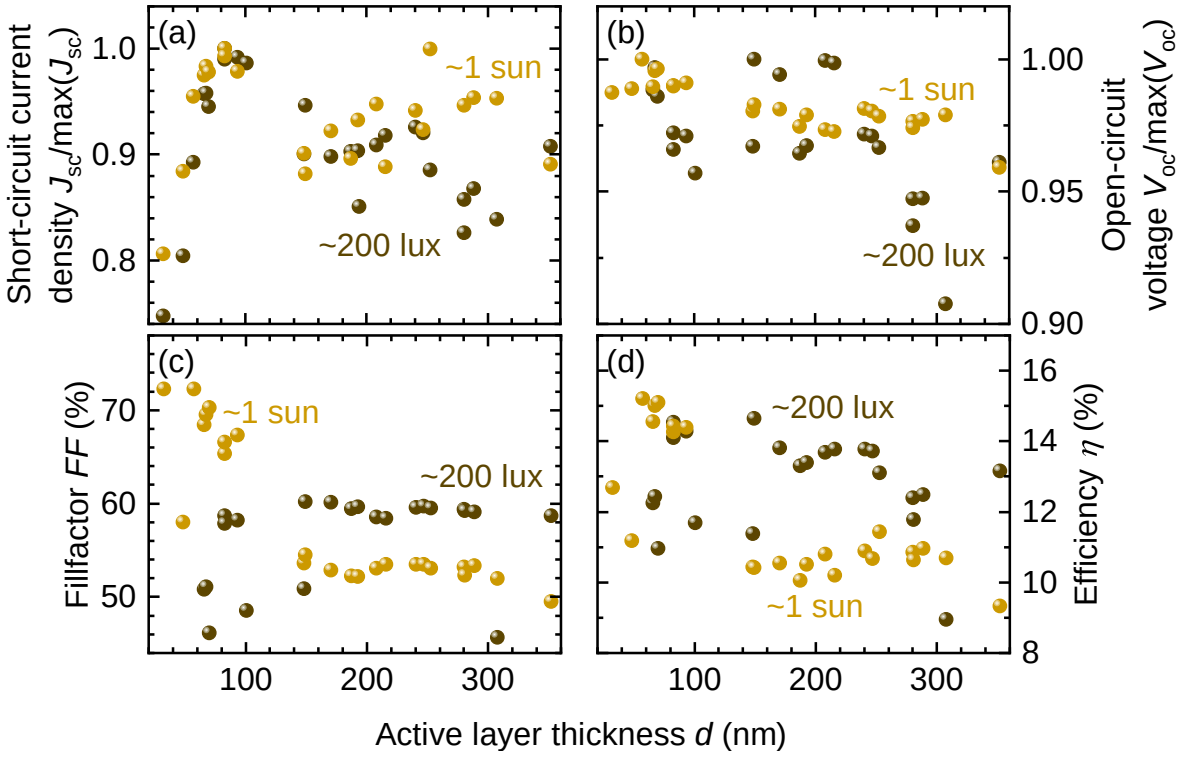

Figure 4.2: Characteristic parameters of solar cells with varying active layer thickness d extracted from JV curves measured under a solar simulator and under LED illumination with an illuminance of around 200 lux. (a) The short-circuit current density J_{sc} normalized by its highest value features two maxima, below 100 nm and between 200 and 300 nm. (b) The open-circuit voltage V_{oc} normalized by its maximum is more scattered under low illumination than high illumination. (c) The fill factor FF for thin active layers is higher under 1 sun illumination but falls below 200 lux for thick devices. (d) In terms of power-conversion efficiency η, the solar cells perform better under low light conditions for most active layer thicknesses.

these pinholes occur randomly, some devices might be more affected than others causing the scattering of the performance parameters. However, thick active layers could be less prone to pinhole formation, explaining the decrease in scattering of open-circuit voltage V_{oc} and fill factor FF in Figure 4.2. Under high illumination, the current flow through the intact active layer is dominant causing the fill factor to be higher at low active layer thicknesses than under low light illumination. For thicker devices, though, the fill factor under 1 sun illumination drops below the values for 200 lux. This phenomenon indicates light-intensity and thickness dependent collection problems that could be caused by space charge effects.[200] Consequently, the solar cells with active layer thicknesses above 100 nm exhibit a better power-conversion efficiency η under low light illumination in Figure 4.2d than under the solar simulator. Only very thin devices

perform better under solar illumination. This initial analysis has therefore primarily aided to understand interference effects and to identify possible influence of leakage currents on the performance of the solar cell system PBDB-TF-T1:BTP-4F-12. For the development of more efficient solar cells, it is however also crucial to gain insights into the recombination pathways of the solar cell. There are numerous approaches to characterize recombination in organic solar cells that can be found in literature. Amongst the most popular ones are the analysis of the short-circuit current density and open-circuit voltage as a function of light intensity[20–45] due to its simplicity and the extraction of the Urbach energy E_{U} as an indicator for the energetic disorder from photothermal deflection spectroscopy measurements.[20–45] Therefore, I herein will first follow the characterization procedure that is typically used in literature for a new solar cell system before discussing the techniques in more detail in the scope of this work.

4.2. Basic Characterization of Recombination Mechanisms

Very simple measurements to perform for an initial characterization of the recombination inside a solar cell are light-intensity dependent JV measurements. From these JV curves, the short-circuit current density J_{sc} as well as the open-circuit voltage V_{oc} as a function of irradiance E_{e} can be calculated. The logarithmic slope of the open-circuit voltage V_{oc} yields the ideality factor n_{id} as presented in Chapter 3.2.1. The analysis of this measurement has already been extensively discussed in literature.[19,47,196,201] However, the rationale underlying the traditional analysis of the light-intensity dependence of the short-circuit current density J_{sc} has been, to the best of my knowledge, first been explained in our publication *Understanding the Light-Intensity Dependence of the Short-Circuit Current of Organic Solar Cells* by Paula Hartnagel and Thomas Kirchartz published by Wiley Online Library,[202] even though it has been applied for over a decade in the characterization of organic solar cells.[21,39,45,116,203,204] The interpretation of light-intensity dependent short-circuit current density measurements is based on a 0D model. Therefore, an understanding of the ideal situation at short circuit is required. When there is no recombination occurring inside a solar cell at short circuit, all charge carriers generated are also extracted by the electric field. Therefore,

the maximum short-circuit current density $J_{\mathrm{sc,max}}$ can be written as

$$J_{\mathrm{sc,max}} = q \int_0^d G(x)\,\mathrm{d}x = qdG_{\mathrm{av}}, \tag{4.1}$$

where q is the elementary charge and d is the thickness of the absorber. The average generation rate G_{av} is defined as arithmetic mean of the generation rate G over the position x in the active layer, creating a linear correlation between $J_{\mathrm{sc,max}}$ and the generation rate and therefore the irradiance. This maximum short-circuit current density is reduced by recombination of free charge carriers. Nongeminate, monomolecular recombination is one possible recombination mechanisms. The corresponding recombination-current density $J_{\mathrm{rec,SRH}}$ introduced in Equation (2.45) is proportional to the charge-carrier density in a 0D approximation. The charge-carrier density in turn is assumed to scale linearly with the generation rate. Hence, the recombination-current density results in

$$J_{\mathrm{rec,SRH}}(G_{\mathrm{av}}) = m_1 G_{\mathrm{av}} \tag{4.2}$$

where m_1 is a coefficient determining the intensity of the monomolecular recombination.

Secondly, bimolecular, direct recombination can reduce the maximum short-circuit current density by the direct recombination-current density $J_{\mathrm{rec,dir}}$ from Equation (2.37) which is proportional to the product of electron and hole density. In case of the average electron density n_{av} and the average hole density p_{av} scaling linearly with the generation rate, $J_{\mathrm{rec,dir}}$ can be written as

$$J_{\mathrm{rec,dir}}(G_{\mathrm{av}}) = m_2 G_{\mathrm{av}}^2 \tag{4.3}$$

where m_2 is a coefficient indicating the amount of direct recombination.

In a solar cell with both mono- and bimolecular recombination, the recombination-current densities diminish the optimum short-circuit current density to the actual short-circuit current density

$$J_{\mathrm{sc}}(G_{\mathrm{av}}) = qdG_{\mathrm{av}} - m_1 G_{\mathrm{av}} - m_2 G_{\mathrm{av}}^2. \tag{4.4}$$

With this approach, an expression for J_{sc} is acquired linking it to the average generation rate. Both the maximum short-circuit current density and the monomolecular

recombination-current density scale linearly with the generation rate whereas bimolecular recombination scales in quadratic order. For better visualization, one can calculate the slope

$$\gamma = \frac{\mathrm{d}\ \ln(J_{\mathrm{sc}})}{\mathrm{d}\ln(G_{\mathrm{av}})} = 1 + \frac{\mathrm{d}\ln(qd - m_1 - m_2 G_{\mathrm{av}})}{\mathrm{d}\ \ln(G_{\mathrm{av}})} \tag{4.5}$$

of the double-logarithmic plot which represents the correlation between J_{sc} and G_{av}. It appears that in case of no bimolecular, direct recombination ($m_2 = 0$), $\gamma = 1$ and J_{sc} scales linearly with the generation rate. In the presence of direct recombination ($m_2 > 0$), a sublinear trend can be observed. Thereby, the measurement of the short-circuit current density for different light intensities and therefore different generation rates promises an easy way of identifying bimolecular recombination in an organic solar cell from a sublinear relation.

In literature, this rationale is typically applied by fitting the short-circuit current density as a function of light intensity and comparing the slope of different devices to identify differences in the bimolecular recombination. Figure 4.3a shows an example for such light-intensity dependent J_{sc} data for solar cells discussed in the previously in Figure 4.1. The J_{sc} values for both devices almost lie on top of each other on the double-logarithmic scale. The dashed lines represent linear fits to this data, yielding the slope $\gamma = 0.977$ for the thin device and $\gamma = 0.955$ for the thicker device. According to the rationale presented above, these slopes imply that the contribution of bimolecular recombination is more significant in the thick device than in the thinner one. From the light-intensity dependent current-voltage curves, one can also extract the open-circuit voltage V_{oc} as a function of J_{sc}, which is depicted in Figure 4.3b. The ideality factor n_{id}, which is calculated from the slope of the fits in Figure 4.3b, is higher for the thicker solar cell at a value of 1.29 compared to 1.09 for the thin solar cell. As discussed in Chapter 3.2.1, such an ideality factor between 1 and 2 indicates recombination via shallow defects to be dominant in the solar cell.[47,127] Such shallow defects are not included in the traditional analysis of light-intensity dependent J_{sc} measurements and can therefore not be identified from these. In contrast to these measurements, I only fitted the high light-intensity regime for the ideality factor in Figure 4.3b to avoid the high slopes at lower intensities, especially for the thin device. As discussed by Proctor and Nguyen, the drop in V_{oc} and increase in ideality factor is just an artifact of the dark shunt resistance limiting the open-circuit voltage.[199] Therefore, in Figure 4.3b,

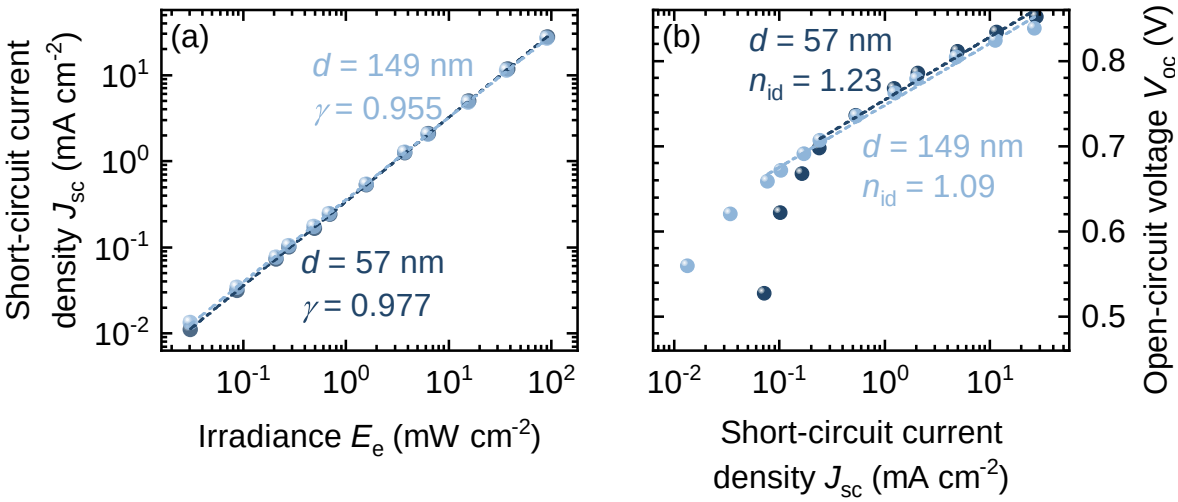

Figure 4.3: (a) Experimental short-circuit current density J_{sc} for varying irradiance E_e for the devices that perform best at 1 sun or 200 lux. The dashed lines represent linear fits on the double-logarithmic scale. Traditionally, a low slope γ is treated as an indicator for direct recombination. (b) Open-circuit voltage V_{oc} as a function of short-circuit current density J_{sc}. The ideality factor n_{id} extracted from the slope of semi-logarithmic fits is higher for the thicker device.

extracting the ideality factor from the unaffected regimes indicates recombination via shallow defect states. Hence, the characterization of these shallow defects is essential.

A common approach to characterizing the shallow defects originating from energetic disorder is measuring the absorption coefficient α from photothermal deflection spectroscopy (PDS) around the band edge. The result of such a PDS measurement for the material system at hand is shown in Figure 4.4. The absorption coefficient α increases rapidly around the band edge of around 1.4 eV. Assuming exponential tail states below the band gap as described in Figure 2.6b and equal densities of defect states above the valence band and below the conduction band, one can fit the absorption coefficient α for its exponential slope. The resulting fit for the data in Figure 4.4 is shown in the dashed line. The inverse of the slope yields the Urbach energy $E_{U,PDS}$ of 29 meV which is relatively low. Such a low Urbach energy would, however, not explain the ideality factor extracted previously from Figure 4.3b. Hence, the recombination mechanisms in these solar cells must be too complex to be characterized by these simple tools.

The data set presented in this thesis was obtained by Barbara Urbano in the scope of her master thesis and analyzed in more detail. For example, her results imply that surface recombination is not dominant in these solar cells which allows us to focus on bulk recombination in this work.[194] This chapter concludes the analysis of recom-

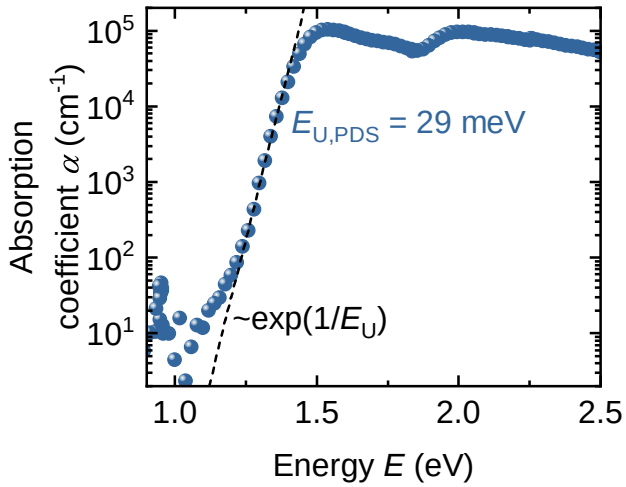

Figure 4.4: Absorption coefficient α as a function of energy E calculated from photothermal deflection spectroscopy (PDS) measurements. At the absorption edge, the non-abrupt decrease can indicate the presence of shallow defects. In the picture of exponential band tails, the inverse slope of the band tail describes the Urbach energy $E_{\mathrm{U,PDS}}$, which is found to be 29 meV in the case of this measurement.

bination mechanisms that is very frequently used in publications to explain superior performance of a newly developed solar cell system. However, they are mostly based on very simple models as explained above and therefore are prone to misinterpretation. So, in this thesis, I aim to not only properly characterize the recombination mechanisms in the material system, but also deepen the understanding of these methods to aid future researchers in correctly analyzing their data.

5

Analyzing the Light-Intensity Dependent Short-Circuit Current

When trying to assess the impact of bimolecular recombination on newly developed organic solar cells, light-intensity-dependent measurements of the short-circuit current are the most frequently used method.[20–45] The corresponding data analysis is based on a zero-dimensional approximation as introduced in the previous chapter. While it has been discussed in literature that the approach can underestimate the impact of bimolecular recombination,[75,94,205,206] the correct interpretation of light-intensitydependent short-circuit current density measurements requires a thorough analysis of loss mechanisms beyond bimolecular recombination. This chapter presents such a theoretical study on the limitations of the 0D model in order to understand the light-intensity dependence of the short-circuit current density and thereby charge-carrier recombination and extraction in organic bulk heterojunction solar cells. I first extend the model with the principle of space charge and its effect on the photocurrent in the presence of different recombination mechanisms in Chapter 5.1. Next, in Chapter 5.2, numerical drift-diffusion simulations enable the analysis of the light-intensity dependence of the short-circuit current density for a variety of dominating recombination mechanisms to identify the limitations of the 0D approximation. Then, the impact of space charge in thick devices is examined in more detail in Chapter 5.3. Finally, I try to apply the new findings from this theoretical study to the experimental data on PBDB-TF-T1:BTP-4F-12-based solar cells in Chapter 5.4 and derive recommendations on how to measure the short-circuit current density as a function of light intensity in organic solar cells. This chapter is based on the publication *Understanding the Light-Intensity Dependence of the Short-Circuit Current of Organic Solar Cells* by Paula Hartnagel and Thomas Kirchartz published in Advanced Theory and Simulation by Wiley Online Library.[202]

5.1. Analytical Description of Space-Charge Effects

Apart from neglecting the spatial dependence of the generation and the recombination rate, the traditional evaluation of the light-intensity dependence of the short-circuit current density also only considers recombination via deep traps and direct recombination. However, recombination via shallow defect states as introduced in Chapter 2.3.2 can be a substantial loss mechanism in organic solar cells.[48,79] Therefore, it is essential to understand the impact of tail states on such a widely used characterization technique. These defect states in the energy gap can be a source for space charge.[200,207,208] When capturing an electron, an acceptor-like defect is negatively charged. This density n_T of trapped electrons is then also accounted in the total charge density $\rho = q(p - n - n_\mathrm{T})$. Vice versa, a donor-like defect is a spatially localized positive charge when it is occupied by a hole. Consequently, the trapped hole density p_T changes the total charge density $\rho = q(p - n + p_\mathrm{T})$. According to Poisson's equation, which connects the charge density, electric field and electrostatic potential in Equation (2.25), when there is a large amount of one type of charge carrier trapped in the tail states, this spatial increase in charge density causes a change in electric field. Therefore, the presence of space charge is correlated with a high change of the electric field in the space-charge region. To identify the effect of space charge in simulations, one can set an infinitely high relative permittivity forcing a constant electric field as explained in Chapter 2.2. In a sufficiently thin active layer, the width of the space-charge region is equal to the layer thickness and no effect can be observed. However, when the layer thickness is exceeding the width of the space-charge region, a nonconstant electric field occurs. Within the space-charge region, the accumulated charge carriers, for example holes, have the drift length $L_\mathrm{drift} = \mu_\mathrm{p}\tau_\mathrm{p}F$, where μ_p is the hole mobility and τ_p the hole lifetime. The electric field $F = \Delta\varphi/w_\mathrm{SCR}$ can be approximated by the drop $\Delta\varphi$ of electrostatic potential over the space-charge region and the width w_SCR of the space-charge region. When assuming $L_\mathrm{drift} = w_\mathrm{SCR}$,[209,210] the photocurrent in the space-charge region is given by[209]

$$J_\mathrm{ph} = qG_\mathrm{av}w_\mathrm{SCR} = qG_\mathrm{av}(\mu_\mathrm{p}\tau_\mathrm{p})^{1/2}\Delta\varphi^{1/2}, \tag{5.1}$$

where G_av is the generation rate G that is averaged over the entire active layer. In the space-charge region, where there is a strong accumulation of charges, the current

density flowing is described by the space-charge limited current density[211]

$$J_{\mathrm{SCL}} = \frac{9}{8}\varepsilon_0\varepsilon_{\mathrm{r}}\mu_{\mathrm{p}}\frac{\Delta\varphi^2}{w_{\mathrm{SCR}}^3} \tag{5.2}$$

and was first derived for a unipolar device by Mott and Gurney, but was later applied to diodes as well.[209,210] When $J_{\mathrm{ph}} = J_{\mathrm{SCL}}$, the width of the space-charge region can be written as[210]

$$w_{\mathrm{SCR}} = \frac{\varepsilon_0\varepsilon_{\mathrm{r}}\mu_{\mathrm{p}}}{8qG_{\mathrm{av}}}^{1/4}\Delta\varphi^{1/2}. \tag{5.3}$$

Inserting this expression into Equation (5.1), the maximum photocurrent in a space-charge limited device is given by[209]

$$J_{\mathrm{ph}} = q\left(\frac{\varepsilon_0\varepsilon_{\mathrm{r}}\mu_{\mathrm{p}}}{8q}\right)^{1/4}G_{\mathrm{av}}^{3/4}\Delta\varphi^{1/2}. \tag{5.4}$$

It is notable that in this case the photocurrent scales with $G_{\mathrm{av}}^{3/4}$. This dependence has also been found by Wilken et al. who additionally considered the spatial dependence of the electron and hole current.[212] The correlation has already been used in previous studies to identify space-charge limited photocurrent in organic solar cells with asymmetric carrier mobilities.[23,210] However, Equation (5.2) is only valid in a defect free device with sharp band edges.[213] For tail states in a unipolar device, the Mark-Helfrich equation describes the space-charge limited current density

$$J_{\mathrm{SCL,MH}} = q^{1-l}\mu_{\mathrm{p}}N_{\mathrm{V}}\left(\frac{\varepsilon_0\varepsilon_{\mathrm{r}}l}{N_{\mathrm{t}}(l+1)}\right)^{l}\left(\frac{2l+1}{l+1}\right)^{l+1}\frac{\Delta\varphi^{l+1}}{w_{\mathrm{SCR}}^{2l+1}} \tag{5.5}$$

with the density of states N_{V} in the valence band, the trap density N_{t} and $l = E_{\mathrm{U}}/k_{\mathrm{B}}T$, where $k_{\mathrm{B}}T$ is the thermal energy and E_{U} the Urbach energy.[214] Since Equation (5.5) neglects diffusion currents,[213,215] it is rather a qualitative description than a precise analytical expression for the space-charge limited current. To the best of my knowledge, the Mark-Helfrich equation has not yet been applied to a bipolar device (i.e., a solar cell), though. Therefore, in order to study the light-intensity dependence of the photocurrent in a solar cell, the derivation for the defect-free case can be adapted by using Equation (5.5) for a diode with tail states. Thereby, the photocurrent following

the Mark-Helfrich equation yields

$$J_{\mathrm{ph,MH}} \propto G_{\mathrm{av}}^{1-1/(2l+2)} \tag{5.6}$$

with the slope

$$\gamma_{\mathrm{MH}} = \frac{\mathrm{d}\ln(J_{\mathrm{ph,MH}})}{\mathrm{d}\ln(G_{\mathrm{av}})} = 1 - \frac{1}{2(E_{\mathrm{U}}/k_{\mathrm{B}}T + 1)} \tag{5.7}$$

indicating a sublinear increase of the photocurrent with illumination depending on the Urbach energy E_{U}. When E_{U} approaches the thermal energy, Equation (5.7) yields the same light-intensity dependence of $\gamma_{\mathrm{MH}} = 3/4$ as the defect-free case in Equation (5.4). According to Equation (5.7), wider Urbach tails should feature a light-intensity dependence of the photocurrent closer to linearity than tails with small values of E_{U}; a result which appears counter intuitive at first. Both this relation and the more commonly used approach to calculating the space-charge limited photocurrent without trap states demonstrate that a sublinear correlation of the short-circuit current density J_{sc} and the irradiance E_{e} can be expected in organic solar cells with and without defect states. These space-charge effects that require a spatially resolved analysis of the processes inside a solar cell are also not considered in the 0D model from Equation (4.5).

So, in this analytical background section, I have extended the basis of the traditional model with a derivation for space-charge effects caused by band tails. Along with the J_{sc}-E_{e} relation shown in Equation (4.5) in the previous chapter, these expressions rely on a spatially constant generation, recombination rate and charge-carrier densities throughout the solar cell. To study these assumptions and their limitations, I performed numerical drift-diffusion simulations of organic solar cells using the advanced semiconductor analysis (ASA) software[152] and the assumptions introduced in Chapter 3.4. The simulation parameters specific to this chapter are listed in Table A.1. Figure 5.1 shows the current-voltage characteristics at 1 sun of the simulated solar cells that are further analyzed in this chapter.

To first identify the impact of each recombination mechanism on the linearity of the short-circuit current density with irradiance, I modeled a thin solar cell with an absorber thickness $d = 100\,\mathrm{nm}$ and constant generation rate within the active layer. In this case, space-charge effects do not play an important role since the system is symmetric and the width of the space-charge region exceeds the active layer thickness.

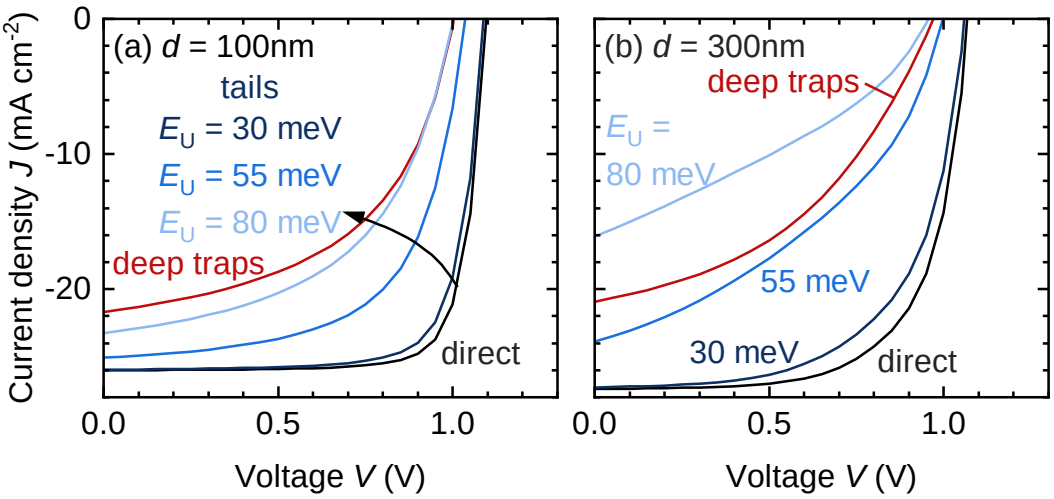

Figure 5.1: (a) Current-density voltage characteristics of the solar cells modeled with an active layer thickness $d = 100\,\text{nm}$ and constant generation throughout the solar cell under 1 sun illumination. Each simulation contains only one recombination mechanism, namely direct recombination, tail state recombination with three different Urbach energies E_U or recombination via deep traps in the middle of the band gap. The recombination parameters were chosen to create a decreasing power conversion efficiency from direct recombination to trap-assisted recombination. (b) Characteristics for a higher absorber layer thickness $d = 300\,\text{nm}$ with spatial dependence of the generation rate.

I implemented five types of recombination mechanisms including direct recombination, recombination via exponential band tails with Urbach energies E_U of 30 meV, 55 meV, and 80 meV and recombination via deep defect states in the middle of the band gap. I chose the simulation parameters in a way that the power conversion efficiency under 1 sun illumination decreases from direct to deep-trap recombination (see Figure 5.1a). Thereby, I associate the efficiency under the influence of each recombination mechanism with the position of its trap states in the energy gap. In a next step, I modeled a solar cell with an active layer thickness $d = 300\,\text{nm}$ incorporating optical data according to Chapter 3.4 and simulated these under air mass (AM)1.5G spectrum. These thicker devices with more spatial asymmetry allow the investigation of the role of space charges on the light-intensity dependence of the short-circuit current density J_sc with different recombination mechanisms. Figure 5.1b displays the corresponding current-voltage characteristics under 1 sun. Once again, the solar cell with dominating direct recombination features the highest power-conversion efficiency.

5.2. Nonlinearity in Thin Devices

In the following, I study an organic solar cell with constant generation throughout a thin active layer and discuss the different limitations of the 0D approximation that occur for each recombination mechanism. For this purpose, I performed simulations of the 100 nm-thick solar cell in Figure 5.1a at different irradiance levels. Figure 5.2a shows the resulting short-circuit current density J_{sc} as a function of irradiance E_e for all recombination mechanisms. As the short-circuit current density J_{sc} does not differ strongly between the cells on a logarithmic scale, the curves nearly coincide and appear linear on this scale. Only looking at the derivative $\gamma = \mathrm{d}\ln(J_{sc})/\mathrm{d}\ln(E_e)$, as shown in Figure 5.2b, reveals the different trends with irradiance between the recombination mechanisms, although all values for γ remain close to 1. In case of recombination via tail states, the slope differs from 1 at high light intensities. With increasing Urbach energy E_U, the degree of nonlinearity increases and the onset of slopes below 1 shifts towards lower light intensities. Thereby, the nonlinearity appears at lower light intensities in comparison to direct recombination for the Urbach energies of 55 and 80 meV. When treating tail state recombination as monomolecular, first-order recombination, this behavior contradicts the 0D model which supposes a linear correlation between the recombination and generation rate as explained in Chapter 4.2. According to my simulations, a highly linear J_{sc}-E_e relation rather indicates the absence of severe band tails. In contrast, J_{sc} mostly scales linearly with irradiance up to one sun, when all recombination occurs via trap states in the middle of the bandgap as predicted by the rationale in Equation (4.5). A sublinear trend of the short-circuit current density with irradiance at low light intensities therefore suggests that recombination via deep traps is not the dominant recombination mechanism in a device. Yet, at light intensities above 1 sun, recombination via deep traps also causes a slope below unity in the $\log(J_{sc}) - \log(E_e)$ plot. Hence, any kind of trap-assisted recombination can result in a sublinear trend, especially recombination via tail states, making it impossible to uniquely identify bimolecular recombination from J_{sc}-E_e measurements. This observation is further supported by the fact that J_{sc} of a solar cell with direct, bimolecular recombination does also not follow the trend predicted by Equation (4.5) but scales linearly with irradiance until high values, where the slope decreases.

It has been previously observed that substantial amounts of bimolecular recombination can still yield a linear J_{sc}-E_e correlation.[75, 205] Figure 5.3 visualizes the explanation

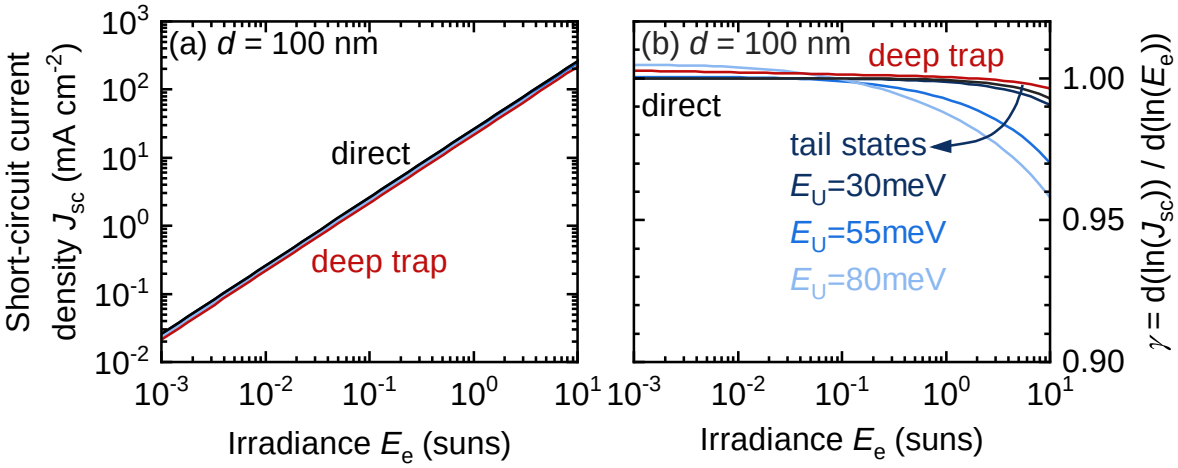

Figure 5.2: (a) Irradiance dependent short-circuit current density J_{sc} of a solar cell with an active layer thickness $d = 100\,\text{nm}$. The recombination mechanisms are either exclusively direct recombination, only trap-assisted recombination via trap states in the middle of the bandgap, or recombination via tail states. (b) Slope $\gamma = \mathrm{d}\ln(J_{sc})/\mathrm{d}\ln(E_e)$ as a function of irradiance E_e for every recombination mechanism. In each case, J_{sc} deviates from a linear correlation with E_e at high light intensities indicated by a slope below 1 with the strongest effect by exponential tail states with an Urbach energy E_U =80 meV.

for this linear behavior that was first presented by Würfel et al.[75] Figure 5.3a shows the electron densities n and the hole density p as a function of the position x in the active layer for different light intensities. In the center of the absorber layer, both charge-carrier densities scale with irradiance E_e. At the contacts, however, only the minority-charge carrier densities depend on E_e. As the recombination rate U_{dir} scales with the product of both charge-carrier concentrations according to Equation (2.35), the correlation with light intensity changes within the active layer in Figure 5.3b. Under low illumination, the recombination rate near the contact is orders of magnitude higher than in the center. With increasing light intensity, the recombination in the middle becomes increasingly significant. Figure 5.3c shows the recombination rate U_{dir} at the contact and in the middle of the active layer as a function of irradiance E_e. It has a slope of 2 in the center indicating a quadratic correlation since both electron density and hole density scale with irradiance. At the contacts, the slope is 1 as only the minority-charge carrier concentration increases. The total recombination-current density $J_{rec,dir}(E_e) = q\int_0^d U_{dir}(x, E_e)\,\mathrm{d}x$ follows the trend of the recombination at the contacts for low light intensities. As the recombination in the center of the active layer becomes more significant at high light intensities, $J_{rec,dir}$ increases more rapidly causing

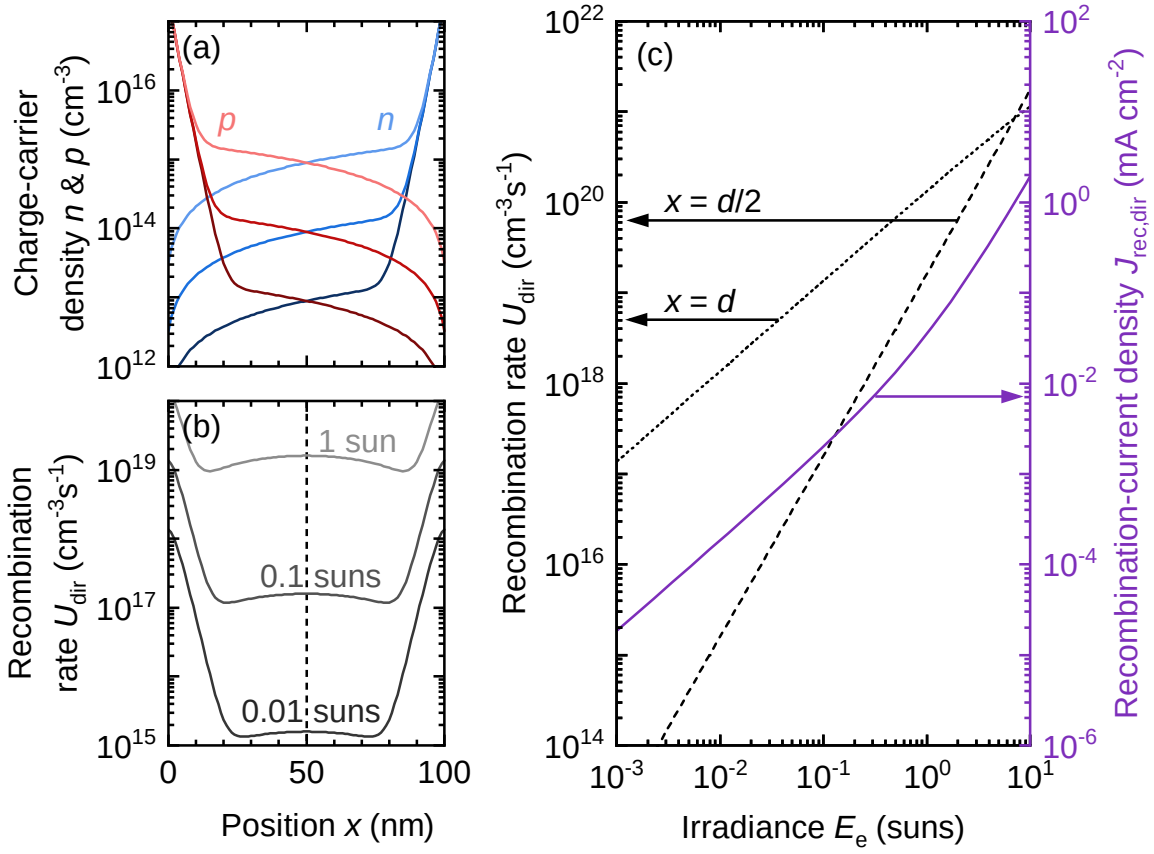

Figure 5.3: (a) Charge-carrier density $n(x)$ and $p(x)$ of the electrons and holes, respectively, as a function of the position x in the active layer at different light intensities in a solar cell with direct recombination only. (b) Recombination rate $U_{\mathrm{dir}}(x)$ for an irradiance E_{e} of 0.01 suns, 0.1 suns, and 1 sun. (c) Recombination rate U_{dir} in the center ($x = d/2$) and at the contact ($x = d$) of the active layer and the total recombination-current density $J_{\mathrm{rec,dir}}$ as a function of irradiance E_{e}. For low light intensities, the recombination at the edges dominates where only the minority-charge carrier densities scale with irradiance.

a nonlinear trend of the short-circuit current density J_{sc} with irradiance E_{e}. With this approach, Würfel et al. demonstrated that a slope of 1 does not imply the absence of direct recombination.[75] Yet, in their picture a slope below 1 is still a unique indicator for the process. With my simulations, I have shown that other recombination mechanisms can also exhibit sublinear behavior.

In the presence of Urbach tails in an organic solar cell, the nonlinearity of the short-circuit current density J_{sc} originates from a light-intensity dependence of the trapped charge-carrier densities. The density of states of exponential band tails has its occupation maximum around the quasi-Fermi level as illustrated in Figure 5.4a. Since

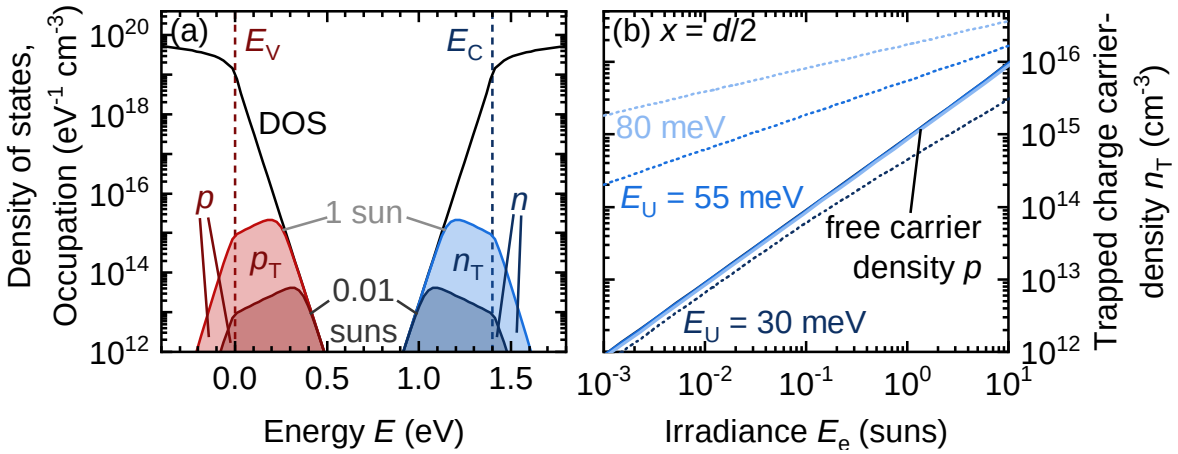

Figure 5.4: (a) Energetic distribution of the density of states in a solar cell with exponential band tails and the occupation of these states at irradiance levels of 1 sun and 0.01 suns. The maximum of the occupation by trapped charge carriers follows the quasi-Fermi level and therefore also changes with light intensity. (b) Trapped electron density n_T as a function of irradiance E_e for Urbach energies E_U of 30 meV, 55 meV, and 80 meV. The dotted lines represent the free hole density p. Since the trapped carrier concentrations also increase with irradiance, the recombination, which scales with the product of the trapped and free carrier concentrations, is nonlinear.

the quasi-Fermi energy approaches the band edge with increasing light intensity, also an increasing number of trap states is occupied, as indicated by the filled area in Figure 5.4a. The increase of the trapped charge-carrier density n_T with irradiance is shown for a wider range of light intensities in the center of the active layer in Figure 5.4b for Urbach energies E_U of 30 meV, 55 meV, and 80 meV. As both the free hole density and the trapped electron density increase with irradiance, the recombination rate scales superlinearly with E_e causing in turn a sublinear J_{sc}-E_e relation. In addition, I note that in Urbach tails with high values of E_U, n_T increases less rapidly than for a low Urbach energy E_U. Consequently, a device with high E_U is supposed to feature a J_{sc}-E_e relation closer to unity.

To identify the reason for this discrepancy to Figure 5.2, I performed simulations on organic solar cells with different tail slope but similar efficiencies. Figure 5.5a shows the resulting JV characteristics. In Figure 5.5b, one can see that indeed for solar cells with similar efficiency but different Urbach energies, the one with the lowest Urbach energy E_U shows the strongest degree of sublinearity in the slope γ. However, since I chose to have the highest power-conversion efficiency under 1-sun illumination at $E_U = 30$ meV and the lowest at $E_U = 80$ meV for the simulations, the correlation with E_U is opposite

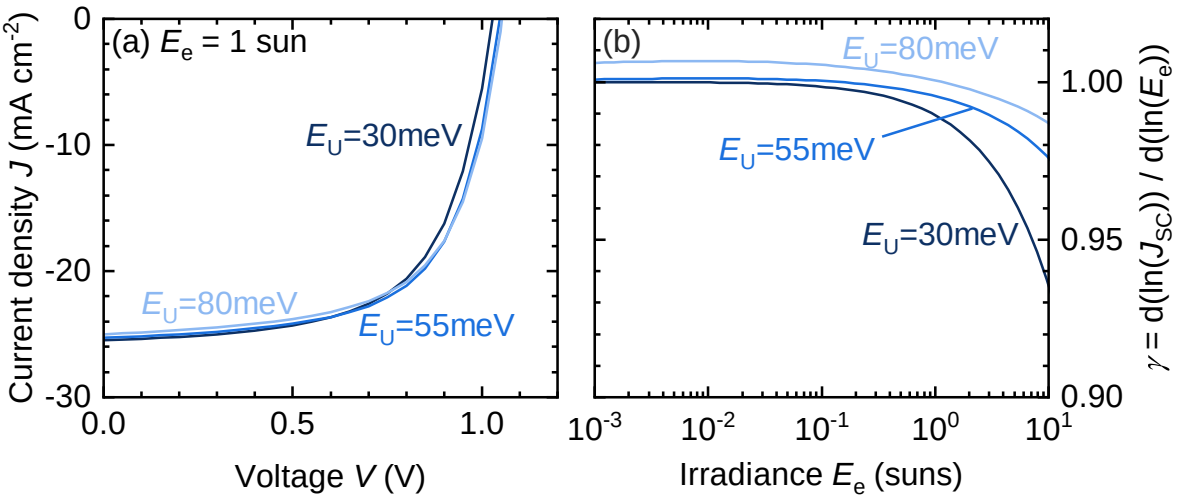

Figure 5.5: (a) Current-density voltage characteristics of solar cells with different Urbach energies E_U under 1 sun with an active layer thickness $d = 100\,\text{nm}$ and constant generation throughout the solar cell. The density of tails states ($2 \times 10^{19}, 10^{19}$ & $5 \times 10^{18}\text{cm}^{-3}\text{eV}^{-1}$) and the capture rates ($2 \times 10^{-10}, 2 \times 10^{-11}$ & $\times 10^{-11}\text{cm}^3\text{s}^{-1}$ for β_2) vary to ensure similar power-conversion efficiency. (b) Slope $\gamma = \mathrm{d}\ln(J_{sc})/\mathrm{d}\ln(E_e)$ of solar cells with similar efficiency but different values of E_U. The device with the lowest Urbach energy E_U features the strongest non-linearity since its trapped carrier concentrations scale the strongest with irradiance.

in Figure 5.2b in comparison to Figure 5.5b, since the total recombination rate is higher.

Another phenomenon that can be observed in Figure 5.2b and 5.5b alike is a slope γ above one for a high Urbach energy and deep defects. To understand this observation, I focus on the deep defects for simplicity and analyze the resulting light-intensity dependence of the short-circuit current density. In the zero-dimensional device model, one would expect a strictly linear relationship between the irradiance and short-circuit current density as the recombination is linear, since only one charge-carrier density scales with irradiance. However, Figure 5.2b reveals that at low light intensities, the slope γ can even increase above 1 and for high illumination, it will also drop below 1. Once again, the discrepancy originates in the position dependence of the charge-carrier densities and the recombination rate. Figure 5.6a shows the free electron density n and the free hole density p for different positions x in the active layer and irradiances from 10^{-3} suns to 100 suns at short circuit. The black lines represent the corresponding equilibrium carrier concentrations. Similar to the case of direct recombination only in Figure 5.3, the free charge-carrier densities increase linearly in the center of the active layer while being dominated by the equilibrium-charge carrier density close to the con-

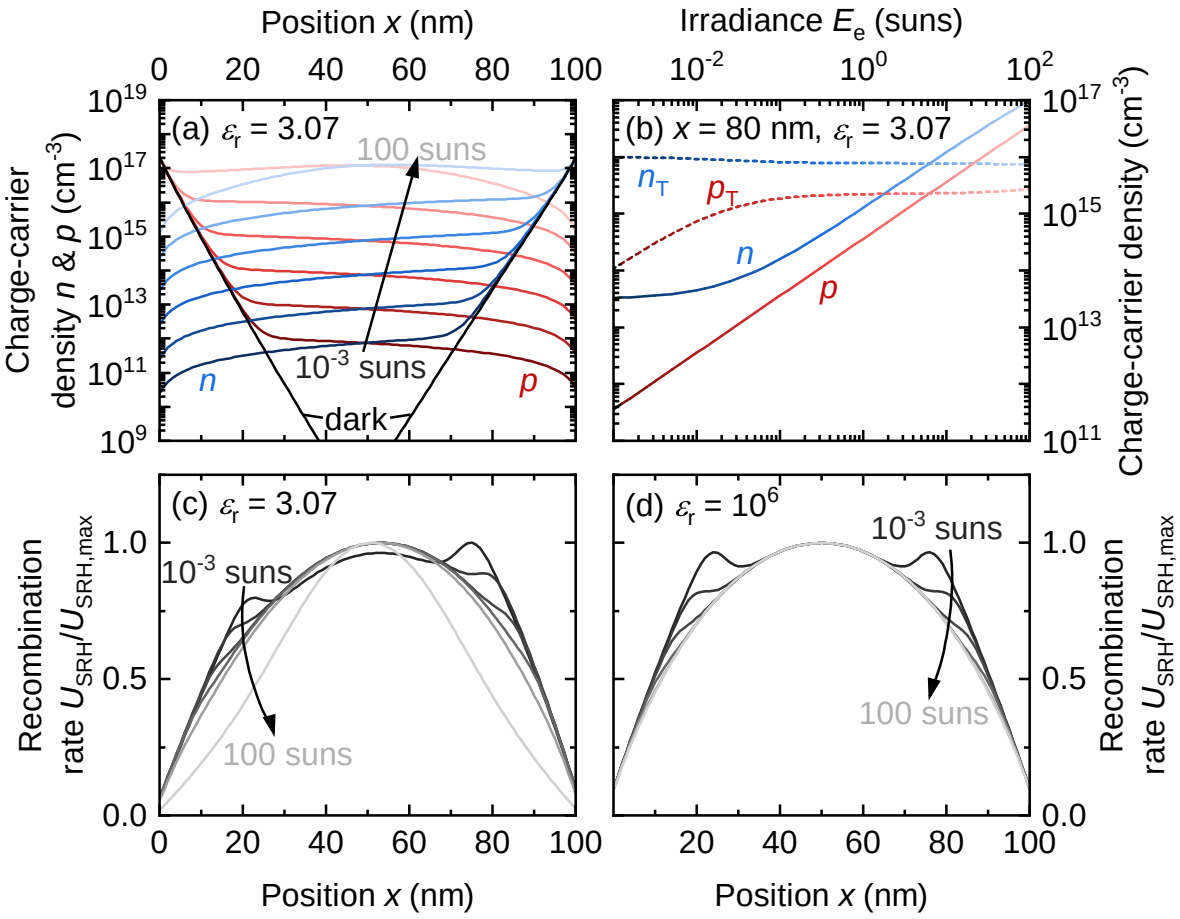

Figure 5.6: (a) Electron density $n(x)$ and hole density $p(x)$ for irradiances from 10^{-3} suns to 100 suns and in the dark in a solar cell with recombination via deep traps for a realistic relative permittivity ε_r. At low light intensities, the majority-charge carrier density (electrons at cathode, holes at anode) is dominated by the injected carrier density (black lines). (b) Free and trapped charge-carrier densities as a function of irradiance E_e at the position $x = 80$ nm. Where the electron density n saturates, the recombination rate $U_{SRH} = n_T p + n p_T$ becomes sublinear with irradiance. (c,d) Normalized recombination rate $U_{SRH}/U_{SRH,max}$ for increasing light intensities with (c) ε_r =3.07 and (d) high ε_r. At high light intensities, the width of the recombination rate decreases in a realistic cell causing nonlinearity of the short-circuit current density J_{sc} due to space-charge effects.

tacts. For decreasing irradiance, this region, where there is little influence from the change in irradiance, reaches far into the bulk, up to 20 nm on each side. Figure 5.6b shows the free charge carrier densities n and p of electrons and holes at this position $x = 80$ nm at the cathode. While both exhibit linear behavior at high light intensities, n saturates at lower light intensities to a value set by the equilibrium-electron concentration at this point. The free charge-carrier densities determine the

occupancy θ_{SRH} of the trap states. For a trap located in the middle of the energy gap with equal capture coefficients for electrons and holes, the occupancy can be expressed by

$$\theta_{\mathrm{SRH,n}} = \frac{n(E_{\mathrm{e}})}{n(E_{\mathrm{e}}) + p(E_{\mathrm{e}})} \tag{5.8}$$

for electrons and

$$\theta_{\mathrm{SRH,p}} = \frac{p(E_{\mathrm{e}})}{n(E_{\mathrm{e}}) + p(E_{\mathrm{e}})} \tag{5.9}$$

for holes. At $x = 80\,\mathrm{nm}$, the electron density consists of a photogenerated electron density n_{ph} and an equilibrium electron density n_{i}, while the equilibrium density can be neglected for holes leaving the photogenerated hole density p_{ph}. Hence, the occupation probability for the defect states with holes can be rewritten as

$$\theta_{\mathrm{SRH,p}} = \frac{p_{\mathrm{ph}}(E_{\mathrm{e}})}{p_{\mathrm{ph}}(E_{\mathrm{e}}) + n_{\mathrm{ph}}(E_{\mathrm{e}}) + n_{\mathrm{i}}}. \tag{5.10}$$

When $p_{\mathrm{ph}} << n_{\mathrm{i}}$ and $n_{\mathrm{ph}} << n_{\mathrm{i}}$, the occupancy will approach zero. Indeed, at the cathode, where there is only injected electrons, all trap states are occupied by electrons as well. Alternatively, for $n_{\mathrm{ph}} >> n_{\mathrm{i}}$, the photogenerated charge-carrier densities determine the occupation of the trap states. In the center, where $n_{\mathrm{ph}} = p_{\mathrm{ph}}$, the occupancy is 1/2 and the densities of trapped electrons and holes are equal and constant with light intensity. According to Equation 5.10, the density of trapped holes can be at the most linearly with irradiance. Since the recombination rate scales with the product of trapped and free charge carrier density, the dependence of p_{T} on the irradiance that can be observed in Figure 5.6b cannot compensate the saturation of n to the injected carrier density and the product np_{T} will scale sublinearly with irradiance. In addition, the density of trapped electrons n_{T} decreases in Figure 5.6b according to $n_{\mathrm{T}} = N_{\mathrm{dt}} - p_{\mathrm{T}}$. Therefore, also the product $n_{\mathrm{T}}p$ increases sublinearly with E_{e}. Consequently, the total recombination rate near the electrodes also has a logarithmic slope below 1. To examine the influence of the recombination rate near the contacts on the total recombination rate, Figure 5.6c shows the recombination rate U normalized by the maximum recombination rate U_{max} as a function of position x in the active layer. As to be expected for recombination via midgap traps, the maximum is located in the center where the density of trapped carriers is constant and the recombination

rate scales linearly with irradiance. However, the distribution of the recombination rate is relatively flat causing the values closer to the contacts to still be relevant for the total integrated recombination-current density. Especially at low light intensities, the influence of the injected charge carriers causes the formation of local side maxima, even intensifying the influence of the sublinear recombination rate at these positions. Additionally, the curves exhibit significant asymmetry around the center of the active layer. This observation can be explained when comparing the shape of the recombination rate in Figure 5.6c to the case of a very high dielectric constant which prevents space-charge effects. Indeed, the recombination rate in Figure 5.6d appears symmetric around the center of the active layer at all light intensities. The space-charge effects at low light intensities are evoked by the fact that the charge inside the traps is less evenly distributed in the active layer. As explained previously, the injected carriers cause the trap states to be mostly filled by their respective carrier type. For the donor-like defects implemented in these simulations, the occupancy close to 1 for holes near the anode results in a large positive charge density in this volume, enhancing the extraction and reducing the recombination rate. In consequence, the electric field near the cathode is reduced, increasing the recombination rate. Therefore, the influence of injected charge carriers at low light intensities causes both an asymmetry within the active layer due to space-charge effects and a sublinear recombination-current density which explains the slope above 1 in the J_{sc}-E_{e} relation. Shockley-Read-Hall recombination for more shallow defects features a similar influence of the injected carrier density. However, for steep tail states, the intrinsic light intensity dependence of the trapped carrier densities will compensate this effect. Therefore, only at high Urbach energies, short-circuit current density will increase superlinearly with irradiance at low illumination. At high light intensities, in contrast, the slope for deep defects drops even below 1. Here, also the comparison of Figure 5.6c and 5.6d reveals that space charge effects cause a more narrow distribution of the recombination rate for a realistic relative permittivity. In Figure 5.6c, the normalized recombination rate $U_{\mathrm{SRH}}/U_{\mathrm{SRH,max}}$ is maximum in the center but its width decreases with irradiance. In contrast, in Figure 5.6d, the width of the recombination-rate distribution remains the same. Therefore, deep defects cause space-charge effects both for high and low light intensities influencing short-circuit current density even in thin devices.

Thereby, I have demonstrated that nonlinear recombination losses can occur for all recombination mechanisms caused by either a changing light-intensity dependence

of charge-carrier densities at different positions in the active layer or by increasing numbers of carriers trapped in tail states. These effects violate the 0D approximation for thin active layers and constant generation. Even when the recombination mechanism itself is mostly linear, weak space-charge effects may occur in thin devices. However, organic solar cell research aims at achieving higher active layer thicknesses for commercialization.[44,216–218] In these layers, the generation rate can no longer be approximated as constant throughout the absorber and space-charge effects are increasingly significant. Therefore, I performed simulations implementing spatially dependent generation in solar cells with an absorber thickness $d = 300\,\mathrm{nm}$.

5.3. Space-Charge Effects in Thick Devices

In devices with a high absorber thickness, space-charge effects become increasingly significant as the layer thickness exceeds the width of the space-charge region. To illustrate the impact of different energetic distributions of defect states on the solar cell, Figure 5.7 shows the band diagrams under 1 sun illumination and the corresponding generation and recombination rates as a function of the position x. For direct recombination only, the field within the active layer in Figure 5.7a is mostly constant with only little band bending at the contacts. In the case of tail states, with increasing Urbach energies from Figure 5.7b-d, a low-field zone appears in the region, where generation and recombination are high in Figure 5.7g-i. In analogy to the phenomenon reported by Wu et al.,[207] holes are extracted at the illuminated contact whereas electrons diffuse to the opposite contact. At the cathode however, holes are neither created in large amounts due to the position-dependent generation rate nor can they diffuse from the anode to the cathode because of the opposing electric field. Therefore, a negative space charge builds up opposite to the illuminated contact causing a high-field and a low-field region.[195,200,207] The band diagram in Figure 5.7e for a solar cell with recombination via deep traps also shows band bending similar to the case of $E_\mathrm{U} = 30\,\mathrm{meV}$ and thereby indicates that space-charge formation also matters for deep defects at light intensities around 1 sun. The normalized nonuniform generation rate causing the asymmetry and the subsequent built-up of space charge is shown in 5.7g-i along with the recombination rate U normalized by its average U_av for 0.01 suns, 0.1 suns and 1 sun. One can see that at increasing light intensities more recombination takes place near the illuminated surface where generation is high which is also the potential low-field region. Therefore,

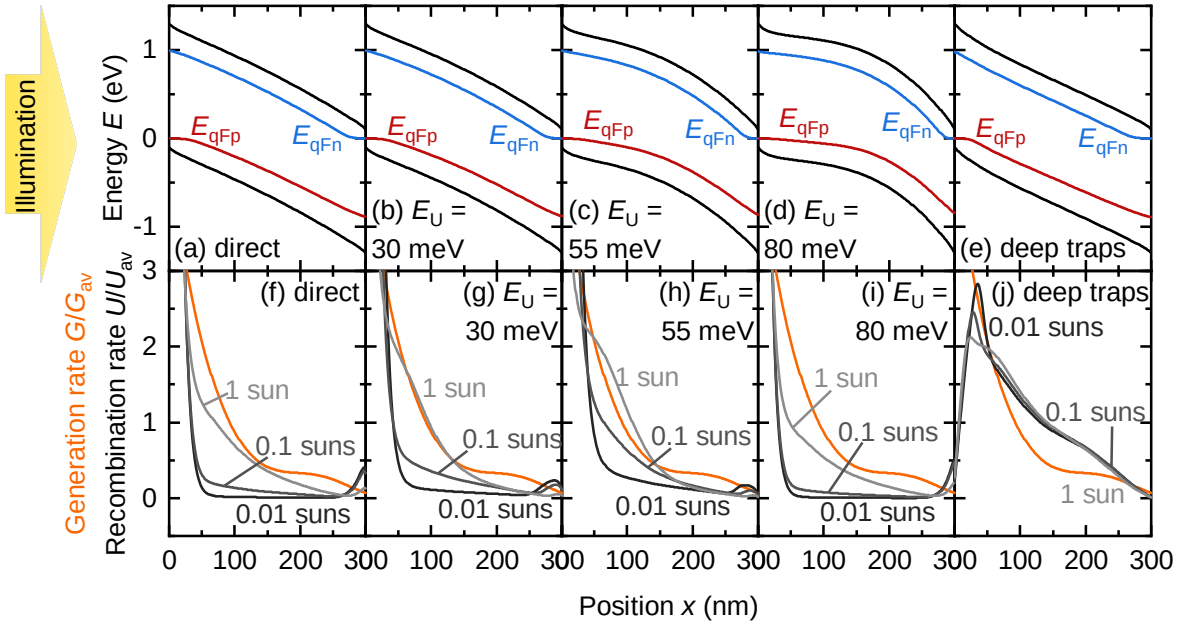

Figure 5.7: (a-e) Band diagrams of solar cells with an active layer thickness $d = 300\,\text{nm}$ that are illuminated from the left with 1 sun illumination. (f-j) Normalized generation rate G/G_{av} and recombination rate U/U_{av} as a function of position x in the active layer. Each simulation contains only one recombination mechanism, namely: (a,f) direct recombination, (a-d,g-i) recombination via tail states with increasing Urbach energy E_{U}, and (e,j) recombination via deep traps. For more severe band tails, a low-field region forms where generation and recombination rates peak.

the diffusion-dominated low-field regime limits the short-circuit current density as most charge carriers recombine here (see Figure 5.7g-i).

Whereas the light-intensity dependence of space charge caused by asymmetric mobilities has already been analyzed by Wilken et al.,[212] the influence on the J_{sc}-E_{e} relation of the space-charge region due to defect states as observed in Figure 5.7 still has to be investigated. For this purpose, Figure 5.8 shows the slope $\gamma = \mathrm{d}\ln(J_{\text{sc}})/\mathrm{d}\ln(E_{\text{e}})$ as a function of irradiance E_{e}. For a realistic device in Figure 5.8a, there is substantially more nonlinearity occurring at lower light intensities than in Figure 5.8b for a device with high relative permittivity and therefore constant electric field. This observation indicates that space-charge effects are significant for each recombination mechanism investigated. A device with direct recombination also appears to be impacted by space-charge effects. For defect states in the form of exponential band tails, a strong nonlinearity of J_{sc} can be observed at low light intensities already. The strongest impact can be seen for high Urbach energies E_{U} as these exhibit the most

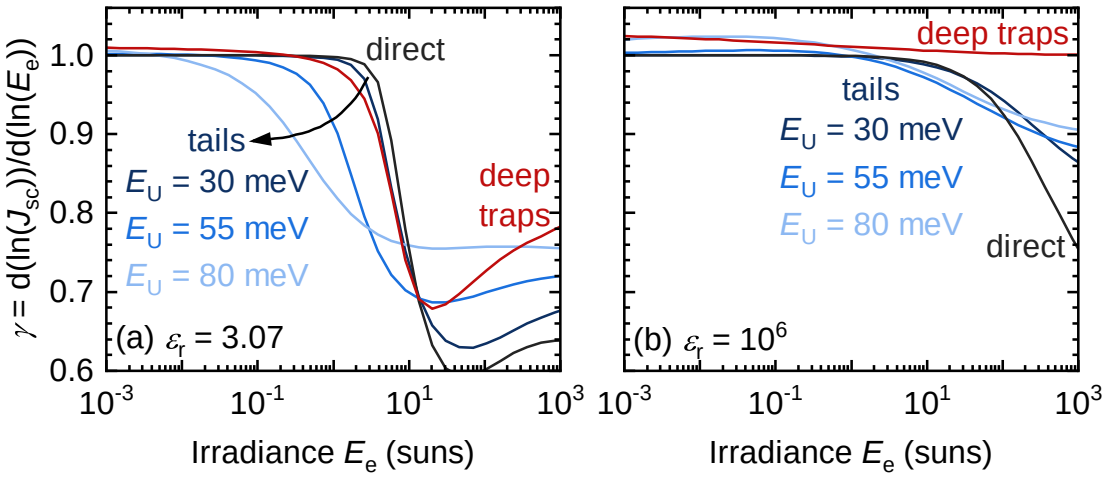

Figure 5.8: Slope $\gamma = \mathrm{d}\ln(J_{\mathrm{sc}})/\mathrm{d}\ln(E_{\mathrm{e}})$ of the irradiance-dependent short-circuit current density in a solar cell with an active layer thickness $d = 300\,\mathrm{nm}$ and spatially dependent generation. Recombination either takes place exclusively through direct, bimolecular recombination or via trap states which can be localized in the middle of the band gap or distributed in band tails. For a (a) realistic relative permittivity ε_{r} =3.07, nonlinear effects are more dominant than for a (b) high permittivity where the electric field is constant.

space charge. Thus, a highly linear J_{sc}-E_{e} relation indicates the absence of strong tail states as already observed for thin devices. However, the trend with E_{U} reverses under high illumination which is in line with Equation (5.7). The trend with E_{U} from the simulation coincides with the analytical solution for space-charge limited currents with tail states and contradicts the behavior that one might intuitively predict. When comparing Figure 5.8a and 5.8b, it occurs that next to direct and tail state recombination, a device with recombination via deep traps also exhibits strong space-charge effects. After showing a slope even above 1 for low values of E_{e}, γ then falls below direct recombination around 1 sun and saturates to a relatively high value.

When comparing the recombination mechanisms, most strikingly, direct recombination features the least sublinearity up to irradiances above 1 sun out of all recombination parameters chosen. This observation opposes the conventional approach of analyzing the relation between the short-circuit current density and the irradiance. For the correct interpretation, neither the 0D model nor the consideration of space charges with a $J_{\mathrm{sc}} \propto G^{3/4}$ relation is sufficient. Instead, the application of the Mark-Helfrich equation to a diode is required to explain the tail states' impact.

5.4. Applicability to Experimental Data

So far, I have delivered an in-depth analysis of the implications of the light-intensity dependence of the short-circuit density J_{sc}. To apply these insights to the material system, which is characterized in this work, I calculated the logarithmic slope γ for devices with an active layer thickness d ranging from 32 nm to 352 nm. The resulting values of γ are displayed in Figure 5.9 with the yellow points corresponding to a low active layer thickness and the purple ones representing the thickest devices. At high light intensities, the slope γ appears to be independent of the active layer thickness and can be found at values of $\gamma \approx 0.95$. While γ increases with decreasing irradiance E_e, a dip can be observed at the position of the filter change marked by the gray dashed line. For the medium filter setting, the pattern appears to repeat itself. Only for the very low irradiance, the slope γ scatters more drastically with thickness with the thin cells showing a high slope γ while the slope decreases with irradiance E_e for the majority of devices. None of these effects have been described in the theoretical analysis presented above but instead originate in systematic errors from the measurements. First, the use of neutral density filters is problematic in the scope of this measurement technique. As discussed by Lübke et al.,[196] neutral density filters as used in this work only provide a wavelength independent transmission spectrum in the visible range but can change drastically for lower wavelengths. Applying such a filter to an LED that also emits light in this wavelength range will lead to a red shifted spectrum at the same total power density. As the solar cell absorbs in the near-infrared region, the short-circuit current density J_{sc} will change according to its external quantum efficiency even if the number of incoming photons remains constant. Hence, the points in the logarithmic slope γ of the short-circuit current density J_{sc} with irradiance E_e before or after a filter change are calculated using a short-circuit current density J_{sc} from a different incoming spectrum. Therefore, they only contain limited information on recombination and need to be disregarded in an analysis. However, even the two values in between filter changes do not form a continuous curve. Here, it is relevant to consider the methodology with which the incoming irradiance E_e on the x-axis was estimated. The exact spectrum was only measured at certain LED driving currents. Assuming linearity of the LED's output power density and its driving current, the irradiance from the exact spectral measurements is scaled accordingly (for a detailed description, see Chapter A.5). However, for this purpose, the assumption of linearity does not suffice as

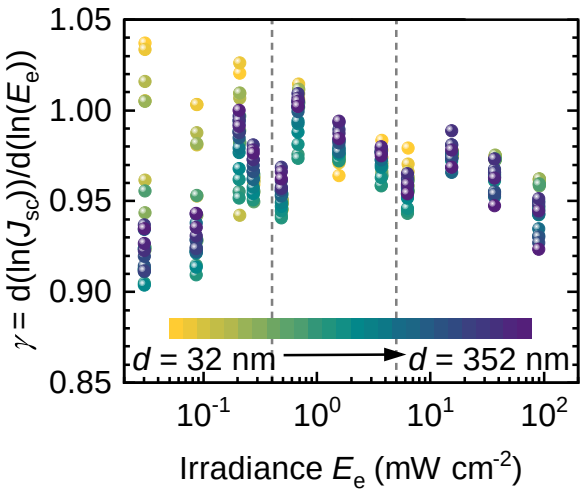

Figure 5.9: Logarithmic slope γ of the short-circuit current density J_{sc} with irradiance E_e for solar cells fabricated with an active layer thickness d ranging from 32 nm to 352 nm. The incoming light is supplied by an LED and varied by changing the LED driving current and applying neutral density filters, which change at the gray, dashed lines. While there is large scattering at the filter setting for the lowest light intensity, the irradiance dependence of γ resembles each other in the other two filter settings and does not feature any trend with thickness.

the output-power density of the LED also scales with the driving current with a non-constant logarithmic slope (see Figure A.14 in the Appendix). Therefore, the change in the slope γ is further altered by the nonlinearity of the LED. Only at very low light intensities, the trend is reversed and the slope γ decreases with decreasing irradiance E_e for most devices. Under such low levels of irradiance (down to 31 lux), stray light from ambient light sources becomes increasingly important. Once the LED light intensity drops significantly below the one of the stray light, the short-circuit current density J_{sc} saturates. Even at the irradiances measured in this work, a decrease in the slope due to ambient light is possible. The few cells that feature a high slope γ at these low light intensities could either be caused by a particularly good alignment of the measurement box with the LED table sealing off any ambient light or by the ambient light source being covered or turned off during these measurements. This hypothesis is supported by the fact that the exceptions always include all functioning cells on one substrate, which face the same measurement conditions.

Therefore, a variety of sources for errors in the measurements hinder the analysis of the recombination mechanism for light-intensity dependent J_{sc} measurements. To avoid these errors, knowledge of the incoming spectrum's power density is crucial. Either measurements of the irradiance at each point of the short-circuit current density J_{sc}

are required or a highly linear relationship between the driving current of the LED and its output-light power has to be tested beforehand. The usage of neutral density filters should be avoided except for monochromatic light sources. Alternatively, the light intensity can be varied by changing the distance between the light source and the device under test. All these suggestions to avoid mistaking systematic measurement errors for recombination features require more advanced measurements setups than currently often used in literature and highlight how care needs to be taken both while conducting and analyzing light-intensity dependent short-circuit current density measurements.

5.5. Conclusions

In this chapter, I presented a detailed discussion on the light-intensity depend measurements of the short-circuit current density J_{sc}, which is a method widely used to identify bimolecular recombination in organic solar cells.[21–23,25–34] The simplicity of the method is based on neglecting any spatial dependence of the generation and recombination rate and of space charge. Würfel et al.[75] have demonstrated that bimolecular recombination scales linearly with irradiance E_e as long as recombination at the contacts dominates. Picking up on these findings, I examined other recombination mechanisms. With simulations, I have shown that devices with trap-assisted recombination exhibit a sublinear J_{sc}-E_e relation that might be falsely identified as bimolecular recombination by this method. Recombination via tail states features a sublinear trend due to the light-intensity dependence of the trapped carrier concentrations. In the presence of trap states in the middle of the energy gap, the spatial resolution of the recombination rate U gains importance as the volume with significant recombination changes with irradiance E_e. The effect is evoked by space charges but remains small for thin devices. I have further discussed the increasing impact of charged trap states on the J_{sc}-E_e relation under nonuniform generation in thick devices which cannot be explained by the conventional model for space-charge limited photocurrent in diodes. Lastly, I have analyzed experimental data for the J_{sc}-E_e relation and have identified criteria for correct measurements. The use of neutral density filters should be avoided and the variation in irradiance should be implemented by varying the power density of the light source making sure that the exact spectra are known. Also, any ambient light source has to be switched off during measurements.

By implementing these criteria into the measurements, the simulations presented in

this chapter deliver a better understanding of the influence of different recombination mechanisms on the J_{sc}-E_e relation that allows analyzing experimental data accordingly. A sublinear trend measured in thin devices at low light intensities rules out recombination via deep traps as dominant recombination mechanisms. In contrast, a highly linear correlation might still include direct and deep trap recombination but not major losses via tail states independent of the absorber thickness. Instead, strong band tails are indicated by sublinear behavior at low light intensities in thick devices. Therefore, the findings in this chapter offer new understanding of the processes determining the J_{sc}-E_e relation and thereby deliver a new approach to interpreting the measurements considering several recombination mechanisms and active layer thicknesses.

6

Comparing Methods of Characterizing Energetic Disorder

The previous chapter has shown, how energetic disorder in the form of tail states can influence even the short-circuit current density of an organic solar cell. Under forward bias, the recombination via these defect states and their influence on space charge becomes even more relevant. In fact, for a long time during the development of organic photovoltaics, efficiencies were struggling to reach 10%, where shallow defects could limit the device performance.[46–48] Over the last several years, however, new polymers and especially new acceptor molecules have completely changed the situation. By now, organic solar cell efficiencies exceed 19% in single-junction devices[12,41,219–221] and 20% for tandem organic solar cells.[13] Thus, while structural and energetic disorder will certainly still be present in current state-of-the-art organic solar cells, either the degree or the impact of the disorder has to be substantially reduced. Hence, a closer look at energetic disorder and its impact on device performance for current generations of organic solar cells is needed. To achieve this goal, it is crucial to use sensible parameters to quantify disorder, to use reliable measurement methods and to be aware of potential limitations of the methods. However, most publications presenting a new material system, for which they characterize energetic disorder, only apply one of numerous measurements techniques. These different methods can differ substantially in their working principles. The most frequently used method is photothermal deflection spectroscopy (PDS) that I therefore analyzed in Chapter 4 on the material system that is under test in this work. The comparability of these results with other techniques is yet unknown, which hinders deeper understanding of the phenomenon of energetic disorder throughout different publications. Therefore, this chapter, which is based on the publication *Comparing Methods of Characterizing Energetic Disorder in Organic*

Solar Cells by Hartnagel et al.[146] published in Advanced Energy Materials by Wiley Online Library, aims at delivering a thorough analysis of different characterization techniques for energetic disorder. For this purpose, I first further motivate this work by performing an analysis of the literature on characterization of energetic disorder in Chapter 6.1. Then, I explain and test the applicability of admittance spectroscopy for this use in Chapter 6.2. Afterwards, I present experimental results in Chapter 6.3 of different techniques on the same material systems and analyze them with different frameworks found in literature. Lastly, I discuss discrepancies in the results between measurement techniques with the help of numerical simulation in Chapter 6.4 to identify their advantages and limitations. Thereby, I not only intend to characterize the energetic disorder of the material system that is characterized in this work but also deliver an extensive framework on the interpretation of measurements of the energetic disorder in organic solar cells.

6.1. Energetic Disorder in Literature

Energetic disorder as observed, for example, in absorption and emission measurements is explained by two significantly different physical concepts that are usually referred to as static and dynamic disorder. Static disorder originates from a broadened density of states that is caused by structural disorder of e.g. polymer chains.[222] Dynamic disorder is caused by a combination of two effects: The first is the presence of a non-zero reorganization energy, i.e. a displacement of the vibrational ground state of the electronically excited state relative to the electronic ground state, which was introduced in Chapter 3.1.1. The second factor is the thermal broadening of these states, i.e. the existence of vibrationally excited states with a non-zero occupation probability.[223] The corresponding reorganization energy after absorption or emission is frequently used to characterize disorder by extracting the width of a Gaussian fit to the data.[223–227] Alternatively, it is equally common to describe the experimentally observable disorder in absorption and emission spectra using an exponential Urbach-tail whose temperature dependence provides some information about the relative importance of static and dynamic disorder.[225,228] The debate is ongoing which effect is dominating, the energetic disorder of the actual density of states or the reorganization energy.[224,225,227,229] However, both effects are detrimental for device performance via their impact on charge transport and recombination.[47,71,230] Thus, the experimental

quantification of energetic disorder remains important independent of the exact origin of the disorder. There are several different methods to measure the disorder, the most prominent among them are optical methods where absorption or emission of a sample is recorded.[24,190,191,193,231–233] These are followed by electrical methods, where the voltage is varied to move the quasi-Fermi levels over the subband-gap density of states and thereby fill or empty the broadened density of states.[118,207,234,235] Given that observables such as the current or the capacitance depend on the carrier density inside a device under certain conditions, measurements such as charge extraction[118,207,234] or capacitance voltage[235] have been used to extract information on the band tails. Figure 6.1 shows how typical values of the reported Urbach energies depend on the type of device and the mode of measurement. The histogram shown in Figure 6.1a provides evidence that the development of nonfullerene acceptors (NFAs) has not only improved power-conversion efficiencies of organic solar cells but has also generally reduced the reported Urbach energies relative to the formerly predominant fullerene acceptors (FAs). A substantial number of reports of Urbach tails are now close to the thermal energy $k_{\mathrm{B}}T$, which is highly significant for device performance from a theoretical and practical perspective.[236] Figure 6.1b shows a histogram of Urbach energies resolved for the general class of measurement technique. Here, I discriminate between optical techniques such as photothermal deflection spectroscopy (PDS) or Fourier-transform photocurrent spectroscopy (FTPS) that probe photon absorption and essentially measure the joint density of states and electrical techniques that use changes in applied voltage to scan the energy-dependent density of states. Here, I note that optical techniques very frequently lead to fairly low Urbach energies around $k_{\mathrm{B}}T$ or slightly higher, while electrical techniques give values in a very broad range with a significant number of cases going up to $3k_{\mathrm{B}}T$. Thus, Figure 6.1c suggests that different methods may systematically lead to different Urbach energies, which would stipulate a closer look at the methods themselves. However, the assessment of Figure 6.1b is insofar incomplete as it provides only statistic evidence for a method specific difference, but does not provide data, where several techniques have been explored on the same samples.

Here, I compare four different types of measurements that were performed on two different types of organic solar cells. For the optical measurements, I analyzed PDS on the material films on glass and FTPS on full solar cells. These solar cells, I also characterized with electrical, voltage-dependent methods, where I chose admittance spectroscopy and extracted the Urbach energy from measurements in the dark and at

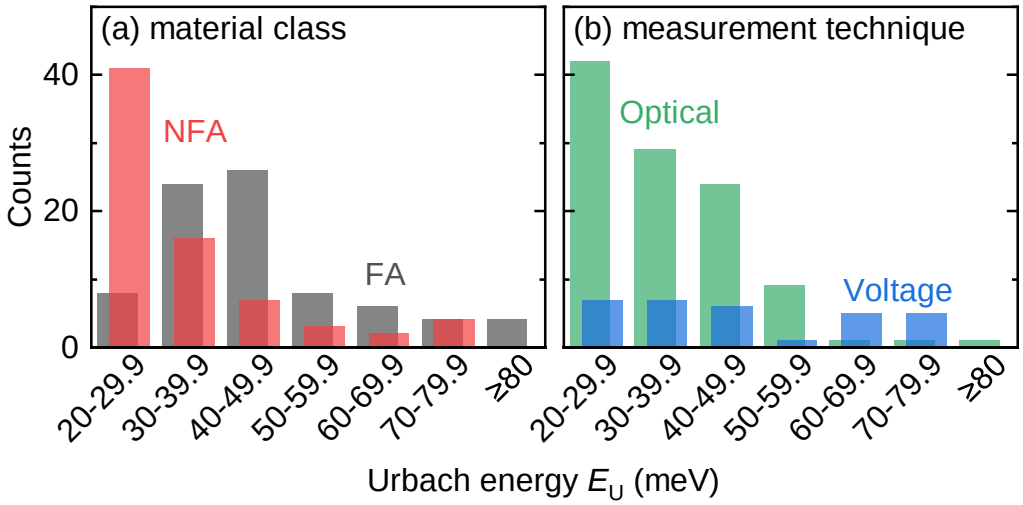

Figure 6.1: Urbach energies reported in literature differ between (a) fullerene[20, 78, 79, 181, 183, 185, 186, 189, 190, 207, 233–235, 237–252, 252–261] and nonfullerene acceptors[24, 40, 118, 178, 181, 186–193, 218, 231–233, 235, 243, 244, 262–274] and especially between (b) optical[20, 24, 40, 79, 181, 183, 185–189, 189–193, 218, 231–233, 237, 238, 244–253, 262–272] and voltage-dependent[118, 178, 207, 234, 235, 241, 242, 257–260, 274] measurement techniques highlighting inconsistencies in the characterization of energetic disorder in organic solar cells. Table A.2 in the Appendix lists all materials, methods and references from this figure.

open circuit. While I introduced the working principles of all measurement techniques in the Method Section in Chapter 3.2 and 3.3, the extraction of the Urbach energy from admittance spectroscopy requires several assumptions and therefore its applicability needs to be confirmed. Thus, I introduce the rationale behind the method in the following and test it using drift-diffusion simulations.

6.2. Extracting the Urbach Energy from Admittance Spectroscopy

As introduced in Chapter 2.3.2, in a simplified case, the static disorder in the form of shallow defect states can be modeled by an exponential with the inverse slope E_U, the Urbach energy,[92] as shown in Figure 6.2a. Previously, I have investigated the filling of these tail states with increasing quasi-Fermi level splitting caused by increasing illumination intensity in Figure 5.4 in Chapter 5. Similarly, the density of tail states is increasingly filled with increasing applied voltage in Figure 6.2a. The energy-dependent occupation of states, which is illustrated for different applied voltages V in the dark

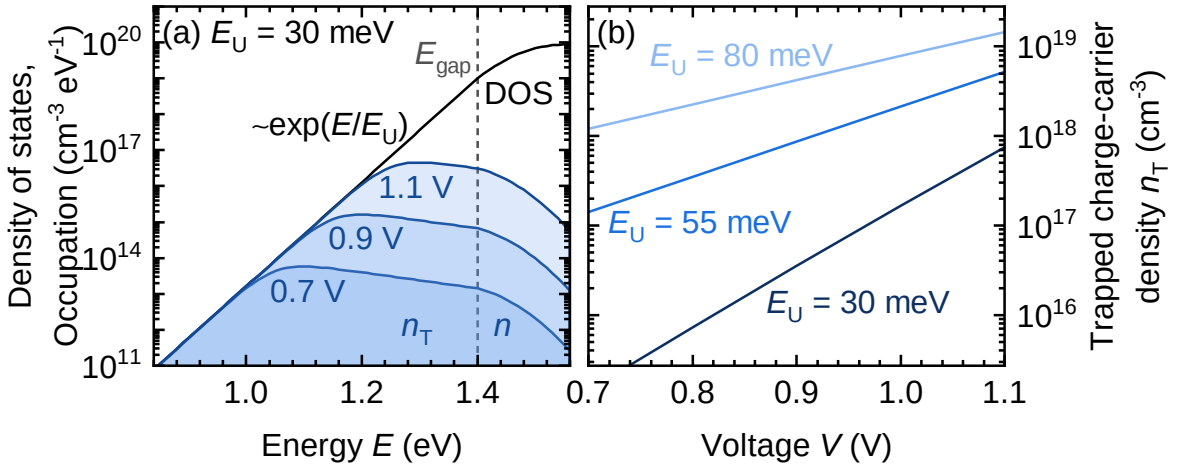

Figure 6.2: (a) Modeled density of states around the LUMO of the acceptor with exponential band tails. As the occupation maximum of the density of states is located at the quasi-Fermi level of electrons, the density n_T of trapped electrons increases with quasi-Fermi level splitting. Consequently, n_T increases with voltage V in (b) for Urbach energies E_U of 30, 55 and 80 meV. Low Urbach energies E_U result in a more rapid increase since the density of tail states is steeper.

in Figure 6.2a, is given by the product of the occupation probability $\theta(E)$ with the density of states N_{cbt} from Equation (2.47). The integral over all occupied states then gives the density of trapped electrons

$$n_T \propto \int_{E_V}^{E_C} \theta(E) N_{cbt}(E) \mathrm{d}E, \tag{6.1}$$

where E_V is the valence-band edge and E_C the conduction-band edge. As the density of states is filled with electrons mostly up to the quasi-Fermi level E_{qFn} of the electrons, the occupation probability can be approximated by a step function and the integral becomes

$$n_T \propto \int_{E_V}^{E_{qFn}} N_{cbt}(E) \mathrm{d}E. \tag{6.2}$$

Solving this integral leads us to

$$n_T \propto \exp\left(\frac{E_{qFn} - E_C}{E_U}\right) - \exp\left(\frac{E_V - E_C}{E_U}\right). \tag{6.3}$$

The second term containing the band gap energy is negligibly small compared to the first term. Also, as the quasi-Fermi level splitting is evoked by an applied voltage, for

a symmetric device, it can be further assumed that

$$n_{\mathrm{T}} \propto \exp\left(\frac{qV}{2E_{\mathrm{U}}}\right). \tag{6.4}$$

This relation allows extracting information on the density of trap states in the form of the Urbach energy from carrier-density data. This dependence is further illustrated in Figure 6.2b which shows n_{T} as a function of voltage for three different Urbach energies E_{U}. The trapped charge-carrier density increases exponentially with voltage with a higher slope for a low Urbach energy since the corresponding density of tail states is steeper. Hence, the voltage dependence of the density of trapped charge carriers n_{T} can reflect the shape of the density of states. As can be seen from Figure 6.2a, the area below the band edge that represents n_{T}, can be significantly larger than the one indicating the free carrier density n in the band, allowing the approximation of the total charge-carrier density $n_{\mathrm{tot}} = n_{\mathrm{T}} + n \approx n_{\mathrm{T}}$. Hence, to extract the Urbach energy from electrical measurements, one can try to measure the charge-carrier density as a function of voltage.

Typical methods for finding the charge-carrier density n are charge-extraction measurements and capacitance-voltage measurements from admittance spectroscopy. While the first measures the current that is extracted when switching a device from open circuit under illumination to short circuit in the dark, the latter uses the fact that a separation of charges is needed to create a capacitance inside a solar cell. Using the common approximation that this chemical capacitance C_{μ} is related to the derivative of the charge-carrier density with voltage as introduced in Equation (3.14) in Chapter 3.2, one can write

$$C_{\mu} \propto \frac{\partial n}{\partial V} \propto \frac{\partial n_{\mathrm{T}}}{\partial V} \propto \frac{\partial}{\partial V}\left[\exp\left(\frac{qV}{2E_{\mathrm{U}}}\right)\right] \propto \exp\left(\frac{qV}{2E_{\mathrm{U}}}\right). \tag{6.5}$$

Hence, from the logarithmic slope of the chemical capacitance C_{μ}, the Urbach energy E_{U} can be extracted in this model. In literature, the chemical capacitance most commonly is further integrated to get the charge-carrier density n and interpret it in terms of recombination mechanisms.[24, 73, 139, 235, 275–277] While the correlation between n and the recombination rate is relatively intuitive, there are multiple approaches and some discussion on how to proceed with this integration and how to estimate the chemical capacitance.[73, 276, 278] For these reasons, I herein refrain from using further calculation steps during integration and directly use the slope of the chemical capacitance for the

Urbach-energy estimation.

To validate this approach and find the most accurate way to calculate the chemical capacitance from admittance data, I modeled a generic organic solar cell using the drift-diffusion simulation software SCAPS.[157,279] For simulations under illumination, I further used the software ASA[5,174]. The assumptions and models have been presented in detail in Chapter 3.4. Simulation parameters specific to this chapter can be extracted from Table A.3. Since the extraction of the chemical capacitance C_μ from admittance data is not obvious, I first performed simulations to find the best estimation for C_μ. These simulations in Figure A.1 show that the chemical capacitance can be best replicated by subtracting the total capacitance at high frequency and reverse bias in the dark, the geometric capacitance C_{geo}, from the total capacitance at low frequencies.

Now being able to estimate the chemical capacitance from the simulated admittance data, I test the method of extracting the Urbach energy from the $C_\mu \propto V$-relation. For this purpose, Figure 6.3 shows the capacitance $C - C_{\text{geo}}$ of three organic solar cells with different tail slopes E_U of 30, 55 and 80 meV that were calculated from admittance spectroscopy simulations (a) under illumination at open circuit and (b) in the dark. The dashed lines represent the exponential increase that can ideally be expected for the respective Urbach energies. In fact, under both conditions, where the quasi-Fermi level splitting can be approximated by the applied voltage, in the dark and at open circuit, the slope of the capacitance $C_\mu \approx C - C_{\text{geo}}$ decreases with increasing Urbach energy. This observation shows that the chemical capacitance is sensitive to the shape of the density of defect states and that the Urbach energy extracted from exponential fits can be used to compare the severity of the energetic disorder in different solar cells even though it differs from the actual Urbach energy. However, when applying this method, the frequency of the alternating voltage has to be selected carefully since the charge carriers inside the active layer need to be able to follow the changes in electric field (see Figure A.2 in the Appendix). If the frequency is too high, the capacitance will saturate to the geometric capacitance.

This introduction of the rationale behind the characterization of energetic disorder with electrical methods already reveals multiple approximations that go into the analysis and therefore must be considered when discussing measurement results. On the other hand, while the principle of exciting an electron to or from a trap state by low energy photons appears more simple, the interpretation of such absorption

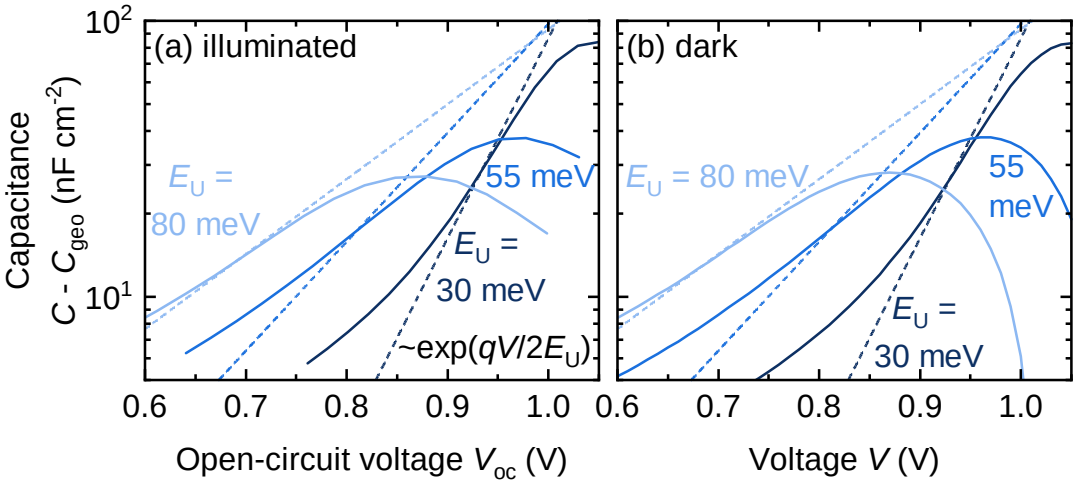

Figure 6.3: Capacitance $C - C_{\mathrm{geo}}$ extracted from simulated admittance spectroscopy measurements as a function of voltage for Urbach energies E_{U} of 30, 55 and 80 meV. The dashed lines indicate an exponential with the corresponding Urbach energy. For both operating conditions, (a) under illumination at open circuit and (b) in the dark, the quasi-Fermi level splitting can be approximated by the applied voltage and thereby the chemical capacitance is sensitive to the respective Urbach energy.

data remains challenging. The static disorder influencing the shape of the absorption tail can be caused by disorder in the charge-transfer state, local excitons or both.[280] Additionally, differentiating between static and dynamic disorder has been a topic of discussion in literature.[224,225,227,229] Therefore, I present in the following both; different approaches to interpreting optical data but also discuss electrical, admittance data in detail.

6.3. Experimental results

While this work is focused on the characterization of PBDB-TF-T1:BTP-4F-12-based solar cells, to study the difference between optical and voltage-dependent measurements of the Urbach energy E_{U}, I additionally fabricated and characterized a solar cell comprising PffBT4T-2OD:EH-IDTBR. The energetic disorder of the high efficiency material system PBDB-TF-T1:BTP-4F-12 to the best of my knowledge has not been investigated so far. Similar materials have been found to exhibit a low Urbach energy.[118,265,274] As a contrast, PffBT4T-2OD:EH-IDTBR has been chosen as an active layer blend for which a relatively high Urbach energy of 76 meV has been reported.[118] Both solar cells were fabricated as described in Chapter 3.1.3 in the same

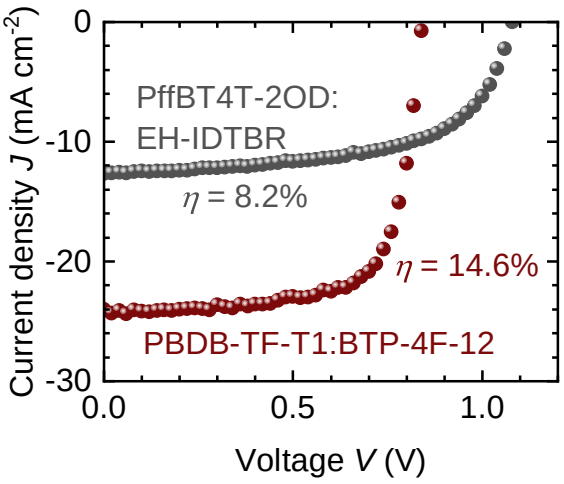

Figure 6.4: Current density J as a function of voltage V of the two organic solar cells incorporating the bulk heterojunctions PffBT4T-2OD:EH-IDTBR and PBDB-TF-T1:BTP-4F-12 that are characterized in terms of their energetic disorder.

cell architecture. Figure 6.4 shows the JV characteristics of the resulting devices. The cell with PffBT4T-2OD:EH-IDTBR as the active layer material exhibits a higher open-circuit voltage due to its higher band gap but significantly less photocurrent than the device with PBDB-TF-T1:BTP-4F-12. However, it is beyond the scope of this work to analyze the various loss mechanisms that set apart the two solar cell systems. Instead, I want to focus on the recombination via shallow defect states.

For this purpose, I analyzed the absorption properties of the devices with Fourier transform photocurrent spectroscopy (FTPS) and of the active layer films with photothermal deflection spectroscopy (PDS). Figure 6.5 shows the normalized signal of the optical measurements on the material systems (a) PffBT4T-2OD:EH-IDTBR and (b) PBDB-TF-T1:BTP-4F-12. For every measurement, I fitted the exponential regime (solid lines) to extract the Urbach energy E_U from the slope $1/E_\mathrm{U}$. Under FTPS, both solar cells show a very steep increase in absorptance which results in an Urbach energy $E_\mathrm{U,FTPS}$ of around 26 meV for PffBT4T-2OD:EH-IDTBR and 23 meV for PBDB-TF-T1:BTP-4F-12. While the FTPS measurements show a dynamic range of around six orders of magnitude, PDS has a lower dynamic range between two and three orders of magnitude. Therefore, the exponential part of the signal could be affected by the saturation at a higher energy resulting in higher Urbach energies $E_\mathrm{U,PDS}$ of 35 meV for PffBT4T-2OD:EH-IDTBR and 29 meV for PBDB-TF-T1:BTP-4F-12. Therefore, by sticking to the traditional analysis presented in Chapter 4, I would have not noticed errors due to the limited dynamic range of the PDS measurement. Similarly, in my li-

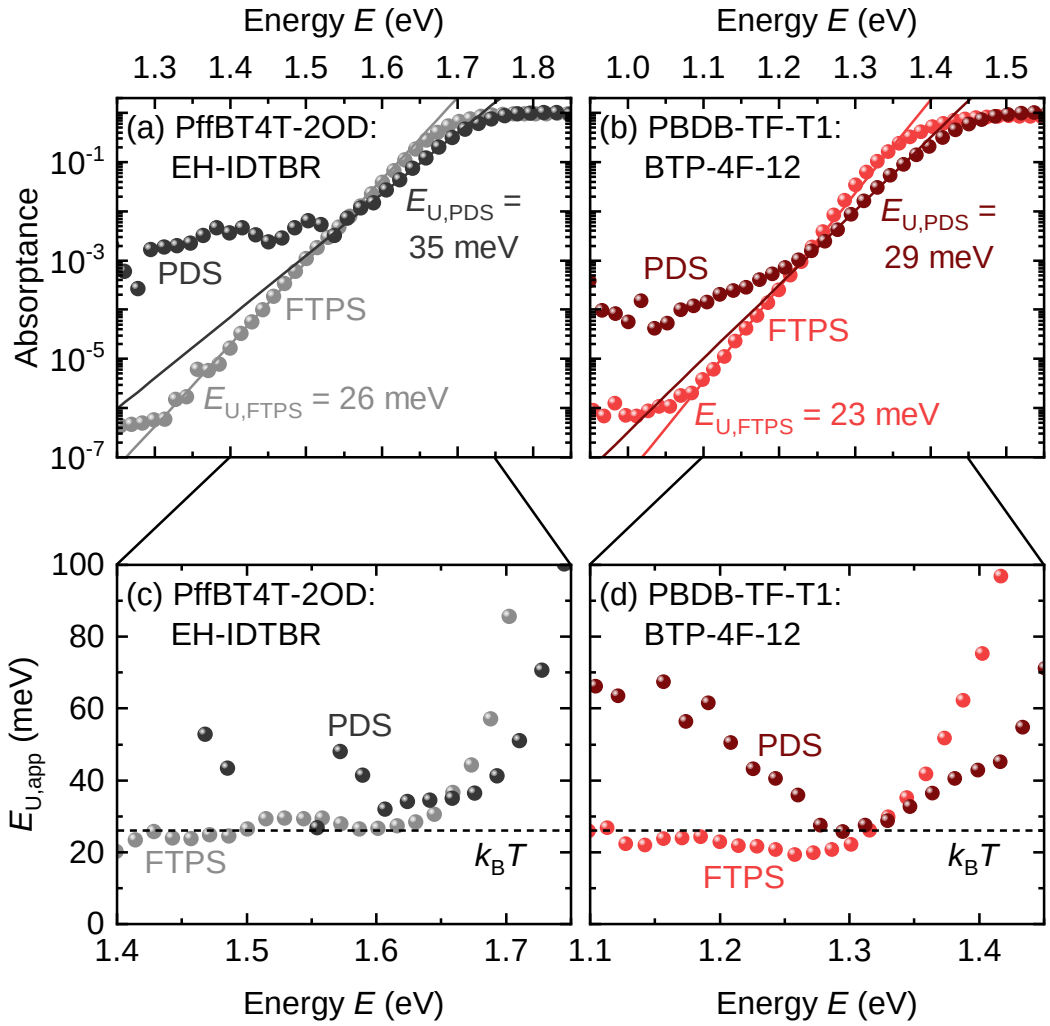

Figure 6.5: Normalized signal of Fourier-transform photocurrent spectroscopy (FTPS) in the lighter colors and photothermal deflection spectroscopy (PDS) in the darker colors as a function of energy E for organic solar cells based on (a, c) PffBT4T-2OD:EH-IDTBR and (b, d) PBDB-TF-T1:BTP-4F-12. The solid lines represent fits to the exponential regime of the experimental data with the slope of $1/E_U$. (c, d) Apparent Urbach energy $E_{U,app}$, the inverse logarithmic slope of the absorptance, for both measurement techniques and material systems. Even though scattering becomes more apparent in the $E_{U,app}$, both the differential slope and the exponential fit yield Urbach energies close to the thermal energy k_BT.

terature research, some of the higher values reported for the Urbach energy E_U from optical measurements could potentially be attributed to the low dynamic range of the measurements.[183,190,193,250] Also, the films on glass that were measured for PDS lack absorption from back reflection on the silver cathode that is included in the FTPS measurements causing further discrepancy between the two methods. On the one hand,

the light traverses twice through the absorber layer in FTPS measurements, on the other hand, interference effects can cause differences in the subgap slope.[280,281] Still, both optical measurements yield relatively low Urbach energies close to thermal energy. This finding coincides well with the model proposed by Kaiser et al., in which they attribute parts of the subgap absorption features to thermal broadening.[280] To better distinguish between the effects of static disorder in the singlet state, thermal broadening and deep defects, they plot the apparent Urbach energy $E_{\mathrm{U,app}} = ((\mathrm{d}\ln(a))/\mathrm{d}E)^{-1}$, where a is the absorptance, as a function of energy. Figure 6.5c and Figure 6.5d show the apparent Urbach energy $E_{\mathrm{U,app}}$ for PDS and FTPS measurements on both material systems. For the measurements on PffBT4T-2OD:EH-IDTBR in Figure 6.5c, the PDS signal first decreases going from high energies to low energies, but does not reach the thermal energy before the limitation in dynamic range causes it to increase again. The FTPS measurements allow further analysis due to the higher dynamic range even though the inverse slope $E_{\mathrm{U,app}}$ is noisy. It exhibits a plateau around thermal energy and higher apparent Urbach energies $E_{\mathrm{U,app}}$ near the optical band edge that can be assigned to the static disorder of the singlet state.[280] The apparent Urbach energy $E_{\mathrm{U,app}}$ for PBDB-TF-T1:BTP-4F-12 in Figure 6.5d behaves similarly. The PDS data features a minimum at thermal energy, whereas the FTPS data further decreases below the value assigned to thermal broadening. As discussed by Kaiser et al., small variations around $k_{\mathrm{B}}T$ can be caused by interference effects.[280] Kay et al. further observed that the conventional device structure, which is also employed in these samples, is most susceptible to interference effects.[281] Thus, interference could be a possible explanation for apparent Urbach energies $E_{\mathrm{U,app}}$ below thermal energy. Note that the increase in apparent Urbach energy $E_{\mathrm{U,app}}$ in the low energy regime is not an indicator for deep traps in the samples but simply caused by the limit in dynamic range of the measurements. Therefore, the exponential fits that I applied to the data in Figure 6.5a and Figure 6.5b according to the traditional approach potentially only fit thermal broadening and contain no material specific information. This observation based on the findings of Kaiser et al. also offers another explanation, why literature values for optically extracted Urbach energies mostly are very low, below 30 meV. A majority of the values above 30 meV that were found in literature either fit features like the charge-transfer state[271] or deep defects,[78,79,218,231,247,252,256,270,271] or the disorder of the singlet state.[20,266] As illustrated in Figure A.3 in the Appendix, organic solar cells comprising fullerene acceptors are more frequently reported to have an Urbach e-

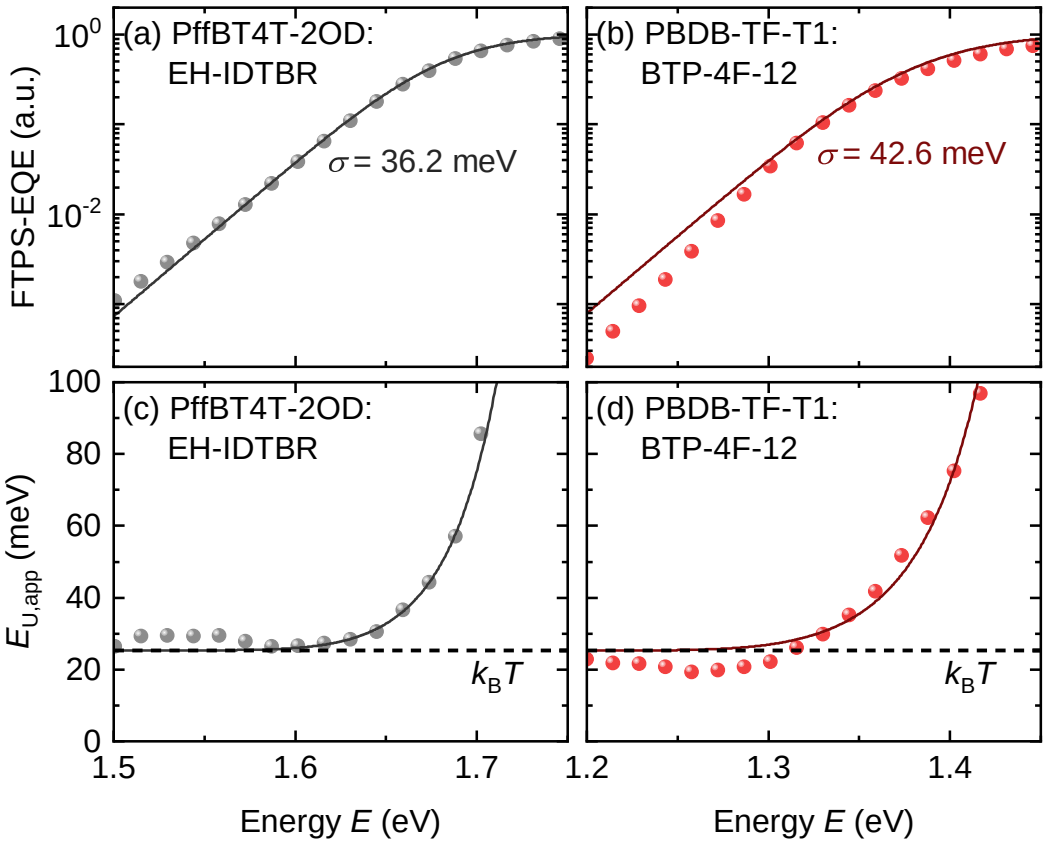

Figure 6.6: (a, b) FTPS signal and (c, d) its inverse derivative for solar cells based on (a, c) PffBT4T-2OD:EH-IDTBR and (b, d) PBDB-TF-T1:BTP-4F-12. The solid lines represent fits of the energy regime around the optical band edge with the model proposed by Kaiser et al.[280] and a Matlab routine based on Kay et al.[281] The average of the 20% best fits results in a higher disorder value for the PBDB-TF-T1:BTP-4F-12-based device (42.6 meV±12 µeV) than for the solar cell comprising PffBT4T-2OD:EH-IDTBR (36.2 meV±7 µeV). However, since its apparent Urbach energy has a minimum below thermal energy, the model fails to fit the data accurately. For the fitting, active layer thicknesses were estimated from the geometric capacitance measured at $V = -3\,\mathrm{V}$ in the dark according to Equation (A.1).

nergy above thermal energy in optical measurements which can be attributed to their typically high energy offsets and more pronounced charge-transfer state absorption.[280] Therefore, fitting of the subgap absorption with an exponential function is highly sensitive to the fitting range. As an alternative approach, Kay et al. proposed fitting the data with the model of Kaiser et al. to extract the standard deviation σ of the Gaussian disorder of the singlet state.[281] In Figure 6.6a and 6.6b, I show such a fit to my FTPS data. While the initial decrease below the band edge can be well replicated for the solar cell comprising PffBT4T-2OD:EH-IDTBR, the slope of the experimental

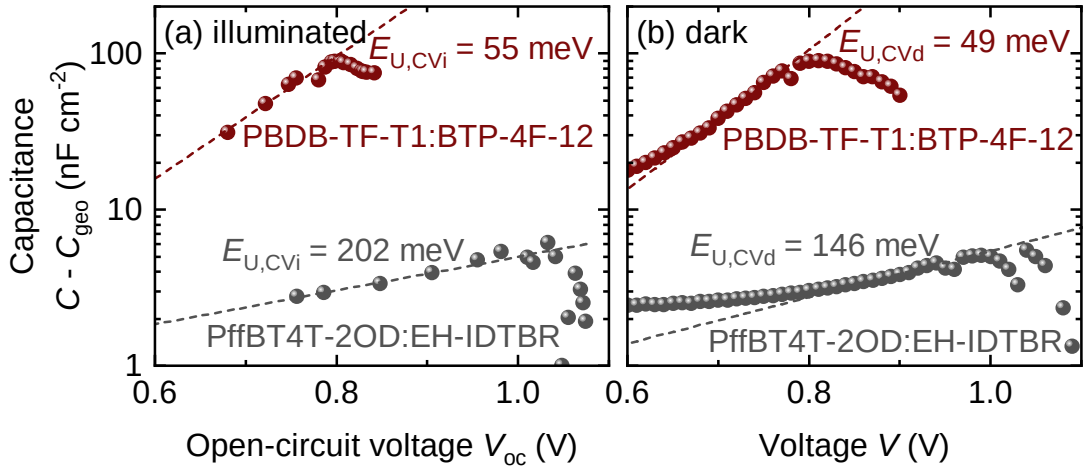

Figure 6.7: Capacitance $C - C_{geo}$ estimated from admittance spectroscopy measurements (a) under illumination at open circuit and (b) in the dark on organic solar cells with an active layer consisting of PffBT4T-2OD:EH-IDTBR or PBDB-TF-T1:BTP-4F-12. The dashed lines represent exponential fits to the experimental data. The Urbach energy $E_{U,CV}$ extracted from the fits for PBDB-TF-T1:BTP-4F-12 is about twice as high as for the optical measurements whereas the values for PffBT4T-2OD:EH-IDTBR are unrealistically high.

data corresponding to PBDB-TF-T1:BTP.4F-12 is too steep to be fitted by the model. Figure 6.6c and 6.6d further illustrate how the model is only capable to fit data with an apparent Urbach energy $E_{U,app} = k_B T$. Contrary to previous observations, the fit yields a higher disorder with a standard deviation of 41.9 meV for the PBDB-TF-T1:BTP.4F-12 based solar cells than for the PffBT4T-2OD:EH-IDTBR based ones with 35.8 meV. However, the quality of the fit is worse for the first one, since the model fails to replicate the apparent Urbach energies $E_{U,app}$ below $k_B T$. Nonetheless, values extracted for the static disorder in these material systems are relatively low.

For the voltage-dependent method, I performed admittance spectroscopy on the same solar cells that were characterized by FTPS. From the experimental admittance data, I calculated the capacitance $C - C_{geo}$ as discussed previously as an estimate for the chemical capacitance C_μ. Figure 6.7a shows the resulting capacitance as a function of open-circuit voltage V_{oc} for both solar cells based on PffBT4T-2OD:EH-IDTBR and PBDB-TF-T1:BTP-4F-12. At low voltages, the capacitance increases before falling at higher voltages. When fitting an exponential function to the increase, one can extract an Urbach energy $E_{U,CVi} = 55$ meV for PBDB-TF-T1:BTP-4F-12 from the data and $E_{U,CVi} = 202$ meV for PffBT4T-2OD:EH-IDTBR. The capacitance $C - C_{geo}$ in the dark in Figure 6.7b behaves similarly resulting in $E_{U,CVd} = 49$ meV and $E_{U,CVd} = 146$ meV

for PBDB-TF-T1:BTP-4F-12 and PffBT4T-2OD:EH-IDTBR, respectively. Therefore, the tail slope extracted from voltage-dependent admittance measurements is more than twice as high for PBDB-TF-T1:BTP-4F-12 as the one from optical measurements. This difference appears to be well in line with my observation on Urbach energies reported in literature. The values extracted from fits of the capacitance of the PffBT4T-2OD:EH-IDTBR solar cell, however, are higher than any typically reported in literature.

6.4. Discussing the Discrepancies Between Optical and Electrical Methods

Understanding these discrepancies between the optical and electrical methods requires a more theoretical comparison of the measurement techniques. First of all, the difference between the methods cannot be explained by including the reorganization energy into the interpretation. For example, one might expect the reorganization energy in optical measurements, where excitonic states or the charge-transfer state are probed, to be different from the reorganization energy of polarons which are considered in electrical measurements. However, while optical techniques measure both, the reorganization energy and static disorder,[224, 225, 227] electrical methods only measure the filling of the lowest excited state with electrons and the highest ground state with holes. So, as there is no charge transfer needed between the states, the reorganization energy of polarons is not reflected in the capacitance data. Therefore, this consideration would even lead to the contrary effect than what I observed in my experiments and in literature with higher disorder measured by optical characterization. To understand these inconsistencies between measurement techniques, I further used drift-diffusion simulations to study possible origins leading to higher Urbach energies from voltage-dependent measurements.

6.4.1. Density of Defect States Beyond the Monoexponential Shape

As the drastic difference in Urbach energy $E_{\mathrm{U,CV}}$ between the two material systems suggests that different effects may occur in the two devices, I will in the following look at the solar cells based on PBDB-TF-T1:BTP-4F-12 and PffBT4T-2OD:EH-IDTBR

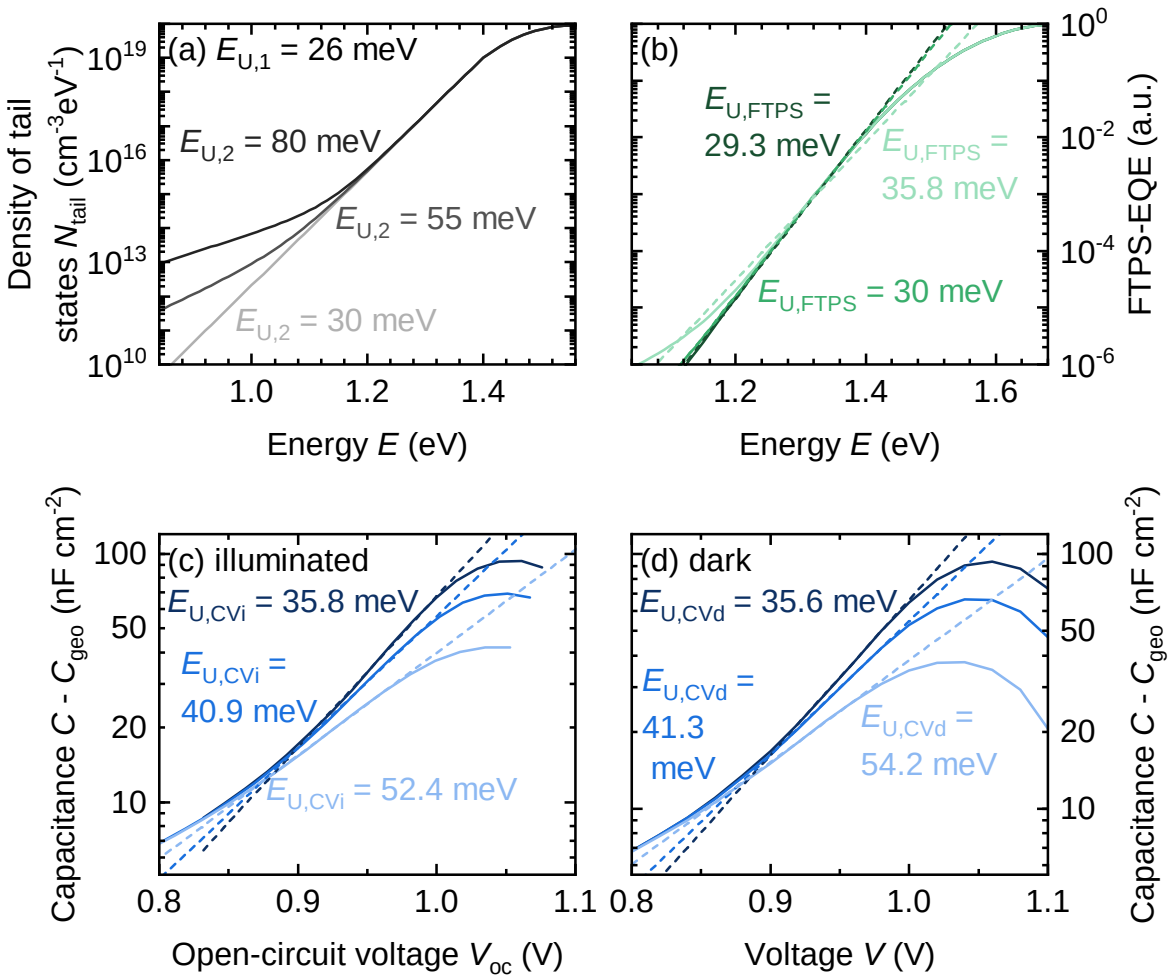

Figure 6.8: (a) Total density of states modeled with a combination of a steep Urbach tail with $E_{U,1}$ = 26 meV and a high density of defect states and a tail with higher Urbach energies $E_{U,2}$ of 30, 55 or 80 meV and low density of states that dominates at lower energies E. (b) FTPS-signal calculated from the density of states with two exponential tails. (c) Corresponding simulated capacitance $C - C_{geo}$ under open-circuit conditions and (d) in the dark. The Urbach energies extracted from the dashed fits of the capacitance measurements show more sensitivity to the slope of the deeper tail than for the optical measurements.

separately. I first focus on the effect observed in the PBDB-TF-T1:BTP-4F-12 cells. For this purpose, I modeled a solar cell with a density of tail states consisting of two tails with different slopes and density of trap states. Figure 6.8a shows the resulting density of tail states for a steep Urbach tail with $E_{U,1}$ = 26 meV that dominates close to the band edge and a more shallow tail with varying Urbach energy $E_{U,2}$ of 30, 55 and 80 meV that dominates further in the band. The FTPS signal that can be calculated from this density of states is displayed in Figure 6.8b. In the range that can be resolved

by the measurement, there is only little influence by the deep tail. Therefore, the Urbach energy $E_{\mathrm{U,FTPS}}$ that could be extracted from these optical measurements only ranges from 29 to 36 meV. In contrast, the admittance measurements in Figure 6.8c and Figure 6.8d are more sensitive to the variation of the deep Urbach tail and result in significantly different fits. Therefore, at the voltages applied to the solar cell, these deep tails are still filled with increasing voltage. So, with the filling according to the quasi-Fermi levels, an energy range of the density of states is probed that can be below the resolution of FTPS measurements. Thereby, the voltage-dependent measurements can in fact show features of deeper traps in the device. Hence, the difference in Urbach energy between optical and voltage-dependent measurements as observed for PBDB-TF-T1:BTP-4F-12 can originate in probing a density of trap states at different energy ranges that is not monoexponential.

Yet, for this effect to evoke Urbach energies $E_{\mathrm{U,CV}}$ as high as observed for PffBT4T-2OD:EH-IDTBR, the slope of the density of deep defect states would need to be extremely low. Therefore, I need to further study the chemical capacitance of this material system and explore the possibility that it does not actually reflect the density of states. As seen in Figure 6.4f, the solar cell based on PffBT4T-2OD:EH-IDTBR only shows a power-conversion efficiency of around 8%. The material system is known to have poor charge-carrier mobilities[282] and due to different energy levels compared to PBDB-TF-T1:BTP-4F-12, the injection barriers might differ. In addition, even though the density of states seems to be steep close to the band edge, recombination via these tail states can still be high due to high capture rates. Even a slightly increased active layer thickness for this solar cell could lead to transport issues and space-charge effects due to less uniform charge-carrier generation. The effect of the injection barriers, the capture rates and the active layer thickness on the capacitance-voltage curves predicted by simulations is shown in Figure A.4 in the Appendix. In the following, I will focus only on the charge-carrier mobility as an example.

6.4.2. Impact of the Voltage-Dependent Electrode Capacitance

Figure 6.9 shows the simulation results for an Urbach energy E_{U} of 30 meV but different charge-carrier mobilities μ to illustrate how limited transport can cause the experimental trends observed in Figure 6.7. Once more, it shows the chemical ca-

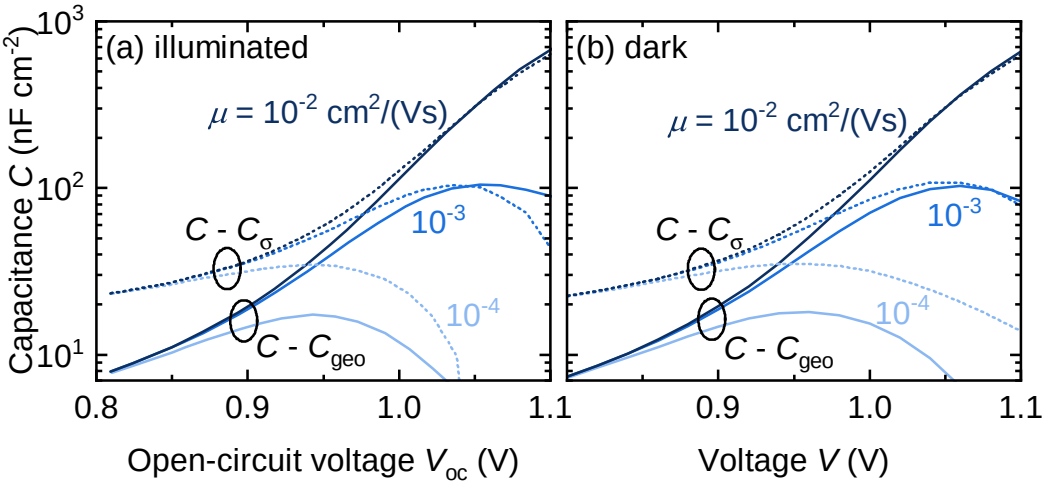

Figure 6.9: Simulated capacitance (a) at open circuit under varying illumination intensity and (b) in the dark for different applied voltages V and multiple charge-carrier mobilities μ. The solid lines represent the difference between the total capacitance C and the geometric capacitance C_{geo}, which is an estimate of the chemical capacitance that can be determined experimentally. The curves flatten for lower mobilities. The dotted line is the difference between C and the electrode capacitance C_{σ}, which is the best approximation for C_{μ} but can only be extracted from simulations. The issue of flat CV-curves does not originate in the assumption $C_{\sigma} \approx C_{\mathrm{geo}}$, since both approaches show a similar behavior at high voltages with decreasing charge-carrier mobility.

pacitance at (a) open circuit and (b) in the dark estimated by the difference between the total capacitance and the geometric capacitance C_{geo} with the solid lines. It appears that under both working conditions, the curves are flattening with decreasing mobilities. Therefore, at low charge-carrier mobilities, the Urbach energy $E_{\mathrm{U,CV}}$ calculated from the slope of the graphs would be an overestimation. There are several assumptions underlying this estimation. One of them is the calculation of the chemical capacitance as the difference $C - C_{\mathrm{geo}}$ of the total capacitance and the constant geometric capacitance C_{geo}. It assumes that the charge on the electrodes that contributes to the geometric capacitance C_{geo} is constant over the entire voltage range. In reality, the electrode capacitance can be voltage dependent. Therefore, for the true chemical capacitance, one needs to subtract the voltage-dependent electrode capacitance C_{σ}. Even though C_{σ} is not experimentally accessible, I can extract it from the drift-diffusion simulations. Consequently, Figure 6.9 shows $C - C_{\sigma}$ with the dashed lines for comparison. It reveals the same trend with mobility as the experimentally accessible $C - C_{\mathrm{geo}}$. So, the flattening of the CV-curves does not originate in capacitive but rather resistive effects.

6.4.3. Determining the Effective Capacitance with an Internal Series Resistance

In the following, I will illustrate how a series resistance R_s inside the active layer causes the flattening of the capacitance-voltage curves. In Figure 6.10, the simulated dark current density is plotted for an organic solar cell with high mobilities and one with low mobilities. Even though external resistances are neglected in the simulations, the current density increases less rapidly at high voltages, typical for a series resistance. This behavior indicates that the limited mobility causes a difference between the externally applied voltage and the quasi-Fermi level splitting inside the active layer, similar to an internal series resistance R_s that increases with decreasing charge-carrier mobility. Therefore, the simple RC-circuit that was used so far for the determination of the total capacitance as the imaginary part of the admittance Y must be extended by a series resistance, which models a drop in the quasi-Fermi levels inside the bulk. The resulting equivalent circuit is shown in Figure 6.10. Here, the imaginary part $\mathrm{Im}[Y]$ of the admittance will yield an effective capacitance $C_\mathrm{eff} = \mathrm{Im}[Y]/\omega$ that is determined by both the resistances and capacitances in the circuit. For the effective capacitance, I therefore first need the admittance of the modified equivalent circuit in Figure 6.10. It is given by

$$Y = \left[R_\mathrm{s} + \left(\frac{1}{R_\mathrm{rec}} + i\omega C_\mu \right)^{-1} \right]^{-1}, \tag{6.6}$$

where R_rec is the recombination resistance. Solving this equation for the imaginary part gives

$$\mathrm{Im}[Y] = \frac{\omega C_\mu}{\left(\frac{R_\mathrm{s}}{R_\mathrm{rec}} + 1 \right)^2 + \left(R_\mathrm{s} \omega C_\mu \right)^2}. \tag{6.7}$$

Therefore, the effective capacitance $C_\mathrm{eff,cir}$, that would be measured is

$$C_\mathrm{eff,cir} = \frac{\mathrm{Im}\left[Y\right]}{\omega} = \frac{C_\mu}{\left(\frac{R_\mathrm{s}}{R_\mathrm{rec}} + 1 \right)^2 + \left(\omega R_\mathrm{s} C_\mu \right)^2}. \tag{6.8}$$

In Equation (6.8), the effective capacitance will reflect the true chemical capacitance C_μ if the denominator is 1. For low frequencies where $\omega \ll R_\mathrm{s} C_\mu$, the second term is

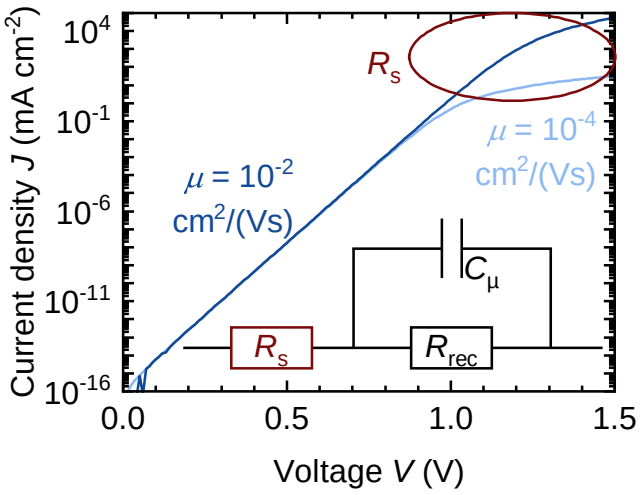

Figure 6.10: Dark JV characteristics of organic solar cells with high and low charge-carrier mobilities μ and no external resistance. The high-voltage regime indicates an internal series resistance R_s. Therefore, the equivalent circuit for alternating voltages is extended by a series resistance as indicated by the inset.

negligibly small. So, the term containing the recombination resistance R_rec is the most relevant. For a high recombination resistance that appears at low voltages, the term goes to 1 and $C_\mathrm{eff,cir} = C_\mu$. However, for high voltages, the recombination resistance decreases to values around R_s or even lower. In this case, $C_\mathrm{eff,cir}$ does not increase as rapidly as C_μ because of the denominator. To test this equivalent circuit and the corresponding effective capacitance $C_\mathrm{eff,cir}$, I estimate $C_\mathrm{eff,cir}$ from steady-state quantities. For this purpose, I first extract R_s by fitting the dark JV characteristics with the diode equation from Equation (3.1). The resulting fits are displayed in Figure A.5. The recombination resistance R_rec describes the slope of the recombination-current density with the internal voltage according to Equation (3.16). Therefore, it can be calculated from

$$R_\mathrm{rec} = \frac{n_\mathrm{id} k_\mathrm{B} T}{J_0} \exp\left(-\frac{q\left(V_\mathrm{ext} - R_\mathrm{s} J\right)}{n_\mathrm{id} k_\mathrm{B} T}\right). \tag{6.9}$$

The analytical estimate of the chemical capacitance $C_\mathrm{\mu,ana}$ is taken from the derivation without series resistance in Equation (3.13) as

$$C_\mathrm{\mu,ana} = q \int_0^d \frac{\partial n\left(x\right)}{\partial V_\mathrm{int}} \mathrm{d}x. \tag{6.10}$$

Figure 6.11a shows this approximation $C_{\mu,\mathrm{ana}}$ without a series resistance in the dashed lines as a function of voltage in the dark. In fact, as predicted by the effective capacitance in Equation (6.8), the chemical capacitance $C_{\mu,\mathrm{ana}}$ follows $C - C_\sigma$ at low voltages where the recombination resistance is high. At high voltages, $C_{\mu,\mathrm{ana}}$ increases with the carrier density while the observed capacitance drops. Thereby, Figure 6.11a illustrates once more the need for the series resistance in Equation (6.8). In fact, the effective capacitance $C_{\mathrm{eff,cir}}$ calculated with this equivalent circuit model is displayed in Figure 6.11b in the dotted line. It features the drop at high voltages that one would expect from the discussion on Equation (6.8), which becomes more severe for a lower mobility and therefore higher series resistance.

The approach stated above explains the flattening of the CV-curves from an electrical engineering point of view, simply assuming a different equivalent circuit. Here, the phase delay due to transport issues is treated as an ohmic resistance. However, this phase delay can also be implemented in the continuity equation in the frequency domain that was derived in Chapter 3.2.3. Instead of assuming that the internal voltage $\widetilde{V}_{\mathrm{int}}$ is in-phase to the external voltage $\widetilde{V}_{\mathrm{ext}}$ in Equation (3.12), an out-of-phase contribution caused by transport problems can be added according to

$$\widetilde{V}_{\mathrm{int}}(x,\omega) = \widetilde{V}_{\mathrm{ext}}(\omega) - R_{\mathrm{s}}(x)\,\widetilde{J}(\omega)\,. \tag{6.11}$$

Here, the internal series resistance R_{s} does not have to be an ohmic resistance but can be position and voltage dependent. Thus, the ratio between the internal and external voltage is given by

$$\frac{\widetilde{V}_{\mathrm{int}}(x,\omega)}{\widetilde{V}_{\mathrm{ext}}(\omega)} = 1 - R_{\mathrm{s}}(x)\,Y(\omega)\,. \tag{6.12}$$

Using this expression in Equation (3.12) yields

$$Y(\omega) = q\int_0^d \left[1 - R_{\mathrm{s}}(x)\,Y\right]\left[i\omega\left(\frac{\partial\bar{n}(x)}{\partial\bar{V}_{\mathrm{int}}(x)}\right) + \left(\frac{\partial\bar{U}(x)}{\partial\bar{V}_{\mathrm{int}}(x)}\right)\right]\mathrm{d}x. \tag{6.13}$$

Solving Equation (6.13) for the admittance gives

$$Y(\omega) = \frac{q\int_0^d \left[i\omega\left(\frac{\partial\bar{n}(x)}{\partial\bar{V}_{\mathrm{int}}(x)}\right) + \left(\frac{\partial\bar{U}(x)}{\partial\bar{V}_{\mathrm{int}}(x)}\right)\right]\mathrm{d}x}{1 + q\int_0^d R_{\mathrm{s}}(x)\left[i\omega\left(\frac{\partial\bar{n}(x)}{\partial\bar{V}_{\mathrm{int}}(x)}\right) + \left(\frac{\partial\bar{U}(x)}{\partial\bar{V}_{\mathrm{int}}(x)}\right)\right]\mathrm{d}x}. \tag{6.14}$$

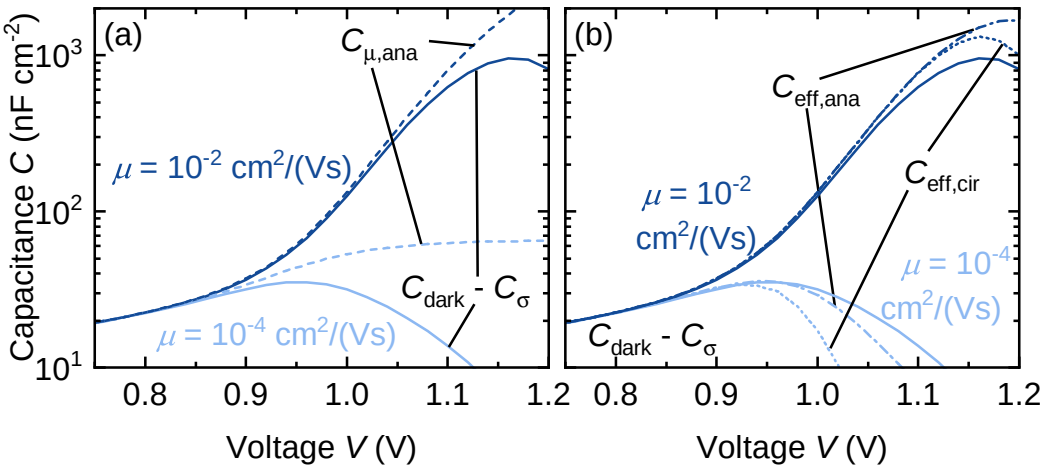

Figure 6.11: Dark capacitance-voltage simulations for organic solar cells with high and low charge-carrier mobility μ. (a) The analytical chemical capacitance $C_{\mu,\mathrm{ana}}$ continues to increase at high voltages whereas the difference between the electrode capacitance C_σ and the capacitance $C_{\mathrm{dark}} = \mathrm{Im}[Y]/\omega$ from simulated admittance values decreases. (b) Approaches to model this effective capacitance either analytically ($C_{\mathrm{eff,ana}}$, dash-dotted lines) or with an equivalent circuit ($C_{\mathrm{eff,cir}}$, dotted lines) feature a similar drop and therefore show the role of internal resistive effects.

Now, the goal is to rewrite Equation (6.14) in a way that enables the extraction of the imaginary part of the admittance, since it relates directly to the effective capacitance measured. For this purpose, I extend it with the complex conjugate. Thereby, I get the imaginary part that correlates to the effective analytical capacitance

$$C_{\mathrm{eff,ana}} = \frac{\mathrm{Im}\left[Y\left(\omega\right)\right]}{\omega} = \frac{q\int_0^d \frac{\partial \bar{n}(x)}{\partial \bar{V}_{\mathrm{int}}(x)}\mathrm{d}x}{\left[1+q\int_0^d R_{\mathrm{s}}\left(x\right)\frac{\partial \bar{U}(x)}{\partial \bar{V}_{\mathrm{int}}(x)}\mathrm{d}x\right]^2 + \left[q\omega\int_0^d R_{\mathrm{s}}\left(x\right)\frac{\partial \bar{n}(x)}{\partial \bar{V}_{\mathrm{int}}(x)}\mathrm{d}x\right]^2}. \quad (6.15)$$

Comparing Equation (6.15) with the effective capacitance from the equivalent circuit in Equation (6.8), there is a striking resemblance. The numerator in Equation (6.15) is the analytical chemical capacitance. In the denominator, $\frac{\partial \bar{U}(x')}{\partial \bar{V}_{\mathrm{int}}(x')}$ can be viewed as a spatially resolved recombination resistance and $\frac{\partial \bar{n}(x')}{\partial \bar{V}_{\mathrm{int}}(x')}$ as a chemical capacitance. Therefore, both, an analytical and an equivalent circuit approach yield a capacitance that is reduced by transport problems in a similar manner. Figure 6.11b compares Equation (6.8) and (6.15) for different charge-carrier mobilities. Once again, as one cannot directly extract the position and voltage-dependent series resistance, I use the series resistance extracted from the dark JV curves as a rough estimate in both Equation (6.8) and (6.15). It is visible that both models feature a drop in the effective

capacitance similar to the one that is observed from the simulated admittance data (solid lines). The drop in the analytical model is less steep than in the equivalent-circuit model which can be attributed to the difference in calculating the recombination resistance. Therefore, I have shown both analytically and with the consideration of different equivalent circuit models that the flattening of the capacitance-voltage curves is caused by the imaginary part of the admittance containing more than just the analytical chemical capacitance. This observation is relevant independent of the actual underlying shape of the subgap density of states and the model applied to it. As illustrated in Figure A.6, for a Gaussian density of states, the same trend with mobility as discussed for exponential tail states is observed. In contrast, transport issues are not relevant for the PDS measurement and much less significant in FTPS measurements due to the stronger internal electric field under the operation at short circuit. Thus, the high susceptibility of admittance measurements to bad electronic properties can lead to the discrepancies in the reported Urbach energy compared to the less sensitive optical measurements.

6.5. Conclusions

The characterization of energetic disorder plays an important role in the search for material systems that enable high efficiency organic solar cells. Optical methods are often used for this purpose where electrons are excited from or into defect states by incident photons. For instance, photothermal deflection spectroscopy (PDS),[190,191,193] Fourier transform photocurrent spectroscopy (FTPS)[231,232] or highly sensitive external quantum efficiency (EQE) measurements[24,233] are frequently applied in literature. But apart from these absorption-based methods, the density of defect states can also be probed by varying the quasi-Fermi level splitting with an applied voltage in for example charge extraction[118,207,234] or admittance measurements.[235] I found that both in my meta-analysis of the literature and in my experiments these electrical, voltage-dependent measurements yield overall higher Urbach energies than the techniques based on optical excitation. I analyzed optical FTPS and PDS measurements and electrical admittance spectroscopy under illumination and in the dark on the material system PBDB-TF-T1:BTP-4F-12 and the complementary PffBT4T-2OD:EH-IDTBR. In all cases, the Urbach energy extracted by the voltage-dependent methods was at least twice as high as their optical counterparts.

In my analysis, I show that care must be taken when analyzing experimental data as different effects can be mistakenly interpreted as features of energetic disorder. Even for purely optical data, I have observed that a low dynamic range in PDS measurements can lead to a lower slope at the band edge than in FTPS on the same material. Voltage-dependent admittance measurements have proven to be even more delicate as the analysis in terms of energetic disorder is based on a high number of assumptions. The experimental and simulation results on the extreme case of a solar cell based on PffBT4T-2OD:EH-IDTBR have demonstrated how bad transport properties can lead to an internal series resistance overlaying the exponential regime of the capacitance-voltage measurements. Thereby, the discrepancy in the Urbach energy between optical and voltage-dependent measurements can originate in an overestimation in voltage-dependent measurements due to bad electronic properties.

Knowing the limitations of the characterization techniques, I have also highlighted the potential that both optical and electrical methods correctly reflect the subband-gap density of states even though they yield different values for the Urbach energy. Moving away from a strictly monoexponential band tail, I have shown that the quasi-Fermi level splitting that is typical for voltage-dependent measurements probes energy ranges of the density of states where the signal of the optical measurements is below its resolution. Therefore, different approaches may detect different features of a density of defect states. So, I recommend the combination of different characterization techniques to not only be able to minimize the chance of unknowingly running into the limitations of a method but also to maximize the information gain on the energetic disorder in organic solar cells.

7

Parameter Estimation Using Machine Learning

While material properties of solar cell materials like crystalline silicon are widely known and tabulated,[283, 284] such data for organic solar cells is scarce. This lacking knowledge about material properties can on the one hand be attributed to the high variety in organic semiconductors but on the other hand is also caused by the highly correlated material parameters. Whereas, for instance, optical measurements directly yield the absorption properties of the material, most measurements depend on a variety of material parameters. As the previous chapters have shown, in these cases simple analytical models for the extraction of these parameters do not suffice but numerical simulations are needed to understand the measured data. Thus, in the past, fitting of drift-diffusion models to experimental data has been used to identify material parameters.[79, 165, 239, 285] However, the vast number of fitting parameters together with the non-negligible computation time of typical drift-diffusion equation solvers limit the accuracy of such models. Additionally, most of the computational time is used on creating information in the fitting steps towards the optimum that remains unused. One attempt to address these disadvantages is to implement machine learning into the process of estimating material parameters with the help of simulation tools. There have been attempts to train a neural network with simulated data to predict material parameters for input experimental data.[286, 287] This approach can yield a parameter combination that decently fits the experimental data but information on the surrounding parameter space providing some confidence for the fit remains unknown. With the goal of retrieving this information, Bayesian inference has been used, where the parameter space is probed in a statistical way based on Bayes' theorem[288] instead of using an optimization algorithm. While Bayesian parameter estimation was used by several different groups,[289–292] the

computational costs remained immense.[291] To reduce computational time, Ren et al. replaced the simulation software by a neural network that was trained with simulated data on gallium arsenide solar cells[293] and the method has later been applied to thin-film photovoltaics by Basita Das.[294] Thereby, the process of Bayesian inference was significantly sped up. This approach of using a neural network instead of a simulation software has not been applied to organic photovoltaics, yet. While the field of machine learning has also found growing interest,[295] efforts were mainly focused on material screening,[296–300] optimizing the donor-acceptor ratio[301,302] or for device fabrication.[303–305] However, in the field of device characterization, the opportunities arising from machine learning are relatively unexplored in organic photovoltaics with few notable exceptions by Majeed et al.[286] and Raba et al.[290] But especially the combination of fast computation with a neural network and exploring the high-dimensional parameter space has not been investigated so far. Such an approach goes beyond the traditional fitting procedure, where all simulations except the best fit are discarded and their information is lost, as instead all simulations with the numerical solver are used for the neural network training. Since the neural network does not only store this information but also is able to interpolate between the points, new opportunities for the analysis of a material system arise. Therefore, I herein first attempt to establish a routine of parameter estimation using a neural network on the organic solar cells based on PBDB-TF-T1:BTP-4F-12. For this purpose, I first introduce the basic workflow that was adapted from the work of Basita Das[294] in Chapter 7.1. Chapter 7.2 and Chapter 7.3 then guide through the process of training data generation and training the neural network, before I test the fitting procedure and the scanning of the parameter space on a set of simulated data in Chapter 7.4. After this validation of the method on a synthetic data set, Chapter 7.5 shows the application of the procedure to a set of light-intensity dependent JV curves of a device with a thin active layer. Afterwards, I compare these results to the ones from different experimental data sets in Chapter 7.6 and then find improvements to the model in Chapter 7.7 for future application of parameter estimation using machine learning. Within this chapter, I propose practices of handling and interpreting such large amounts of data and high-dimensional spaces. Therein, I always keep a focus on computational costs, since all calculations presented here have been performed on a conventional laptop with a laptop graphic processing unit NVIDIA T500. Hence, the framework presented here should be applicable for many researchers without elaborate computational equipment.

7.1. Introducing Machine Learning into Traditional Fitting Procedures

Before starting the actual process of parameter estimation, some effort has to be made in the preparation of the experimental data and the training of a neural network. So, for an overview, the workflow underlying this chapter is illustrated in Figure 7.1. First, the choice of experiment (Figure 7.1a) is essential. This experiment can be one simple JV curve or a capacitance-voltage curve but also a combination of several different measurements, since they could contain different information on the material parameters. After the choice of experiment, a device model has to be defined (Figure 7.1b) that in theory accurately describes the experiment that was performed. Such a device model can be anything from an analytical equation to a software like ASA or SCAPS. In this case, the model is defined in Chapter 3.4 with optical and electrical simulations in ASA using the one-medium approximation. However, such simulations require a high number of input parameters. For example, a drift-diffusion simulation with an optical solver requires 40 parameters just to cover all recombination mechanisms that were introduced in this work. Since every parameter adds a dimension to the parameter space that is investigated, the number of variables needs to be reduced (Figure 7.1c) to keep the computational effort to an acceptable level. Here, on the one hand, it is crucial to choose the parameters that have the biggest influence on the system, but also to set the remaining parameters to a reasonable value. Also, setting a reasonable range for the variables is important as it should be assured that the expected values lie within that range. Once the variable material parameters and their boundaries were selected, in a traditional fitting routine, a fitting algorithm would be applied that runs the model, i.e. the numerical simulations, until it has reached an optimum. This procedure is time consuming, especially considering that the information gain is limited on the best fit while all the other simulations during fitting are discarded. Therefore, instead of using the model directly for the fitting of the experimental data, a training data set can be generated (Figure 7.1d). Here, the goal is to create a large set of parameter combinations and their corresponding outcome, for example JV curves, that cover the entire parameter space. A high number of these combinations of material parameters and simulation results is needed to then train a neural network (Figure 7.1e). The more material parameters are selected to be variable, the more input data for training the neural network is needed for the higher dimensionality. Since the neu-

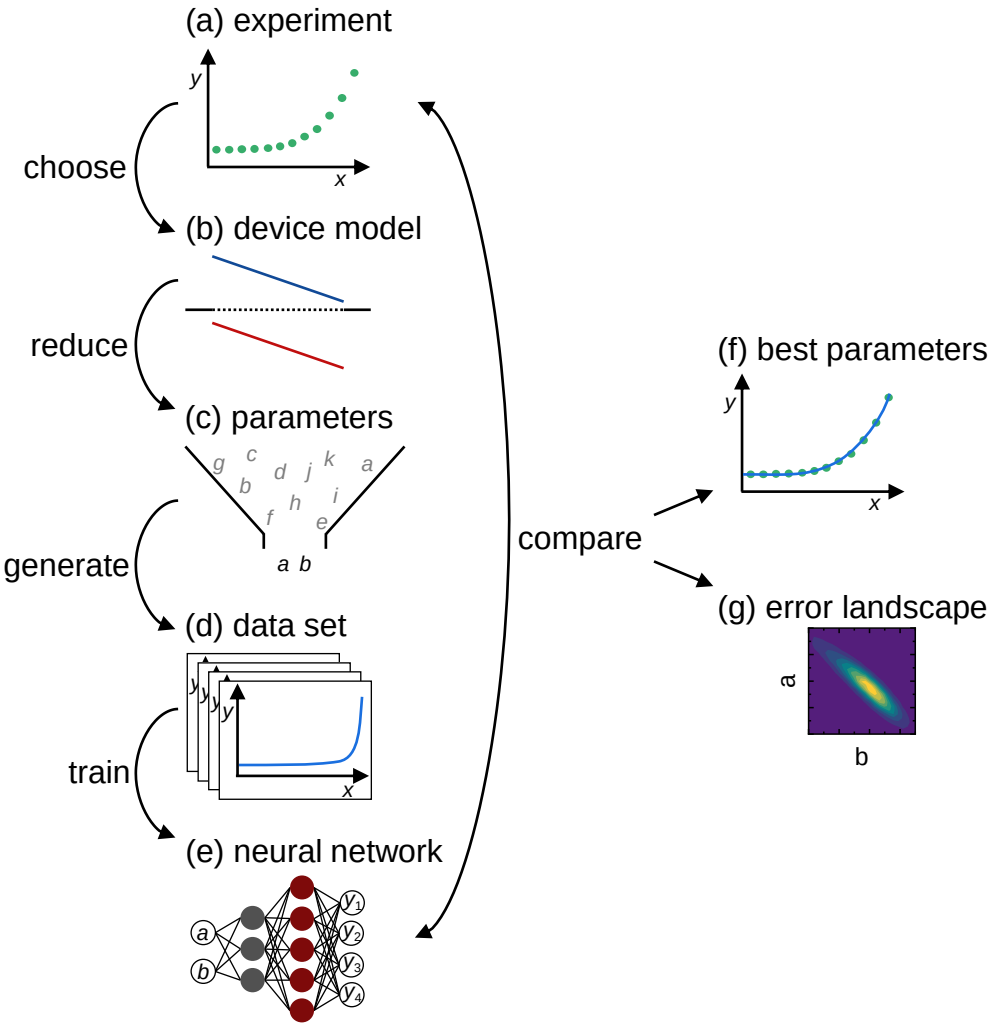

Figure 7.1: Workflow for parameter estimation using machine learning. After collecting (a) the experimental data, (b) a device model has to be chosen that best describes the experimental data. Often, a reduction of the dimensionality of the problem is required, meaning that (c) variable material parameters are selected while others are fixed. Using the device model, (d) a training data set is generated by varying the selected parameters. (e) A neural network is then trained with the data to replace the device model. Comparing the output of the neural network to the experimental data allows the calculation of an error and thereby (f) finding the best parameter set with a fitting procedure and (g) visualizing the error as a function of material parameters.

ral network is able to interpolate between these data points in a fraction of the time needed for numerical simulations, it can later replace the device simulator. The goal is for the neural network to accurately predict information with any given parameter set that lies within the boundaries defined by the training data simulations. Having a neural network that can replace the device model enables high throughput predictions

that can be compared to the experimental data. By doing so, one can, on the one hand, fit the experimental data for the parameter set that describes the data the best (Figure 7.1f), which would have otherwise been challenging in the high-dimensional space. On the other hand, going beyond this best point is also possible by scanning the entire parameter space and calculating the error of the predicted data at each point compared to the actual experiment (Figure 7.1g). This allows an examination on how the error depends on each material parameter in the parameter landscape. Therefore, creating the framework sketched on the left side of Figure 7.1 of the experimental data and the corresponding neural network enables high throughput analysis. Exemplary approaches to such an analysis are displayed on the right side of Figure 7.1 but the method is not limited to them.

7.2. Preprocessing and Training Data Generation

For the application of the parameter estimation routine presented above, I chose the light-intensity and thickness dependent current-density voltage curves that were measured by Barbara Urbano in the scope of her master thesis[194] and that I already analyzed in the previous chapters of this work. As this data set comprises a high number of JV characteristics, I narrowed it down to four solar cells with active layer thicknesses of 83, 171, 247 and 308 nm to cover characteristic maxima and minima in the thickness-dependence of the performance parameters in Figure 4.2. For the different light intensities, I chose the highest four values for the irradiance, 91, 37, 16 and 6 mW/cm^2, to make sure that they are unaffected by the dark shunt resistance. Thereby, I reduce the large set of original JV curves to a set of 16 in a four-by-four matrix with four values for the irradiance and four active layer thicknesses.

Figure 7.2 shows an example for a data set that is treated in the first parameter estimation run. Here, I attempt to extract information on the material parameters from the light-intensity dependence of the JV curves by fitting them in the same run. Figure 7.2a shows the JV characteristics for a solar cell with an active layer thickness of 83 nm for an irradiance of 91 and 37 mW/cm^2, while Figure 7.2b shows the lower irradiance values of 16 and 6 mW/cm^2. As the JV curves differ significantly in their short-circuit current density J_{sc}, treating them all together on a linear scale would lead to an emphasis on the higher light intensities since every error that is calculated would be dominated by the higher current densities. Instead, I shift the current densities into

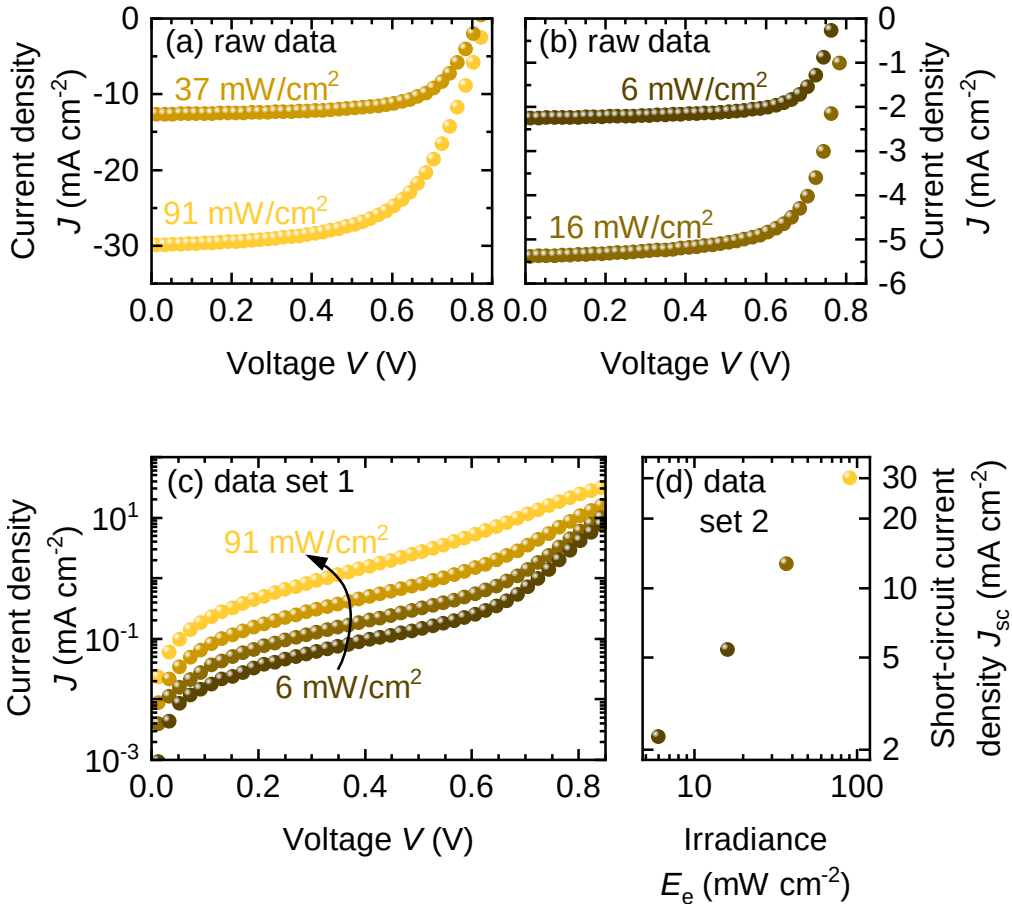

Figure 7.2: Example for an experimental data set for parameter estimation. Four current-density voltage curves of a solar cell with an active layer thickness of 83 nm under an irradiance of approximately (a) 91 and 37 mW/cm² and (b) 16 and 6 mW/cm². (c) *JV* curves shifted into the first quadrant by adding the short-circuit current density. The logarithm emphasizes the photoshunt regime at low voltages that contains information on the recombination. (d) Logarithmic J_{sc} values for a second neural network to enforce a control on the J_{sc}.

the first quadrant by adding the short-circuit current density J_{sc} for each light intensity, enabling the plotting of the *JV* curves on a logarithmic scale as displayed in Figure 7.2c. The shifted *JV* curves resemble the shape of a dark *JV* characteristic with a photoshunt regime that increases with irradiance. Thereby, this way of treating the data emphasizes the recombination losses at lower voltages.[196] Typically, the lower light intensities feature a lower photoshunt plateau as there is less recombination of photogenerated charge carriers. In addition to the emphasis on the recombination losses, this preprocessing brings the advantage of reducing errors caused by a mismatch in J_{sc}. This effect is especially welcome as the optical model has proven to be the most

error-prone in previous iterations of this project. So, the four shifted JV curves are treated together on a logarithmic scale and serve as the first type of data set for parameter estimation. The training data will be processed accordingly and the neural network only trains on the combination of shifted JV curves. However, to not fully discard the J_{sc} and risk a complete mismatch, I extract the values of all four curves and use them on a logarithmic scale as a second type of data set as displayed in Figure 7.2d. This type of data set is later used for a second neural network that serves as a control mechanism for the shifted JV curves.

With the knowledge of what experimental data should be analyzed, in a next step, the number of variable device parameters for the simulations and later fitting has to be reduced. Here, I decided to allow the algorithm to vary the energetics in the device, meaning the injection barriers for the anode and cathode $\phi_{\mathrm{an/cat}}$ and the band gap E_{g} as these parameters are hard to measure and especially the equivalent to an electronic band gap in organic solar cells is not well defined. For recombination, I included direct recombination as well as trap assisted recombination via tail states and a deep defect. As the Fourier-transform photocurrent spectroscopy (FTPS) in Chapter 6.3 has shown, the Urbach energy of the tail states is very low at $E_{\mathrm{U}} = 23\,\mathrm{meV}$. Therefore, I defined recombination via these shallow defects to be not dominant with constant recombination coefficients. Instead, I chose to vary the direct recombination coefficient k_{dir} and the density N_{dt} of defect states in the center of the energy gap to describe the recombination in the system. When defining the polarity of the deep defect states, it is important to consider where they would create a space-charge region. Acceptor-like defects cause a region with a high electric field close to the cathode, whereas donor-like defects evoke a space-charge region near the anode. Since most of the charge carriers are generated close to the transparent anode, space charge in this region promotes charge extraction and causes the thickness dependence of the short-circuit current density to clearly exhibit interference maxima. When the space-charge region is opposite to the illuminated contact, the system is limited by the diffusion through the low-field region and the interference maxima in the J_{sc}-thickness relation are less pronounced.[195] As the second interference maximum is still clearly visible in the experimental data in Figure 4.2, I define the deep defects as donor-like to allow the formation of a space-charge region at the illuminated anode. To include another source of space charge, I also varied the charge carrier mobilities separately. Thereby, seven variable material parameters were selected, which are listed in Table 7.1. All remaining parameters that

Table 7.1: Material parameters chosen as variable parameters with their upper and lower boundaries that are set for the training data generation.

Parameter	Lower Boundary	Upper Boundary
Injection barrier anode ϕ_{an} (eV)	0	0.4
Injection barrier cathode ϕ_{cat} (eV)	0	0.4
Energy gap E_{g} (eV)	1.3	1.43
Electron mobility μ_{n} ($\mathrm{cm^2\,V^{-1}\,s^{-1}}$)	10^{-4}	1
Hole mobility μ_{p} ($\mathrm{cm^2\,V^{-1}\,s^{-1}}$)	10^{-4}	1
Direct recombination coefficient k_{dir} ($\mathrm{cm^3\,s^{-1}}$)	10^{-12}	10^{-6}
Density of deep trap states N_{dt} ($\mathrm{cm^{-3}}$)	10^{14}	10^{17}

were needed in the simulations were kept constant as defined in Chapter 3.4, except for the temperature T that was set to 20 °C for the lab temperature since fitting requires more accuracy here. After deciding on the ranges, in which the material parameters are supposed to be varied (see Table 7.1), training data can be simulated with ASA. For this purpose, I generate a set of parameter combinations as a Sobol sequence, which ensures good coverage of the entire parameter space.[306] For this work, I simulated 210,000 JV curves for each light intensity. Despite the high number of simulations, this data set only equates to five to six points per parameter in this seven-dimensional space. Depending on the number of points simulated in the active layer with ASA, i.e. the active layer thickness here, training data generation can take between 12 and 22 hours. Once the simulation of JV curves is finished, the set of training data is further processed to match the experimental data in Figure 7.2. Therefore, the set of JV characteristics is split into two data sets; one combining the current densities, which are shifted into the first quadrant by the short-circuit current density J_{sc}, on a logarithmic scale and a second data set containing the logarithmic values of J_{sc}.

To test whether the training data represents the experimental data that is supposed to be fitted, it is essential to perform some analysis before proceeding to the training of the neural networks. As statistics on the shape of the full shifted JV curve might not be intuitive, I chose the dynamic range Z of these simulations for comparison. Here, the dynamic range Z was defined as

$$Z(E_{\mathrm{e}}) = \log_{10}\left[\frac{\max(J(V,E_{\mathrm{e}}) + J_{\mathrm{sc}}(E_{\mathrm{e}}))}{\min(J(V,E_{\mathrm{e}}) + J_{\mathrm{sc}}(E_{\mathrm{e}}))}\right]. \tag{7.1}$$

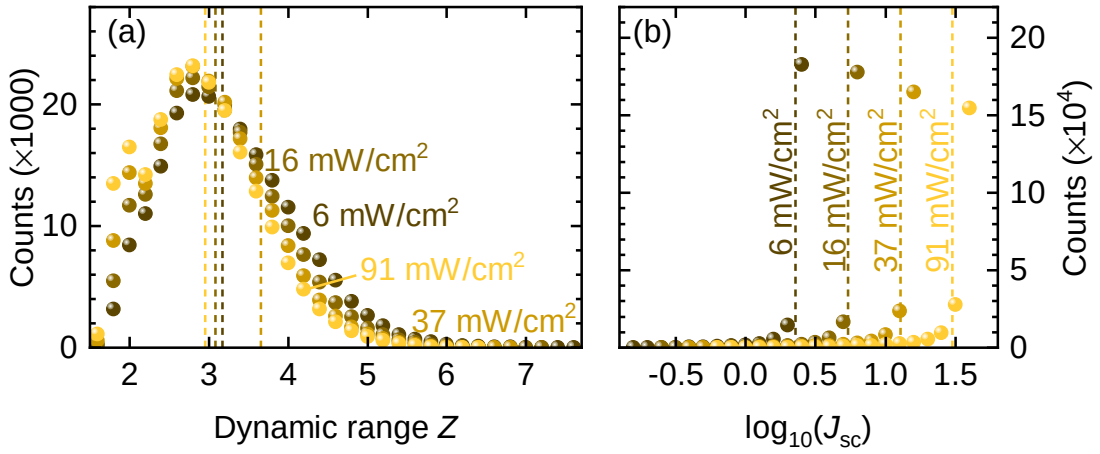

Figure 7.3: Statistics on the training data for (a) the dynamic range Z of the training data and (b) the short-circuit current densities. The vertical dashed lines represent the experimental values to check if they are included in the training data.

Here, $J(V, E_\mathrm{e}) + J_\mathrm{sc}(E_\mathrm{e})$ is the JV curve at a certain irradiance E_e shifted into the first quadrant by its respective short-circuit current density. The difference between the maximum and the minimum value of this shifted JV characteristic on a logarithmic scale then gives the dynamic range Z. So, for a JV curve, where the recombination of photogenerated charge carriers is high, the plateau at low voltages will be high, too. Consequently, the difference in the logarithmic current density at the highest and lowest point will small. In contrast, a JV curve with very little recombination in the low voltage region will feature a high dynamic range. Thereby, the dynamic range Z is an indicator for the shape of the shifted, logarithmic JV characteristics. To be able to compare the simulated data with the experiment, Figure 7.3a shows, how many times a certain dynamic range Z was featured in the training data. This type of histogram is displayed for all four levels of irradiance included in the simulations, 91, 37, 16 and 6 $\mathrm{mW/cm^2}$. For all light intensities in Figure 7.3a, most training data exhibits a dynamic range slightly below three orders of magnitude. However, the distribution is shifted further to higher orders of magnitude for the lower values of irradiance and the highest light intensity features a relatively high number of curves with a very low dynamic range. The dashed lines indicate the dynamic ranges of the experimental data. Figure 7.3a therefore visualizes that for each light intensity, there are at least 12,000 simulations with a dynamic range similar to experiment. The same procedure can be applied to the second type of data set, the short-circuit current density J_sc. Here, no additional measure for comparison is needed as the data set contains only one value per

simulation run and light intensity. For the J_{sc} values, the highest amount of data points is located in the region, where J_{sc} is close to the maximum photogenerated current density, the generation-current density J_{gen}. The dashed lines for the experimental data lie below this value but still have several thousands of simulations that feature a similar short-circuit current density J_{sc}. Thereby, I confirmed that the training data sets for both neural networks contain the values that are required by the experimental data. If they were not included in the data set, revisiting the stage of selecting the parameters and their ranges would be required. In the case displayed in Figure 7.3, the simulated data sets at hand can be used for the actual training step.

7.3. Neural Network Training

For the neural network training, I first split the data sets into 10% that are held back for later verification and 90%, which are now used for neural network training. Here I use convolutional neural networks as proposed in Reference [293] and [294]. Convolutional neural networks are inspired by the visual nervous system[307] and are frequently used for image recognition due to their low computational costs.[308] Their ability to identify relevant features in 2D images can also be applied to a one-dimensional series of data,[308] such as the current density values in this work. I trained such neural networks that accurately reproduce simulated data sets with the hyper parameters that are listed in Table A.4. The resulting errors and time used for training of the neural networks trained for this work are summarized in Table A.5. An example is shown in Figure 7.4a and 7.4b, which display shifted JV curves and short-circuit current densities of a simulation that was part of the 10% held back prior to the neural network training. Therefore, the neural networks have not been in contact with this combination of material parameters. Nevertheless, the dashed lines that show the prediction of the neural networks for the parameter set coincide well with the simulated data. Therefore, even though the neural networks were trained with only around five points per dimension, they are still able to interpolate in between and predict the right data. Hence, the neural networks are able to replace the drift-diffusion simulator as a surrogate model for the later steps in the parameter estimation routine. Still, care has to be taken in their usage, since they are only functional within the boundaries that they have been trained in. So, they cannot handle parameter variations beyond their input parameters and will give wrong results when given input parameters outside of

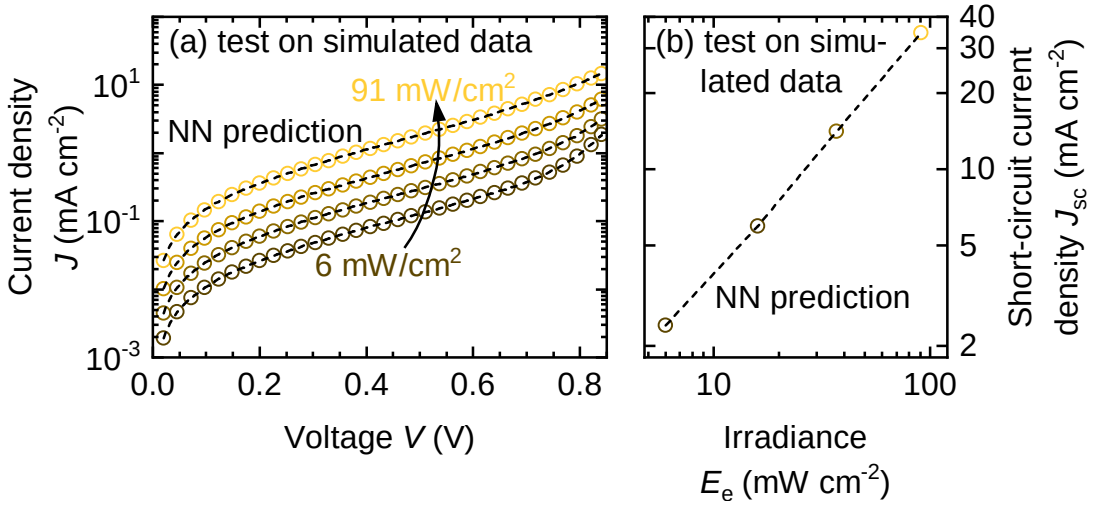

Figure 7.4: Output of the trained neural networks (NN, dashed black lines) and the drift-diffusion simulator (open symbols) for the same randomly selected parameter set that was not used during the neural network training. Both the neural network (a) for the shifted JV curves and (b) the one for the J_{sc} give good predictions.

the boundaries. Also, varying any parameter that was assumed as fix in the training data set cannot be replicated by the neural networks. Therefore, they act as a highly simplified model which empowers high-throughput data analysis.

7.4. Test on Synthetic Data

With the neural networks at hand that can replace ASA for more computation-heavy fitting procedures, I can proceed to compare the predictions of the neural networks to the experimental data to find the parameter combination that best describes the system. Here, the separate data sets are used, to first calculate the root-mean-square error of the predicted shifted JV curves that is then multiplied by a penalty depending on the root-mean-square error of the short-circuit current density J_{sc} predictions. The penalty is designed as a hyperbolic tangent function to allow a certain tolerance for the J_{sc} before applying the penalty (see Figure A.7). This tolerance is customized to the parameter estimation run. Thereby, inaccuracies of the optical model are less detrimental to the fitting procedure. With the definition of the error, the parameter estimation can be executed. For the purpose of fitting the experimental data, Basita Das proposes in her thesis[294] to apply a covariance matrix adaptation evolution strategy (CMA-ES) algorithm,[309] which I also use in this work. It is a relatively fast algorithm

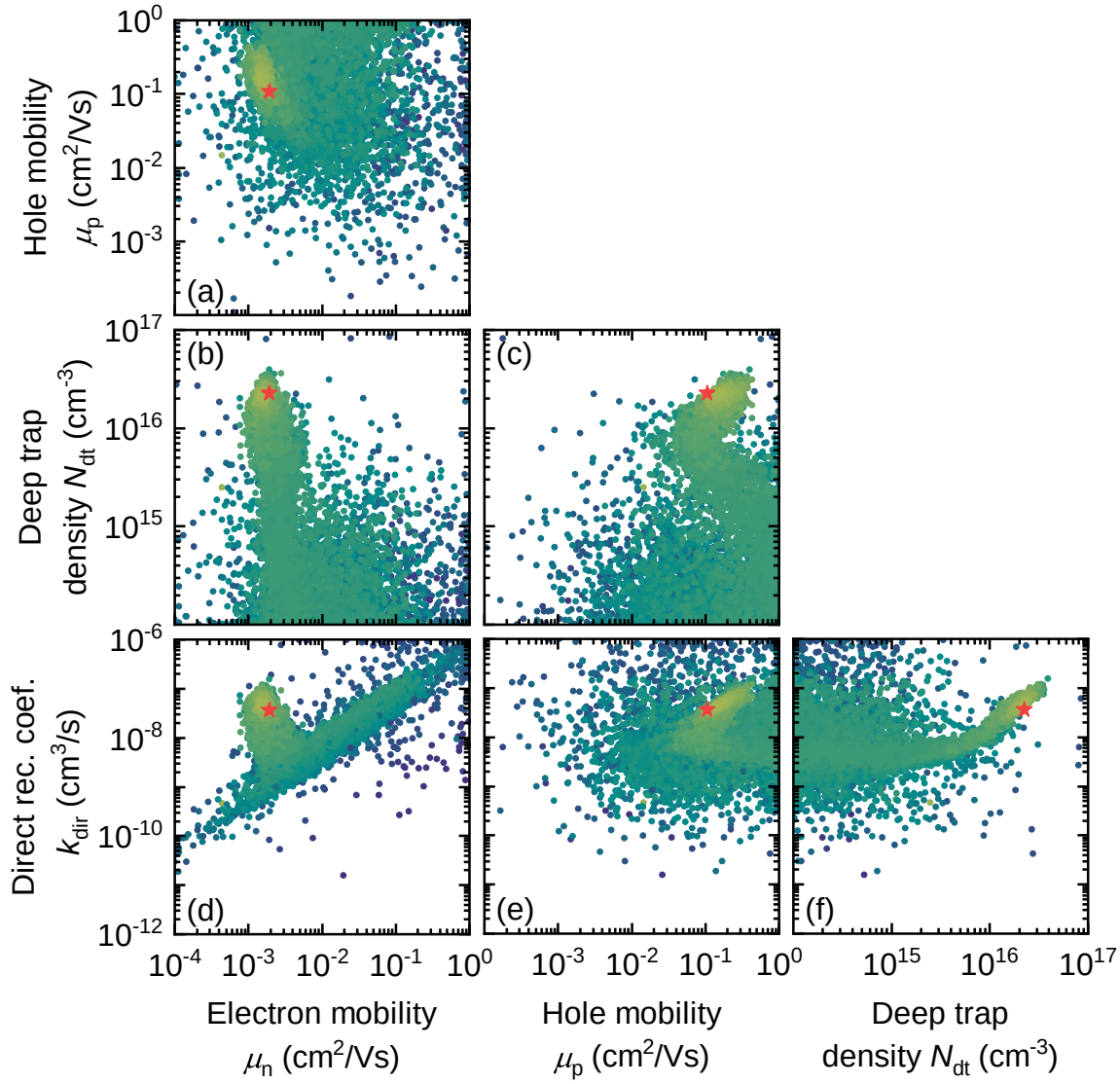

Figure 7.5: Visualization of the fitting algorithm on a synthetic data set where the actual material parameters (red stars) are known. The electron mobility μ_n, hole mobility μ_p, defect density N_{dt} and direct recombination coefficient k_{dir} were selected for visualization. Each point represents one test of the optimization algorithm in the 7-dimensional space that contains the two parameters corresponding to the axes. The error decreases from the violet to the light green points. It is visible that the algorithm tests few parameter combinations with a bad error in the entire space before moving on a path towards the optimum.

that is found to work well on high-dimensional problems and with interdependent variables.[310]

Figure 7.5 visualizes the fitting procedure of the optimization algorithm. For this purpose, I fitted a simulated data set to be able to compare the fitting results with

the actual input parameters. In Figure 7.5, I plot a subset of the seven material parameters that were variable in this run and focus on the transport and recombination parameters, namely the electron mobility μ_n, hole mobility μ_p, defect density N_dt and direct recombination coefficient k_dir. Figure 7.5 displays a point for each calculation performed by the optimization algorithm. So, for example, Figure 7.5a contains a point for each combination of electron and hole mobility that was tried independent of the other dimensions. The color code indicates a decreasing error going from purple to light green. It is visible that few points are distributed over the entire space with a higher concentration closer to the actual parameter marked by the red star. At some point a path along a valley in the error can be observed leading to the absolute minimum. Therefore, despite the high dimensionality of the problem, the optimization algorithm appears to find the minimum close to the actual parameter set underlying the fitted data. However, to make sure that the global minimum is not missed due to little probing in some areas of the parameter space (as in the example of Figure A.8), the algorithm is restarted several times from different starting points. One of these runs of the algorithm can require between 30,000 and 70,000 calculations. For the numerical solver ASA, one run of the fitting alone would take up to eight hours. In contrast, the fast output by the neural network allows fitting within a few minutes. Hence, the neural network is already crucial for a fast fitting procedure.

Such a fast computation also allows the exploration of certain areas in the parameter space. One point of interest is the parameter combination that was identified as the best fit to the data by the optimization algorithm. Figure 7.6a slices through the parameter space at the point of the best fit for the transport and recombination parameters and shows the inverse error for each point. For the line plots on the diagonal, all parameters are held at their best value except the one on the x-axis. The contour plots are the equivalent in two dimensions, where all parameters are kept at their optimum except the ones on the axis. These plots illustrate, how sharp the maximum is in the parameter space. All parameters have very localized maxima, leading to a particularly small feature in their shared contour plot. For the deep defect density N_dt and the direct recombination coefficient k_dir, the values determined by the optimization algorithm coincide well with the actual values that were set in the simulations that were fitted. The charge-carrier mobilities μ_n and μ_p, while still giving good fitting results, show some discrepancy between the optimization result and the actual values. The largest difference can be found in the electron mobility, which also has the widest distribution

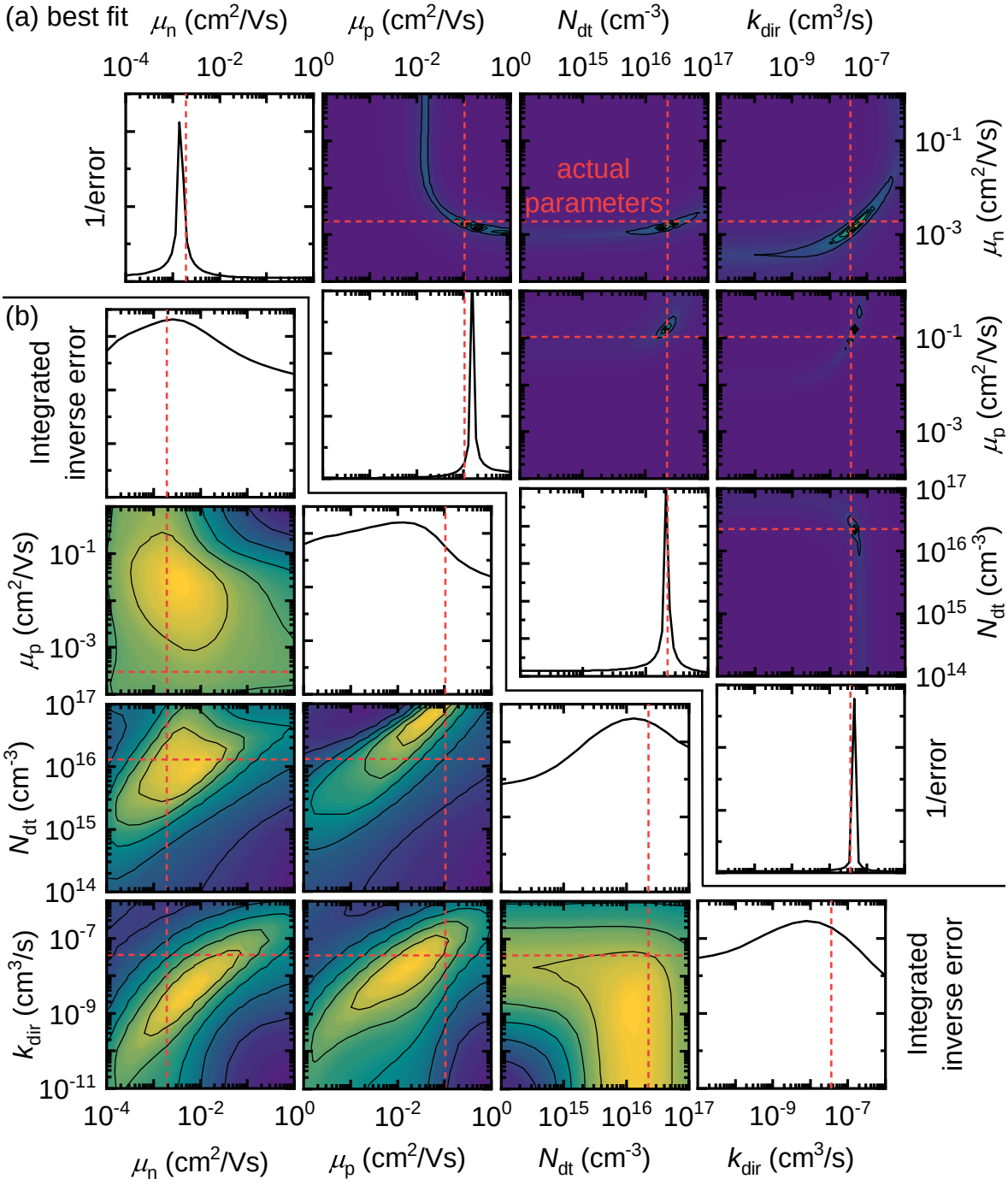

Figure 7.6: (a) Corner plot of the inverse error around the best fit of a synthetic data set where the actual device parameters are known. The line plots on the diagonal represent a one-dimensional slice through the 7-dimensional parameter space at the point of the best fit, while the contour plots show a two-dimensional slice. The red dashed lines indicate the actual material parameters used to create the synthetic data. While the algorithm finds some of the actual parameters, it has some inaccuracy in others. (b) Corner plot of the inverse error integrated up in every dimension except the one displayed on the axis. The maxima do not coincide with the best fit but show more relations between parameters.

of its inverse error in the line and contour plots. This observation could be an indicator that this parameter is less dominant in the solar cell that was simulated. So, a small change in the parameter that the algorithm made for testing might not have caused enough change in the data to cause a detectable difference in the error. For example, the accuracy of the neural network poses a limitation on the process because a step in the electron mobility μ_n could invoke a deviation that is below the neural network's resolution. Therefore, testing the procedure of parameter estimation on a set of synthetic data can give indications on the limitation of the neural networks and the optimization algorithm.

An issue with these high-dimensional problems is the inability to visualize the full parameter space. An attempt to include the entire space is to integrate the inverse error over all dimensions except the ones that are plotted, which is shown in Figure 7.6b. Here, the contour plots show the inverse error that resulted from the integration over five dimensions. For the line plots, an additional integration step was performed, which means they are a result of the contour plots beneath them that were integrated over their y-axis. The maxima of these integrated plots are located further away from the actual parameters of the simulations that are indicated with the red dashed lines than the fit in Figure 7.6a. Especially the maximum for the hole mobility μ_p is significantly below its actual value. The cause of this difference to the best fit can be best explained by the comparison of the contour plot featuring the deep defect density N_dt and the direct recombination coefficient k_dir with the line plot of k_dir in the lower right corner of Figure 7.6b. In the line plot, the direct recombination coefficient shows a clear maximum around $10^{-8}\,\mathrm{cm}^3/\mathrm{s}$, while in the contour plot, there is no visible difference in the integrated inverse error for several orders of magnitude. At these low values of k_dir, trap assisted recombination is dominant and therefore k_dir can be chosen arbitrarily. At a direct recombination coefficient of around $10^{-8}\,\mathrm{cm}^3/\mathrm{s}$, however, direct recombination starts to dominate, creating a large area with medium high inverse error. When integrating the contour plot over the trap density N_dt to create the line plot for k_dir, the sum over all these integrated inverse errors that are high but not a maximum will dominate over the actual maxima in the contour plot at lower direct recombination coefficients. Therefore, the integration can yield areas of maximum integrated inverse error that suggest a good fit but might actually stem from integration over large volumes of medium high inverse error. Still, the integration in Figure 7.6b enables us to see more trends in the errors as the landscape is less steep

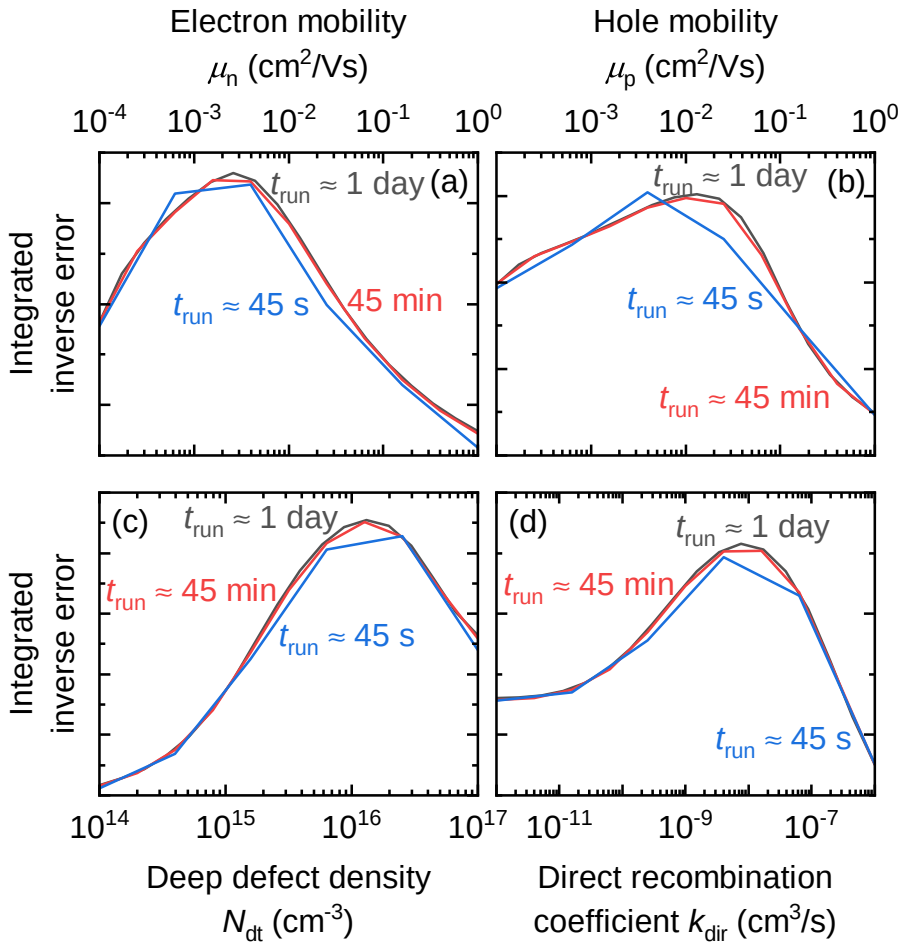

Figure 7.7: Inverse error integrated over six dimensions except the (a) electron mobility μ_n, (b) hole mobility μ_p, (c) deep defect density N_{dt} and (d) direct recombination coefficient k_{dir}. Three grid search runs are displayed with 6, 11 and 18 points per axis. Especially between 11 and 18 points, there is barely a difference in accuracy but a massive difference in runtime t_{run}.

than in the slices in Figure 7.6a. Of course, these integrated inverse error plots have to be interpreted with care for the reason explained above, but still the rough trends in the relation between some of the parameters seem to match between the Figure 7.6a and 7.6b. For example, in the contour plots of the electron and hole mobility both feature an L-shape, the direct recombination coefficient k_{dir} increases with electron mobility μ_n and the contour plots of the trap density N_{dt} and the direct recombination coefficient k_{dir} create a vertical feature for low values of k_{dir}. Therefore, the integrated error can give an overview over the entire parameter space.

To create these integrated plots, calculations have to be performed in all dimensions on a grid with a certain number of points per axis. Due to the high number of

dimensions, the computational effort strongly scales with the number of points. So, just calculating the error for three points per dimension, for example the highest and lowest electron mobility and one in the middle, would require 2187 calculations. But just doubling points to six per dimension will already result in 128 times more error calculations and therefore take much more time. To illustrate this issue and investigate the number of points needed per dimension, Figure 7.7 shows the integrated inverse error for (a) the electron mobility μ_n, (b) the hole mobility μ_p, (c) the deep defect density N_dt and (d) the direct recombination coefficient k_dir for different numbers of points per dimension and the corresponding runtime t_run. All lines follow the same trends, but for the blue line with only six points, there are some deviations to the integrated inverse error from calculation with more points per dimension, especially in Figure 7.7b. However, taken into account the short runtime of these calculations, they could still be used if a fast estimate was needed. Especially using simple interpolation tools as displayed in Figure A.9 can even improve the accuracy of runs with few points per axis. Especially between the line that contains 11 points per dimension and the one with 18 points, there is barely a difference. In contrast to the small improvement in accuracy, the runtime scales drastically, causing these calculations to take an entire day instead of less than an hour. Therefore, treating these problems with multiple dimensions requires careful considerations of the accuracy needed in calculations versus the time consumption.

7.5. Parameter Estimation for a Thin Organic Solar Cell

After having tested the procedure on synthetic, simulated data where the actual material parameters were known, I now proceed to the analysis of actual experimental data sets. Here, I start by analyzing the light-intensity dependent measurements on a thin cell as presented in Figure 7.2 in detail. For this purpose, Figure 7.8 shows the same combination of plots as Figure 7.6 now for the inverse error of the neural network prediction compared to the actual experimental data. The one-dimensional slices on the diagonal in Figure 7.8a illustrate that all parameters except the electron mobility μ_n ran into the upper boundary during optimization, implying that the correct combination of the material parameters was not contained in the parameter space. It

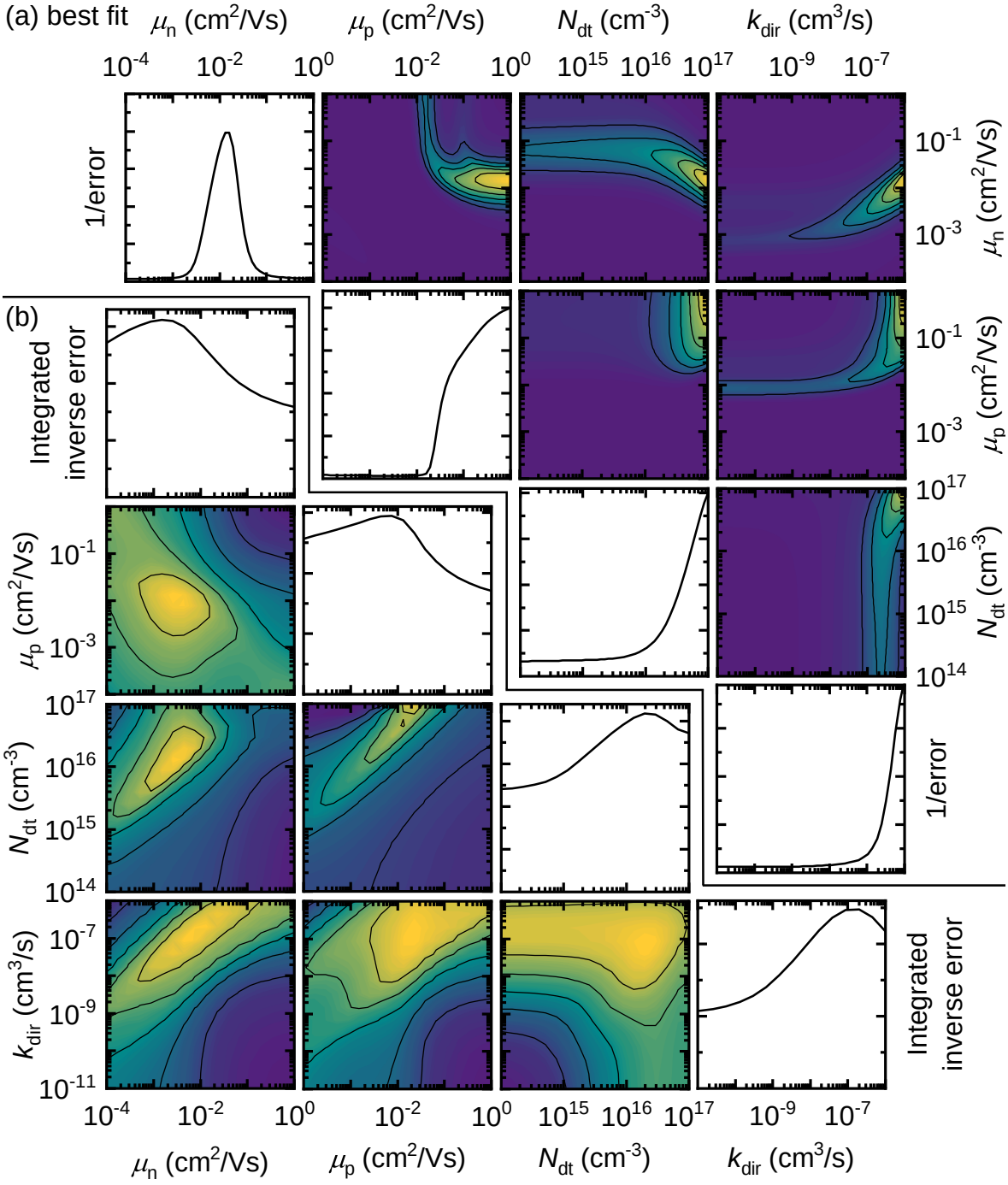

Figure 7.8: Corner plots displaying the inverse error between the experimental data and the predictions by the neural network (a) as slices through the dimensions around the best fit and (b) integrated up over all dimensions except the ones displayed on the axes. While the fit seems to run into the boundaries for the hole mobility μ_p, deep defect density N_dt and direct recombination coefficient k_dir, the integrated plots show maxima within the boundaries and imply correlations in the contour plots.

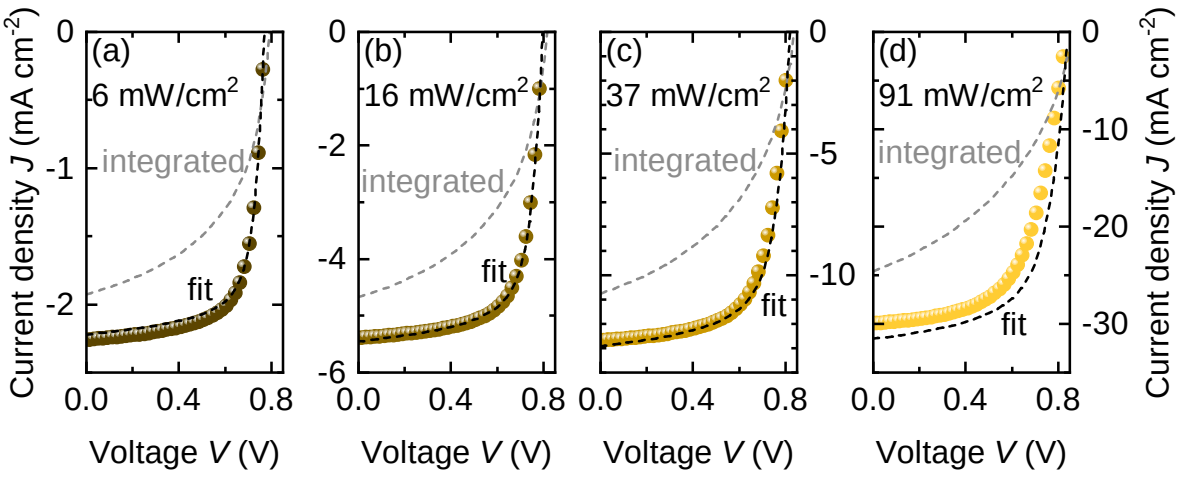

Figure 7.9: JV characteristics for an irradiance of (a) 6 mW/cm^2, (b) 16 mW/cm^2, (c) 37 mW/cm^2 and (d) 91 mW/cm^2. The parameters determined by the optimization algorithm produce a JV curve that matches the experiment relatively well, whereas the parameters with the highest integrated inverse error do not yield similar results. Therefore, the integrated corner plots should not be mistaken for giving accurate parameter sets.

is also notable that the features are less sharp than for the synthetic data, also in the contour plots, leading to larger areas of similarly high inverse error. So, for example, at an electron mobility μ_n of 4×10^{-2}cm^2/(Vs), the deep trap density N_dt can vary several orders of magnitude without significantly changing the inverse error. The integrated inverse error in Figure 7.8b shows a less steep error landscape in the contour plots compared to the slices in Figure 7.8a, similar to the case for the synthetic data discussed previously. Also, it features correlations between the electron mobility μ_n and the recombination parameters and the hole mobility μ_p with the trap density N_dt. For the one-dimensional plots on the diagonal, all parameters exhibit a maximum integrated inverse error, even though the distribution is relatively shallow. However, as discussed on the example of synthetic data, these parameters should not be mistaken for an actual parameter set.

This difference between the parameters set with the highest multi-dimensional inverse error, the best fit, and the maxima of the integrated inverse errors is further illustrated in Figure 7.9. It shows the experimental JV curves under the irradiance of (a) 6 mW/cm^2, (b) 16 mW/cm^2, (c) 37 mW/cm^2 and (d) 91 mW/cm^2 together with their respective fits in the black, dashed lines. For the lower light intensities, the fits match the experimental data well, while the short-circuit current density J_sc and the fill factor FF are too high for the highest irradiance in Figure 7.9d. The simulations

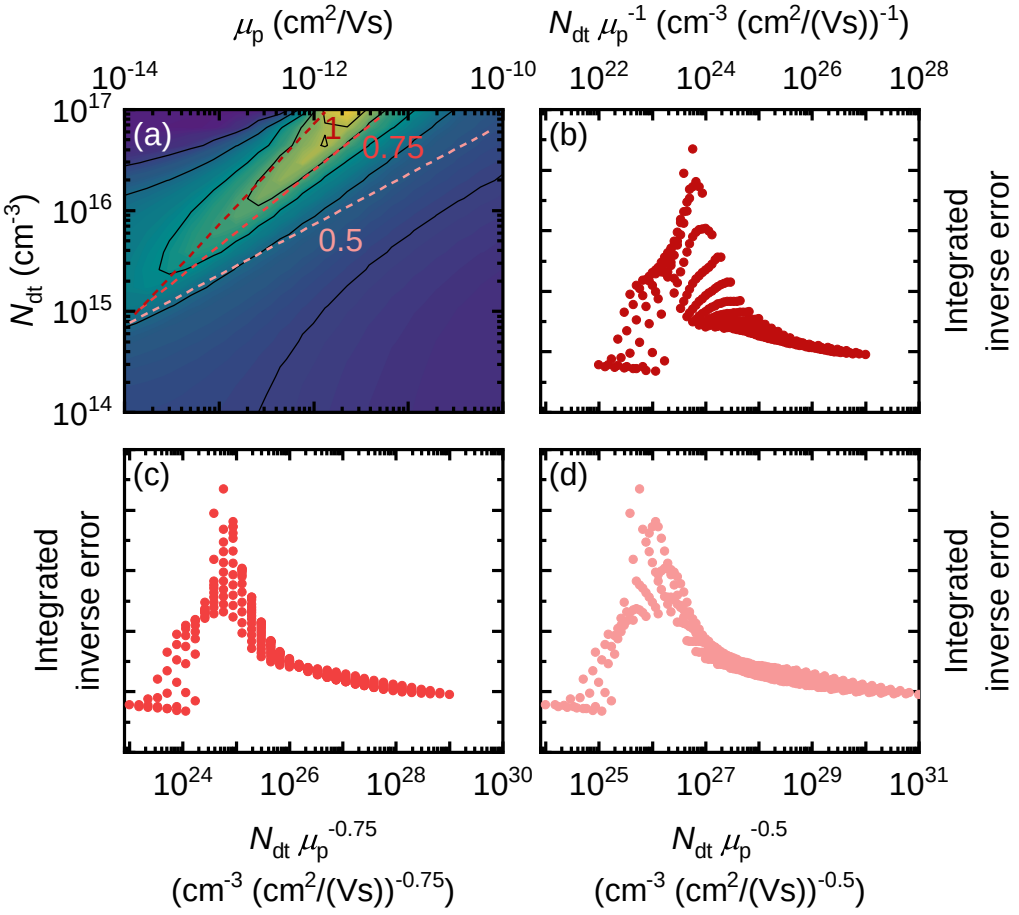

Figure 7.10: (a) Contour plot of the integrated inverse error for the deep defect density N_{dt} and the hole mobility μ_{p}, which show strong correlation. The dashed lines indicate a double-logarithmic slope of 0.5, 0.75 and 1. If the parameters were to show the same correlation throughout the hole contour plot, plotting their product with the respective exponent versus the integrated inverse error would cause all points to lay on one line with a sharp maximum. Product of the defect density and the hole mobility for an exponent of (b) -1, (c) -0.75 and (d) -0.5. For none of the exponents, the points lay exactly on one line but the relation seems to be closest for $N_{\mathrm{dt}}\mu_{\mathrm{p}}^{-0.75}$.

of the JV characteristics with the parameters that yielded the highest integrated inverse error do not replicate the experimental data at all, though. Both J_{sc} and FF are too low, illustrating that the results from integration should not be confused with fitting results.

Instead, the parameter landscape that is retrieved from the integration of the inverse error can give an indication on which parameter combinations are relevant for the error. So, for example, the one-dimensional plots of the integrated inverse error of the hole mobility μ_{p} and the deep defect density N_{dt} are relatively flat, but their shared contour

plot shows some sort of ridge, meaning the integrated inverse error depends on a relation between μ_p and N_dt. Figure 7.10 investigates this relation in more detail. Figure 7.10a once again shows the inverse integrated error as a function of hole mobility μ_p and deep defect density N_dt with dashed lines as indicators for possible relations. So, for the red line $N_\mathrm{dt} \propto \mu_\mathrm{p}$, whereas for the other lines, there is a sublinear relationship between the two parameters with $N_\mathrm{dt} \propto \mu_\mathrm{p}^{0.75}$ and $N_\mathrm{dt} \propto \mu_\mathrm{p}^{0.5}$. Rearranging these relations implies that the integrated inverse error can be a function of either $N_\mathrm{dt}\mu_\mathrm{p}^{-1}$, $N_\mathrm{dt}\mu_\mathrm{p}^{-0.75}$ or $N_\mathrm{dt}\mu_\mathrm{p}^{-0.5}$, which is shown in Figure 7.10b, 7.10c and 7.10d. If the two material parameters were directly related forming a straight rim in Figure 7.10a, the correct relation would yield all points laying on top of each other. As this is not the case for this data set, none of the relations fits perfectly but overall, the points in Figure 7.10c lie closest to each other, which means that parameter combinations with the same $N_\mathrm{dt}\mu_\mathrm{p}^{-0.75}$ product will give similar values in the integrated inverse error and are therefore less likely to add to the information gain on these material parameters. Hence, finding relations like this can help identifying the need for further experiments that feature opposite relations. So, in the example of the hole mobility μ_p and the deep defect density N_dt, combining these light-intensity dependent measurements with a measurement that gives $N_\mathrm{dt} \propto \mu_\mathrm{p}^{-4/3}$ for the integrated error could maximize the knowledge on these parameters.

7.6. Analysis of Different Experimental Data Sets

So far, I have only discussed one parameter estimation run on a set of JV curves measured on a thin device with different levels of irradiance. This analysis has revealed, how further experiments are needed to narrow down information on the material system. As introduced in Chapter 7.2, I have selected JV characteristics for four different light intensities and active layer thicknesses for the parameter estimation. Consequently, I have performed three more runs. First, I performed another light-intensity dependent study on a thick solar cell. In addition, I analyzed the data for all four active layer thicknesses once under the lowest irradiance $E_\mathrm{e} = 6\,\mathrm{mW/cm^2}$ and once at the highest one with $E_\mathrm{e} = 91\,\mathrm{mW/cm^2}$. The four parameter estimation runs are summarized in Table A.6 for clarity. The runs were executed in the same way, only the short-circuit current density was treated on a logarithmic scale for the light-intensity dependent runs and on a linear scale when the irradiance was kept constant. Accord-

ingly, the penalty factor for the J_{sc} was modified for each run. The corner plot results are shown in Figure A.10, A.11 and A.12 for the run with a thick device, the one under dim illumination conditions and the run for bright illumination conditions. While the plots differ in their maxima and the sharpness of the landscape, the trends of the parameters remain similar in the integrated plots. Thus, the different runs are not very complementary in terms of narrowing down specific parameters. When comparing the different fit parameters in Table 7.2, some trends become more obvious. On the one hand, the optimizer seems to favor high space charge, since the electron and hole mobility are mostly chosen asymmetrically and the deep defect density is always high. On the other hand, both mobility and recombination parameters are predicted to be at very high values compared to what is usually expected for organic solar cells. However, it is not obvious, which effect causes this trend, since one parameter that is set really high will cause the others to follow to maintain the right fill factor and ratio between direct and Shockley-Read-Hall recombination. So, to better compare the results of the different runs, Figure 7.11 tests the applicability of the fits from different experiments to the entire data set. The power-conversion efficiency of the solar cells is plotted against their active layer thickness d for an irradiance of (a) $6\,\mathrm{mW/cm^2}$, (b) $16\,\mathrm{mW/cm^2}$, (c) $37\,\mathrm{mW/cm^2}$ and (d) $91\,\mathrm{mW/cm^2}$, with the measurements, which were

Table 7.2: Set of parameters that yield the best fit for four light-intensity dependent JV curves measured on a *thin* cell or on a *thick* device, or JV curves for four active layer thicknesses under *dim* or *bright* illumination conditions.

Parameter	thin	thick	dim	bright
Injection barrier anode ϕ_{an} (eV)	0	0.4	0	0
Injection barrier cathode ϕ_{cat} (eV)	0.27	0.4	0.15	0
Energy gap E_g (eV)	1.41	1.34	1.4	1.43
Electron mobility μ_n ($\mathrm{cm^2\,V^{-1}\,s^{-1}}$)	1.46×10^{-2}	0.98	4.12×10^{-3}	1.9×10^{-2}
Hole mobility μ_p ($\mathrm{cm^2\,V^{-1}\,s^{-1}}$)	1	0.41	0.18	0.2
Density of states deep traps N_{dt} ($\mathrm{cm^{-3}}$)	10^{17}	8.46×10^{16}	10^{17}	2.81×10^{16}
Direct recombination coefficient k_{dir} ($\mathrm{cm^3\,s^{-1}}$)	10^{-6}	1.41×10^{-7}	3.35×10^{-8}	10^{-6}

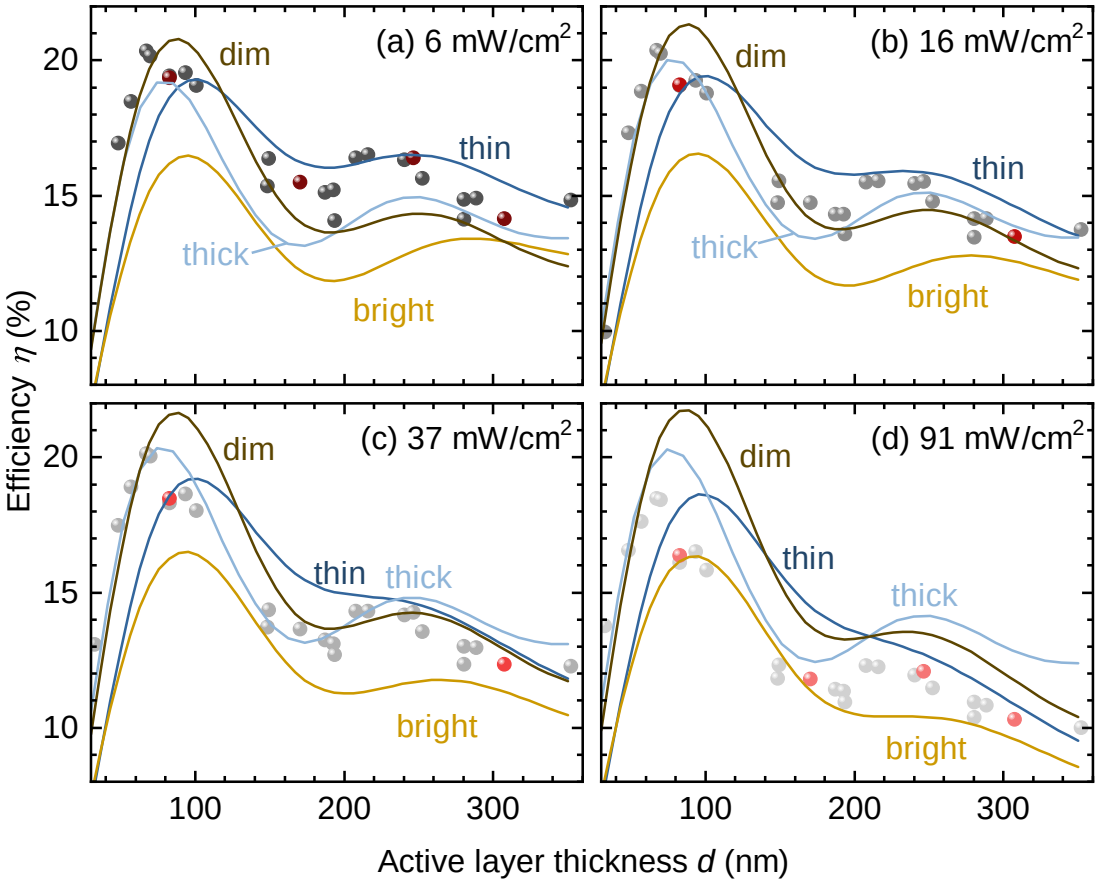

Figure 7.11: Power conversion efficiency η as a function of active layer thickness d for an irradiance of (a) $6\,\mathrm{mW/cm^2}$, (b) $16\,\mathrm{mW/cm^2}$, (c) $37\,\mathrm{mW/cm^2}$ and (d) $91\,\mathrm{mW/cm^2}$. The points represent the experimental data with the ones that were subject to the parameter estimation highlighted in red. The lines correspond to the best parameter combinations that resulted from different parameter estimation runs. More specifically using four different thicknesses under dim or bright illumination and four levels of irradiance for a thin and a thick cell. None of the parameter sets fit the experimental data over the entire range with the run on the thick cell giving the best results, yet.

subject to the parameter estimation, marked in red. Even though all four attempts of parameter estimation were performed on the same material system, they yield significantly different results, often only matching the points that they were confronted with. So, for the run, where experimental data for four different active layer thicknesses was used at the brightest illumination conditions, the predicted efficiency η for the lower light intensities in Figure 7.11a, 7.11b and 7.11c lies significantly below the experimental values. Only in Figure 7.11d, it matches at least the values marked in red, which were subject to fitting, relatively well. Similarly, the parameter estimation run that used different active layer thicknesses under dim lighting gives a decent prediction at

a low irradiance but overestimates the efficiency η at the highest irradiance in Figure 7.11d. Hence, the parameter combinations that were extracted without the knowledge of the light-intensity dependence of the system fail to reproduce it. The same phenomenon can be observed for the series, where multiple values for the irradiance were used but only on a thin cell. Here, the simulated power-conversion efficiency always matches the experimental one for this specific cell but cannot reproduce the thickness-dependence of the system. Of all four parameter estimation runs, the one matching the entire experimental data set the best is the one that used four light intensities for a thick active layer. Only the values at higher thickness and irradiance, especially in Figure 7.11d, are not covered by the simulated curves. Hence, none of the parameter estimation runs yielded a set of material parameters that can describe the entire system. Instead, they can help understanding the shortcomings of these attempts and guide towards a more successful application in future works.

7.7. Outlook

One observation from the comparison of the different parameter estimation runs was that the resulting parameter sets are not able to reproduce light-intensity or thickness dependence that was not included in the respective experimental data. Therefore, one approach to describing the entire data set would simply be to combine the errors and thereby include data at different light intensities and active layer thicknesses. The parameters that result from such a fit are used to once again simulate the thickness-dependent power-conversion efficiency η, which is shown in Figure 7.12 for an irradiance of (a) $6\,\mathrm{mW/cm^2}$, (b) $16\,\mathrm{mW/cm^2}$, (c) $37\,\mathrm{mW/cm^2}$ and (d) $91\,\mathrm{mW/cm^2}$. Instead of matching all the experimental data, it does not reproduce any of it very well. These results further imply that the material parameters that were chosen herein are not sufficient to describe the problem. So, in a next step, I tried to investigate possible shortcomings of the parameter choice. For this purpose, I varied the parameter set that worked best from the runs so far, which is the light-intensity dependent fit of a thick device, systematically to improve the fit to the entire experimental data set in Figure 7.12. As it appeared like the light-intensity dependence of the original fit is not sufficient, especially at high thicknesses, the direct recombination needs to be increased with respect to the trap-assisted recombination. However, the high-level of space charge is relevant for the quality of the fit. Therefore, the assumption that the

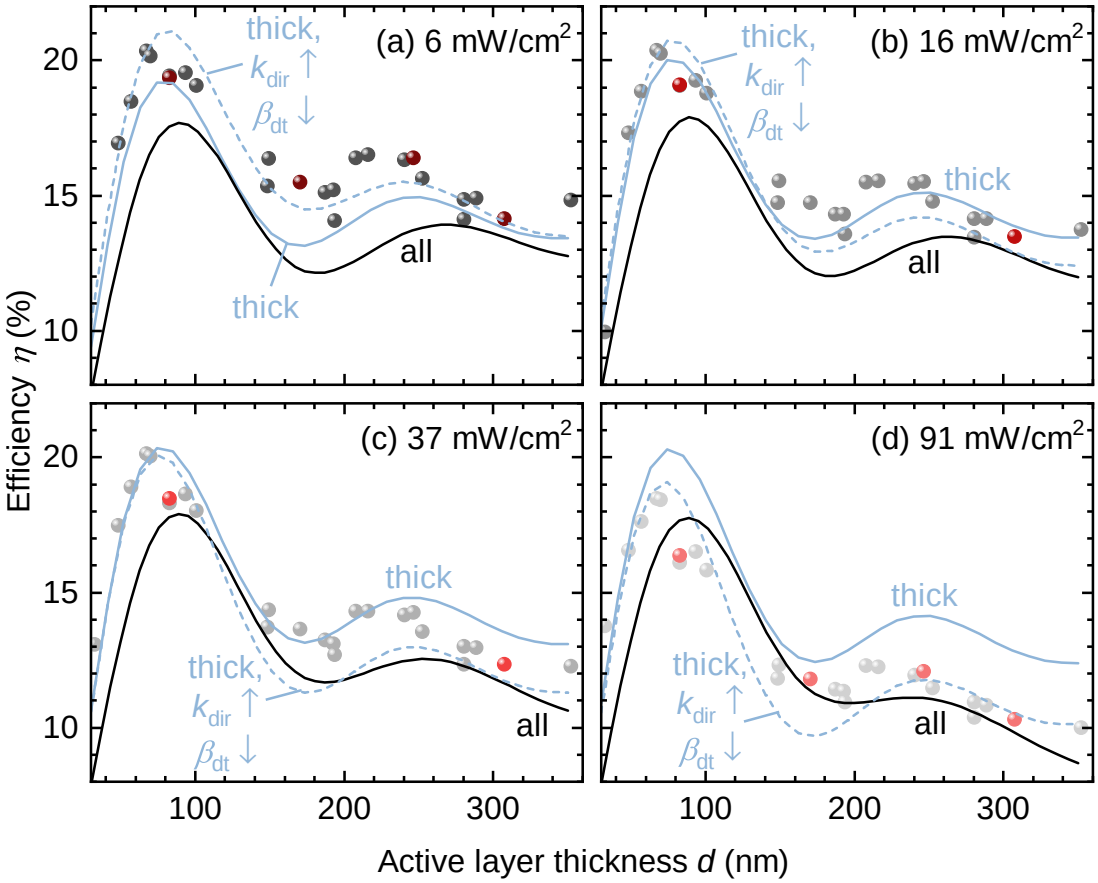

Figure 7.12: Attempts to better fit the experimental data points of the thickness-dependent power-conversion efficiency η for illumination with an irradiance of (a) $6\,\mathrm{mW/cm^2}$, (b) $16\,\mathrm{mW/cm^2}$, (c) $37\,\mathrm{mW/cm^2}$ and (d) $91\,\mathrm{mW/cm^2}$. The black lines show a parameter combination that results from fitting all the data that was previously treated separately at once, which does not yield good results. Manipulating the best of the previous results by increasing direct recombination and lowering trap-assisted recombination while maintaining the space charge improves the fit and hints towards improvements in the parameter choice.

rate of trap-assisted recombination is only changed by the defect density N_{dt} and not the recombination coefficient β_{dt} might be incorrect. By reducing the number of fitting parameters for trap-assisted recombination, the Shockley-Read-Hall recombination rate is thereby directly coupled with the amount of space charge in the system. So, Figure 7.12 shows a simulation in the dashed lines with the combination of material parameters that was extracted from parameter estimation with an increased direct recombination coefficient $k_{\mathrm{dir}} = 10^{-6}\mathrm{cm}^3/\mathrm{s}$ and a corresponding decrease in the deep defect recombination coefficient $\beta_{\mathrm{dt}} = 10^{-11}\mathrm{cm}^3/\mathrm{s}$. Indeed, the dashed line seems to fit the experimental data points better than any of the previous parameter combinations. Hence, including

the recombination coefficient of the defects and thereby decoupling space charge and trap-assisted recombination could be the key towards successful parameter estimation on this data set in future works. Thus, in the picture of the workflow in Figure 7.1, we have to close the cycle and return to the step of the parameter selection in Figure 7.1c.

Therefore, in this chapter, I have introduced machine-learning assisted parameter estimation and exploration of the parameter space to organic photovoltaics. On a set of JV curves under different light intensities, I have established a routine for generating training data and training a neural network and I have applied it to other combinations of JV curves with varying thickness and illumination conditions. By investigating the parameter space in slices around the parameter set that best fits the experimental data and by integration of a grid in all dimensions, I have proposed approaches to plot and interpret such high-dimensional parameter spaces. Identifying possible hurdles in the process and ultimately the potential limit for this specific experimental data set, has set the stage for successful parameter estimation on this system but also other experimental data in the future. The fact that all calculations needed for one run of parameter estimation take less than two days on conventional laptop further underlines the applicability and potential of machine learning tools in the material characterization of solar cells.

8 Conclusions

The rapid development of novel organic solar cell systems with new materials synthesized, donor-acceptor combination tested and different contact layers implemented demands for simple characterization techniques to compare solar cells and find ways to improve them. However, some of the methods most frequently used in literature so far have lacked a theoretical framework for the analysis. In this work, I provided guidance to analyzing recombination and transport in organic solar cells on the example of the devices based on PBDB-TF-T1:BTP-4F-12. Studying some of the most frequently used characterization techniques in the field of organic photovoltaics, light-intensity dependent measurements of the short-circuit current density and quantification of the energetic disorder, I revealed that some of the models underlying the traditional interpretation of these measurements need to be treated with care as they neglect any spatial dependence inside the solar cell. Instead, I highlighted what can be learned from the light-intensity dependence of the short-circuit current density and gave recommendations on how to measure energetic disorder in organic solar cells. Due to the complexity of the interpretation of these measurements and the need for further measurements to fully characterize a device, I proposed an alternative method to increase knowledge on transport and recombination in organic solar cells by establishing a routine of estimating material parameters with the help of machine learning. Thereby, this thesis did not only provide deeper understanding of basic characterization techniques that have partly been established for decades but also helped moving device characterization into the twenty-first century.

To first set the ground, I used measurements on PBDB-TF-T1:BTP-4F-12 based solar cells to give an example of how new organic solar cell systems are typically char-

acterized when they are reported in literature. Therein, I also introduced the rationale that the traditional interpretation of the light-intensity dependence of the short-circuit current density J_{sc} is based on, which claims that only direct recombination can cause nonlinearity. Here, I highlighted that all quantities like the charge-carrier densities, recombination and generation rates are assumed constant throughout the entire active layer. As this assumption can be problematic, I first summarized models that go beyond the traditional rationale introducing space charge by doping or asymmetric mobilities and extended them with space-charge effects caused by charge trapped in tail states. With the help of drift-diffusion simulations, I showed that tail-state recombination actually features more nonlinearity in the J_{sc} with illumination than direct recombination due to light-intensity dependent trap filling. Looking at the case of a simulated, thick solar cell illustrated that in the case of space-charge effects, direct recombination features the least nonlinearity out of all recombination mechanisms under test up to an irradiance of 1 sun. With the application of the method to experimental data, I identified the accuracy of the irradiance values to be an additional limiting factor and gave recommendations on how to improve the measurement procedure. Thereby, experimental challenges were identified but more importantly a more theoretically sound framework for the interpretation of the light-intensity dependence of the short-circuit current density in organic solar cells was established.

Similar to the case of the light-intensity dependent measurements of the short-circuit current density, certain models have also been prevalent in the interpretation of energetic-disorder characterization. However, there is a diversity of measurement techniques that use these models to characterize energetic disorder in organic photovoltaics. My literature research revealed that there seems to be systematic differences between the most commonly applied techniques based on optical or electrical measurements. For the measurements based on optical excitation, Fourier-transform photocurrent spectroscopy and photothermal deflection spectroscopy, I performed analyses both based on the traditional Urbach tails and on the more recently proposed model by Kaiser et al.,[280] revealing that the optical measurements might show thermal broadening instead of actual energetic disorder. For the electrical capacitance-voltage measurements that I performed, I found that, on the one hand, they could probe a different energy range than the optical measurements. On the other hand, I have shown that the increase and subsequent drop of the capacitance at high voltages is attributed to transport issues introducing an additional series resistance inside the active layer. Thereby, I found

several possible causes for the discrepancies between optical and electrical characterization that occurred both in literature and in my experiments. These findings can help future characterization of energetic disorder in organic solar cells and improve the interpretation of capacitance-voltage measurements even beyond the extraction of a measure for energetic disorder.

In these studies on established characterization techniques, a reoccurring problem was the simplification of the drift-diffusion equations to analytical models that often neglect spatial dependences inside the solar cell. Alternatively, one can keep the differential equations and use a numerical solver to fit them to the experimental data. Here, I introduced a fitting routine that utilizes a neural network to replace the slow numerical solver and make better use of the simulated data. On the example of light-intensity and thickness dependent JV curves, I described the process of choosing appropriate fitting parameters, generating training data and training the neural network. I then was able to verify the fitting procedure on the example of simulated JV curves, where the actual material parameters have been known, before applying it to experimental data. Apart from fitting, the fast computation of the neural network also enables scanning the error between the experiment and the simulation in the entire parameter space. Here, I analyzed one- and two-dimensional slices in the parameter space around the best fit and compared it to the integration of the inverse error over a grid in all dimensions. The results showed that the slices through the parameter space exhibit much sharper features than the integrated plots. Also, I could show how the integration of the error can indicate that the error might depend on a relation between material parameters instead of them separately. Thereby, extracting these relations can help identifying further experiments with opposite relations that could maximize information gain on the material parameters. After comparing fitting results of different combination of light-intensity and thickness dependent JV curves, I concluded that the set of parameters chosen for this example of parameter estimation does not sufficiently describe the experimental data and suggested including both the trap density and the recombination coefficient for traps as variable parameters to describe trap-assisted recombination. Therefore, I presented a routine for fitting and analyzing experimental data with the help of machine learning and identified promising measures for successful application on the data set of PBDB-TF-T1:BTP-4F-12-based solar cells in the future.

The method of parameter estimation is not limited to JV characteristics, though. The framework is applicable to any type of measurement that can be simulated and

therefore also to the other characterization techniques discussed in this work. With a reliable optical model, the neural network could also predict the light-intensity dependence of specific performance parameters like the short-circuit current density or the open-circuit voltage. Alternatively, using the simulation software SCAPS to generate training data allows parameter estimation on frequency-domain methods like capacitance-voltage curves. The numerous opportunities for application are promising in terms of finding experiment combinations that maximize information gain on the material system. Thereby, this work delivered in-depth understanding of measurements that researchers are frequently using today to characterize recombination and energetic disorder in organic solar cells and provided the groundwork for future characterization with the usage of machine learning.

Bibliography

[1] IEA, "Net Zero by 2050," report, IEA, 2021.

[2] A. Shah, P. Torres, R. Tscharner, N. Wyrsch, and H. Keppner, "Photovoltaic Technology: The Case for Thin-Film Solar Cells," *Science*, vol. 285, no. 5428, pp. 692–698, 1999.

[3] T. D. Lee and A. U. Ebong, "A review of thin film solar cell technologies and challenges," *Renewable and Sustainable Energy Reviews*, vol. 70, pp. 1286–1297, 2017.

[4] L. Portilla, K. Loganathan, H. Faber, A. Eid, J. G. D. Hester, M. M. Tentzeris, M. Fattori, E. Cantatore, C. Jiang, A. Nathan, G. Fiori, T. Ibn-Mohammed, T. D. Anthopoulos, and V. Pecunia, "Wirelessly powered large-area electronics for the Internet of Things," *Nature Electronics*, 2022.

[5] T. Kirchartz and J. Nelson, "Device modelling of organic bulk heterojunction solar cells," *Topics in Current Chemistry*, vol. 352, pp. 279–324, 2014.

[6] A. Wadsworth, M. Moser, A. Marks, M. S. Little, N. Gasparini, C. J. Brabec, D. Baran, and I. McCulloch, "Critical review of the molecular design progress in non-fullerene electron acceptors towards commercially viable organic solar cells," *Chemical Society Reviews*, vol. 48, no. 6, pp. 1596–1625, 2019.

[7] C. J. Brabec, A. Distler, X. Du, H.-J. Egelhaaf, J. Hauch, T. Heumueller, and N. Li, "Material Strategies to Accelerate OPV Technology Toward a GW Technology," *Advanced Energy Materials*, vol. 10, no. 43, p. 2001864, 2020.

[8] F. C. Krebs, T. Tromholt, and M. Jorgensen, "Upscaling of polymer solar cell fabrication using full roll-to-roll processing," *Nanoscale*, vol. 2, no. 6, pp. 873–86, 2010.

[9] J. Lee, Y.-H. Seo, S.-N. Kwon, D.-H. Kim, S. Jang, H. Jung, Y. Lee, H. Weerasinghe, T. Kim, J. Y. Kim, D. Vak, and S.-I. Na, "Slot-Die and Roll-to-Roll Processed Single Junction Organic Photovoltaic Cells with the Highest Efficiency," *Advanced Energy Materials*, vol. 9, no. 36, 2019.

[10] H. Zhao, B. Lin, J. Xue, H. B. Naveed, C. Zhao, X. Zhou, K. Zhou, H. Wu, Y. Cai, D. Yun, Z. Tang, and W. Ma, "Kinetics Manipulation Enables High-Performance Thick Ternary Organic Solar Cells via R2R-Compatible Slot-Die Coating," *Advanced Materials*, p. e2105114, 2021.

[11] F. Padinger, R. S. Rittberger, and N. S. Sariciftci, "Effects of postproduction treatment on plastic solar cells," *Advanced Functional Materials*, vol. 13, no. 1, pp. 85–88, 2003.

[12] L. Zhu, M. Zhang, J. Xu, C. Li, J. Yan, G. Zhou, W. Zhong, T. Hao, J. Song, X. Xue, Z. Zhou, R. Zeng, H. Zhu, C. C. Chen, R. C. I. MacKenzie, Y. Zou, J. Nelson, Y. Zhang, Y. Sun, and F. Liu, "Single-junction organic solar cells with over 19% efficiency enabled by a refined double-fibril network morphology," *Nature Materials*, vol. 21, no. 6, pp. 656–663, 2022.

[13] Z. Zheng, J. Wang, P. Bi, J. Ren, Y. Wang, Y. Yang, X. Liu, S. Zhang, and J. Hou, "Tandem Organic Solar Cell with 20.2% Efficiency," *Joule*, vol. 6, no. 1, pp. 171–184, 2021.

[14] "Best Research-Cell Efficiency Chart." `https://www.nrel.gov/pv/cell-efficiency.html`, 2023. Accessed: 2023/09/08.

[15] V. Shrotriya, G. Li, Y. Yao, T. Moriarty, K. Emery, and Y. Yang, "Accurate Measurement and Characterization of Organic Solar Cells," *Advanced Functional Materials*, vol. 16, no. 15, pp. 2016–2023, 2006.

[16] F. Fabregat-Santiago, G. Garcia-Belmonte, I. Mora-Sero, and J. Bisquert, "Characterization of nanostructured hybrid and organic solar cells by impedance spectroscopy," *Physical Chemistry Chemical Physics*, vol. 13, no. 20, pp. 9083–118, 2011.

[17] K. Vandewal, L. Goris, I. Haeldermans, M. Nesládek, K. Haenen, P. Wagner, and J. V. Manca, "Fourier-Transform Photocurrent Spectroscopy for a fast and highly sensitive spectral characterization of organic and hybrid solar cells," *Thin Solid Films*, vol. 516, no. 20, pp. 7135–7138, 2008.

[18] M. Azzouzi, P. Calado, A. M. Telford, F. Eisner, X. Hou, T. Kirchartz, P. R. F. Barnes, and J. Nelson, "Overcoming the Limitations of Transient Photovoltage Measurements for Studying Recombination in Organic Solar Cells," *Solar RRL*, vol. 4, no. 5, p. 1900581, 2020.

[19] T. Kirchartz, F. Deledalle, P. S. Tuladhar, J. R. Durrant, and J. Nelson, "On the Differences between Dark and Light Ideality Factor in Polymer:Fullerene Solar Cells," *The Journal of Physical Chemistry Letters*, vol. 4, no. 14, pp. 2371–2376, 2013.

[20] N. Chandrasekaran, E. Gann, N. Jain, A. Kumar, S. Gopinathan, A. Sadhanala, R. H. Friend, A. Kumar, C. R. McNeill, and D. Kabra, "Correlation between Photovoltaic Performance and Interchain Ordering Induced Delocalization of Electronics States in Conjugated Polymer Blends," *ACS Applied Energy Materials*, vol. 8, no. 31, pp. 20243–50, 2016.

[21] S. R. Cowan, A. Roy, and A. J. Heeger, "Recombination in polymer-fullerene bulk heterojunction solar cells," *Physical Review B*, vol. 82, no. 24, p. 245207, 2010.

[22] L. J. A. Koster, V. D. Mihailetchi, H. Xie, and P. W. M. Blom, "Origin of the light intensity dependence of the short-circuit current of polymer/fullerene solar cells," *Applied Physics Letters*, vol. 87, no. 20, p. 203502, 2005.

[23] L. J. Koster, M. Kemerink, M. M. Wienk, K. Maturova, and R. A. Janssen, "Quantifying bimolecular recombination losses in organic bulk heterojunction solar cells," *Advanced Materials*, vol. 23, no. 14, pp. 1670–4, 2011.

[24] A. Karki, J. Vollbrecht, A. J. Gillett, P. Selter, J. Lee, Z. Peng, N. Schopp, A. L. Dixon, M. Schrock, V. Nádaždy, F. Schauer, H. Ade, B. F. Chmelka, G. C. Bazan, R. H. Friend, and T.-Q. Nguyen, "Unifying Charge Generation, Recombination, and Extraction in Low-Offset Non-Fullerene Acceptor Organic Solar Cells," *Advanced Energy Materials*, vol. 10, no. 29, p. 2001203, 2020.

[25] C. Sun, F. Pan, H. Bin, J. Zhang, L. Xue, B. Qiu, Z. Wei, Z. G. Zhang, and Y. Li, "A low cost and high performance polymer donor material for polymer solar cells," *Nature Communications*, vol. 9, no. 1, p. 743, 2018.

[26] B. Guo, W. Li, X. Guo, X. Meng, W. Ma, M. Zhang, and Y. Li, "High Efficiency Nonfullerene Polymer Solar Cells with Thick Active Layer and Large Area," *Advanced Materials*, vol. 29, no. 36, pp. 1702291–1702n/a, 2017.

[27] G. Zhang, G. Yang, H. Yan, J. H. Kim, H. Ade, W. Wu, X. Xu, Y. Duan, and Q. Peng, "Efficient Nonfullerene Polymer Solar Cells Enabled by a Novel Wide Bandgap Small Molecular Acceptor," *Advanced Materials*, vol. 29, no. 18, pp. 1606054–1606n/a, 2017.

[28] L. Yang, S. Zhang, C. He, J. Zhang, H. Yao, Y. Yang, Y. Zhang, W. Zhao, and J. Hou, "New Wide Band Gap Donor for Efficient Fullerene-Free All-Small-Molecule Organic Solar Cells," *Journal of the American Chemical Society*, vol. 139, no. 5, pp. 1958–1966, 2017.

[29] Y. Lin, F. Zhao, Y. Wu, K. Chen, Y. Xia, G. Li, S. K. Prasad, J. Zhu, L. Huo, H. Bin, Z. G. Zhang, X. Guo, M. Zhang, Y. Sun, F. Gao, Z. Wei, W. Ma, C. Wang, J. Hodgkiss, Z. Bo, O. Inganas, Y. Li, and X. Zhan, "Mapping Polymer Donors toward High-Efficiency Fullerene Free Organic Solar Cells," *Advanced Materials*, vol. 29, no. 3, p. 1604155, 2017.

[30] F. Zhao, S. Dai, Y. Wu, Q. Zhang, J. Wang, L. Jiang, Q. Ling, Z. Wei, W. Ma, W. You, C. Wang, and X. Zhan, "Single-Junction Binary-Blend Nonfullerene Polymer Solar Cells with 12.1% Efficiency," *Advanced Materials*, vol. 29, no. 18, pp. 1700144–1700n/a, 2017.

[31] Y. Ding, X. Zhang, H. Feng, X. Ke, L. Meng, Y. Sun, Z. Guo, Y. Cai, C. Jiao, X. Wan, C. Li, N. Zheng, Z. Xie, and Y. Chen, "Subtle Morphology Control with Binary Additives for High-Efficiency Non-Fullerene Acceptor Organic Solar Cells," *ACS Applied Materials & Interfaces*, vol. 12, no. 24, pp. 27425–27432, 2020.

[32] F. Qi, K. Jiang, F. Lin, Z. Wu, H. Zhang, W. Gao, Y. Li, Z. Cai, H. Y. Woo, Z. Zhu, and A. K. Y. Jen, "Over 17% Efficiency Binary Organic Solar Cells with

Photoresponses Reaching 1000 nm Enabled by Selenophene-Fused Nonfullerene Acceptors," *ACS Energy Letters*, vol. 6, no. 1, pp. 9–15, 2020.

[33] W. Gao, Q. An, M. Hao, R. Sun, J. Yuan, F. Zhang, W. Ma, J. Min, and C. Yang, "Thick-Film Organic Solar Cells Achieving over 11% Efficiency and Nearly 70% Fill Factor at Thickness over 400 nm," *Advanced Functional Materials*, vol. 30, no. 10, p. 1908336, 2020.

[34] Z. Xiao, X. Jia, D. Li, S. Wang, X. Geng, F. Liu, J. Chen, S. Yang, T. P. Russell, and L. Ding, "26 mA cm^{-2} J_{sc} from organic solar cells with a low-bandgap nonfullerene acceptor," *Science Bulletin*, vol. 62, no. 22, pp. 1494–1496, 2017.

[35] G. Chai, Y. Chang, J. Zhang, X. Xu, L. Yu, X. Zou, X. Li, Y. Chen, S. Luo, B. Liu, F. Bai, Z. Luo, H. Yu, J. Liang, T. Liu, K. S. Wong, H. Zhou, Q. Peng, and H. Yan, "Fine-tuning of Side-chain Orientations on Nonfullerene Acceptors Enables Organic Solar Cells with 17.7% Efficiency," *Energy & Environmental Science*, vol. 14, no. 6, pp. 3469–3479, 2021.

[36] Y. Chang, J. Zhang, Y. Chen, G. Chai, X. Xu, L. Yu, R. Ma, H. Yu, T. Liu, P. Liu, Q. Peng, and H. Yan, "Achieving Efficient Ternary Organic Solar Cells Using Structurally Similar Non-Fullerene Acceptors with Varying Flanking Side Chains," *Advanced Energy Materials*, vol. 11, no. 14, p. 2100079, 2021.

[37] Y. Chen, F. Bai, Z. Peng, L. Zhu, J. Zhang, X. Zou, Y. Qin, H. K. Kim, J. Yuan, L.-K. Ma, J. Zhang, H. Yu, P. C. Y. Chow, F. Huang, Y. Zou, H. Ade, F. Liu, and H. Yan, "Asymmetric Alkoxy and Alkyl Substitution on Nonfullerene Acceptors Enabling High-Performance Organic Solar Cells," *Advanced Energy Materials*, vol. 11, no. 3, p. 2003141, 2020.

[38] Y. Chen, P. Ye, Z. G. Zhu, X. Wang, L. Yang, X. Xu, X. Wu, T. Dong, H. Zhang, J. Hou, F. Liu, and H. Huang, "Achieving High-Performance Ternary Organic Solar Cells through Tuning Acceptor Alloy," *Advanced Materials*, vol. 29, no. 6, 2017.

[39] H. Choi, S. J. Ko, T. Kim, P. O. Morin, B. Walker, B. H. Lee, M. Leclerc, J. Y. Kim, and A. J. Heeger, "Small-bandgap polymer solar cells with unprecedented short-circuit current density and high fill factor," *Advanced Materials*, vol. 27, no. 21, pp. 3318–24, 2015.

[40] Y. Cui, H. Yao, J. Zhang, K. Xian, T. Zhang, L. Hong, Y. Wang, Y. Xu, K. Ma, C. An, C. He, Z. Wei, F. Gao, and J. Hou, "Single-Junction Organic Photovoltaic Cells with Approaching 18% Efficiency," *Advanced Materials*, vol. 32, no. 19, p. 1908205, 2020.

[41] Y. Cui, Y. Xu, H. Yao, P. Bi, L. Hong, J. Zhang, Y. Zu, T. Zhang, J. Qin, J. Ren, Z. Chen, C. He, X. Hao, Z. Wei, and J. Hou, "Single-Junction Organic Photovoltaic Cell with 19% Efficiency," *Advanced Materials*, vol. 33, no. 41, p. 2102420, 2021.

[42] B. Fan, D. Zhang, M. Li, W. Zhong, Z. Zeng, L. Ying, F. Huang, and Y. Cao, "Achieving over 16% efficiency for single-junction organic solar cells," *Science China Chemistry*, vol. 62, no. 6, pp. 746–752, 2019.

[43] Q. Liu, Y. Jiang, K. Jin, J. Qin, J. Xu, W. Li, J. Xiong, J. Liu, Z. Xiao, K. Sun, S. Yang, X. Zhang, and L. Ding, "18% Efficiency organic solar cells," *Science Bulletin*, vol. 65, no. 4, pp. 272–275, 2020.

[44] L. Ma, Y. Xu, Y. Zu, Q. Liao, B. Xu, C. An, S. Zhang, and J. Hou, "A ternary organic solar cell with 300 nm thick active layer shows over 14% efficiency," *Science China Chemistry*, vol. 63, no. 1, pp. 21–27, 2019.

[45] E. Moustafa, M. Méndez, J. G. Sánchez, J. Pallarès, E. Palomares, and L. F. Marsal, "Thermal Activation of PEDOT:PSS/PM6:Y7 Based Films Leads to Unprecedent High Short-Circuit Current Density in Nonfullerene Organic Photovoltaics," *Advanced Energy Materials*, vol. 13, no. 4, p. 2203241, 2022.

[46] A. Armin, W. Li, O. J. Sandberg, Z. Xiao, L. Ding, J. Nelson, D. Neher, K. Vandewal, S. Shoaee, T. Wang, H. Ade, T. Heumüller, C. Brabec, and P. Meredith, "A History and Perspective of Non-Fullerene Electron Acceptors for Organic Solar Cells," *Advanced Energy Materials*, vol. 11, no. 15, p. 2003570, 2021.

[47] T. Kirchartz, B. E. Pieters, J. Kirkpatrick, U. Rau, and J. Nelson, "Recombination via tail states in polythiophene:fullerene solar cells," *Physical Review B*, vol. 83, no. 11, p. 115209, 2011.

[48] G. Garcia-Belmonte and J. Bisquert, "Open-circuit voltage limit caused by recombination through tail states in bulk heterojunction polymer-fullerene solar cells," *Applied Physics Letters*, vol. 96, no. 11, p. 113301, 2010.

[49] W. Shockley and H. J. Queisser, "Detailed Balance Limit of Efficiency of p-n Junction Solar Cells," *Journal of Applied Physics*, vol. 32, no. 3, pp. 510–519, 1961.

[50] J.-F. Guillemoles, T. Kirchartz, D. Cahen, and U. Rau, "Guide for the perplexed to the Shockley–Queisser model for solar cells," *Nature Photonics*, vol. 13, no. 8, pp. 501–505, 2019.

[51] P. Würfel, "The chemical potential of radiation," *Journal of Physics C: Solid State Physics*, vol. 15, no. 18, p. 3967, 1982.

[52] T. Kirchartz, D. Abou-Ras, and U. Rau, "Introduction to Thin-Film Photovoltaics," in *Advanced Characterization Techniques for Thin Film Solar Cells* (D. Abou-Ras, T. Kirchartz, and U. Rau, eds.), vol. 1, pp. 6–9, 2016.

[53] P. W. Bridgman, "Note on the Principle of Detailed Balancing," *Physical Review*, vol. 31, no. 1, pp. 101–102, 1928.

[54] J. A. Nelson, *The physics of solar cells*, p. 11. World Scientific Publishing Company, 2003.

[55] T. Kirchartz, K. Ding, and U. Rau, "Fundamental electrical characterization of thin-film solar cells," in *Advanced Characterization Techniques for Thin Film Solar Cells* (D. Abou-Ras, T. Kirchartz, and U. Rau, eds.), vol. 1, p. 52, 2016.

[56] J. A. Nelson, *The physics of solar cells*, p. 68. World Scientific Publishing Company, 2003.

[57] W. Tress, "Photovoltaic Energy Conversion," in *Organic Solar Cells: Theory, Experiment, and Device Simulation*, p. 43, Cham: Springer International Publishing, 2014.

[58] W. Tress, "Modeling," in *Organic Solar Cells: Theory, Experiment, and Device Simulation*, p. 223, Cham: Springer International Publishing, 2014.

[59] J. A. Nelson, *The physics of solar cells*, p. 79. World Scientific Publishing Company, 2003.

[60] B. E. Pieters, K. Decock, M. Burgelman, R. Stangl, and T. Kirchartz, "One-Dimensional Electro-Optical Simulations of Thin-Film Solar Cells," in *Advanced*

Characterization Techniques for Thin Film Solar Cells (T. Kirchartz, K. Ding, and U. Rau, eds.), vol. 2, p. 633, 2016.

[61] J. A. Nelson, *The physics of solar cells*, pp. 88–89. World Scientific Publishing Company, 2003.

[62] W. Tress, "Modeling," in *Organic Solar Cells: Theory, Experiment, and Device Simulation*, p. 250, Cham: Springer International Publishing, 2014.

[63] L. A. A. Pettersson, L. S. Roman, and O. Inganäs, "Modeling photocurrent action spectra of photovoltaic devices based on organic thin films," *Journal of Applied Physics*, vol. 86, no. 1, pp. 487–496, 1999.

[64] C. Deibel, T. Strobel, and V. Dyakonov, "Role of the charge transfer state in organic donor-acceptor solar cells," *Advanced Materials*, vol. 22, no. 37, pp. 4097–111, 2010.

[65] C. Göhler, A. Wagenpfahl, and C. Deibel, "Nongeminate Recombination in Organic Solar Cells," *Advanced Electronic Materials*, vol. 4, no. 10, p. 1700505, 2018.

[66] J. Bisquert and I. Mora-Seró, "Simulation of Steady-State Characteristics of Dye-Sensitized Solar Cells and the Interpretation of the Diffusion Length," *The Journal of Physical Chemistry Letters*, vol. 1, no. 1, pp. 450–456, 2009.

[67] T. Kirchartz and J. Nelson, "Meaning of reaction orders in polymer:fullerene solar cells," *Physical Review B*, vol. 86, no. 16, p. 165201, 2012.

[68] I. Zonno, B. Krogmeier, V. Katte, D. Lübke, A. Martinez-Otero, and T. Kirchartz, "Discriminating between surface and bulk recombination in organic solar cells by studying the thickness dependence of the open-circuit voltage," *Applied Physics Letters*, vol. 109, no. 18, p. 183301, 2016.

[69] C. M. Proctor, M. Kuik, and T.-Q. Nguyen, "Charge carrier recombination in organic solar cells," *Progress in Polymer Science*, vol. 38, no. 12, pp. 1941–1960, 2013.

[70] T. Kirchartz, T. Markvart, U. Rau, and D. A. Egger, "Impact of Small Phonon Energies on the Charge-Carrier Lifetimes in Metal-Halide Perovskites," *Journal of Physical Chemistry Letters*, vol. 9, no. 5, pp. 939–946, 2018.

[71] J. Benduhn, K. Tvingstedt, F. Piersimoni, S. Ullbrich, Y. Fan, M. Tropiano, K. A. McGarry, O. Zeika, M. K. Riede, C. J. Douglas, S. Barlow, S. R. Marder, D. Neher, D. Spoltore, and K. Vandewal, "Intrinsic non-radiative voltage losses in fullerene-based organic solar cells," *Nature Energy*, vol. 2, no. 6, pp. 1–6, 2017.

[72] S. Zhou, J. Sun, C. Zhou, and Z. Deng, "Comparison of recombination models in organic bulk heterojunction solar cells," *Physica B: Condensed Matter*, vol. 415, pp. 28–33, 2013.

[73] I. Zonno, H. Zayani, M. Grzeslo, B. Krogmeier, and T. Kirchartz, "Extracting Recombination Parameters from Impedance Measurements on Organic Solar Cells," *Physical Review Applied*, vol. 11, no. 5, p. 054024, 2019.

[74] T. Kirchartz, J. A. Márquez, M. Stolterfoht, and T. Unold, "Photoluminescence-Based Characterization of Halide Perovskites for Photovoltaics," *Advanced Energy Materials*, vol. 10, no. 26, p. 1904134, 2020.

[75] U. Würfel, L. Perdigón-Toro, J. Kurpiers, C. M. Wolff, P. Caprioglio, J. J. Rech, J. Zhu, X. Zhan, W. You, S. Shoaee, D. Neher, and M. Stolterfoht, "Recombination between Photogenerated and Electrode-Induced Charges Dominates the Fill Factor Losses in Optimized Organic Solar Cells," *Journal of Physical Chemistry Letters*, vol. 10, no. 12, pp. 3473–3480, 2019.

[76] G. Lakhwani, A. Rao, and R. H. Friend, "Bimolecular Recombination in Organic Photovoltaics," *Annual Review of Physical Chemistry*, vol. 65, no. 1, pp. 557–581, 2014.

[77] R. Noriega, J. Rivnay, K. Vandewal, F. P. Koch, N. Stingelin, P. Smith, M. F. Toney, and A. Salleo, "A general relationship between disorder, aggregation and charge transport in conjugated polymers," *Nature Materials*, vol. 12, no. 11, pp. 1038–44, 2013.

[78] R. A. Street, A. Krakaris, and S. R. Cowan, "Recombination Through Different Types of Localized States in Organic Solar Cells," *Advanced Functional Materials*, vol. 22, no. 21, pp. 4608–4619, 2012.

[79] S. A. Hawks, G. Li, Y. Yang, and R. A. Street, "Band tail recombination in polymer:fullerene organic solar cells," *Journal of Applied Physics*, vol. 116, no. 7, p. 074503, 2014.

[80] L. N. S. Murthy, D. Barrera, L. Xu, A. Gadh, F.-Y. Cao, C.-C. Tseng, Y.-J. Cheng, and J. W. P. Hsu, "Probing Defect States in Organic Polymers and Bulk Heterojunctions Using Surface Photovoltage Spectroscopy," *Journal of Physical Chemistry C*, vol. 123, no. 17, pp. 10795–10801, 2019.

[81] R. A. Street and D. M. Davies, "Kinetics of light induced defect creation in organic solar cells," *Applied Physics Letters*, vol. 102, no. 4, p. 043305, 2013.

[82] W. Shockley and W. T. Read, "Statistics of the Recombinations of Holes and Electrons," *Physical Review*, vol. 87, no. 5, pp. 835–842, 1952.

[83] R. N. Hall, "Electron-Hole Recombination in Germanium," *Physical Review*, vol. 87, no. 2, pp. 387–387, 1952.

[84] B. E. Pieters, K. Decock, M. Burgelman, R. Stangl, and T. Kirchartz, "One-Dimensional Electro-Optical Simulations of Thin-Film Solar Cells," in *Advanced Characterization Techniques for Thin Film Solar Cells* (T. Kirchartz, K. Ding, and U. Rau, eds.), vol. 2, pp. 640–641, 2016.

[85] B. E. Pieters, K. Decock, M. Burgelman, R. Stangl, and T. Kirchartz, "One-Dimensional Electro-Optical Simulations of Thin-Film Solar Cells," in *Advanced Characterization Techniques for Thin Film Solar Cells* (T. Kirchartz, K. Ding, and U. Rau, eds.), vol. 2, p. 636, 2016.

[86] A. Schenk, "Simulation of Silicon Devices: An Overview," in *Advanced Physical Models for Silicon Device Simulation*, pp. 1–126, Vienna: Springer Vienna, 1998.

[87] D. Credgington and J. R. Durrant, "Insights from Transient Optoelectronic Analyses on the Open-Circuit Voltage of Organic Solar Cells," *Journal of Physical Chemistry Letters*, vol. 3, no. 11, pp. 1465–78, 2012.

[88] J. Nelson, "Diffusion-limited recombination in polymer-fullerene blends and its influence on photocurrent collection," *Physical Review B*, vol. 67, no. 15, p. 155209, 2003.

[89] R. A. Street, J. E. Northrup, and A. Salleo, "Transport in polycrystalline polymer thin-film transistors," *Physical Review B*, vol. 71, no. 16, p. 165202, 2005.

[90] N. C. Giebink, G. P. Wiederrecht, M. R. Wasielewski, and S. R. Forrest, "Ideal diode equation for organic heterojunctions. I. Derivation and application," *Physical Review B*, vol. 82, no. 15, p. 155305, 2010.

[91] M. Tachiya and K. Seki, "Theory of bulk electron-hole recombination in a medium with energetic disorder," *Physical Review B*, vol. 82, no. 8, p. 085201, 2010.

[92] F. Urbach, "The Long-Wavelength Edge of Photographic Sensitivity and of the Electronic Absorption of Solids," *Physical Review*, vol. 92, no. 5, pp. 1324–1324, 1953.

[93] J. A. Nelson, *The physics of solar cells*, p. 110. World Scientific Publishing Company, 2003.

[94] R. A. Street, M. Schoendorf, A. Roy, and J. H. Lee, "Interface state recombination in organic solar cells," *Physical Review B*, vol. 81, no. 20, p. 205307, 2010.

[95] J. A. Nelson, *The physics of solar cells*, pp. 73–74. World Scientific Publishing Company, 2003.

[96] M. L. Ball, Q. Burlingame, H. L. Smith, T. Liu, S. R. Parkin, A. Kahn, and Y.-L. Loo, "Design of UV-Absorbing Donor Molecules for Nearly Imperceptible Organic Solar Cells," *ACS Energy Letters*, vol. 7, no. 1, pp. 180–188, 2021.

[97] Y. Cui, Y. Wang, J. Bergqvist, H. Yao, Y. Xu, B. Gao, C. Yang, S. Zhang, O. Inganäs, F. Gao, and J. Hou, "Wide-gap non-fullerene acceptor enabling high-performance organic photovoltaic cells for indoor applications," *Nature Energy*, vol. 4, no. 9, pp. 768–775, 2019.

[98] N. Espinosa, R. García-Valverde, A. Urbina, and F. C. Krebs, "A life cycle analysis of polymer solar cell modules prepared using roll-to-roll methods under ambient conditions," *Solar Energy Materials and Solar Cells*, vol. 95, no. 5, pp. 1293–1302, 2011.

[99] M. Riede, D. Spoltore, and K. Leo, "Organic Solar Cells—The Path to Commercial Success," *Advanced Energy Materials*, vol. 11, no. 1, p. 2002653, 2020.

[100] J. Nelson, "Polymer:fullerene bulk heterojunction solar cells," *Materials Today*, vol. 14, no. 10, pp. 462–470, 2011.

[101] M. Fox, "Molecular materials," in *Optical properties of solids*, vol. 3, pp. 220–222, Oxford University Press, Incorporated, 2 ed., 2002.

[102] A. J. Heeger, "Nobel Lecture: Semiconducting and metallic polymers: The fourth generation of polymeric materials," *Reviews of Modern Physics*, vol. 73, no. 3, pp. 681–700, 2001.

[103] P. W. M. Blom, V. D. Mihailetchi, L. J. A. Koster, and D. E. Markov, "Device Physics of Polymer:Fullerene Bulk Heterojunction Solar Cells," *Advanced Materials*, vol. 19, no. 12, pp. 1551–1566, 2007.

[104] G. Li, R. Zhu, and Y. Yang, "Polymer solar cells," *Nature Photonics*, vol. 6, no. 3, pp. 153–161, 2012.

[105] M. Wright, R. Lin, M. J. Y. Tayebjee, and G. Conibeer, "Effect of Blend Composition on Bulk Heterojunction Organic Solar Cells: A Review," *Solar RRL*, vol. 1, no. 3-4, p. 1700035, 2017.

[106] T. Stübinger and W. Brütting, "Exciton diffusion and optical interference in organic donor–acceptor photovoltaic cells," *Journal of Applied Physics*, vol. 90, no. 7, pp. 3632–3641, 2001.

[107] K. Jiang, J. Zhang, Z. Peng, F. Lin, S. Wu, Z. Li, Y. Chen, H. Yan, H. Ade, Z. Zhu, and A. K. Y. Jen, "Pseudo-bilayer architecture enables high-performance organic solar cells with enhanced exciton diffusion length," *Nature Communications*, vol. 12, no. 1, p. 468, 2021.

[108] C. W. Tang, "Two-layer organic photovoltaic cell," *Applied Physics Letters*, vol. 48, no. 2, pp. 183–185, 1986.

[109] S. D. Dimitrov and J. R. Durrant, "Materials Design Considerations for Charge Generation in Organic Solar Cells," *Chemistry of Materials*, vol. 26, no. 1, pp. 616–630, 2013.

[110] G. Yu, J. Gao, J. C. Hummelen, F. Wudl, and A. J. Heeger, "Polymer photovoltaic cells: enhanced efficiencies via a network of internal donor-acceptor heterojunctions," *Science*, vol. 270, no. 5243, pp. 1789–1791, 1995.

[111] J. J. M. Halls, C. A. Walsh, N. C. Greenham, E. A. Marseglia, R. H. Friend, S. C. Moratti, and A. B. Holmes, "Efficient photodiodes from interpenetrating polymer networks," *Nature*, vol. 376, no. 6540, pp. 498–500, 1995.

[112] H. Cha, J. Wu, A. Wadsworth, J. Nagitta, S. Limbu, S. Pont, Z. Li, J. Searle, M. F. Wyatt, D. Baran, J. S. Kim, I. McCulloch, and J. R. Durrant, "An Efficient, "Burn in" Free Organic Solar Cell Employing a Nonfullerene Electron Acceptor," *Advanced Materials*, vol. 29, no. 33, p. 1701156, 2017.

[113] L. Hong, H. Yao, Z. Wu, Y. Cui, T. Zhang, Y. Xu, R. Yu, Q. Liao, B. Gao, K. Xian, H. Y. Woo, Z. Ge, and J. Hou, "Eco-Compatible Solvent-Processed Organic Photovoltaic Cells with Over 16% Efficiency," *Advanced Materials*, vol. 31, no. 39, p. 1903441, 2019.

[114] S. Holliday, R. S. Ashraf, A. Wadsworth, D. Baran, S. A. Yousaf, C. B. Nielsen, C. H. Tan, S. D. Dimitrov, Z. Shang, N. Gasparini, M. Alamoudi, F. Laquai, C. J. Brabec, A. Salleo, J. R. Durrant, and I. McCulloch, "High-efficiency and air-stable P3HT-based polymer solar cells with a new non-fullerene acceptor," *Nature Communications*, vol. 7, p. 11585, 2016.

[115] C. McDowell and G. C. Bazan, "Organic solar cells processed from green solvents," *Current Opinion in Green and Sustainable Chemistry*, vol. 5, pp. 49–54, 2017.

[116] Y. Cui, H. Yao, J. Zhang, T. Zhang, Y. Wang, L. Hong, K. Xian, B. Xu, S. Zhang, J. Peng, Z. Wei, F. Gao, and J. Hou, "Over 16% efficiency organic photovoltaic cells enabled by a chlorinated acceptor with increased open-circuit voltages," *Nature Communications*, vol. 10, no. 1, p. 2515, 2019.

[117] D. Wang, G. Zhou, Y. Li, K. Yan, L. Zhan, H. Zhu, X. Lu, H. Chen, and C.-Z. Li, "High-Performance Organic Solar Cells from Non-Halogenated Solvents," *Advanced Functional Materials*, vol. 32, no. 4, p. 2107827, 2021.

[118] J. Wu, J. Lee, Y.-C. Chin, H. Yao, H. Cha, J. Luke, J. Hou, J.-S. Kim, and J. R. Durrant, "Exceptionally low charge trapping enables highly efficient organic bulk heterojunction solar cells," *Energy & Environmental Science*, vol. 13, no. 8, pp. 2422–2430, 2020.

[119] X. Gu, X. Lai, Y. Zhang, T. Wang, W. L. Tan, C. R. McNeill, Q. Liu, P. Sonar, F. He, W. Li, C. Shan, and A. K. K. Kyaw, "Organic Solar Cell With Efficiency Over 20% and V_{OC} Exceeding 2.1 V Enabled by Tandem With All-Inorganic Perovskite and Thermal Annealing-Free Process," *Advanced Science*, vol. 9, no. 28, p. 2200445, 2022.

[120] H. Liu, L. Hu, F. Wu, L. Chen, and Y. Chen, "Polyfluorene Electrolytes Interfacial Layer for Efficient Polymer Solar Cells: Controllably Interfacial Dipoles by Regulation of Polar Groups," *ACS Applied Materials & Interfaces*, vol. 8, no. 15, pp. 9821–8, 2016.

[121] R. Sorrentino, E. Kozma, S. Luzzati, and R. Po, "Interlayers for non-fullerene based polymer solar cells: distinctive features and challenges," *Energy & Environmental Science*, vol. 14, no. 1, pp. 180–223, 2021.

[122] B. Qi and J. Wang, "Fill factor in organic solar cells," *Physical Chemistry Chemical Physics*, vol. 15, no. 23, pp. 8972–8982, 2013.

[123] T. Kirchartz, K. Ding, and U. Rau, "Fundamental electrical characterization of thin-film solar cells," in *Advanced Characterization Techniques for Thin Film Solar Cells* (D. Abou-Ras, T. Kirchartz, and U. Rau, eds.), vol. 1, p. 47, 2016.

[124] P. Kaienburg, P. Hartnagel, B. E. Pieters, J. Yu, D. Grabowski, Z. Liu, J. Haddad, U. Rau, and T. Kirchartz, "How Contact Layers Control Shunting Losses from Pinholes in Thin-Film Solar Cells," *The Journal of Physical Chemistry C*, vol. 122, no. 48, pp. 27263–27272, 2018.

[125] W. Tress, "Organic Solar Cells," in *Organic Solar Cells: Theory, Experiment, and Device Simulation*, p. 138, Cham: Springer International Publishing, 2014.

[126] T. Kirchartz, K. Ding, and U. Rau, *Fundamental electrical characterization of thin-film solar cells*, vol. 1 of *Advanced Characterization Techniques for Thin Film Solar Cells*. 2016.

[127] C. van Berkel, M. J. Powell, A. R. Franklin, and I. D. French, "Quality factor in a-Si:H nip and pin diodes," *Journal of Applied Physics*, vol. 73, no. 10, pp. 5264–5268, 1993.

[128] I. Mathews, S. N. Kantareddy, T. Buonassisi, and I. M. Peters, "Technology and Market Perspective for Indoor Photovoltaic Cells," *Joule*, vol. 3, no. 6, pp. 1415–1426, 2019.

[129] M. Seri, F. Mercuri, G. Ruani, Y. Feng, M. Li, Z.-X. Xu, and M. Muccini, "Toward Real Setting Applications of Organic and Perovskite Solar Cells: A Comparative Review," *Energy Technology*, vol. 9, no. 5, p. 2000901, 2021.

[130] P. Asghari, A. M. Rahmani, and H. H. S. Javadi, "Internet of Things applications: A systematic review," *Computer Networks*, vol. 148, pp. 241–261, 2019.

[131] D. Lübke, P. Hartnagel, J. Angona, and T. Kirchartz, "Comparing and Quantifying Indoor Performance of Organic Solar Cells," *Advanced Energy Materials*, vol. 11, no. 34, 2021.

[132] H. S. Ryu, S. Y. Park, T. H. Lee, J. Y. Kim, and H. Y. Woo, "Recent progress in indoor organic photovoltaics," *Nanoscale*, vol. 12, no. 10, pp. 5792–5804, 2020.

[133] Anonymous, "ISO 80000-7:2019(en) Quantities and units — Part 7: Light and radiation." `https://www.iso.org/obp/ui/#iso:std:iso:80000:-7:ed-2:v1:en`, 2019. Accessed: 2023/02/08.

[134] Anonymous, "ISO 9845-1:2022 Solar energy — Reference solar spectral irradiance at the ground at different receiving conditions — Part 1: Direct normal and hemispherical solar irradiance for air mass 1,5." `https://www.iso.org/obp/ui/#iso:std:iso:9845:-1:ed-2:v1:en`, 2022. Accessed: 2023/02/08.

[135] J. Bisquert, "Chemical capacitance of nanostructured semiconductors: its origin and significance for nanocomposite solar cells," *Physical Chemistry Chemical Physics*, vol. 5, no. 24, p. 5360, 2003.

[136] J. Heath and P. Zabierowski, "Capacitance spectroscopy of thin-film solar cells," in *Advanced characterization techniques for thin film solar cells* (T. Kirchartz, K. Ding, and U. Rau, eds.), vol. 1, pp. 93–95, 2016.

[137] E. von Hauff, "Impedance Spectroscopy for Emerging Photovoltaics," *The Journal of Physical Chemistry C*, vol. 123, no. 18, pp. 11329–11346, 2019.

[138] V. Lvovich, "Examples of Ideal Equivalent Circuit Models," in *Impedance Spectroscopy*, p. 51, John Wiley & Sons, 2012.

[139] V. V. Brus, C. M. Proctor, N. A. Ran, and T.-Q. Nguyen, "Capacitance Spectroscopy for Quantifying Recombination Losses in Nonfullerene Small-Molecule Bulk Heterojunction Solar Cells," *Advanced Energy Materials*, vol. 6, no. 11, p. 1502250, 2016.

[140] J. Bisquert, I. Mora-Sero, and F. Fabregat-Santiago, "Diffusion-Recombination Impedance Model for Solar Cells with Disorder and Nonlinear Recombination," *ChemElectroChem*, vol. 1, no. 1, pp. 289–296, 2014.

[141] L. Xu, J. Wang, and J. W. P. Hsu, "Transport Effects on Capacitance-Frequency Analysis for Defect Characterization in Organic Photovoltaic Devices," *Physical Review Applied*, vol. 6, no. 6, p. 064020, 2016.

[142] J. M. Montero and J. Bisquert, "Features of Capacitance and Mobility of Injected Carriers in Organic Layers Measured by Impedance Spectroscopy," *Israel Journal of Chemistry*, vol. 52, no. 6, pp. 519–528, 2012.

[143] J. Angona, "Herstellung und Charakterisierung von organischen Solarzellen mit hohen Bandlücken für die Anwendung in Tandemzellen," bachelor thesis, Universität Duisburg-Essen, 2019.

[144] T. Kirchartz, K. Ding, and U. Rau, "Fundamental electrical characterization of thin-film solar cells," in *Advanced Characterization Techniques for Thin Film Solar Cells* (D. Abou-Ras, T. Kirchartz, and U. Rau, eds.), vol. 1, pp. 55–59, 2016.

[145] T. C. M. Müller and T. Kirchartz, "Absorption and photocurrent spectroscopy with high dynamic range," in *Advanced Characterization Techniques for Thin Film Solar Cells* (D. Abou-Ras, T. Kirchartz, and U. Rau, eds.), vol. 1, pp. 193–194, 2016.

[146] P. Hartnagel, S. Ravishankar, B. Klingebiel, O. Thimm, and T. Kirchartz, "Comparing Methods of Characterizing Energetic Disorder in Organic Solar Cells," *Advanced Energy Materials*, vol. 13, no. 15, 2023.

[147] T. C. M. Müller and T. Kirchartz, "Absorption and photocurrent spectroscopy with high dynamic range," in *Advanced Characterization Techniques for Thin Film Solar Cells* (D. Abou-Ras, T. Kirchartz, and U. Rau, eds.), vol. 1, pp. 195–200, 2016.

[148] Z. Liu, L. Krückemeier, B. Krogmeier, B. Klingebiel, J. A. Márquez, S. Levcenko, S. Öz, S. Mathur, U. Rau, T. Unold, and T. Kirchartz, "Open-Circuit Voltages Exceeding 1.26 V in Planar Methylammonium Lead Iodide Perovskite Solar Cells," *ACS Energy Letters*, vol. 4, no. 1, pp. 110–117, 2018.

[149] J. Li, R. W. Collins, M. N. Sestak, P. Koirala, N. J. Podraza, S. Marsillac, and A. A. Rockett, "Spectroscopic Ellipsometry," in *Advanced Characterization Techniques for Thin Film Solar Cells*, p. 215, 2016.

[150] A. Biber, "Optical characterization of new materials for photovoltaics by using a specially constructed measurement setup of a spectroscopic ellipsometry," master thesis, Universität zu Lübeck, 2016.

[151] W. S. M. Werner, K. Glantschnig, and C. Ambrosch-Draxl, "Optical Constants and Inelastic Electron-Scattering Data for 17 Elemental Metals," *Journal of Physical and Chemical Reference Data*, vol. 38, no. 4, pp. 1013–1092, 2009.

[152] M. Zeman and J. Krc, "Optical and electrical modeling of thin-film silicon solar cells," *Journal of Materials Research*, vol. 23, no. 4, pp. 889–898, 2008.

[153] J. L. Gray, "A computer model for the simulation of thin-film silicon-hydrogen alloy solar cells," *IEEE Transactions on Electron Devices*, vol. 36, no. 5, pp. 906–912, 1989.

[154] P. P. Altermatt, G. Heiser, and M. A. Green, "Numerical quantification and minimization of perimeter losses in high-efficiency silicon solar cells," *Progress in Photovoltaics: Research and Applications*, vol. 4, no. 5, pp. 355–367, 1996.

[155] P. D. DeMoulin and M. S. Lundstrom, "Projections of GaAs solar-cell performance limits based on two-dimensional numerical simulation," *IEEE Transactions on Electron Devices*, vol. 36, no. 5, pp. 897–905, 1989.

[156] T. Stellwag, P. Dodd, M. Carpenter, M. Lundstrom, R. Pierret, M. Melloch, E. Yablonovitch, and T. Gmitter, "Effects of perimeter recombination on GaAs-based solar cells," in *IEEE Conference on Photovoltaic Specialists*, pp. 442–447, IEEE.

[157] M. Burgelman, P. Nollet, and S. Degrave, "Modelling polycrystalline semiconductor solar cells," *Thin Solid Films*, vol. 361, pp. 527–532, 2000.

[158] X. Sun, T. Silverman, R. Garris, C. Deline, and M. A. Alam, "An Illumination- and Temperature-Dependent Analytical Model for Copper Indium Gallium Diselenide (CIGS) Solar Cells," *IEEE Journal of Photovoltaics*, vol. 6, no. 5, pp. 1298–1307, 2016.

[159] S. van Reenen, M. Kemerink, and H. J. Snaith, "Modeling Anomalous Hysteresis in Perovskite Solar Cells," *Journal of Physical Chemistry Letters*, vol. 6, no. 19, pp. 3808–14, 2015.

[160] G. Richardson, S. E. J. O'Kane, R. G. Niemann, T. A. Peltola, J. M. Foster, P. J. Cameron, and A. B. Walker, "Can slow-moving ions explain hysteresis in the current–voltage curves of perovskite solar cells?," *Energy & Environmental Science*, vol. 9, no. 4, pp. 1476–1485, 2016.

[161] P. Caprioglio, C. M. Wolff, O. J. Sandberg, A. Armin, B. Rech, S. Albrecht, D. Neher, and M. Stolterfoht, "On the Origin of the Ideality Factor in Perovskite Solar Cells," *Advanced Energy Materials*, vol. 10, no. 27, p. 2000502, 2020.

[162] J. Siekmann, S. Ravishankar, and T. Kirchartz, "Apparent Defect Densities in Halide Perovskite Thin Films and Single Crystals," *ACS Energy Letters*, vol. 6, no. 9, pp. 3244–3251, 2021.

[163] J. A. Barker, C. M. Ramsdale, and N. C. Greenham, "Modeling the current-voltage characteristics of bilayer polymer photovoltaic devices," *Physical Review B*, vol. 67, no. 7, p. 075205, 2003.

[164] G. A. Buxton and N. Clarke, "Predicting structure and property relations in polymeric photovoltaic devices," *Physical Review B*, vol. 74, no. 8, p. 085207, 2006.

[165] N. Christ, S. W. Kettlitz, S. Züfle, S. Valouch, and U. Lemmer, "Nanosecond response of organic solar cells and photodiodes: Role of trap states," *Physical Review B*, vol. 83, no. 19, p. 195211, 2011.

[166] W. Tress, A. Petrich, M. Hummert, M. Hein, K. Leo, and M. Riede, "Imbalanced mobilities causing S-shaped IV curves in planar heterojunction organic solar cells," *Applied Physics Letters*, vol. 98, no. 6, p. 063301, 2011.

[167] D. Di Nuzzo, S. van Reenen, R. A. J. Janssen, M. Kemerink, and S. C. J. Meskers, "Evidence for space-charge-limited conduction in organic photovoltaic cells at open-circuit conditions," *Physical Review B*, vol. 87, no. 8, p. 085207, 2013.

[168] U. Würfel, D. Neher, A. Spies, and S. Albrecht, "Impact of charge transport on current-voltage characteristics and power-conversion efficiency of organic solar cells," *Nature Communications*, vol. 6, p. 6951, 2015.

[169] I. Zonno, A. Martinez-Otero, J.-C. Hebig, and T. Kirchartz, "Understanding Mott-Schottky Measurements under Illumination in Organic Bulk Heterojunction Solar Cells," *Physical Review Applied*, vol. 7, no. 3, p. 034018, 2017.

[170] L. Krückemeier, P. Kaienburg, J. Flohre, K. Bittkau, I. Zonno, B. Krogmeier, and T. Kirchartz, "Developing design criteria for organic solar cells using well-absorbing non-fullerene acceptors," *Communications Physics*, vol. 1, no. 1, pp. 1–10, 2018.

[171] G. Burwell, O. J. Sandberg, W. Li, P. Meredith, M. Carnie, and A. Armin, "Scaling Considerations for Organic Photovoltaics for Indoor Applications," *Solar RRL*, vol. 6, no. 7, p. 2200315, 2022.

[172] L. J. A. Koster, E. C. P. Smits, V. D. Mihailetchi, and P. W. M. Blom, "Device model for the operation of polymer/fullerene bulk heterojunction solar cells," *Physical Review B*, vol. 72, no. 8, p. 085205, 2005.

[173] T. Kirchartz, P. Kaienburg, and D. Baran, "Figures of Merit Guiding Research on Organic Solar Cells," *The Journal of Physical Chemistry C*, vol. 122, no. 11, pp. 5829–5843, 2018.

[174] B. E. Pieters, K. Decock, M. Burgelman, R. Stangl, and T. Kirchartz, "One-Dimensional Electro-Optical Simulations of Thin-Film Solar Cells," in *Advanced Characterization Techniques for Thin Film Solar Cells* (T. Kirchartz, K. Ding, and U. Rau, eds.), vol. 2, pp. 653–654, 2016.

[175] O. Almora, J. Wiegand, P. López-Varo, G. J. Matt, and C. J. Brabec, "Degradation through Directional Self-Doping and Homogeneous Density of Recombination Centers Hindered by 1,8-Diiodooctane Additive in Non-Fullerene Organic Solar Cells," *Solar RRL*, vol. 5, no. 4, p. 2100024, 2021.

[176] Q. An, F. Zhang, L. Li, J. Wang, Q. Sun, J. Zhang, W. Tang, and Z. Deng, "Simultaneous improvement in short circuit current, open circuit voltage, and fill factor of polymer solar cells through ternary strategy," *ACS Applied Materials & Interfaces*, vol. 7, no. 6, pp. 3691–8, 2015.

[177] Q. An, J. Wang, X. Ma, J. Gao, Z. Hu, B. Liu, h. sun, X. Guo, X. L. Zhang, and F. Zhang, "Two compatible polymer donors contribute synergistically for ternary organic solar cells with 17.53% efficiency," *Energy & Environmental Science*, vol. 13, no. 12, pp. 5039–5047, 2020.

[178] D. Baran, N. Gasparini, A. Wadsworth, C. H. Tan, N. Wehbe, X. Song, Z. Hamid, W. Zhang, M. Neophytou, T. Kirchartz, C. J. Brabec, J. R. Durrant, and I. McCulloch, "Robust nonfullerene solar cells approaching unity external quantum efficiency enabled by suppression of geminate recombination," *Nature Communications*, vol. 9, no. 1, p. 2059, 2018.

[179] H. Cha, D. S. Chung, S. Y. Bae, M.-J. Lee, T. K. An, J. Hwang, K. H. Kim, Y.-H. Kim, D. H. Choi, and C. E. Park, "Complementary Absorbing Star-Shaped Small Molecules for the Preparation of Ternary Cascade Energy Structures in Organic Photovoltaic Cells," *Advanced Functional Materials*, vol. 23, no. 12, pp. 1556–1565, 2013.

[180] N. Gasparini, L. Lucera, M. Salvador, M. Prosa, G. D. Spyropoulos, P. Kubis, H.-J. Egelhaaf, C. J. Brabec, and T. Ameri, "High-performance ternary organic solar cells with thick active layer exceeding 11% efficiency," *Energy & Environmental Science*, vol. 10, no. 4, pp. 885–892, 2017.

[181] S. Liu, J. Yuan, W. Deng, M. Luo, Y. Xie, Q. Liang, Y. Zou, Z. He, H. Wu, and Y. Cao, "High-efficiency organic solar cells with low non-radiative recombination loss and low energetic disorder," *Nature Photonics*, vol. 14, no. 5, pp. 300–305, 2020.

[182] J. Wang, C. Han, J. Han, F. Bi, X. Sun, S. Wen, C. Yang, C. Yang, X. Bao, and J. Chu, "Synergetic Strategy for Highly Efficient and Super Flexible Thick-film Organic Solar Cells," *Advanced Energy Materials*, vol. 12, no. 31, p. 2201614, 2022.

[183] H. Yin, S. H. Cheung, J. H. L. Ngai, C. H. Y. Ho, K. L. Chiu, X. Hao, H. W. Li, Y. Cheng, S. W. Tsang, and S. K. So, "Thick-Film High-Performance Bulk-Heterojunction Solar Cells Retaining 90% PCEs of the Optimized Thin Film Cells," *Advanced Electronic Materials*, vol. 3, no. 4, p. 1700007, 2017.

[184] X. Yuan, Y. Zhao, D. Xie, L. Pan, X. Liu, C. Duan, F. Huang, and Y. Cao, "Polythiophenes for organic solar cells with efficiency surpassing 17%," *Joule*, vol. 6, no. 3, pp. 647–661, 2022.

[185] N. A. Ran, J. A. Love, C. J. Takacs, A. Sadhanala, J. K. Beavers, S. D. Collins, Y. Huang, M. Wang, R. H. Friend, G. C. Bazan, and T. Q. Nguyen, "Harvesting the Full Potential of Photons with Organic Solar Cells," *Advanced Materials*, vol. 28, no. 7, pp. 1482–8, 2016.

[186] T. F. Hinrichsen, C. C. S. Chan, C. Ma, D. Palecek, A. Gillett, S. Chen, X. Zou, G. Zhang, H. L. Yip, K. S. Wong, R. H. Friend, H. Yan, A. Rao, and P. C. Y. Chow, "Long-lived and disorder-free charge transfer states enable endothermic charge separation in efficient non-fullerene organic solar cells," *Nature Communications*, vol. 11, no. 1, p. 5617, 2020.

[187] M. B. Upama, M. Wright, M. A. Mahmud, N. K. Elumalai, A. Mahboubi Soufiani, D. Wang, C. Xu, and A. Uddin, "Photo-degradation of high efficiency fullerene-free polymer solar cells," *Nanoscale*, vol. 9, no. 47, pp. 18788–18797, 2017.

[188] Y. Firdaus, Q. He, Y. Lin, F. A. A. Nugroho, V. M. Le Corre, E. Yengel, A. H. Balawi, A. Seitkhan, F. Laquai, C. Langhammer, F. Liu, M. Heeney, and T. D. Anthopoulos, "Novel wide-bandgap non-fullerene acceptors for efficient tandem organic solar cells," *Journal of Materials Chemistry A*, vol. 8, no. 3, pp. 1164–1175, 2020.

[189] A. Yin, D. Zhang, S. H. Cheung, S. K. So, Z. Fu, L. Ying, F. Huang, H. Zhou, and Y. Zhang, "On the understanding of energetic disorder, charge recombination and voltage losses in all-polymer solar cells," *Journal of Materials Chemistry C*, vol. 6, no. 29, pp. 7855–7863, 2018.

[190] C. Xu, M. Wright, D. Ping, H. Yi, X. Zhang, M. A. Mahmud, K. Sun, M. B. Upama, F. Haque, and A. Uddin, "Ternary blend organic solar cells with a non-

fullerene acceptor as a third component to synergistically improve the efficiency," *Organic Electronics*, vol. 62, pp. 261–268, 2018.

[191] C. Zhang, J. Yuan, J. K. W. Ho, J. Song, H. Zhong, Y. Xiao, W. Liu, X. Lu, Y. Zou, and S. K. So, "Correlating the Molecular Structure of A-DA´D-A Type Non-Fullerene Acceptors to Its Heat Transfer and Charge Transport Properties in Organic Solar Cells," *Advanced Functional Materials*, vol. 31, no. 32, p. 2101627, 2021.

[192] C. Zhang, J. Yuan, K. L. Chiu, H. Yin, W. Liu, G. Zheng, J. K. W. Ho, S. Huang, G. Yu, F. Gao, Y. Zou, and S. K. So, "A disorder-free conformation boosts phonon and charge transfer in an electron-deficient-core-based non-fullerene acceptor," *Journal of Materials Chemistry A*, vol. 8, no. 17, pp. 8566–8574, 2020.

[193] H. Yin, S. Chen, P. Bi, X. Xu, S. H. Cheung, X. Hao, Q. Peng, X. Zhu, and S. K. So, "Rationalizing device performance of perylenediimide derivatives as acceptors for bulk-heterojunction organic solar cells," *Organic Electronics*, vol. 65, pp. 156–161, 2019.

[194] B. Urbano, "Characterization of Ternary Organic Solar Cells for Indoor Applications," master thesis, Universität Duisburg-Essen, 2021.

[195] T. Kirchartz, T. Agostinelli, M. Campoy-Quiles, W. Gong, and J. Nelson, "Understanding the Thickness-Dependent Performance of Organic Bulk Heterojunction Solar Cells: The Influence of Mobility, Lifetime, and Space Charge," *Journal of Physical Chemistry Letters*, vol. 3, no. 23, pp. 3470–5, 2012.

[196] D. Lübke, P. Hartnagel, M. Hülsbeck, and T. Kirchartz, "Understanding the Thickness and Light-Intensity Dependent Performance of Green-Solvent Processed Organic Solar Cells," *ACS Materials Au*, vol. 3, no. 3, pp. 215–230, 2023.

[197] C. Kaiser, S. Zeiske, P. Meredith, and A. Armin, "Determining Ultralow Absorption Coefficients of Organic Semiconductors from the Sub-Bandgap Photovoltaic External Quantum Efficiency," *Advanced Optical Materials*, vol. 8, no. 1, p. 1901542, 2019.

[198] R. Steim, T. Ameri, P. Schilinsky, C. Waldauf, G. Dennler, M. Scharber, and C. J. Brabec, "Organic photovoltaics for low light applications," *Solar Energy Materials and Solar Cells*, vol. 95, no. 12, pp. 3256–3261, 2011.

[199] C. M. Proctor and T.-Q. Nguyen, "Effect of leakage current and shunt resistance on the light intensity dependence of organic solar cells," *Applied Physics Letters*, vol. 106, no. 8, p. 083301, 2015.

[200] S. Beuel, P. Hartnagel, and T. Kirchartz, "The Influence of Photo-Induced Space Charge and Energetic Disorder on the Indoor and Outdoor Performance of Organic Solar Cells," *Advanced Theory and Simulations*, vol. 4, no. 3, p. 2000319, 2021.

[201] G. A. H. Wetzelaer, M. Kuik, M. Lenes, and P. W. M. Blom, "Origin of the dark-current ideality factor in polymer:fullerene bulk heterojunction solar cells," *Applied Physics Letters*, vol. 99, no. 15, p. 153506, 2011.

[202] P. Hartnagel and T. Kirchartz, "Understanding the Light-Intensity Dependence of the Short-Circuit Current of Organic Solar Cells," *Advanced Theory and Simulations*, vol. 3, no. 10, p. 2000116, 2020.

[203] P. Schilinsky, C. Waldauf, and C. J. Brabec, "Recombination and loss analysis in polythiophene based bulk heterojunction photodetectors," *Applied Physics Letters*, vol. 81, no. 20, pp. 3885–3887, 2002.

[204] I. Riedel, N. Martin, F. Giacalone, J. L. Segura, D. Chirvase, J. Parisi, and V. Dyakonov, "Polymer solar cells with novel fullerene-based acceptor," *Thin Solid Films*, vol. 451-452, pp. 43–47, 2004.

[205] C. Deibel and A. Wagenpfahl, "Comment on "Interface state recombination in organic solar cells"," *Physical Review B*, vol. 82, no. 20, p. 207301, 2010.

[206] R. A. Street, "Reply to "Comment on 'Interface state recombination in organic solar cells' "," *Physical Review B*, vol. 82, no. 20, p. 207302, 2010.

[207] J. Wu, J. Luke, H. K. H. Lee, P. Shakya Tuladhar, H. Cha, S.-Y. Jang, W. C. Tsoi, M. Heeney, H. Kang, K. Lee, T. Kirchartz, J.-S. Kim, and J. R. Durrant, "Tail state limited photocurrent collection of thick photoactive layers in organic solar cells," *Nature Communications*, vol. 10, no. 1, p. 5159, 2019.

[208] R. S. Crandall, Q. Wang, and E. A. Schiff, "Field collapse due to band-tail charge in amorphous silicon solar cells," in *Conference Record of the Twenty Fifth IEEE Photovoltaic Specialists Conference-1996*, pp. 1113–1116, IEEE, 1996.

[209] A. M. Goodman and A. Rose, "Double Extraction of Uniformly Generated Electron-Hole Pairs from Insulators with Noninjecting Contacts," *Journal of Applied Physics*, vol. 42, no. 7, pp. 2823–2830, 1971.

[210] V. D. Mihailetchi, J. Wildeman, and P. W. M. Blom, "Space-Charge Limited Photocurrent," *Physical Review Letters*, vol. 94, no. 12, p. 126602, 2005.

[211] N. F. Mott and R. W. Gurney, *Electronic processes in ionic crystals*, vol. 1. New York: Oxford University Press, 1948.

[212] S. Wilken, O. J. Sandberg, D. Scheunemann, and R. Österbacka, "Watching Space Charge Build Up in an Organic Solar Cell," *Solar RRL*, vol. 4, no. 3, p. 1900505, 2020.

[213] J. A. Röhr, D. Moia, S. A. Haque, T. Kirchartz, and J. Nelson, "Exploring the validity and limitations of the Mott–Gurney law for charge-carrier mobility determination of semiconducting thin-films," *Journal of Physics: Condensed Matter*, vol. 30, no. 10, p. 105901, 2018.

[214] P. Mark and W. Helfrich, "Space-Charge-Limited Currents in Organic Crystals," *Journal of Applied Physics*, vol. 33, no. 1, pp. 205–215, 1962.

[215] T. Kirchartz, "Influence of diffusion on space-charge-limited current measurements in organic semiconductors," *Beilstein Journal of Nanotechnology*, vol. 4, no. 1, pp. 180–188, 2013.

[216] J. Gao, W. Gao, X. Ma, Z. Hu, C. Xu, X. Wang, Q. An, C. Yang, X. Zhang, and F. Zhang, "Over 14.5% efficiency and 71.6% fill factor of ternary organic solar cells with 300 nm thick active layers," *Energy & Environmental Science*, vol. 13, no. 3, pp. 958–967, 2020.

[217] Y. Zhang, H. Feng, L. Meng, Y. Wang, M. Chang, S. Li, Z. Guo, C. Li, N. Zheng, Z. Xie, X. Wan, and Y. Chen, "High Performance Thick-Film Nonfullerene Organic Solar Cells with Efficiency over 10% and Active Layer Thickness of 600 nm," *Advanced Energy Materials*, vol. 9, no. 45, p. 1902688, 2019.

[218] L. Ma, S. Zhang, H. Yao, Y. Xu, J. Wang, Y. Zu, and J. Hou, "High-Efficiency Nonfullerene Organic Solar Cells Enabled by 1000 nm Thick Active Layers with

a Low Trap-State Density," *ACS Applied Materials & Interfaces*, vol. 12, no. 16, pp. 18777–18784, 2020.

[219] W. Gao, F. Qi, Z. Peng, F. R. Lin, K. Jiang, C. Zhong, W. Kaminsky, Z. Guan, C. S. Lee, T. J. Marks, H. Ade, and A. K. Jen, "Achieving 19% Power Conversion Efficiency in Planar-Mixed Heterojunction Organic Solar Cells Using a Pseudo-Symmetric Electron Acceptor," *Advanced Materials*, vol. 34, p. 2202089, 2022.

[220] C. He, Y. Pan, Y. Ouyang, Q. Shen, Y. Gao, K. Yan, J. Fang, Y. Chen, C.-Q. Ma, J. Min, C. Zhang, L. Zuo, and H. Chen, "Manipulating the D:A interfacial energetics and intermolecular packing for 19.2% efficiency organic photovoltaics," *Energy & Environmental Science*, vol. 15, no. 6, pp. 2537–2544, 2022.

[221] Y. Wei, Z. Chen, G. Lu, N. Yu, C. Li, J. Gao, X. Gu, X. Hao, G. Lu, Z. Tang, J. Zhang, Z. Wei, X. Zhang, and H. Huang, "Binary Organic Solar Cells Breaking 19% via Manipulating Vertical Component Distribution," *Advanced Materials*, vol. 34, no. 33, p. 2204718, 2022.

[222] J. M. Frost, J. Kirkpatrick, T. Kirchartz, and J. Nelson, "Parameter free calculation of the subgap density of states in poly(3-hexylthiophene)," *Faraday Discussions*, vol. 174, pp. 255–66, 2014.

[223] K. Vandewal, K. Tvingstedt, A. Gadisa, O. Inganäs, and J. V. Manca, "Relating the open-circuit voltage to interface molecular properties of donor:acceptor bulk heterojunction solar cells," *Physical Review B*, vol. 81, no. 12, p. 125204, 2010.

[224] J. Yan, E. Rezasoltani, M. Azzouzi, F. Eisner, and J. Nelson, "Influence of static disorder of charge transfer state on voltage loss in organic photovoltaics," *Nature Communications*, vol. 12, no. 1, p. 3642, 2021.

[225] K. Tvingstedt, J. Benduhn, and K. Vandewal, "Temperature dependence of the spectral line-width of charge-transfer state emission in organic solar cells; staticvs.dynamic disorder," *Materials Horizons*, vol. 7, no. 7, pp. 1888–1900, 2020.

[226] T. M. Burke, S. Sweetnam, K. Vandewal, and M. D. McGehee, "Beyond Langevin Recombination: How Equilibrium Between Free Carriers and Charge Transfer States Determines the Open-Circuit Voltage of Organic Solar Cells," *Advanced Energy Materials*, vol. 5, no. 11, p. 1500123, 2015.

[227] F.-J. Kahle, A. Rudnick, H. Bässler, and A. Köhler, "How to interpret absorption and fluorescence spectra of charge transfer states in an organic solar cell," *Materials Horizons*, vol. 5, no. 5, pp. 837–848, 2018.

[228] G. D. Cody, T. Tiedje, B. Abeles, B. Brooks, and Y. Goldstein, "Disorder and the Optical-Absorption Edge of Hydrogenated Amorphous Silicon," *Physical Review Letters*, vol. 47, no. 20, pp. 1480–1483, 1981.

[229] C. Göhler, M. Saladina, Y. Wang, D. Spoltore, J. Benduhn, K. Leo, and C. Deibel, "Temperature-Dependent Charge-Transfer-State Absorption and Emission Reveal the Dominant Role of Dynamic Disorder in Organic Solar Cells," *Physical Review Applied*, vol. 15, no. 6, p. 064009, 2021.

[230] M. Azzouzi, J. Yan, T. Kirchartz, K. Liu, J. Wang, H. Wu, and J. Nelson, "Non-radiative Energy Losses in Bulk-Heterojunction Organic Photovoltaics," *Physical Review X*, vol. 8, no. 3, p. 031055, 2018.

[231] L. Zhang, W. Deng, B. Wu, L. Ye, X. Sun, Z. Wang, K. Gao, H. Wu, C. Duan, F. Huang, and Y. Cao, "Reduced Energy Loss in Non-Fullerene Organic Solar Cells with Isomeric Donor Polymers Containing Thiazole pi-Spacers," *ACS Applied Materials & Interfaces*, vol. 12, no. 1, pp. 753–762, 2020.

[232] C. He, Y. Li, Y. Liu, Y. Li, G. Zhou, S. Li, H. Zhu, X. Lu, F. Zhang, C.-Z. Li, and H. Chen, "Near infrared electron acceptors with a photoresponse beyond 1000 nm for highly efficient organic solar cells," *Journal of Materials Chemistry A*, vol. 8, no. 35, pp. 18154–18161, 2020.

[233] P. K. Nayak, S. Mahesh, H. J. Snaith, and D. Cahen, "Photovoltaic solar cell technologies: analysing the state of the art," *Nature Reviews Materials*, vol. 4, no. 4, pp. 269–285, 2019.

[234] C. Deibel, D. Rauh, and A. Foertig, "Order of decay of mobile charge carriers in P3HT:PCBM solar cells," *Applied Physics Letters*, vol. 103, no. 4, p. 043307, 2013.

[235] S. D. Collins, C. M. Proctor, N. A. Ran, and T.-Q. Nguyen, "Understanding Open-Circuit Voltage Loss through the Density of States in Organic Bulk Heterojunction Solar Cells," *Advanced Energy Materials*, vol. 6, no. 4, p. 1501721, 2016.

[236] H. Wang, Z. Zhang, J. Yu, P. C. Lin, C. C. Chueh, X. Liu, S. Guang, S. Qu, and W. Tang, "Over 15% Efficiency in Ternary Organic Solar Cells by Enhanced Charge Transport and Reduced Energy Loss," *ACS Applied Materials & Interfaces*, vol. 12, no. 19, pp. 21633–21640, 2020.

[237] N. A. Ran, J. A. Love, M. C. Heiber, X. Jiao, M. P. Hughes, A. Karki, M. Wang, V. V. Brus, H. Wang, D. Neher, H. Ade, G. C. Bazan, and T.-Q. Nguyen, "Charge Generation and Recombination in an Organic Solar Cell with Low Energetic Offsets," *Advanced Energy Materials*, vol. 8, no. 5, p. 1701073, 2018.

[238] R. A. Street, Y. Yang, B. C. Thompson, and I. McCulloch, "Capacitance Spectroscopy of Light Induced Trap States in Organic Solar Cells," *Journal of Physical Chemistry C*, vol. 120, no. 39, pp. 22169–22178, 2016.

[239] M. Soldera, K. Taretto, and T. Kirchartz, "Comparison of device models for organic solar cells: Band-to-band vs. tail states recombination," *physica status solidi (a)*, vol. 209, no. 1, pp. 207–215, 2012.

[240] J. Yan, Q. Liang, K. Liu, J. Miao, H. Chen, S. Liu, Z. He, H. Wu, J. Wang, and Y. Cao, "Optimized Phase Separation and Reduced Geminate Recombination in High Fill Factor Small-Molecule Organic Solar Cells," *ACS Energy Letters*, vol. 2, no. 1, pp. 14–21, 2016.

[241] A. Maurano, C. G. Shuttle, R. Hamilton, A. M. Ballantyne, J. Nelson, W. Zhang, M. Heeney, and J. R. Durrant, "Transient Optoelectronic Analysis of Charge Carrier Losses in a Selenophene/Fullerene Blend Solar Cell," *Journal of Physical Chemistry C*, vol. 115, no. 13, pp. 5947–5957, 2011.

[242] T. Ripolles-Sanchis, S. R. Raga, A. Guerrero, M. Welker, M. Turbiez, J. Bisquert, and G. Garcia-Belmonte, "Molecular Electronic Coupling Controls Charge Recombination Kinetics in Organic Solar Cells of Low Bandgap Diketopyrrolopyrrole, Carbazole, and Thiophene Polymers," *Journal of Physical Chemistry C*, vol. 117, no. 17, pp. 8719–8726, 2013.

[243] L. Duan, H. Yi, Y. Zhang, F. Haque, C. Xu, and A. Uddin, "Comparative study of light- and thermal-induced degradation for both fullerene and non-fullerene-based organic solar cells," *Sustainable Energy & Fuels*, vol. 3, no. 3, pp. 723–735, 2019.

[244] L. Duan, Y. Zhang, H. Yi, C. Xu, F. Haque, and A. Uddin, "Degradation Mechanism Identified for the Fullerene and Non-fullerene based Organic Solar Cells under Ambient Condition," in *2019 IEEE 46th Photovoltaic Specialists Conference (PVSC)*, pp. 0461–0464, IEEE.

[245] A. Rana, A. Kumar, N. Vashistha, K. K. Garg, S. Chand, and R. K. Singh, "Origin of depressed fill factor in organic solar cells due to S-shape current–voltage characteristics," *Journal of Applied Physics*, vol. 127, no. 5, p. 053101, 2020.

[246] W. Gong, M. A. Faist, N. J. Ekins-Daukes, Z. Xu, D. D. C. Bradley, J. Nelson, and T. Kirchartz, "Influence of energetic disorder on electroluminescence emission in polymer:fullerene solar cells," *Physical Review B*, vol. 86, no. 2, p. 024201, 2012.

[247] N. Felekidis, A. Melianas, and M. Kemerink, "The Role of Delocalization and Excess Energy in the Quantum Efficiency of Organic Solar Cells and the Validity of Optical Reciprocity Relations," *Journal of Physical Chemistry Letters*, vol. 11, no. 9, pp. 3563–3570, 2020.

[248] W. Deng, K. Gao, J. Yan, Q. Liang, Y. Xie, Z. He, H. Wu, X. Peng, and Y. Cao, "Origin of Reduced Open-Circuit Voltage in Highly Efficient Small-Molecule-Based Solar Cells upon Solvent Vapor Annealing," *ACS Applied Materials & Interfaces*, vol. 10, no. 9, pp. 8141–8147, 2018.

[249] N. Jain, U. Bothra, D. Moghe, A. Sadhanala, R. H. Friend, C. R. McNeill, and D. Kabra, "Negative Correlation between Intermolecular vs Intramolecular Disorder in Bulk-Heterojunction Organic Solar Cells," *ACS Applied Materials & Interfaces*, vol. 10, no. 51, pp. 44576–44582, 2018.

[250] M. B. Upama, M. Wright, B. Puthen-Veettil, N. K. Elumalai, M. A. Mahmud, D. Wang, K. H. Chan, C. Xu, F. Haque, and A. Uddin, "Analysis of burn-in photo degradation in low bandgap polymer PTB7 using photothermal deflection spectroscopy," *RSC Advances*, vol. 6, no. 106, pp. 103899–103904, 2016.

[251] L. Duan, Y. Zhang, H. Yi, F. Haque, C. Xu, S. Wang, and A. Uddin, "Thermal annealing dependent dielectric properties and energetic disorder in PffBT4T-2OD based organic solar cells," *Materials Science in Semiconductor Processing*, vol. 105, p. 104750, 2020.

[252] R. A. Street, "Localized state distribution and its effect on recombination in organic solar cells," *Physical Review B*, vol. 84, no. 7, p. 075208, 2011.

[253] S. M. Menke, A. Sadhanala, M. Nikolka, N. A. Ran, M. K. Ravva, S. Abdel-Azeim, H. L. Stern, M. Wang, H. Sirringhaus, T. Q. Nguyen, J. L. Bredas, G. C. Bazan, and R. H. Friend, "Limits for Recombination in a Low Energy Loss Organic Heterojunction," *ACS Nano*, vol. 10, no. 12, pp. 10736–10744, 2016.

[254] R. C. I. MacKenzie, C. G. Shuttle, G. F. Dibb, N. Treat, E. von Hauff, M. J. Robb, C. J. Hawker, M. L. Chabinyc, and J. Nelson, "Interpreting the Density of States Extracted from Organic Solar Cells Using Transient Photocurrent Measurements," *Journal of Physical Chemistry C*, vol. 117, no. 24, pp. 12407–12414, 2013.

[255] N. Jain, N. Chandrasekaran, A. Sadhanala, R. H. Friend, C. R. McNeill, and D. Kabra, "Interfacial disorder in efficient polymer solar cells: the impact of donor molecular structure and solvent additives," *Journal of Materials Chemistry A*, vol. 5, no. 47, pp. 24749–24757, 2017.

[256] R. A. Street, J. E. Northrup, and B. S. Krusor, "Radiation induced recombination centers in organic solar cells," *Physical Review B*, vol. 85, no. 20, p. 205211, 2012.

[257] Z. M. Beiley, E. T. Hoke, R. Noriega, J. Dacuña, G. F. Burkhard, J. A. Bartelt, A. Salleo, M. F. Toney, and M. D. McGehee, "Morphology-Dependent Trap Formation in High Performance Polymer Bulk Heterojunction Solar Cells," *Advanced Energy Materials*, vol. 1, no. 5, pp. 954–962, 2011.

[258] C. G. Shuttle, A. Maurano, R. Hamilton, B. O'Regan, J. C. de Mello, and J. R. Durrant, "Charge extraction analysis of charge carrier densities in a polythiophene/fullerene solar cell: Analysis of the origin of the device dark current," *Applied Physics Letters*, vol. 93, no. 18, p. 183501, 2008.

[259] A. Maurano, R. Hamilton, C. G. Shuttle, A. M. Ballantyne, J. Nelson, B. O'Regan, W. Zhang, I. McCulloch, H. Azimi, M. Morana, C. J. Brabec, and J. R. Durrant, "Recombination dynamics as a key determinant of open circuit voltage in organic bulk heterojunction solar cells: a comparison of four different donor polymers," *Advanced Materials*, vol. 22, no. 44, pp. 4987–92, 2010.

[260] D. Kiermasch, A. Baumann, M. Fischer, V. Dyakonov, and K. Tvingstedt, "Revisiting lifetimes from transient electrical characterization of thin film solar cells; a capacitive concern evaluated for silicon, organic and perovskite devices," *Energy & Environmental Science*, vol. 11, no. 3, pp. 629–640, 2018.

[261] P. Yu, A. Migan-Dubois, J. Alvarez, A. Darga, V. Vissac, D. Mencaraglia, Y. Zhou, and M. Krueger, "Study of traps in P3HT:PCBM based organic solar cells using fractional thermally stimulated current (FTSC) technique," *Journal of Non-Crystalline Solids*, vol. 358, no. 17, pp. 2537–2540, 2012.

[262] A. Karki, J. Vollbrecht, A. L. Dixon, N. Schopp, M. Schrock, G. N. M. Reddy, and T. Q. Nguyen, "Understanding the High Performance of over 15% Efficiency in Single-Junction Bulk Heterojunction Organic Solar Cells," *Advanced Materials*, vol. 31, no. 48, p. 1903868, 2019.

[263] Y. Zhang, G. Cai, Y. Li, Z. Zhang, T. Li, X. Zuo, X. Lu, and Y. Lin, "An Electron Acceptor Analogue for Lowering Trap Density in Organic Solar Cells," *Advanced Materials*, vol. 33, no. 14, p. 2008134, 2021.

[264] F. Hamada and A. Saeki, "Mobility Relaxation of Holes and Electrons in Polymer:Fullerene and Non-Fullerene Acceptor Solar Cells," *ChemSusChem*, vol. 14, no. 17, pp. 3528–3534, 2021.

[265] T. Yang, R. Ma, H. Cheng, Y. Xiao, Z. Luo, Y. Chen, S. Luo, T. Liu, X. Lu, and H. Yan, "A compatible polymer acceptor enables efficient and stable organic solar cells as a solid additive," *Journal of Materials Chemistry A*, vol. 8, no. 34, pp. 17706–17712, 2020.

[266] X. Chen, B. Kan, Y. Kan, M. Zhang, S. B. Jo, K. Gao, F. Lin, F. Liu, X. Peng, Y. Cao, and A. K. Y. Jen, "As-Cast Ternary Organic Solar Cells Based on an Asymmetric Side-Chains Featured Acceptor with Reduced Voltage Loss and 14.0% Efficiency," *Advanced Functional Materials*, vol. 30, no. 11, p. 1909535, 2020.

[267] L. Duan, M. Guli, Y. Zhang, H. Yi, F. Haque, and A. Uddin, "The Air Effect in the Burn-In Thermal Degradation of Nonfullerene Organic Solar Cells," *Energy Technology*, vol. 8, no. 5, p. 1901401, 2020.

[268] G. K. Poduval, L. Duan, M. A. Hossain, B. Sang, Y. Zhang, Y. Zou, A. Uddin, and B. Hoex, "High-Efficiency Nonfullerene Organic Solar Cells Enabled by Atomic Layer Deposited Zirconium-Doped Zinc Oxide," *Solar RRL*, vol. 4, no. 10, p. 2000241, 2020.

[269] N. Schopp, V. V. Brus, J. Lee, A. Dixon, A. Karki, T. Liu, Z. Peng, K. R. Graham, H. Ade, G. C. Bazan, and T.-Q. Nguyen, "Effect of Palladium-Tetrakis(Triphenylphosphine) Catalyst Traces on Charge Recombination and Extraction in Non-Fullerene-based Organic Solar Cells," *Advanced Functional Materials*, vol. 31, no. 15, p. 2009363, 2021.

[270] Y. N. Chen, M. Li, Y. Wang, J. Wang, M. Zhang, Y. Zhou, J. Yang, Y. Liu, F. Liu, Z. Tang, Q. Bao, and Z. Bo, "A Fully Non-fused Ring Acceptor with Planar Backbone and Near-IR Absorption for High Performance Polymer Solar Cells," *Angewandte Chemie, International Edition in English*, vol. 59, no. 50, pp. 22714–22720, 2020.

[271] K. Zhou, Y. Liu, A. Alotaibi, J. Yuan, C. Jiang, J. Xin, X. Liu, B. A. Collins, F. Zhang, and W. Ma, "Molecular and Energetic Order Dominate the Photocurrent Generation Process in Organic Solar Cells with Small Energetic Offsets," *ACS Energy Letters*, vol. 5, no. 2, pp. 589–596, 2020.

[272] L. Duan, Y. Zhang, M. He, R. Deng, H. Yi, Q. Wei, Y. Zou, and A. Uddin, "Burn-In Degradation Mechanism Identified for Small Molecular Acceptor-Based High-Efficiency Nonfullerene Organic Solar Cells," *ACS Applied Materials & Interfaces*, vol. 12, no. 24, pp. 27433–27442, 2020.

[273] Z. Zhang, Y. Li, G. Cai, Y. Zhang, X. Lu, and Y. Lin, "Selenium Heterocyclic Electron Acceptor with Small Urbach Energy for As-Cast High-Performance Organic Solar Cells," *Journal of the American Chemical Society*, vol. 142, no. 44, pp. 18741–18745, 2020.

[274] T. Wang, M. S. Niu, Z. C. Wen, Z. N. Jiang, C. C. Qin, X. Y. Wang, H. Y. Liu, X. Y. Li, H. Yin, J. Q. Liu, and X. T. Hao, "High-Efficiency Thickness-Insensitive Organic Solar Cells with an Insulating Polymer," *ACS Applied Materials & Interfaces*, vol. 13, no. 9, pp. 11134–11143, 2021.

[275] G. Garcia-Belmonte, P. P. Boix, J. Bisquert, M. Sessolo, and H. J. Bolink, "Simultaneous determination of carrier lifetime and electron density-of-states in P3HT:PCBM organic solar cells under illumination by impedance spectroscopy," *Solar Energy Materials and Solar Cells*, vol. 94, no. 2, pp. 366–375, 2010.

[276] M. C. Heiber, T. Okubo, S.-J. Ko, B. R. Luginbuhl, N. A. Ran, M. Wang, H. Wang, M. A. Uddin, H. Y. Woo, G. C. Bazan, and T.-Q. Nguyen, "Measuring the competition between bimolecular charge recombination and charge transport in organic solar cells under operating conditions," *Energy & Environmental Science*, vol. 11, no. 10, pp. 3019–3032, 2018.

[277] C. M. Proctor, C. Kim, D. Neher, and T.-Q. Nguyen, "Nongeminate Recombination and Charge Transport Limitations in Diketopyrrolopyrrole-Based Solution-Processed Small Molecule Solar Cells," *Advanced Functional Materials*, vol. 23, no. 28, pp. 3584–3594, 2013.

[278] J. Vollbrecht and V. V. Brus, "On Charge Carrier Density in Organic Solar Cells Obtained via Capacitance Spectroscopy," *Advanced Electronic Materials*, vol. 6, no. 10, p. 2000517, 2020.

[279] M. Burgelman, K. Decock, S. Khelifi, and A. Abass, "Advanced electrical simulation of thin film solar cells," *Thin Solid Films*, vol. 535, pp. 296–301, 2013.

[280] C. Kaiser, O. J. Sandberg, N. Zarrabi, W. Li, P. Meredith, and A. Armin, "A universal Urbach rule for disordered organic semiconductors," *Nature Communications*, vol. 12, no. 1, pp. 1–9, 2021.

[281] A. M. Kay, O. J. Sandberg, N. Zarrabi, W. Li, S. Zeiske, C. Kaiser, P. Meredith, and A. Armin, "Quantifying the Excitonic Static Disorder in Organic Semiconductors," *Advanced Functional Materials*, vol. 32, no. 32, p. 2113181, 2022.

[282] G. Zhang, R. Xia, Z. Chen, J. Xiao, X. Zhao, S. Liu, H.-L. Yip, and Y. Cao, "Overcoming Space-Charge Effect for Efficient Thick-Film Non-Fullerene Organic Solar Cells," *Advanced Energy Materials*, vol. 8, no. 25, p. 1801609, 2018.

[283] A. Fell, K. R. McIntosh, P. P. Altermatt, G. J. M. Janssen, R. Stangl, A. Ho-Baillie, H. Steinkemper, J. Greulich, M. Muller, B. Min, K. C. Fong, M. Hermle, I. G. Romijn, and M. D. Abbott, "Input Parameters for the Simulation of Silicon

Solar Cells in 2014," *IEEE Journal of Photovoltaics*, vol. 5, no. 4, pp. 1250–1263, 2015.

[284] P. P. Altermatt, "Models for numerical device simulations of crystalline silicon solar cells—a review," *Journal of Computational Electronics*, vol. 10, no. 3, pp. 314–330, 2011.

[285] Z. Tang, J. Wang, A. Melianas, Y. Wu, R. Kroon, W. Li, W. Ma, M. R. Andersson, Z. Ma, W. Cai, W. Tress, and O. Inganäs, "Relating open-circuit voltage losses to the active layer morphology and contact selectivity in organic solar cells," *Journal of Materials Chemistry A*, vol. 6, no. 26, pp. 12574–12581, 2018.

[286] N. Majeed, M. Saladina, M. Krompiec, S. Greedy, C. Deibel, and R. C. I. MacKenzie, "Using Deep Machine Learning to Understand the Physical Performance Bottlenecks in Novel Thin-Film Solar Cells," *Advanced Functional Materials*, vol. 30, no. 7, 2019.

[287] Y. Li, Y. Li, J. Shi, L. Lou, X. Xu, Y. Cui, J. Wu, D. Li, Y. Luo, H. Wu, Q. Shen, and Q. Meng, "Accelerating defect analysis of solar cells via machine learning of the modulated transient photovoltage," *Fundamental Research*, 2023.

[288] T. Bayes and R. Price, "LII. An essay towards solving a problem in the doctrine of chances. By the late Rev. Mr. Bayes, F. R. S. communicated by Mr. Price, in a letter to John Canton, A. M. F. R. S," *Philosophical Transactions of the Royal Society of London*, vol. 53, pp. 370–418, 1763.

[289] R. E. Brandt, R. C. Kurchin, V. Steinmann, D. Kitchaev, C. Roat, S. Levcenco, G. Ceder, T. Unold, and T. Buonassisi, "Rapid Photovoltaic Device Characterization through Bayesian Parameter Estimation," *Joule*, vol. 1, no. 4, pp. 843–856, 2017.

[290] A. Raba, Y. Leroy, M. Kohlstadt, U. Wurfel, and A.-S. Cordan, "Organic Solar Cells: Extraction of Physical Parameters by Means of Markov Chain Monte Carlo Techniques," *IEEE Journal of Photovoltaics*, vol. 7, no. 4, pp. 1098–1104, 2017.

[291] C. Fai, A. J. C. Ladd, and C. J. Hages, "Machine learning for enhanced semiconductor characterization from time-resolved photoluminescence," *Joule*, vol. 6, no. 11, pp. 2585–2610, 2022.

[292] R. Kurchin, G. Romano, and T. Buonassisi, "Bayesim: A tool for adaptive grid model fitting with Bayesian inference," *Computer Physics Communications*, vol. 239, pp. 161–165, 2019.

[293] Z. Ren, F. Oviedo, M. Thway, S. I. P. Tian, Y. Wang, H. Xue, J. Dario Perea, M. Layurova, T. Heumueller, E. Birgersson, A. G. Aberle, C. J. Brabec, R. Stangl, Q. Li, S. Sun, F. Lin, I. M. Peters, and T. Buonassisi, "Embedding physics domain knowledge into a Bayesian network enables layer-by-layer process innovation for photovoltaics," *npj Computational Materials*, vol. 6, no. 1, p. 9, 2020.

[294] B. Das, "Defect tolerant device geometries for lead-halide perovskite solar cells," thesis, Rheinisch-Westfälischen Technischen Hochschule Aachen, 2022.

[295] A. Mahmood and J.-L. Wang, "Machine learning for high performance organic solar cells: current scenario and future prospects," *Energy & Environmental Science*, vol. 14, no. 1, pp. 90–105, 2021.

[296] P. B. Jorgensen, M. Mesta, S. Shil, J. M. Garcia Lastra, K. W. Jacobsen, K. S. Thygesen, and M. N. Schmidt, "Machine learning-based screening of complex molecules for polymer solar cells," *Journal of chemical physics*, vol. 148, no. 24, p. 241735, 2018.

[297] D. Padula, J. D. Simpson, and A. Troisi, "Combining electronic and structural features in machine learning models to predict organic solar cells properties," *Materials Horizons*, vol. 6, no. 2, pp. 343–349, 2019.

[298] Y. Wu, J. Guo, R. Sun, and J. Min, "Machine learning for accelerating the discovery of high-performance donor/acceptor pairs in non-fullerene organic solar cells," *npj Computational Materials*, vol. 6, no. 1, p. 120, 2020.

[299] A. Mahmood, A. Irfan, and J.-L. Wang, "Machine learning and molecular dynamics simulation-assisted evolutionary design and discovery pipeline to screen efficient small molecule acceptors for PTB7-Th-based organic solar cells with over 15% efficiency," *Journal of Materials Chemistry A*, vol. 10, no. 8, pp. 4170–4180, 2022.

[300] B. L. Greenstein and G. R. Hutchison, "Screening Efficient Tandem Organic Solar Cells with Machine Learning and Genetic Algorithms," *The Journal of Physical Chemistry C*, vol. 127, no. 13, pp. 6179–6191, 2023.

[301] N. G. An, J. Y. Kim, and D. Vak, "Machine learning-assisted development of organic photovoltaics via high-throughput in situ formulation," *Energy & Environmental Science*, vol. 14, no. 6, pp. 3438–3446, 2021.

[302] X. Rodríguez-Martínez, E. Pascual-San-José, Z. Fei, M. Heeney, R. Guimerà, and M. Campoy-Quiles, "Predicting the photocurrent–composition dependence in organic solar cells," *Energy & Environmental Science*, vol. 14, no. 2, pp. 986–994, 2021.

[303] B. Cao, L. A. Adutwum, A. O. Oliynyk, E. J. Luber, B. C. Olsen, A. Mar, and J. M. Buriak, "How To Optimize Materials and Devices via Design of Experiments and Machine Learning: Demonstration Using Organic Photovoltaics," *ACS Nano*, vol. 12, no. 8, pp. 7434–7444, 2018.

[304] A. Kirkey, E. J. Luber, B. Cao, B. C. Olsen, and J. M. Buriak, "Optimization of the Bulk Heterojunction of All-Small-Molecule Organic Photovoltaics Using Design of Experiment and Machine Learning Approaches," *ACS Applied Materials & Interfaces*, vol. 12, no. 49, pp. 54596–54607, 2020.

[305] X. Du, L. Lüer, T. Heumueller, J. Wagner, C. Berger, T. Osterrieder, J. Wortmann, S. Langner, U. Vongsaysy, M. Bertrand, N. Li, T. Stubhan, J. Hauch, and C. J. Brabec, "Elucidating the Full Potential of OPV Materials Utilizing a High-Throughput Robot-Based Platform and Machine Learning," *Joule*, vol. 5, no. 2, pp. 495–506, 2021.

[306] I. M. Sobol', "On the distribution of points in a cube and the approximate evaluation of integrals," *Zhurnal Vychislitel'noi Matematiki i Matematicheskoi Fiziki*, vol. 7, no. 4, pp. 784–802, 1967.

[307] K. Fukushima, "Neocognitron: A self-organizing neural network model for a mechanism of pattern recognition unaffected by shift in position," *Biological cybernetics*, vol. 36, no. 4, pp. 193–202, 1980.

[308] Z. Li, F. Liu, W. Yang, S. Peng, and J. Zhou, "A Survey of Convolutional Neural Networks: Analysis, Applications, and Prospects," *IEEE transactions on neural networks and learning systems*, vol. 33, no. 12, pp. 6999–7019, 2022.

[309] N. Hansen, "The CMA evolution strategy: a comparing review," *Towards a new evolutionary computation: Advances in the estimation of distribution algorithms*, pp. 75–102, 2006.

[310] N. Hansen, A. Auger, R. Ros, S. Finck, and P. Pošík, "Comparing results of 31 algorithms from the black-box optimization benchmarking BBOB-2009," in *Proceedings of the 12th annual conference companion on Genetic and evolutionary computation*, pp. 1689–1696.

[311] A. Foertig, J. Rauh, V. Dyakonov, and C. Deibel, "Shockley equation parameters of P3HT:PCBM solar cells determined by transient techniques," *Physical Review B*, vol. 86, no. 11, p. 115302, 2012.

[312] S. Torabi, M. Cherry, E. A. Duijnstee, V. M. Le Corre, L. Qiu, J. C. Hummelen, G. Palasantzas, and L. J. A. Koster, "Rough Electrode Creates Excess Capacitance in Thin-Film Capacitors," *ACS Applied Materials & Interfaces*, vol. 9, no. 32, pp. 27290–27297, 2017.

[313] Y. Cui, L. Hong, T. Zhang, H. Meng, H. Yan, F. Gao, and J. Hou, "Accurate photovoltaic measurement of organic cells for indoor applications," *Joule*, vol. 5, no. 5, pp. 1016–1023, 2021.

[314] X. Rodríguez-Martínez, P. Hartnagel, S. Riera-Galindo, G. Beket, T. Österberg, F. Gao, T. Kirchartz, and O. Inganäs, "Air Processing of Thick and Semitransparent Laminated Polymer:Non-Fullerene Acceptor Blends Introduces Asymmetric Current–Voltage Characteristics," *Advanced Functional Materials*, p. 2301192, 2023.

A
Appendix

A.1. List of Symbols

Symbol	Name
A	Area of the solar cell
a	Absorptance
C	Capacitance
c	Speed of light
C_{dark}	Capacitance in the dark
$C_{\mathrm{eff,ana}}$	Effective capacitance calculated with an analytical approach
$C_{\mathrm{eff,cir}}$	Effective capacitance calculated with an equivalent circuit
C_{geo}	Geometric capacitance
C_{σ}	Electrode capacitance
C_{μ}	Chemical capacitance
$C_{\mu,\mathrm{ana}}$	Analytical approximation of the chemical capacitance
d	Active layer thickness
D_{n}	Diffusion constant of electrons
D_{p}	Diffusion constant of holes
E	Energy
E_{abs}	Energy absorbed during electron excitation

Symbol	**Name**
E_{C}	Energy of the conduction-band edge
E_{dt}	Energy level deep traps
E_{e}	Irradiance
$E_{\mathrm{e},\lambda}$	Spectral irradiance
E_{em}	Energy emitted during electron recombination
E_{F}	Fermi-level energy
E_{g}	Band gap energy
$E_{\mathrm{HOMO,don}}$	Energy of the highest occupied molecular orbital of the donor
$E_{\mathrm{HOMO,acc}}$	Energy of the highest occupied molecular orbital of the acceptor
$E_{\mathrm{LUMO,don}}$	Energy of the lowest unoccupied molecular orbital of the donor
$E_{\mathrm{LUMO,acc}}$	Energy of the lowest unoccupied molecular orbital of the acceptor
E_{m}	Illuminance
e_{n}	Emission coefficient for trapped electrons
e_{p}	Emission coefficient for trapped holes
E_{qFn}	Energy of the quasi-Fermi level of electrons
E_{qFp}	Energy of the quasi-Fermi level of holes
E_{re}	Reorganization energy
E_{U}	Urbach energy
$E_{\mathrm{U,1}}$	Urbach energy of the steep Urbach tail
$E_{\mathrm{U,2}}$	Urbach energy of the shallow Urbach tail
$E_{\mathrm{U,app}}$	Apparent Urbach energy
$E_{\mathrm{U,CV}}$	Urbach energy from capacitance-voltage measurements
$E_{\mathrm{U,CVd}}$	Urbach energy from capacitance-voltage measurements in the dark
$E_{\mathrm{U,CVi}}$	Urbach energy from capacitance-voltage measurements under illumination
$E_{\mathrm{U,FTPS}}$	Urbach energy from Fourier-transform photocurrent spectroscopy
$E_{\mathrm{U,PDS}}$	Urbach energy from photothermal deflection spectroscopy

Symbol	Name
E_V	Energy of the valence-band edge
F	Electric field
f	Frequency
FF	Fill factor
G	Generation rate
g	Energy-dependent generation rate
$\bar{G}$	Steady-state generation rate
G_av	Spatial average of the generation rate
h	Planck's constant
I_LED	LED driving current
J	Current density
$\tilde{J}$	Out-of-phase contribution to the current density
J_0	Saturation-current density
$J_{0,\mathrm{SQ}}$	Saturation-current density in the Shockley-Queisser model
$J_{\mathrm{d,SQ}}$	Dark current density in the Shockley-Queisser model
J_gen	Generation-current density
J_n	Electron-current density
$\bar{J}_\mathrm{n}$	Steady-state electron current density
$\hat{J}_\mathrm{n}$	Out-of-phase contribution of the electron-current density
$\tilde{J}_\mathrm{n}$	Out-of-phase contribution of the electron-current density in frequency domain
$J_\mathrm{n,diff}$	Diffusion-current density of electrons
$J_\mathrm{n,drift}$	Drift-current density of electrons
J_mpp	Current density at maximum power point
J_p	Hole-current density
$J_\mathrm{p,diff}$	Diffusion-current density of holes
$J_\mathrm{p,drift}$	Drift-current density of holes

Symbol	**Name**
J_{ph}	Photocurrent density
$J_{\mathrm{ph,MH}}$	Photocurrent density derived from the Mark-Helfrich equation
J_{rec}	Recombination-current density
$J_{\mathrm{rec,dir}}$	Recombination-current density from direct recombination
$J_{\mathrm{rec,SQ}}$	Recombination-current density in the Shockley-Queisser model
$J_{\mathrm{rec,SRH}}$	Recombination-current density from Shockley-Read-Hall recombination
$J_{\mathrm{rec,sur}}$	Recombination-current density from surface recombination
J_{sc}	Short-circuit current density
$J_{\mathrm{sc,M}}$	Short-circuit current density measured under an LED
$J_{\mathrm{sc,max}}$	Maximum short-circuit current density
$J_{\mathrm{sc,Q}}$	Short-circuit current density calculated with the external quantum efficiency
$J_{\mathrm{sc,SQ}}$	Short-circuit current density in the Shockley-Queisser model
J_{SCL}	Space-charge limited current density
$J_{\mathrm{SCL,MH}}$	Space-charge limited current density according to Mark and Helfrich
J_{SQ}	Total current density in the Shockley-Queisser model
k	Recombination coefficient
k_{B}	Boltzmann constant
k_{dir}	Direct recombination coefficient
K_{m}	Scaling factor for luminous efficacy
l	Exponent for Mark-Helfrich equation
L_{drift}	Drift length
M	Luminous efficacy
m_1	Coefficient for first-order recombination
m_2	Coefficient for second-order recombination
n	Electron concentration
$\bar{n}$	Steady-state contribution to the electron density

Symbol	Name
$\hat{n}$	Out-of-phase contribution of the electron density
$\tilde{n}$	Out-of-phase contribution of the electron density in frequency domain
n_{av}	Spatial average of the electron concentration
N_{C}	Effective density of states in the conduction band
N_{CBT}	Density of conduction-band tail states
N_{dt}	Density of deep defect states
$N_{\mathrm{eff,CBT}}$	Effective density of conduction-band tail states
$N_{\mathrm{eff,VBT}}$	Effective density of valence-band tail states
n_{i}	Intrinsic charge-carrier density
n_{id}	Ideality factor
n_{ph}	Photogenerated electron density
N_{t}	Density of trap states
N_{VBT}	Density of valence-band tail states
n_{T}	Trapped electron density
n_{tot}	Total electron density
N_{V}	Effective density of states in the valence band
P	Power density
p	Hole concentration
p_{av}	Spatial average of the hole density
p_{i}	Intrinsic hole density
p_{ph}	Photogenerated hole density
P_{SQ}	Power density in the Shockley-Queisser model
p_{T}	Trapped hole density
Q	Nuclear coordinate
q	Elementary charge
Q_{e}	External quantum efficiency
R	Resistance

Symbol	**Name**
R_p	Parallel resistance
R_rec	Recombination resistance
R_s	Series resistance
S	Surface recombination velocity
S_n	Surface recombination velocity of electrons
S_p	Surface recombination velocity of holes
T	Temperature
t	Time
t_run	Runtime
T_SC	Temperature of the solar cell
T_sur	Temperature of the surrounding
U	Recombination rate
U_av	Spatial average of the recombination rate
$\bar{U}$	Steady-state contribution to the recombination rate
$\hat{U}$	Out-of-phase contribution of the recombination rate
$\tilde{U}$	Out-of-phase contribution of the recombination rate in frequency domain
u_1	Rate of electron capture
u_2	Rate of electron emission
u_3	Hole capture rate
u_4	Hole emission rate
U_dir	Rate of direct, bimolecular recombination
U_SRH	Rate of Shockley-Read-Hall recombination
$U_\mathrm{av,SRH}$	Spatial average of the Shockley-Read-Hall recombination rate
$U_\mathrm{SRH,max}$	Maximum Shockley-Read-Hall recombination rate
$U_\mathrm{sur}\delta x$	Rate of recombination at the surface
U_tail	Recombination rate via tail states
$U_\mathrm{av,tail}$	Spatial average of the recombination rate via tail states

Symbol	Name
V	Voltage
V_{bi}	Built-in voltage
V_{ext}	External voltage
$\bar{V}_{\mathrm{ext}}$	Steady state external voltage
$\tilde{V}_{\mathrm{ext}}$	Out-of-phase contribution of the external voltage in the frequency domain
V_{int}	Internal voltage
$\bar{V}_{\mathrm{int}}$	Steady state internal voltage
$\tilde{V}_{\mathrm{int}}$	Out-of-phase contribution of the internal voltage in the frequency domain
V_{mpp}	Voltage at maximum power point
V_{oc}	Open-circuit voltage
$V_{\mathrm{oc,dir}}$	Open-circuit voltage for direct recombination
$V_{\mathrm{oc,SQ}}$	Open-circuit voltage in the Shockley-Queisser model
$V_{\mathrm{oc,SRH}}$	Open-circuit voltage for Shockley-Read-Hall recombination
w_{SCR}	Width of the space-charge region
x	Position in the active layer
x_{an}	Position of the anode
x_{cat}	Position of the cathode
Y	Admittance
$\hat{y}$	Example function in time domain
$\tilde{y}$	Example function in frequency domain
Z	Dynamic range of shifted current-density voltage curves
α	Absorption coefficient
β_1	Valence-band tail hole capture coefficient, conduction-band tail electron capture coefficient
β_2	Valence-band tail electron capture coefficient, conduction-band tail hole capture coefficient
β_{dt}	Capture coefficient deep traps

Symbol	Name
γ	Double-logarithmic slope of the short-circuit current density with irradiance
γ_{MH}	Slope of the double-logarithmic plot of the short-circuit current density derived from the Mark-Helfrich equation
δ	Recombination order
ΔE_{dt}	Deep trap Gaussian width
ε_0	Vacuum permittivity
ε_{r}	Relative permittivity
φ	Electrostatic potential
Φ	Photon flux
$\Phi_{\mathrm{AM1.5}}$	Photon flux by the sun according to the AM1.5G solar spectrum
ϕ_{an}	Injection barrier at the anode
Φ_{bb}	Photon flux of a black body
ϕ_{cat}	Injection barrier at the cathode
Φ_{sur}	Photon flux from the surrounding
η	Power-conversion efficiency
η_{SQ}	Power-conversion efficiency in the Shockley-Queisser model
θ	Occupation probability
$\theta_{\mathrm{SRH,n}}$	Occupation probability for electrons according to Shockley-Read-Hall statistics
$\theta_{\mathrm{SRH,p}}$	Occupation probability for holes according to Shockley-Read-Hall statistics
κ	Extinction coefficient
λ	Wavelength
μ	Charge carrier mobility
μ_{n}	Electron mobility
μ_{p}	Hole mobility
ν	Refractive index

Symbol	Name
ρ	Charge density
σ	Width of the Gaussian distribution of the singlet state
τ_{n}	Lifetime of electrons
τ_{p}	Lifetime of holes
ω	Angular frequency
ψ	Angle of deflection in photothermal deflection spectroscopy

A.2. Supplementary Tables

Table A.1: Simulation parameters for the solar cells modeled in ASA specific to Chapter 5. The simulations for a thin device contain a variation of the generation rate that is constant throughout the active layer. The parameters adapted for a thick device are listed in brackets. For these simulations, the generation rate is generated by ASA under AM1.5G spectrum and varied in intensity.

Parameter	Simulation with direct rec.	Simulation with rec. via tail states	Simulations with rec. via deep traps
Active layer thickness d (nm)	100 (300)	100 (300)	100 (300)
Electron/hole mobility $\mu_{\mathrm{n/p}}$ ($\mathrm{cm^2\,V^{-1}\,s^{-1}}$)	8×10^{-4} (3×10^{-3})	8×10^{-4} (3×10^{-3})	8×10^{-4} (3×10^{-3})
Direct recombination coefficient k_{dir} ($\mathrm{cm^3\,s^{-1}}$)	2×10^{11}	-	-
Urbach energy E_{U} (meV)	-	30/55/80	-
Density of deep defect states N_{dt} ($\mathrm{cm^{-3}}$)	-	-	10^{16}

Table A.2: Urbach energies reported in literature for bulk-heterojunction systems. The energetic disorder was characterized by the following methods: Transient-photocurrent measurements (TPC), charge-extraction measurements (CE), Fourier-transform photocurrent spectroscopy (FTPS), photothermal deflection spectroscopy (PDS), capacitance-voltage measurements (CV), external quantum efficiency measurements (EQE), fitting with simulations (Sim), thermally stimulated current measurements (TSC), fractional thermally stimulated current measurements (FTSC), photoabsorption spectroscopy (PAS), capacitance-frequency measurements (Cf), and space-charge limited current measurements (SCLC). The energy range is probed by optical or thermal excitation, by voltage or frequency variation or by the time-dependence of the signal. Those Urbach energies marked with * were not stated explicitly but calculated from a slope that was reported in the reference.

Material system	Urbach Energy E_U (meV)	Method	Scan type	Ref.
BIT-4F:PC71BM	250*	TPC	Time	[240]
BTR:PC71BM	35	CE	Voltage	[207]
D18:Y6	25.2	FTPS	Optical	[263]
D18:Y6	24.8	FTPS	Optical	[273]
D18:Y6:BTPR	24.9	FTPS	Optical	[263]
D18:Y6Se	21.8	FTPS	Optical	[273]
DF-P3HT:PC61BM	50	PDS	Optical	[20]
DPP1:PC71BM	32*	CV	Voltage	[235]
DPP2:PC71BM	36*	CV	Voltage	[235]
DPP3:PC71BM	34.5*	CV	Voltage	[235]
DPP860:PC71BM	29.5*	CV	Voltage	[242]
DPPEZnP-THD:PC61BM	36	EQE	Optical	[248]
DT-PDPP2T-TT:PC71BM	48	CE	Voltage	[207]
DTS:N2200	25.5*	CV	Voltage	[235]
DTS:PC71BM	28.5*	CV	Voltage	[235]
MDMO-PPV:PC61BM	95	Sim	-	[239]

(to be continued)

Material system	Urbach Energy E_U (meV)	Method	Scan type	Ref.
MDMO-PPV:PC61BM	45	EQE	Optical	[233]
MDMO-PPV:PC61BM	43	EQE	Optical	[246]
MEH-PPV:PC61BM	74	Sim	-	[239]
P1:PC71BM	35.8	PDS	Optical	[189]
P3HS:PC61BM	37.2*	CE	Voltage	[259]
P3HT:PC61BM	32	EQE	Optical	[79]
P3HT:PC61BM	31	Sim	-	[239]
P3HT:PC61BM	38.5*	CE	Voltage	[241]
P3HT:PC61BM	53.8*	CE	Voltage	[258]
P3HT:PC61BM	67.6*	CE	Voltage	[258]
P3HT:PC61BM	40	CE	Voltage	[234]
P3HT:PC61BM	37	EQE	Optical	[252]
P3HT:PC61BM	35	TPC	Time	[252]
P3HT:PC61BM	65	TPC	Time	[252]
P3HT:PC61BM	37	EQE	Optical	[246]
P3HT:PC61BM	57	TSC	Thermal	[311]
P3HT:PC61BM	42.9*	CE	Voltage	[259]
P3HT:PC61BM	60	TPC	Time	[254]
P3HT:PC61BM	62*	CE	Voltage	[260]
P3HT:PC61BM	30	FTSC	Thermal	[261]
P3HT:PC61BM	30	FTSC	Thermal	[261]
P3HT:PC71BM	37.1*	CV	Voltage	[242]
P3HT:PC71BM	109.9	PDS	Optical	[250]
P3TEA:PC71BM	27	PDS	Optical	[186]
P3TEA:SF-PDI2	27	PDS	Optical	[186]

(to be continued)

Material system	Urbach Energy E_U (meV)	Method	Scan type	Ref.
P3TEA:SF-PDI2	27	EQE	Optical	[233]
PBDB-T:H1	24.5	FTPS	Optical	[232]
PBDB-T:H2	24.7	FTPS	Optical	[232]
PBDB-T:H3	23.3	FTPS	Optical	[232]
PBDB-T:IDTA	37.2	PDS	Optical	[188]
PBDB-T:IDTTA	36.5	PDS	Optical	[188]
PBDB-T:IT-4F	40.8	FTPS	Optical	[231]
PBDB-T:ITIC	78	PAS	Optical	[264]
PBDB-T:ITIC	34.4	PDS	Optical	[187]
PBDB-T:ITIC	35.2	PDS	Optical	[187]
PBDB-T:ITIC	60	CE	Voltage	[118]
PBDB-T:m-4TBC-2F	38.7	FTPS	Optical	[270]
PBDB-T:N2200	29.6	PDS	Optical	[189]
PBDB-T:o-4TBC-2F	24.5	FTPS	Optical	[270]
PBDB-T:Y6	41	PAS	Optical	[264]
PBDB-TF:BTP-4Cl	26.3	EQE	Optical	[218]
PBDB-TF:BTP-4Cl	23.2	EQE	Optical	[218]
PBDB-TF:BTP-eC11	24.2	EQE	Optical	[40]
PBDB-TF:BTP-eC7	24.3	EQE	Optical	[40]
PBDB-TF:BTP-eC9	24.1	EQE	Optical	[40]
PBDB-TF:IT-4F	34.2	EQE	Optical	[218]
PBDB-TF:IT-4F	32.2	EQE	Optical	[218]
PBDBTz-2:IT-4F	25.5	FTPS	Optical	[231]
PBDBTz-5:IT-4F	25.3	FTPS	Optical	[231]
PBDTT-DPP:PC61BM	27	EQE	Optical	[79]

(to be continued)

Material system	Urbach Energy E_U (meV)	Method	Scan type	Ref.
PBDTT-DPP:PC61BM	30	Cf	Frequency	[238]
PBDTT-DPP:PC61BM	30	EQE	Optical	[238]
PBDTT-FTTE:m-ITIC	75	CE	Voltage	[118]
PBDTT-FTTE:O-IDTBR	77	CE	Voltage	[118]
PBDTTPD:PC61BM	36	EQE	Optical	[233]
PCDTBT:PC61BM	47	EQE	Optical	[79]
PCDTBT:PC61BM	45	Cf	Frequency	[238]
PCDTBT:PC61BM	45	EQE	Optical	[238]
PCDTBT:PC61BM	45	FTPS	Optical	[247]
PCDTBT:PC61BM	62*	CE	Voltage	[260]
PCDTBT:PC71BM	79	Sim	-	[239]
PCDTBT:PC71BM	40.6*	CV	Voltage	[242]
PCDTBT:PC71BM	75	CE	Voltage	[207]
PCDTBT:PC71BM	45	EQE	Optical	[252]
PCDTBT:PC71BM	45	TPC	Time	[252]
PCDTBT:PC71BM	45	EQE	Optical	[78]
PCDTBT:PC71BM	44.2	EQE	Optical	[256]
PCDTBT:PC71BM	44	SCLC	Voltage	[257]
PCDTBT:PC71BM	54.9	PDS	Optical	[189]
PCPDTBT:PC71BM	70.1*	CE	Voltage	[259]
PCPDTBT:PC71BM	42.7	EQE	Optical	[249]
PCPDTBT:PC71BM	50.5	EQE	Optical	[249]
PCPDTBT:PC71BM	40.2	EQE	Optical	[255]
PCPDTBT:PC71BM	53.4	EQE	Optical	[255]
PDCBT-2F:IT-M	24	EQE	Optical	[233]

(to be continued)

Material system	Urbach Energy E_U (meV)	Method	Scan type	Ref.
PDPP2FT:PC71BM	85	TPC	Time	[254]
PDTTT-EFT:EH-IDTBR	42.9*	CE	Voltage	[178]
PF10TBT:PC61BM	44	Sim	-	[239]
PffBT4T-2OD:EH-IDTBR	76	CE	Voltage	[118]
PffBT4T-2OD:IDFBR	39	PDS	Optical	[190]
PffBT4T-2OD:PC71BM	31.1	EQE	Optical	[251]
PffBT4T-2OD:PC71BM	36	PDS	Optical	[190]
PffBT4T-2OD:PC71BM:IDFBR	32.8	PDS	Optical	[190]
PIPCP:PC61BM	27	EQE	Optical	[237]
PIPCP:PC61BM	27	EQE	Optical	[185]
PIPCP:PC61BM	27	PDS	Optical	[185]
PIPCP:PC61BM	27	PDS	Optical	[253]
PM6:BTP-4Cl	28	CE	Voltage	[118]
PM6:BZ4F-5	31.2	PDS	Optical	[191]
PM6:BZ4F-6	25.6	PDS	Optical	[191]
PM6:BZ4F-7	22.9	PDS	Optical	[191]
PM6:IDIC	46	EQE	Optical	[266]
PM6:IDIC	26	EQE	Optical	[266]
PM6:N3	26.2	EQE	Optical	[268]
PM6:N3	25.4	EQE	Optical	[272]
PM6:PC71BM	46.5	EQE	Optical	[181]
PM6:PC71BM	46.7	FTPS	Optical	[181]
PM6:PIDTC-T	42.8	EQE	Optical	[265]
PM6:TOBDT	64	EQE	Optical	[266]
PM6:TOBDT	35	EQE	Optical	[266]

(to be continued)

Material system	Urbach Energy E_U (meV)	Method	Scan type	Ref.
PM6:TOBDT:IDIC	53	EQE	Optical	[266]
PM6:TOBDT:IDIC	24	EQE	Optical	[266]
PM6:Y11	25.6	EQE	Optical	[181]
PM6:Y11	24.8	FTPS	Optical	[181]
PM6:Y18	22.4	PDS	Optical	[192]
PM6:Y3	27.7	PDS	Optical	[192]
PM6:Y6	26.7	EQE	Optical	[262]
PM6:Y6	30.5	EQE	Optical	[265]
PM6:Y6	28.7	SCLC	Voltage	[274]
PM6:Y6	27	CE	Voltage	[118]
PM6:Y6:PIDTC-T	29.4	EQE	Optical	[265]
PM6:Y6:PP	25.2	SCLC	Voltage	[274]
PM7-LR:N2200	34.4	EQE	Optical	[271]
PM7-MR:N2200	30.2	EQE	Optical	[271]
PM7-SR:N2200	28.9	EQE	Optical	[271]
PTB7:PC71BM	54.6	PDS	Optical	[183]
PTB7:PC71BM	48	EQE	Optical	[255]
PTB7:PC71BM	42	EQE	Optical	[255]
PTB7:PC71BM	48.9	PDS	Optical	[250]
PTB7:PC71BM:DTS	49.9	PDS	Optical	[183]
PTB7-Th:1PDI-ZnP	49.1	PDS	Optical	[193]
PTB7-Th:2PDI-ZnP	42.7	PDS	Optical	[193]
PTB7-Th:4PDI-ZnP	38.1	PDS	Optical	[193]
PTB7-Th:IEICO-4F	39.2	EQE	Optical	[267]
PTB7-Th:IOTIC	25	EQE	Optical	[24]

(to be continued)

Material system	Urbach Energy E_U (meV)	Method	Scan type	Ref.
PTB7-Th:IOTIC-2Fa	25	EQE	Optical	[24]
PTB7-Th:IOTIC-4F	25	EQE	Optical	[24]
PTB7-Th:IOTIC-4F	26.8	EQE	Optical	[269]
PTB7-Th:ITIC	54.4	EQE	Optical	[244]
PTB7-Th:ITIC	54	EQE	Optical	[243]
PTB7-Th:PC71BM	45	EQE	Optical	[244]
PTB7-Th:PC71BM	45	EQE	Optical	[243]
PTB7-Th:PC71BM	31.6	EQE	Optical	[255]
PTB7-Th:PC71BM	32.6	EQE	Optical	[255]
PTzBI:N2200	32.8	PDS	Optical	[189]
rr-P3HT:PC61BM	57	PDS	Optical	[20]
Si-PCPDTBT:PC71BM	65.1*	CE	Voltage	[259]
TQ1:PC71BM	35	FTPS	Optical	[247]

Table A.3: Simulation parameters for the solar cells modeled in SCAPS specific to Chapter 6.

Figure No.	Parameter varied from default	Value
all	Frequency f (kHz)	10
6.3, A.1	Urbach energy E_{U} (meV)	30/55/80
6.8	Urbach energy tail 1 $E_{\mathrm{U},1}$ (eV)	26
	Urbach energy tail 2 $E_{\mathrm{U},2}$ (meV)	30/55/80
	VBT hole/CBT electron capture coefficient tail 2 $\beta_{1,2}$ ($\mathrm{cm^3 s^{-1}}$)	10^8
	VBT electron/CBT hole capture coefficient tail 2 $\beta_{2,2}$ ($\mathrm{cm^3 s^{-1}}$)	5×10^9
6.9, 6.10, 6.11, A.5	Electron/hole mobility $\mu_{\mathrm{n/p}}$ ($\mathrm{cm^2\,V^{-1}\,s^{-1}}$)	$10^{-4}/10^{-3}/10^{-2}$
A.2	Frequency f (Hz)	100 to 10^6
A.4a+b	VBT hole/CBT electron capture coefficient β_1 ($\mathrm{cm^3 s^{-1}}$)	$10^{-7}/10^{-8}/10^{-9}$
	VBT electron/CBT hole capture coefficient β_2 ($\mathrm{cm^3 s^{-1}}$)	$10^{-9}/10^{-10}/10^{-11}$
A.4c+d	Injection barrier anode/cathode $\phi_{\mathrm{an/cat}}$ (eV)	0/0.1/0.2
A.4e+f	Active layer thickness d (nm)	100/200/300
A.6	Electron/hole mobility $\mu_{\mathrm{n/p}}$ ($\mathrm{cm^2\,V^{-1}\,s^{-1}}$)	$10^{-4}/10^{-3}/10^{-2}$
	no Urbach tail	
	Width of the Gaussian trap density σ (meV)	50/100
	Peak density of trap states $N_{\mathrm{dt,peak}}$ ($\mathrm{cm^{-3}\ eV^{-}1}$)	10^{19}

Table A.4: Parameters set for the neural network training. The first neural network (NN 1) was trained to predicted logarithmic, shifted JV curves, the second neural network (NN 2) predicts the short-circuit current density J_{sc}.

Parameter	NN 1		NN 2
Total epochs	3000		10^4
Learning rate	Epochs<250:	10^{-3}	4×10^{-4}
	250<=Epochs<2000:	Reduction by factor 0.99	
		each epoch down to 4×10^{-4}	
	2000<=Epochs:	Reduction by factor 0.99	
		each epoch down to 10^{-4}	
Output points	512		4

Table A.5: Resulting validation error and training time of the neural networks for the different parameter estimation runs. The networks where trained either with illumination-dependent data for a *thin* or *thick* device or with thickness-dependent data under *dim* or *bright* illumination conditions. For each type of experiment, one neural network is trained with the logarithmic, shifted JV curves (NN 1) and one is trained with the short-circuit current densities (NN 2).

Experiment	Validation error NN 1	Training time NN 1	Validation error NN 2	Training time NN 2
Thin	6.7×10^{-7}	14:49h	5.3×10^{-8}	2:03h
Thick	8.9×10^{-7}	15:01h	3.4×10^{-7}	2:02h
Dim	5.7×10^{-7}	15:12h	7.7×10^{-7}	2:32h
Bright	6.5×10^{-7}	15:14h	10^{-6}	2:32h

Table A.6: Combination of experiments used for parameter estimation from four different illumination conditions and four active layer thicknesses. Parameter estimation on illumination-dependent data for a 83 nm thick device are labeled as *thin* and for a 308 nm device as *thick*. Thickness-dependent data is described as *dim* or *bright* corresponding to the illumination conditions.

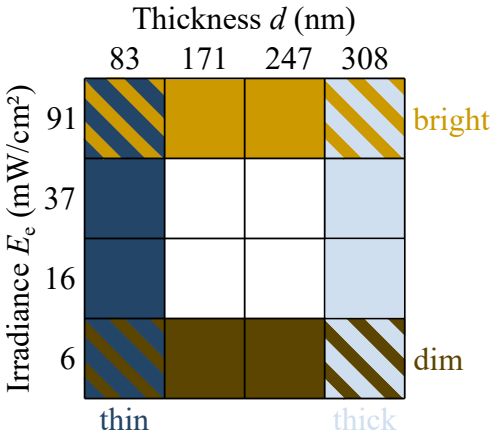

A.3. Supplementary Figures

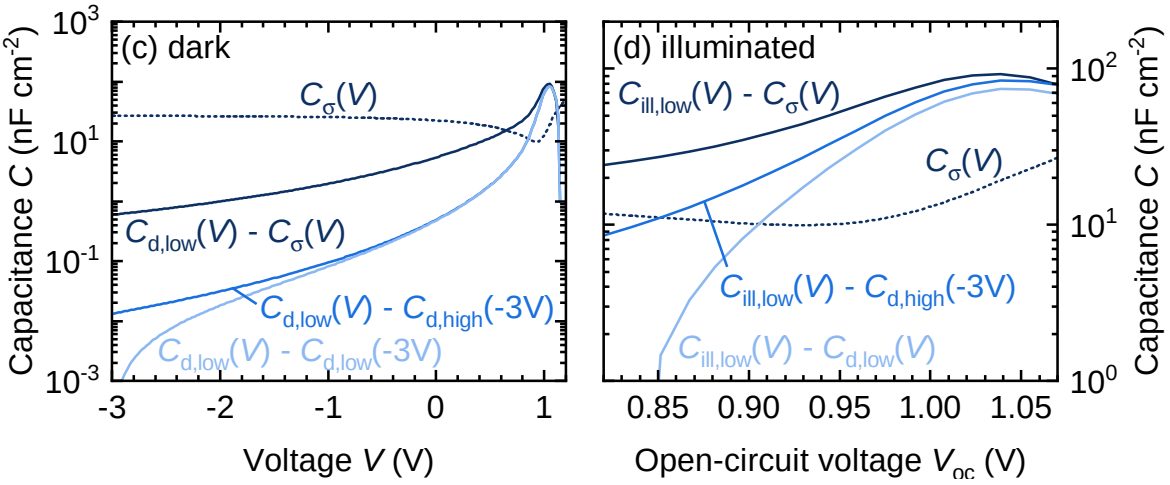

Figure A.1: Capacitances C (a) in the dark and (b) under illumination as a function of voltage V. The actual chemical capacitance C_μ is given by the difference $C_{low} - C_\sigma$ which is best replicated by $C_\mu = C_{low} - C_{d,high}(-3V)$ in this test. The indices "low" and "high" indicate the frequency and "d" and "ill" stand for dark and illumination, respectively.

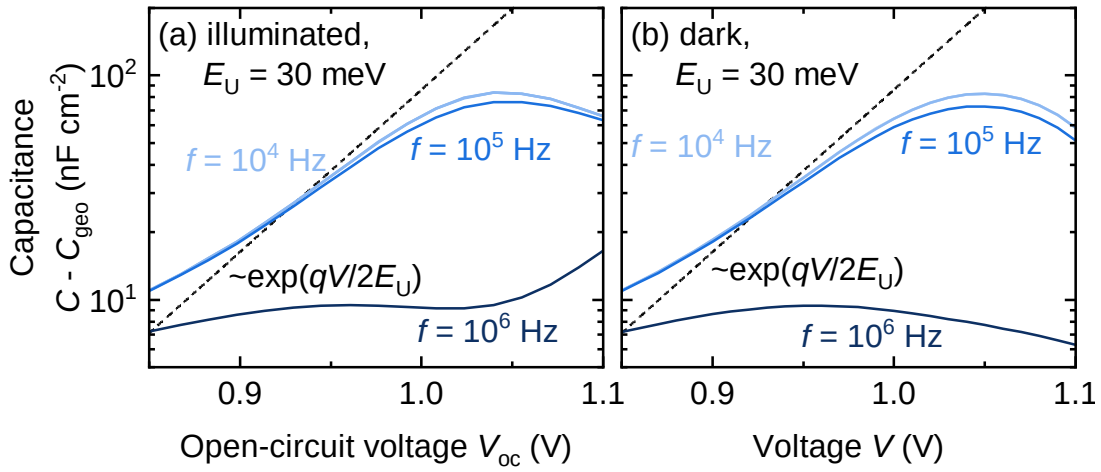

Figure A.2: Estimate of the chemical capacitance, the difference between the total capacitance C and the geometric capacitance C_{geo}, as a function of voltage V for an Urbach energy $E_U = 30$ meV at (a) open circuit and (b) in the dark. The frequency f of the alternating voltage signal was varied from 100 Hz to 1 MHz. While the capacitance is unaffected in the range from 100 Hz to 10 kHz, it decreases for higher frequencies since the charge carriers can no longer follow the changes in electric field and the total capacitance approaches the geometric capacitance.

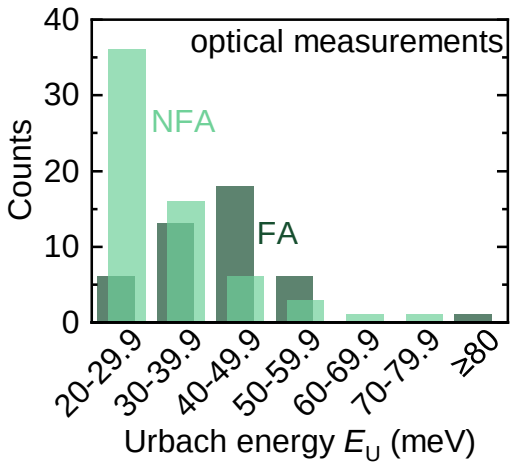

Figure A.3: Urbach energies E_U reported in literature measured by optical techniques.[20, 24, 40, 79, 181, 183, 185–189, 189–193, 218, 231–233, 237, 238, 244, 246–253, 262–272] Nonfullerene acceptors (NFAs) blends typically feature values closer to thermal energy than bulk heterojunctions comprising fullerene acceptors (FA).

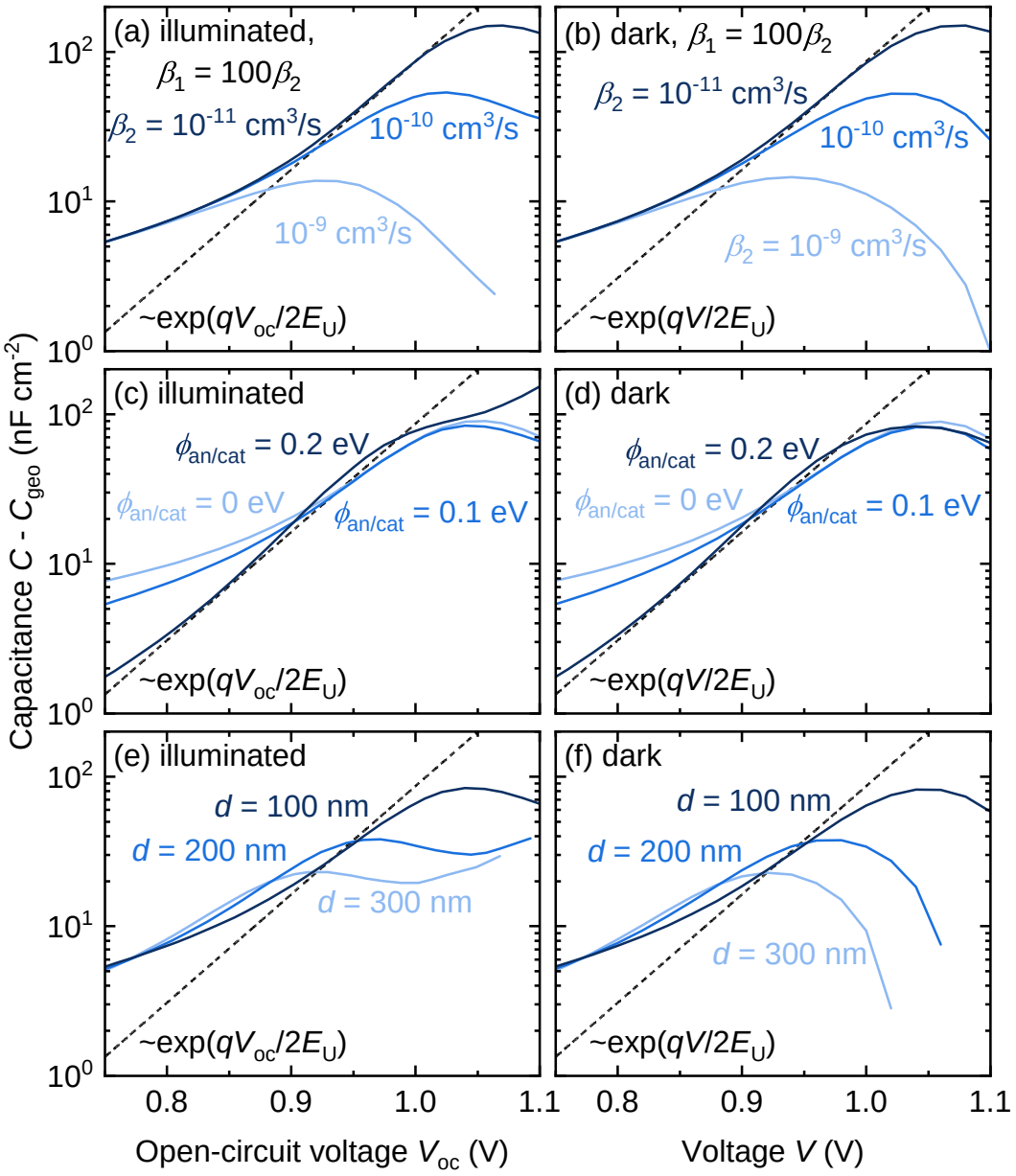

Figure A.4: Simulated capacitance as a function of voltage (a, c, e) under illumination at open circuit and (b, d, f) in the dark. In (a) and (b), recombination via the tail states is increased by increasing the capture rates β. (c) and (d) show a variation of the injection barriers $\phi_{an/cat}$ of the anode and cathode and in (e) and (f), the active layer thickness d is varied from thin layers of 100 nm to thick layers of 300 nm. The dashed lines indicate the slope corresponding to the Urbach energies E_U set in the simulations. In all cases, a flattening of the CV-curves can be observed.

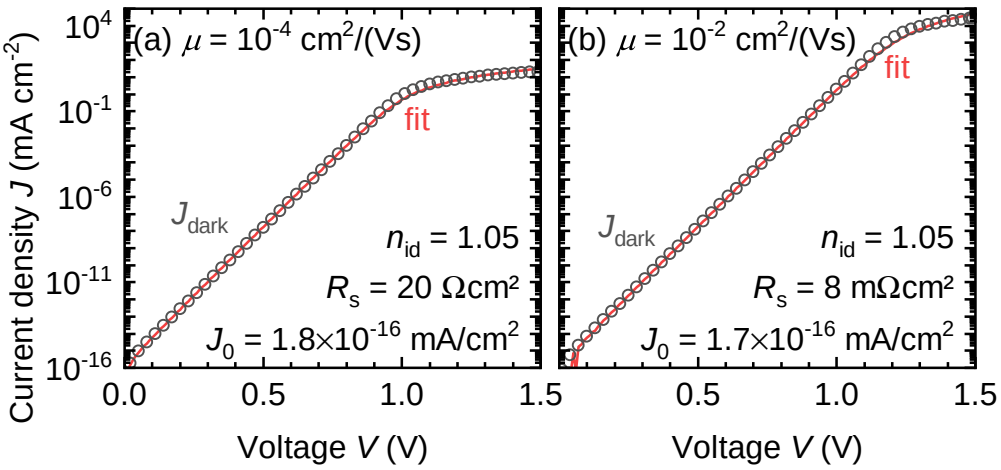

Figure A.5: Current-density voltage curves of a simulated organic solar cell in the open circles with (a) low charge-carrier mobility μ and (b) high mobility. The red line represents a fit with the fit parameters, the ideality factor n_{id}, the series resistance R_{s} and the saturation-current density J_0, displayed in the bottom right.

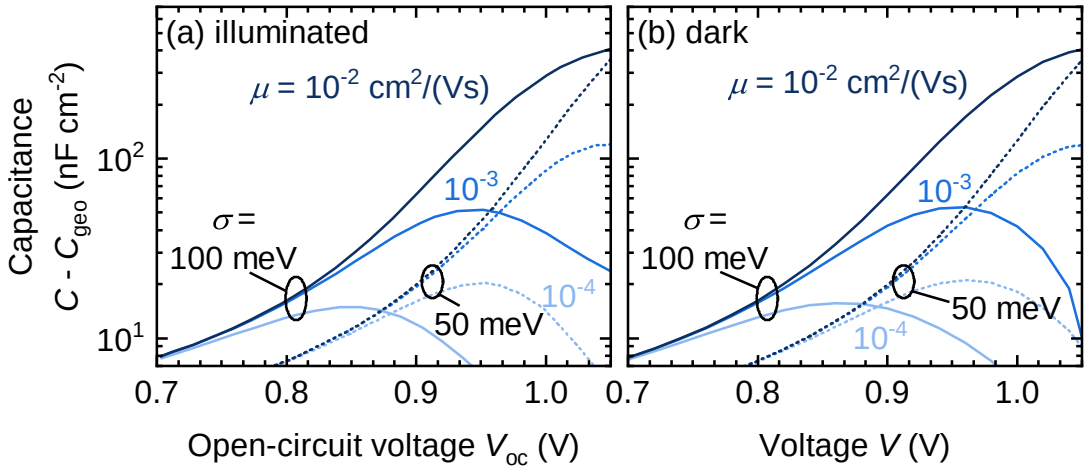

Figure A.6: Simulated capacitance $C - C_{\mathrm{geo}}$ (a) at open circuit under varying illumination intensity and (b) in the dark for different applied voltages V and for charge-carrier mobilities μ ranging from $10^{-4}\,\mathrm{cm}^2/(\mathrm{Vs})$ to $10^{-2}\,\mathrm{cm}^2/(\mathrm{Vs})$. The density of subgap states is set as a Gaussian function with its maximum at the band edge. The width σ of the Gaussian is set as 100 meV for the solid lines and 50 meV for the dotted lines. Similar to an exponential density of tail states, the shape of the CV curves is majorly influenced by the transport properties.

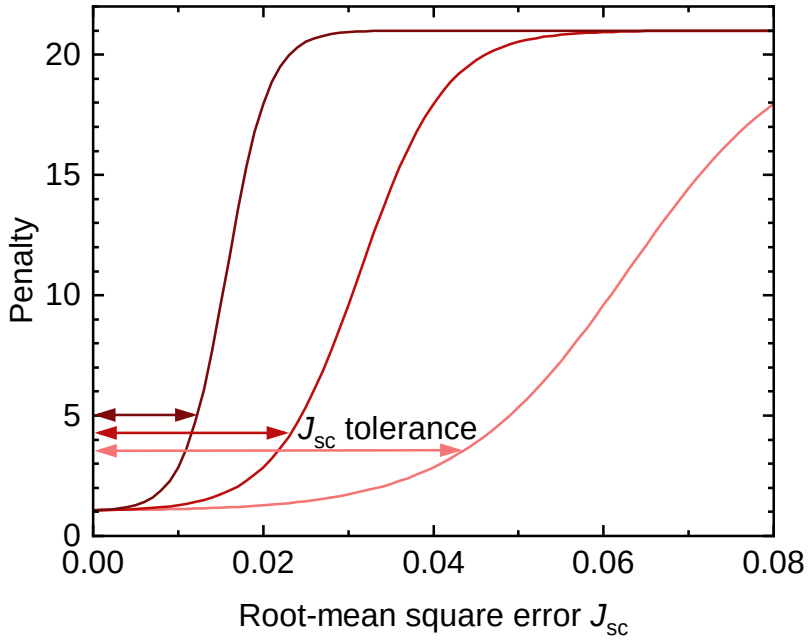

Figure A.7: Penalty function that is multiplied to the root-mean square error of the shifted *JV* curves to account for deviations between the predicted short-circuit current density J_{sc} and the measured one. At low root-mean square errors in the J_{sc}, the error is multiplied by one. At a certain error in J_{sc}, the penalty increases drastically dominating the total error. Thereby, some deviation in the J_{sc} during fitting is tolerated.

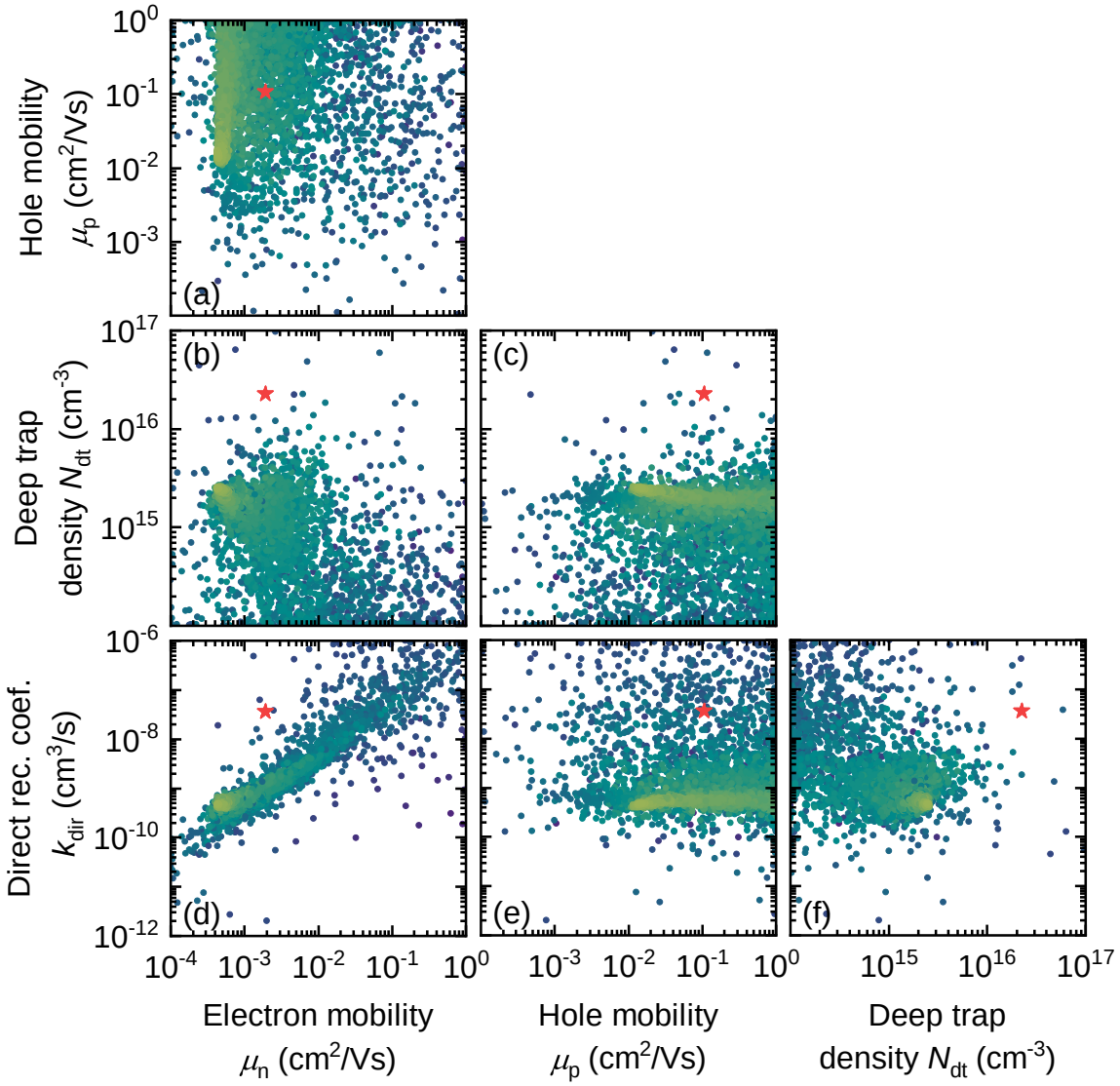

Figure A.8: Visualization of the fitting algorithm that fails to find the actual material parameters (red stars) of a simulated example. The electron mobility μ_n, hole mobility μ_p, defect density N_{dt} and direct recombination coefficient k_{dir} were selected for visualization. Each point represents one test of the optimization algorithm in the 7-dimensional space that contains the two parameters corresponding to the axes. The error decreases from the violet to the light green points. Since the optimization algorithm might miss the global optimum once, several restarts from different starting points are needed to ultimately find the absolute minimum.

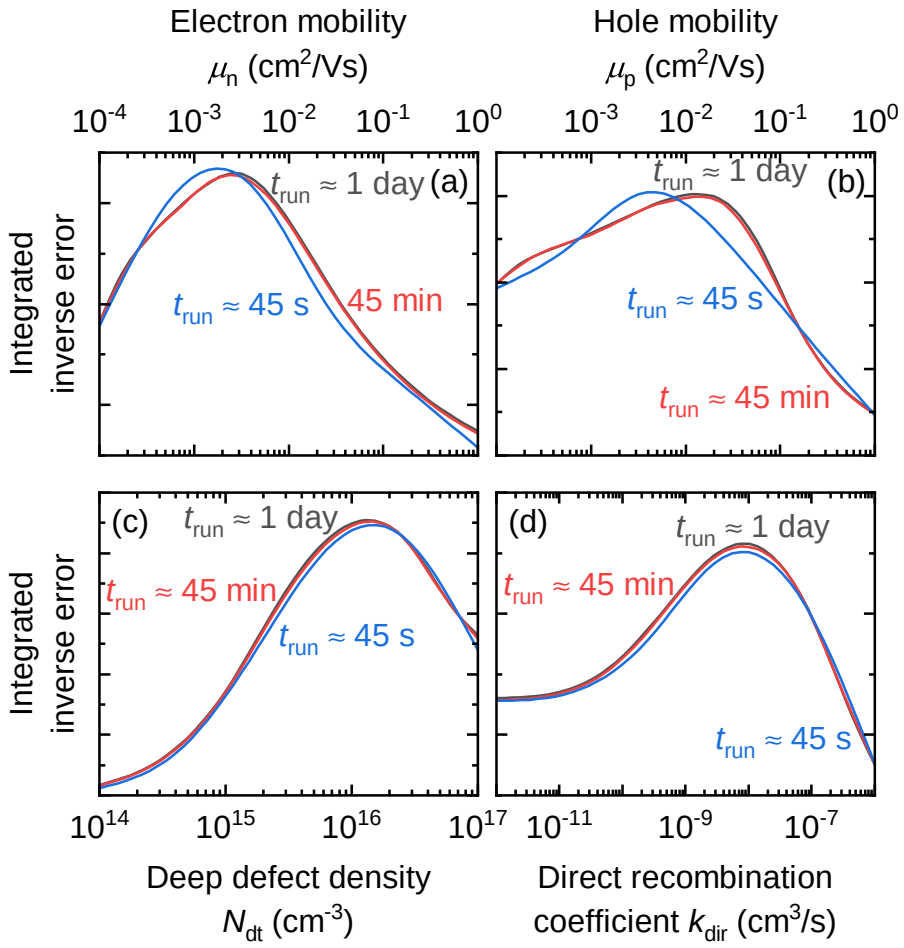

Figure A.9: Three grid search runs with 6(blue), 11(red) and 18(gray) points per axis interpolated with the 'spline' function of OriginPro. The inverse error was integrated over six dimensions except the (a) electron mobility μ_n, (b) hole mobility μ_p, (c) deep defect density N_{dt} and (d) direct recombination coefficient k_{dir}. Using this simple interpolation tool makes grid search runs with a high number of points unnecessary.

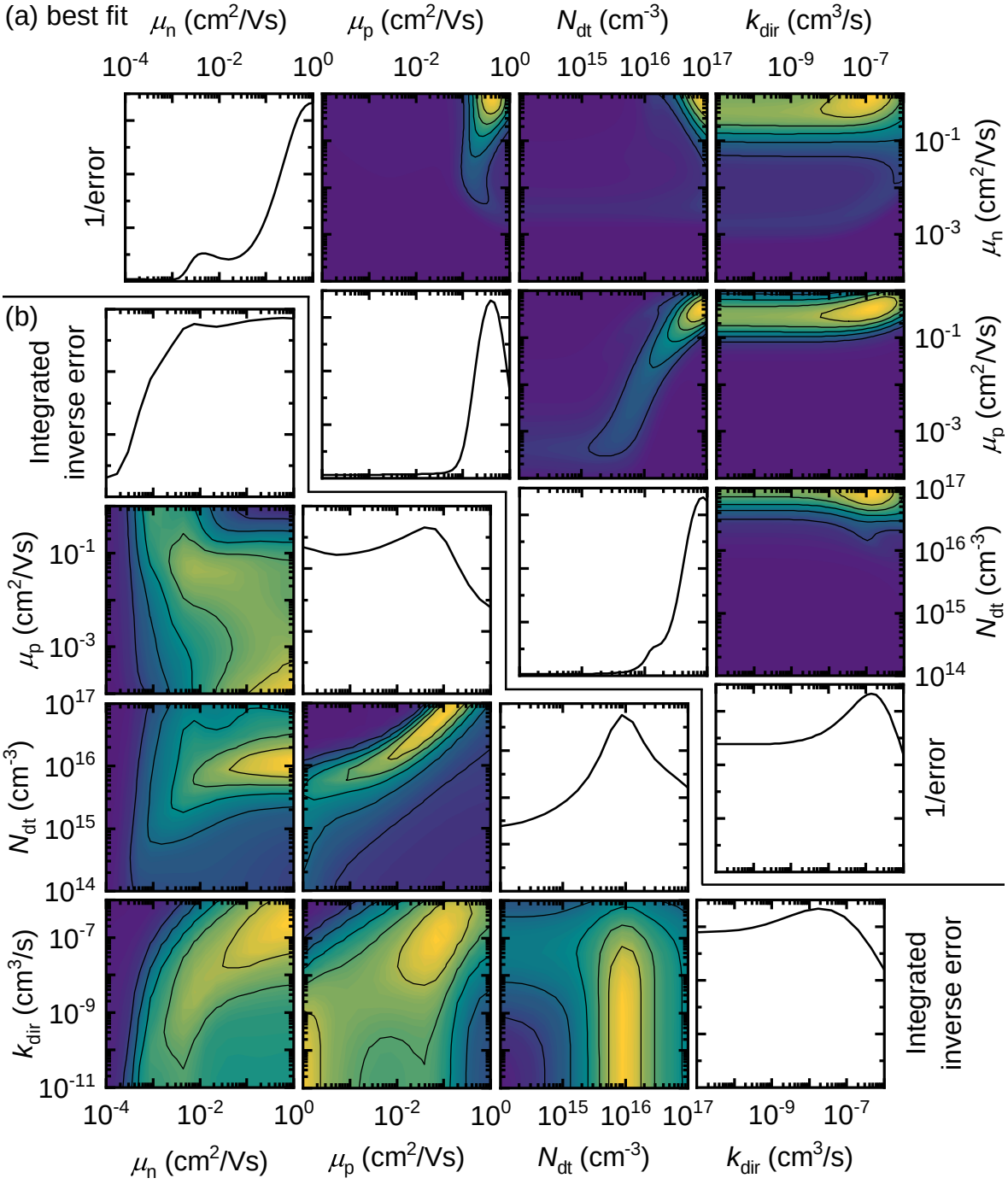

Figure A.10: Corner plots displaying the inverse error between the experimental data and the predictions by the neural network in the case of a solar cell with an active layer thickness 308 nm at irradiance values of 91, 37, 16 and 6 mW/cm^2 (a) as a slice in the six dimensions around the best fit and (b) integrated up over all dimensions except the ones displayed on the axes.

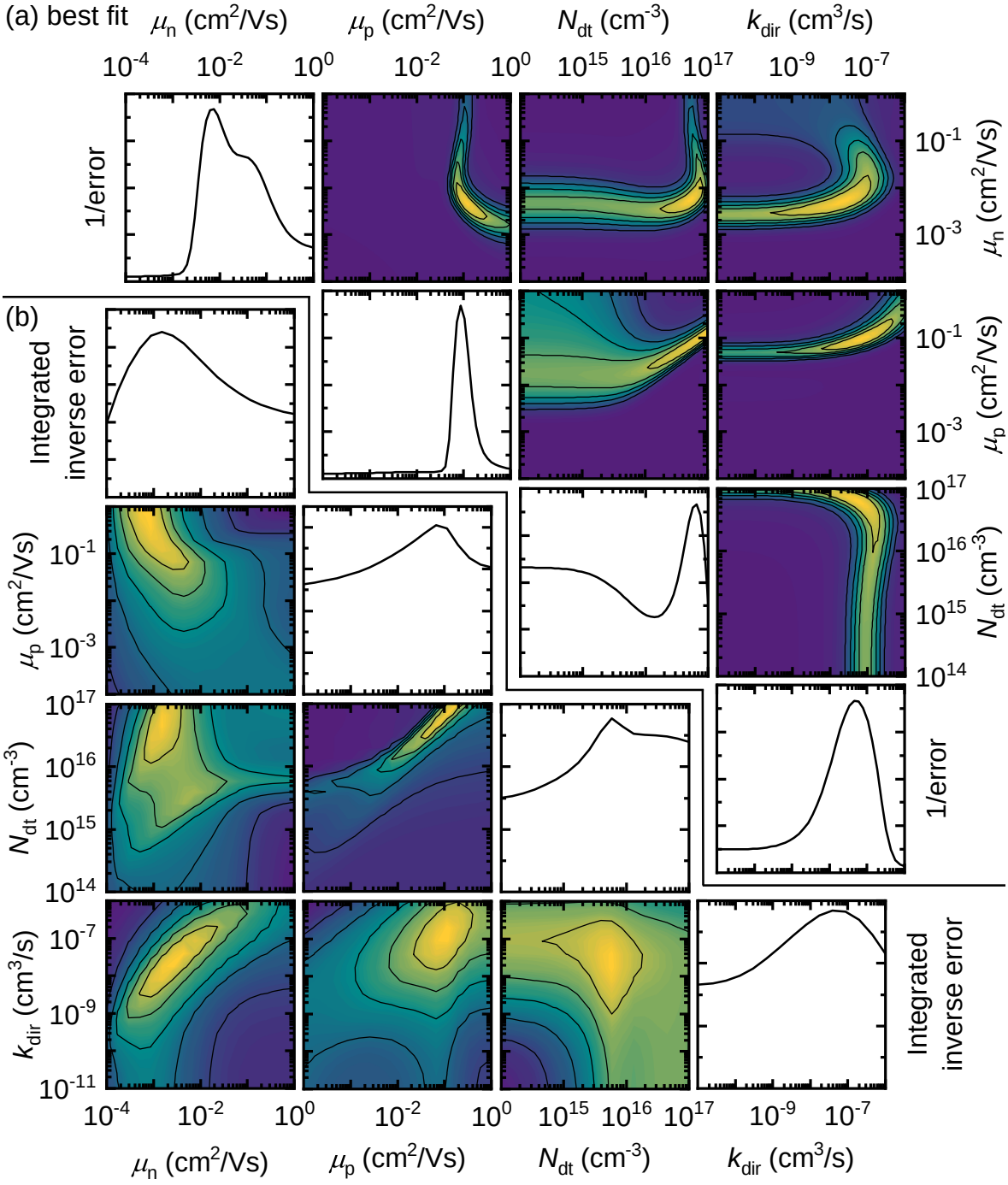

Figure A.11: Corner plots displaying the inverse error between the experimental data and the predictions by the neural network in the case of solar cells with active layer thicknesses of 83, 171, 247 and 308 nm at an irradiance of 6 mW/cm^2 (a) as a slice in the six dimensions around the best fit and (b) integrated up over all dimensions except the ones displayed on the axes.

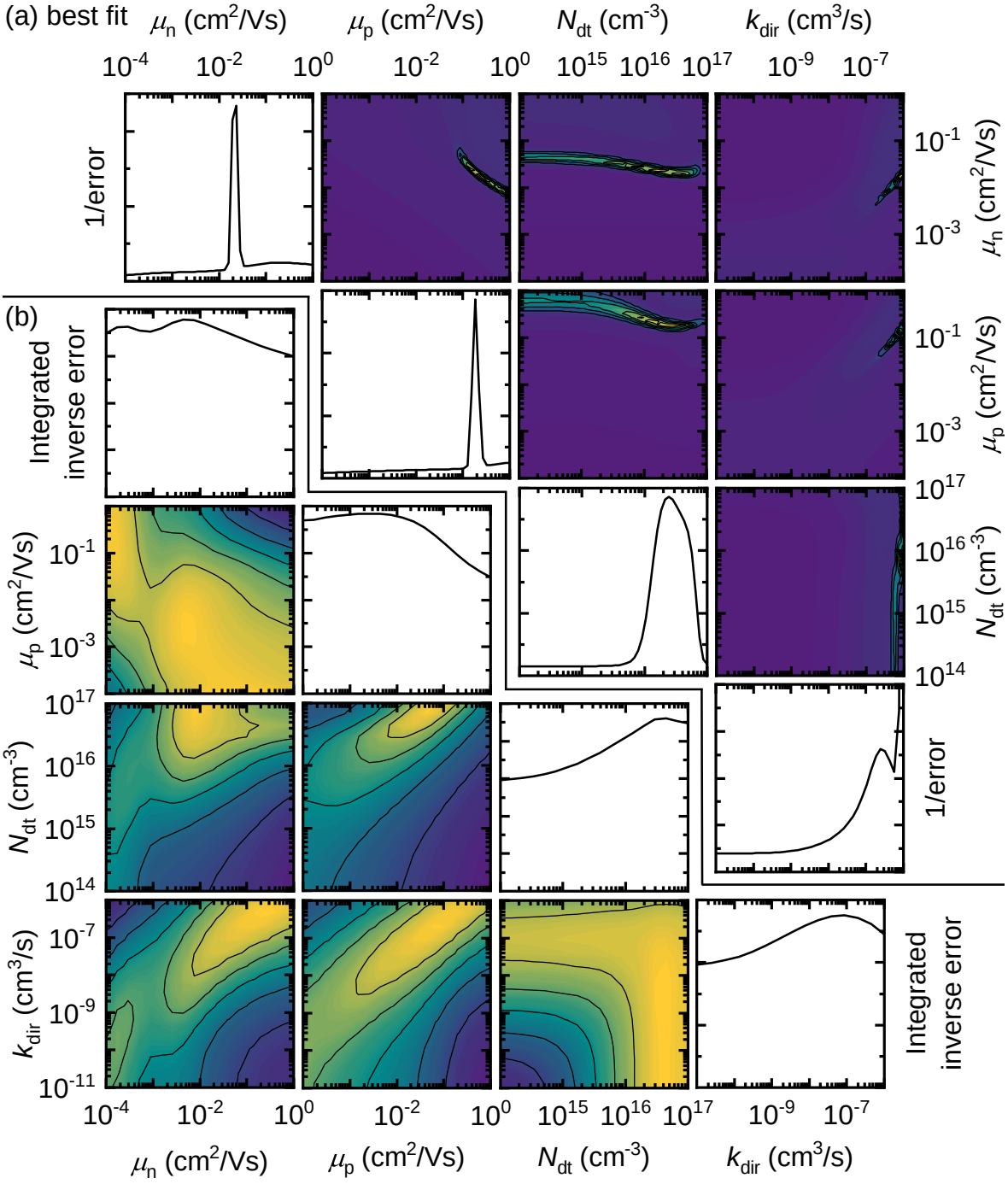

Figure A.12: Corner plots displaying the inverse error between the experimental data and the predictions by the neural network in the case of solar cells with active layer thicknesses of 83, 171, 247 and 308 nm at an irradiance of 91 mW/cm^2 (a) as a slice in the six dimensions around the best fit and (b) integrated up over all dimensions except the ones displayed on the axes.

A.4. Estimating the Active Layer Thickness

The active layer thickness has significant influence on the amount of photons that are absorbed in a solar cell and on the extraction of charge carriers. However, there is no way to directly measure an organic solar cell's active layer thickness since it is part of a full layer stack as presented in Chapter 3.1.2.

One option is producing a layer on glass under the same processing conditions. By scratching the layer, the step at the scratch can be measured with, for example, a profilometer. However, it cannot be assumed that the adhesion of the blend solution and the film growth is the same on glass as it would be on the hole transport layer PEDOT:PSS in the full stack. Furthermore, different solar cells fabricated on one substrate do not necessarily feature the same active layer thickness due to an inhomogeneous sample coverage. Similarly, extracting one active layer thickness for all solar cells produced with the same processing conditions also neglects sample-to-sample variations.

Another nondestructive method of estimating the active layer thickness is by measuring the capacitance of a solar cell under high reverse bias in the dark. As explained in Chapter 3.2.3, under these conditions, it can be assumed that the active layer is completely depleted of charge carriers. When assuming the resulting geometric capacitance C_{geo} as a plate capacitor, the active layer thickness d can be derived as

$$d = \frac{\varepsilon_0 \varepsilon_{\mathrm{r}}}{C_{\mathrm{geo}}} \tag{A.1}$$

with the geometric capacitance in the units [F/m^2]. The method has also been applied in the Reference [131] and [196]. This attempt of calculating the active layer thickness requires the knowledge of the relative permittivity ε_{r}, though, which is in turn hard to quantify. Therefore, guessing the relative permittivity brings great uncertainty to the values estimated from capacitance measurements. In addition, this method assumes the interfaces of the active layer to be completely smooth. Any surface roughness will increase the effective area[312] and therefore lead to an error in the active layer thickness.

A third option for estimating the active layer thickness is measuring the thickness of the full specific solar cell with a profilometer and then subtracting the thicknesses of all contact layers that were measured separately. As this approach yields an individual active layer thickness for each solar cell without assuming a relative permittivity, it

is chosen for the estimation of active layer thicknesses in Chapter 7. Still, it bears the risk that a small systematic error in the profilometer measurements can sum up for all of the contact layers. Comparing the short-circuit current densities J_{sc} for the solar cells characterized in this work with the ones predicted from the optical model, it appears that the interference minima and maxima seem shifted by an additive constant of around 30 nm. So, the first interference maximum in the experimental data appears at an active layer thickness that is 30 nm higher than in the simulated data. This shift cannot be caused by inaccuracy in the extinction coefficient κ, as its influence is multiplicative (see for example Equation 2.29). Hence, to shift the the J_{sc}-d relation by an additive constant, the extinction coefficient would have to be thickness-dependent. Therefore, it is more likely, that the thickness estimation with the profilometer led to an error of 30 nm. So, if each thickness of the other layers in the stack was slightly underestimated, the active layer thickness could potentially be overestimated by 30 nm. In consequence, all values for d that are used in Chapter 7 are corrected by this value. Thereby, the optical data for this material system as extracted by spectroscopic ellipsometry was used for the estimation of the active layer thickness.

A.5. Calculation of the Incoming LED Spectrum

As established in the field of indoor photovoltaics, the knowledge of the incoming photon spectrum is essential for comparability between measurements.[131,313] Since the light-intensity dependent data sets in this work were measured with an LED, here, the knowledge of spectral irradiance $E_{e,\lambda}$ is additionally important for the analysis of the light-intensity dependence of the short-circuit current density in Chapter 5.4 and for the fitting procedures in Chapter 7. The LED was characterized for a previous work in Reference [196] and I scaled the spectral irradiance $E_{e,\lambda}$ to match the measurements conducted by Barbara Urbano[194] that I analyze in this work. Examples of the spectra that were measured are shown in Figure A.13a. Here, the three filter settings that were used for the JV curves are displayed, namely without a filter at an optical density (OD) of zero, with a 1.3OD filter and a 2.5OD filter. The spectrum for 2.5OD was not measured explicitly but calculated from the spectrum without a filter using the trans-

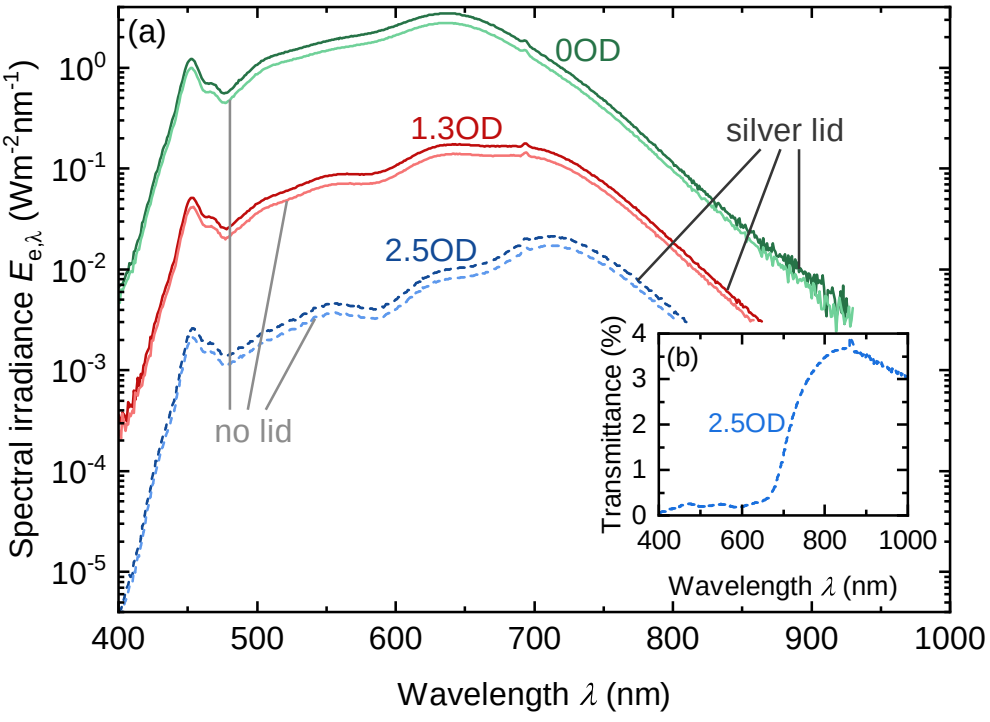

Figure A.13: (a) Spectral irradiance $E_{e,\lambda}$ measured without a filter (0OD) and with a 1.3OD filter at an LED current of 200 mA through a silver lid or without any lid. The spectra for the 2.5OD filter were calculated by multiplying the 0OD spectrum with the transmittance of the 2.5OD filter in (b). The transmittance was supplied by the filters' manufacturer.

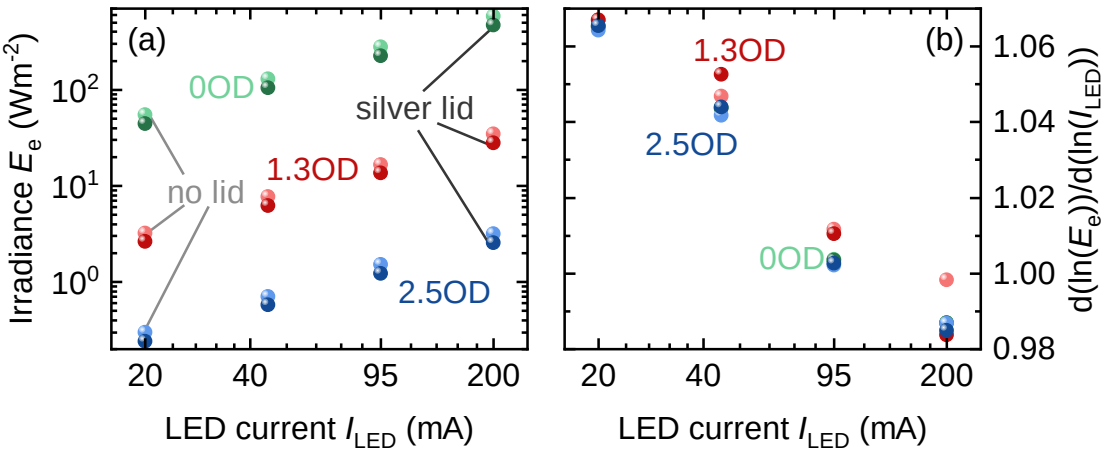

Figure A.14: (a) Irradiance E_e measured for four different LED driving currents I_{LED} with a silver lid and without a lid. (b) Logarithmic slope of the irradiance and the LED current indicating a mostly superlinear relation between the two quantities.

mittance of the filter (see Figure A.13b). For the characterization, the solar cells are encapsulated in measurement boxes to protect them from ambient air. However, some of the metal lids are reflective and silver around the glass window above the solar cell itself, which can have an influence on the light that actually reaches the solar cell inside the measurement box. To estimate the influence of the lids, Figure A.13a shows measurements of the spectral irradiance $E_{e,\lambda}$ through such a lid and without any lid. It visualizes how a reflective lid can influence the amount of light that is coupled into the solar cell. As only some of the solar cells were measured with such a reflective lid, this phenomenon additionally complicates assigning the correct LED spectrum to a given JV characteristic.

To achieve further variation in the light intensity apart from the usage of filters, the driving current I_{LED} of the LED can be changed to scale its spectrum. Here, linearity between the driving current I_{LED} and the irradiance E_e is assumed. Figure A.14 tests this relation by showing (a) the irradiance E_e that was measured for different driving currents I_{LED} and (b) the logarithmic slope of these plots. For all filters and lid configurations, the double-logarithmic slope appears to be close to one indicating a linear relationship between the irradiance E_e and the driving current I_{LED}. So, for fitting purposes, scaling the spectrum according to its driving current appears accurate. However, for the purpose of identifying recombination mechanisms from small deviations in the slope of J_{sc} with the irradiance E_e in Chapter 5.4, the degree of nonlinearity is already severe.

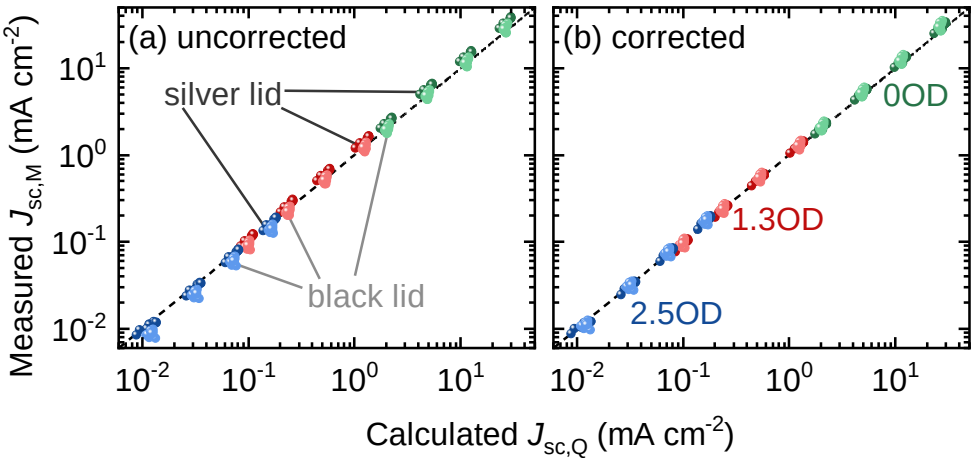

Figure A.15: (a) Short-circuit current density $J_{sc,M}$ measured under LED illumination as a function of the short-circuit current density $J_{sc,Q}$ that was calculated from external quantum efficiency measurements and the scaled LED spectra. Ideally, both values should be the same and lay on the black dashed line. (b) Comparison of the measured and calculated short-circuit current densities for LED spectra that were corrected by a factor for the black lid, the silver lid and the 2.5OD filter, each.

Once the spectra have been scaled to the accurate LED driving current, they can be used to calculate the short-circuit current density $J_{sc,Q}$ with the help of external quantum efficiency measurements. The comparison of these values with the ones that were actually measured can give an indication on the accuracy of the spectra. Figure A.15a shows this measured short-circuit current density $J_{sc,M}$ as a function of $J_{sc,Q}$. For the JV curves that were measured with the silver lid, the corresponding spectrum with the silver lid was used in the calculations. For the other type of lid, a black one with a larger window, I used the spectrum measured without a lid as no influence by the lid is expected. While the points for the black lid lie mostly on the line of equal $J_{sc,Q}$ and $J_{sc,M}$ in Figure A.15a, the measured values are too high compared to the calculated ones for the silver lid. In addition, the estimation of the spectrum for the 2.5OD filter with the transmittance leads to an overestimation of the calculated short-circuit current density $J_{sc,Q}$. In consequence, I used the average deviation for the black lid, the silver lid and the 2.5OD filter to calculate correction factors for the LED spectra. The short-circuit current densities calculated with these corrected spectra are shown in Figure A.15b, which shows that the three correction factors help achieving matching values for the JV measurements and the estimated ones. The spectra used for the calculations in Figure A.15b are therefore used in this work wherever the incoming spectrum is needed.

A.6. List of Publications

The following publications can be viewed as pre-publications of extracts of this thesis:

- P. Hartnagel, S. Ravishankar, B. Klingebiel, O. Thimm, and T. Kirchartz, "Comparing Methods of Characterizing Energetic Disorder in Organic Solar Cells," *Advanced Energy Materials*, vol. 13, no. 15, 2023
- P. Hartnagel and T. Kirchartz, "Understanding the Light-Intensity Dependence of the Short-Circuit Current of Organic Solar Cells," *Advanced Theory and Simulations*, vol. 3, no. 10, p. 2000116, 2020

Further publications by the author:

- X. Rodríguez-Martínez, P. Hartnagel, S. Riera-Galindo, G. Beket, T. Österberg, F. Gao, T. Kirchartz, and O. Inganäs, "Air Processing of Thick and Semitransparent Laminated Polymer:Non-Fullerene Acceptor Blends Introduces Asymmetric Current–Voltage Characteristics," *Advanced Functional Materials*, p. 2301192, 2023
- D. Lübke, P. Hartnagel, M. Hülsbeck, and T. Kirchartz, "Understanding the Thickness and Light-Intensity Dependent Performance of Green-Solvent Processed Organic Solar Cells," *ACS Materials Au*, vol. 3, no. 3, pp. 215–230, 2023
- D. Lübke, P. Hartnagel, J. Angona, and T. Kirchartz, "Comparing and Quantifying Indoor Performance of Organic Solar Cells," *Advanced Energy Materials*, vol. 11, no. 34, 2021
- S. Beuel, P. Hartnagel, and T. Kirchartz, "The Influence of Photo-Induced Space Charge and Energetic Disorder on the Indoor and Outdoor Performance of Organic Solar Cells," *Advanced Theory and Simulations*, vol. 4, no. 3, p. 2000319, 2021
- P. Kaienburg, P. Hartnagel, B. E. Pieters, J. Yu, D. Grabowski, Z. Liu, J. Haddad, U. Rau, and T. Kirchartz, "How Contact Layers Control Shunting Losses from Pinholes in Thin-Film Solar Cells," *The Journal of Physical Chemistry C*, vol. 122, no. 48, pp. 27263–27272, 2018

A.7. Acknowledgments

With the completion of this thesis, I want to thank all the people who have made this accomplishment even possible. First and foremost, I would like to thank Prof. Dr. Thomas Kirchartz for letting me be part of his group for all these years. From being an intern with practically no knowledge on solar cells to the completion of this PhD, I felt like I was leaving each conversation with him a little smarter.

Also, I want to acknowledge the hybrid and organic solar cells group. For our Duisburg group, a huge thank you to my colleagues Dana Lübke, Lenni Christen and Eunji Kim. To Dana, for her open and honest communication and numerous scientific discussions, even though they often left us more confused than ever. To Lenni for always asking the right questions, making it easier for me to leave the organizational work and the labs in his and Eunji's hands. Also part of our Duisburg group were Sebastian Beuel, Barbara Urbano and Anne Krause. In all of our student-supervisor relationships, learning was truly a two-way street.

Thank you to the Jülich group and their warm welcomes every time we actually met in person. I would like to express my gratitude to Dr. Basita Das, for sharing her code and expertise on machine learning and many off-topic conversations with me. A special thank you to Dr. Benjamin Klingebiel for regularly being the savior with his quick replies in any lab related emergency, for all the organizational work and for the FTPS measurements. Thank you to Oliver Thimm for conducting the PDS measurements and Dr. Karsten Bittkau for the ellipsometry measurements. Also, I acknowledge Dr. Sandheep Ravishankar for his efforts in finding an analytical description for the transport problems in admittance measurements.

And lastly thank you to Stefan Behrensmeyer for keeping the NETZ building running and always being helpful beyond his actual obligations.